

The Pennsylvania State University

The Graduate School

Eberly College of Science

**A NEUTRON SCATTERING INVESTIGATION
OF THE COLLECTIVE EXCITATIONS OF
SUPERFLUID HELIUM IN POROUS MEDIA**

A Thesis in Physics

by

Robert M. Dimeo

Submitted in Partial Fulfillment
of the Requirements
for the Degree of

Doctor of Philosophy

May 1999

We approve the thesis of Robert M. Dimeo

Date of Signature

Paul E. Sokol
Professor of Physics
Thesis Advisor
Chair of Committee

Sridhar Komarneni
Professor of Clay Mineralogy

Jay S. Patel
Professor of Physics, Electrical Engineering,
and Materials Research

Roy F. Willis
Professor of Physics

John Yeazell
Assistant Professor of Physics

Jayanth R. Banavar
Professor of Physics
Head of Department of Physics

ABSTRACT

Inelastic neutron scattering has been used to probe the microscopic dynamics of superfluid helium adsorbed in various porous materials. The substrates used to confine the superfluid were porous vycor glass, silica aerogel of two different porosities, and silica xerogel. As in bulk superfluid helium, the confined helium atoms exhibit well-defined cooperative motions, or collective excitations, but modified due to the disorder induced by confinement. Rotons, the helium excitations responsible for the thermodynamic behavior of the bulk liquid above 1 K, confined in aerogel display a unique crossover behavior in temperature dependence where they are relatively temperature independent below 1.9 K and strongly temperature dependent above 1.9 K. A completely new set of excitations are observed for helium in porous vycor glass which are consistent with the layered excitations observed in thin helium films but only predicted to exist in certain porous media. In fact the measurements presented in this thesis not only present the first such observations of the layered excitations in porous media but they also reveal that there are *multiple* layered excitations in the adsorbed helium spectrum. The measurements of helium adsorbed in xerogel show that the layered excitations are present in this system as well. Furthermore these measurements indicate that the layered excitations are relatively independent of helium filling fraction whereas a bulk-like roton present in the confined spectrum displays a very strong dependence on filling fraction.

While the confinement seems to have a profound influence on the excitations of superfluid helium, the modifications in the excitations appear to be consistent with the macroscopic dynamics of the confined liquid as determined via thermodynamic and transport measurements. Therefore these measurements provide a much-needed link between the microscopic excitations of confined helium and the macroscopic properties.

TABLE OF CONTENTS

LIST OF FIGURES.....	vii
LIST OF TABLES	xii
ACKNOWLEDGMENTS	xiii
CHAPTER 1 INTRODUCTION	1
CHAPTER 2 REVIEW OF SUPERFLUIDITY AND POROUS MEDIA.....	6
2.1 Superfluid Helium	6
2.1.1. Macroscopic Properties	6
2.1.2. Microscopic Properties.....	13
2.2 Porous Media	30
2.3 Superfluidity in Porous Media	37
CHAPTER 3 NEUTRON SCATTERING FORMALISM	50
3.1 Neutron Scattering Kinematics	51
3.2 Neutron Scattering Dynamics	53
3.3 The Helium Lineshape.....	60
CHAPTER 4 MEASUREMENT TECHNIQUES.....	66
4.1 Neutron Production	67
4.1.1 Reactor-Based Neutron Sources	68
4.1.2 Spallation Neutron Sources	71
4.2 Neutron Spectrometers	72
4.2.1 The Triple-Axis Spectrometer	73
4.2.2 The Direct Geometry Time-of-Flight Spectrometer	77
4.2.3 The Inverse Geometry Time-of-Flight Spectrometer.....	84
4.3 Instrumental Resolution.....	88
4.4 Experimental Details	93

4.4.1	Common Procedures	94
4.4.2	The Aerogel Measurements.....	96
4.4.3	The Vycor Measurement	102
4.4.4	The Xerogel Measurement	110
CHAPTER 5 SUPERFLUID HELIUM IN SILICA AEROGEL		116
5.1	Data Analysis	117
5.2	Results.....	124
5.3	Connection with Macroscopic Measurements	135
5.4	Recent Measurement of Helium in Aerogel	138
CHAPTER 6 SUPERFLUID HELIUM IN POROUS VYCOR GLASS		143
6.1	Data Analysis	145
6.2	Results.....	151
6.3	Connection with Macroscopic Measurements	159
CHAPTER 7 SUPERFLUID HELIUM IN SILICA XEROGEL		164
7.1	Data Analysis	165
7.2	Results.....	165
7.3	Connection with Macroscopic Measurements	175
CHAPTER 8 CONCLUSION.....		178
8.1	Confinement in Silica Aerogel.....	178
8.2	Confinement in Porous Vycor Glass	180
8.3	Confinement in Silica Xerogel.....	181
8.4	Outstanding Questions and Final Remarks.....	182
APPENDIX A NEUTRON SCATTERING PARAMETERS AND CONSTANTS ...		188
APPENDIX B DATA REDUCTION AND ANALYSIS PROGRAMS		189
APPENDIX C THE STATISTICAL MECHANICS OF TWO DIMENSIONAL ROTONS		195
APPENDIX D PROGRAM LISTING FOR FIT_SCAT.PRO.....		202
APPENDIX E LISTING OF RAW DATA FILES		230
REFERENCES		234

LIST OF FIGURES

Figure 2.1 Illustration of why helium does not solidify at low temperatures.....	8
Figure 2.2 Specific heat of ^4He near T_λ	10
Figure 2.3 Normal and superfluid components for helium below T_λ (dashed line).	11
Figure 2.4 Phase diagrams of (a) ^4He and (b) ^3He [25].....	12
Figure 2.5 The collective excitation spectrum of superfluid helium (solid line).....	15
Figure 2.6 Normal fluid fraction as a function of temperature which incorporates both the phonon and roton contributions (adapted from [24]).....	23
Figure 2.7 The temperature dependence of the roton energy gap, Δ for bulk superfluid helium [48]. Solid line is a fit to theory.	24
Figure 2.8 Pore size distribution for porous vycor glass [54].....	33
Figure 2.9 TEM of silica aerogel (from National Center for Electron Microscopy at the Lawrence Berkeley National Laboratory).....	35
Figure 2.10 TEM of a xerogel sample [57]. Width of image is roughly 1350 Å.....	36
Figure 2.11 Temperature dependence of the superfluid fraction near the transition temperature for confinement in various materials. (Solid line is the superfluid fraction in the bulk liquid). Figure adapted from [67].	40
Figure 2.12 Temperature dependence of the superfluid fraction near the transition temperature for confinement in vycor and aerogel. Data have been plotted to illustrate the power-law behavior of the transition. Figure adapted from [68].	41
Figure 2.13 Contour plot of the excitations in thin superfluid helium films adsorbed onto exfoliated graphite [22].	49
Figure 3.1 Neutron scattering kinematics in real space (top figure), and in reciprocal space (bottom figure).	52
Figure 3.2 Geometry for a neutron scattering measurement.	53

Figure 3.3 The classical mechanical analog of the damped harmonic oscillator model. The phonon created by a neutron is represented by a lumped element, the mass on a spring, while the phonon field is represented by a distributed element, a string attached to the mass. The string provides a channel to carry away the phonon's energy.	61
Figure 4.1 A reactor-based neutron source.	68
Figure 4.2 Energy distributions of neutron flux from a moderator at temperatures of 40 K (cold neutrons) and 300 K (thermal neutrons).	70
Figure 4.3 Principle components of a spallation neutron source.	72
Figure 4.4 Functional diagram of a triple-axis spectrometer.	74
Figure 4.5 Functional diagram of a direct geometry TOF spectrometer.	78
Figure 4.6 Constant angle cuts through Q-E space for a direct geometry TOF instrument (solid line) and an inverse geometry instrument (dotted line), and a constant-Q cut for a TAS (dashed line). Paths in Q-E space for two different detectors on the TOF instruments have been plotted.	80
Figure 4.7 Functional diagram of an indirect geometry TOF spectrometer.	85
Figure 4.8 Resolution ellipsoids for a TAS at various points in the four-dimensional Q-E space. Adapted from [98].	89
Figure 4.9 Effective instrumental resolution function determined at the roton minimum for different instruments used in this thesis.	93
Figure 4.10 Schematic illustration of the gas handling system used in the SPINS and FCS measurements. The large storage volume used in the SPINS measurement (storage volume + manifold = 31.586 liters) was replaced with a 22.24 liter storage volume for the FCS measurement.	96
Figure 4.11 Schematic illustration of the sample cell used in the SPINS measurement.	97
Figure 4.12 Scattering at the roton momentum at 1.48 K. Solid line is a fit of the instrumental resolution function convoluted with the DHO discussed in the text.	99
Figure 4.13 Range of the IRIS spectrometer (solid curves) and the SPINS spectrometer (bold dashed line for reference). The bulk helium dispersion curve is shown as the open circles indicating that both measurements covered the roton excitation. The dashed line indicates the Landau parabolic roton dispersion curve.	100

- Figure 4.14 Range of IN6 (solid curve) in this configuration. Bulk helium dispersion curve shown as circles and dashed line is the Landau parabolic dispersion curve for rotons..... 103
- Figure 4.15 Design drawing for sample cell used in the IN6 measurement of helium in vycor and bulk helium..... 105
- Figure 4.16 Example TOF spectrum from detector group 72 ($2\theta=80.28^\circ$) for helium in vycor. Scattering angle for this detector group is coincident with momentum transfer for the bulk roton. First peak in time is the elastic scattering component and the second peak is the bulk-like roton signal. 108
- Figure 4.17 Design drawing of sample cell for helium in xerogel measurement. 112
- Figure 4.18 Range of FCS (solid curve) in the current configuration. Bulk helium dispersion curve shown as circles and dashed line is the Landau parabolic dispersion curve for rotons..... 114
- Figure 5.1 SPINS scattering data at $Q = 1.92 \text{ \AA}^{-1}$ at temperatures of (a) 1.92 K, (b) 2.01 K, and (c) 2.11 K. 118
- Figure 5.2 Resolution-broadened scattering data for helium in 90% porous aerogel. The vertical axis is in increasing energy and the horizontal axis is momentum transfer. 121
- Figure 5.3 Scattering from helium in aerogel at 1.55 K on the IRIS spectrometer. The solid line is a fit of the DHO model (equation (4.17)) convoluted with the instrumental resolution function. 123
- Figure 5.4 Dispersion of the collective excitations near the roton minimum at each temperature. The solid lines are the fits of the Landau parabolic dispersion relation to the extracted peak centers. 124
- Figure 5.5 Temperature dependence of the roton energy in (a) 90% porous aerogel and (b) 95% porous aerogel. Bulk data shown by squares [48]. In (a) the confined data shown with the circles and in (b) the confined data are shown with circles [75] and diamonds (SPINS data)..... 125
- Figure 5.6 Scattering data indicating the difference in peak position at (a) 1.9 K (IRIS data) and (b) 1.92 K (SPINS data) with respect to the bulk peak position (arrow). The peak position for this data is shown by the solid vertical line..... 126

- Figure 5.7 Roton linewidth (HWHM) in (a) 90% porosity aerogel and (b) 95% porosity aerogel. In (a) and (b) the squares are the bulk linewidths [48]. In (b) the circles are the data of Gibbs et. al. [75] and the diamonds are the SPINS data. 127
- Figure 5.8 Schematic illustration of the competing length scales for helium in aerogel. Intersection of the two curves occurs at the crossover temperature. Above the crossover temperature, roton-roton interactions dominate while below the crossover temperature roton-media interactions dominate. 130
- Figure 5.9 Plot of the temperature dependent roton energy for the bulk superfluid (circles) [48] and confined to 95% porosity aerogel (squares)..... 131
- Figure 5.10 Conceptual drawing of the vortex lines (dashed lines) decorating the interior of the aerogel. Most of the vortex lines terminate on the strands of the aerogel (solid lines) while some close in on themselves (vortex rings). 134
- Figure 5.11 The normal fluid fraction and heat capacity for the bulk liquid (triangles and diamonds) [48,67,113] and confined liquid (squares and circles) [67,112] plotted in a manner to illustrate the validity of the Landau excitation model. The functions plotted in terms of the data are $F_1 = \ln((\rho_n/\rho)T^{1/2})$ and $F_2 = \ln(CT^{3/2})$ vs. Δ/T 137
- Figure 6.1 Specific heat for helium in vycor as a function of pore filling. Full pore vycor (open circles) displays significant rounding in the peak but there is no cusp-like behavior. Adapted from [116]. 144
- Figure 6.2 Illustration of the function used to model the multiphonon component of the scattering. Dashed lines are the narrow and broad gaussians defined in (6.2) and (6.3) and the solid line is the analytic expression (6.4). 147
- Figure 6.3 Constant angle data near the roton minimum for helium in vycor at 500 mK. Dashed lines are the individual components of the total fit and the solid lines are the overall fits. Values of Q at the bulk-like roton energy are (a) 1.78 \AA^{-1} , (b) 1.81 \AA^{-1} , (c). 1.85 \AA^{-1} , (d) 1.89 \AA^{-1} , (e) 1.92 \AA^{-1} , and (f) 1.95 \AA^{-1} 148
- Figure 6.4 Constant angle data near the roton minimum for helium in vycor at 1.1 K. Dashed lines are the individual components of the total fit and the solid lines are the overall fits. Values of Q at the bulk-like roton energy are (a) 1.79 \AA^{-1} , (b) 1.82 \AA^{-1} , (c). 1.86 \AA^{-1} , (d) 1.93 \AA^{-1} , (e) 1.96 \AA^{-1} , and (f) 1.99 \AA^{-1} 149
- Figure 6.5 Temperature variation of the (a) bulk-like roton energy gap (circles) and (b) the roton mass (circles). The bulk values are shown for reference (triangles) [48]. Smooth lines are fits of the BPZ expression to the roton energy gap..... 155

- Figure 6.6 Dispersion of the bulk-like roton (solid circles) and the two additional scattering contributions represented by the lower energy gaussians in figure 6.3. ... 158
- Figure 6.7 Dispersion of the bulk-like roton (solid circles) and the two additional scattering contributions represented by the lower energy gaussians in figure 6.4. ... 159
- Figure 6.8 (a) Heat capacity data [116] and (b) normal fluid fraction data [69] for helium in vycor plotted to illuminate the 2-D and 3-D character in different temperature regimes. 162
- Figure 7.1 Fits to the scattering data of helium in xerogel at the roton minimum (momentum) at fill fractions of (a) 0.4, (b) 0.6, (c) 0.8, and (d) 0.95 and a temperature of 1.36 K. Fit functions are represented by the dashed lines and the sum of the fit functions is shown by the solid line. Detector groups 13-15 have been added together to improve statistics..... 166
- Figure 7.2 The variation of integrated intensity of the bulk-like (circles) and two lower energy components (diamonds and squares) with fill fraction for helium in xerogel. Dashed lines have been added as a guide to the eye..... 168
- Figure 7.3 The variation of the center of the bulk-like (circles) and two lower energy components (diamonds and squares) with fill fraction for helium in Britesorb. Dashed line is the value of the bulk roton energy found on this instrument..... 168
- Figure 7.4 Coverage dependence of the integrated intensity of the bulk-like roton (closed circles) and the two-dimensional roton (open circles) for helium on Graphon. Adapted from [81]. 170
- Figure 7.5 Film geometry used to obtain equation (7.1). 171
- Figure 7.6 Integrated intensity of the two-dimensional roton as a function of pore coverage for helium in xerogel. Solid line is a fit of equation (7.1) to the data..... 173
- Figure 7.7 Coverage dependence of the bulk-like roton energy for helium on Graphon. Adapted from [81]. 174
- Figure 7.8 Normal fluid fraction data for helium in xerogel plotted to illuminate the 2-D and 3-D character in different temperature regimes. 177

LIST OF TABLES

Table 5.1 Summary of roton parameters in 95% porosity aerogel. The asterisk (*) denotes values determined by Gibbs <i>et. al.</i> [75].	119
Table 5.2 The temperature dependence of the roton parameters in 90% porous aerogel.	122
Table 6.1 Summary of the bulk-like roton parameters for helium in vycor.	152
Table C.1 Summary of statistical mechanics of ideal roton gases in two and three dimensions [37].	200
Table E.1 Raw data file listing	230

ACKNOWLEDGMENTS

There are many people who have assisted me during the course of this thesis research and I am very grateful to all of them. First and foremost I thank my advisor Paul Sokol who has taught me many things about research techniques, low temperature physics, data analysis as well as effective teaching methods. His uncommon combination of respectful guidance and dark humor make him a unique advisor and have made my time as a graduate student an enjoyable and educational experience. I would also like to thank my thesis committee members for their valuable input and feedback on this thesis. I thank Bill Stirling at the University of Liverpool for a fruitful collaboration, enlightening discussions, and useful career advice. I also owe a great deal of thanks to Mark Adams at ISIS whose diligence and hard work assisting with the measurements at ISIS and the ILL ultimately paid off with some very interesting results. Mark's expert knowledge of instrumentation and ability to communicate technical difficulties to anyone (even in French) resulted in him unknowingly becoming a role model. There are a number of others who have assisted with measurements and sample preparation to whom I am grateful, namely Charlotte Anderson (Liverpool), Seung-Hun Lee (NCNR), Richard Azuah (Liverpool), David Silva (PSU), Nathan Grube (PSU), Ken Andersen (ILL), Claire Rutiser (PSU MRL), Man Park (PSU MRL), and Don Brown (PSU). I am grateful to the staffs at the ILL, ISIS, and NCNR for help in sample preparation and general technical assistance and the Physics Department machine shop and office staff for their help.

On a personal note, I would like to acknowledge my friendships with Don Brown and David Silva. It has been a pleasure working *with* them and learning *from* them. I also acknowledge many fruitful conversations with Daniel Cartin. These conversations always left me with a better understanding of whatever it was we were discussing and I will miss these conversations. I owe a debt of gratitude to my family for putting up with short holiday breaks and one or two unfortunate absences during the holidays over the past few years. My deepest gratitude goes to my wife, Kathy. Without her loving support, unending patience, and many sacrifices I would not have been able to complete this work.

My father told me a long time ago that diligence and hard work lead to success. My mother taught me that loving ones vocation is a key ingredient to success. They both set excellent examples in each regard and I believe that, in some sense, I have captured a bit of each of their spirits. Therefore I dedicate this thesis to my mother, Judith, and the memory of my father, Michael.

This work was supported by NSF grant DMR No. 9624762, INT. No. 9214242, and INT No. 9600172. I would also like to acknowledge the support of the Physics Department at the Pennsylvania State University.

CHAPTER 1

INTRODUCTION

Superfluid helium is a model system whose unique properties have provided the basis for analogies in such disparate subjects as superconductivity [1] to the birth of the universe [2]. It is one of the most often studied systems in condensed matter physics, due in large part to its purity. For instance, it has been used as a model system in studies of superconductivity [1], strongly interacting Bose systems [3], and critical phenomena [4]. Helium condenses from gas to a colorless liquid at a temperature of 4.2 K. As the temperature of the liquid drops below 2.18 K it undergoes a phase transition where the transport properties of the liquid change dramatically. In this low temperature phase helium can flow without dissipation and supports dissipationless heat transport. This unique phase, in the bulk liquid, has been extensively characterized both macroscopically and microscopically.

Since it is so well-characterized and pure, helium provides a model system with which one can examine the effects of disorder and confinement. Since the first measurements of superfluidity there have been many studies of the macroscopic effects of confinement and disorder on superfluidity, particularly the effects of confinement in porous glasses. However the microscopic effects of disorder and confinement on superfluidity have not received nearly the same attention.

One motivation for studying superfluid helium in a porous glass is that it is a *many-body system* in a *disordered environment*. As a many-body system its dynamics are contained in the collective excitations of the interacting helium system which can be easily accessed using inelastic neutron scattering. In a low energy inelastic neutron scattering measurement of bulk superfluid helium one obtains direct information on the cooperative atomic motions. These cooperative motions are particularly well defined in superfluid helium manifesting themselves as extremely sharp resonances indicative of the *elementary* or *collective* excitations of the liquid [5]. The collective excitations can be used to determine the macroscopic properties of the bulk superfluid, which is the main result of the Landau excitation model (discussed at length in chapter 2).

A many-body system in a disordered environment represents an entire class of problems which are of current interest in condensed matter physics [6,7]. Since most systems in nature are not perfect and contain some form of impurity, an understanding of the role of disorder is not simply academic. For instance liquids frequently have impurities dissolved in them, magnetic crystals are seldom free from defects or magnetic impurities [6], solids usually contain defects which destroy their perfect translational invariance [8], and liquid crystals can contain disclinations (discontinuities in orientation) [9]. Thus the microscopic characterization of “real” materials necessarily involves some consideration of disorder.

As an example of the effects that disorder can have on condensed matter systems we can consider conductivity. In high- T_c superconductors disorder can cause the pinning of vortices which subsequently break up the Bose-condensed Cooper pairs and hence destroy superconductivity [10-12]. In addition, disorder introduced into a simple metal can induce a metal-insulator transition. In this case the disorder can cause a localization of the conduction electrons, a phenomenon known as Anderson localization [8]. These two examples illustrate that very desirable properties of real systems, in these cases conductivity, can be severely affected by the presence of disorder.

The disorder which is induced by confinement of superfluid helium in porous glasses is typically referred to as *quenched*. Quenched disorder is static since the glassy network replaces a finite volume of the liquid, thus destroying the liquid's isotropy. This is in contrast to systems with *annealed* disorder such as dilute ^3He - ^4He mixtures. The effects of confinement are additionally complicated by the fact that the helium interacts with a very large amorphous surface provided by the porous glass. In some sense the situation is less complicated for the case of a thin superfluid helium film where only interactions with the surface are important and surface excitations dominate the cooperative atomic motion.

An understanding of the microscopic excitations of superfluid helium films provides a first step towards an understanding of the confined liquid system. As in the bulk liquid, the characteristics of superfluid films can be traced directly to the microscopic

excitations. Inelastic neutron scattering studies of thin helium films indicate that there are additional excitations present as well as precursors to the bulk superfluid excitations [13]. These additional excitations are caused by interactions with the substrate and the dimensionality of the film. The direct observation of these new excitations in helium films provides agreement with the thermodynamic data and illustrates the clear link between the microscopic and macroscopic dynamics of the films analogous to the link which Landau put forth for the bulk liquid in the Landau excitation model [13-22]. Since the excitation spectrum provides information on the coherent atomic motions of the atoms in the film, knowledge of the spectrum is essential to a fundamental understanding of helium films.

The theoretical and experimental situation is not nearly so complete for helium confined to porous media. To date the inelastic neutron scattering data for helium in porous media are sparse compared with the published thermodynamic measurements. Therefore the measurements discussed in this thesis serve two purposes. First, they provide a much-needed link between the microscopic excitations in confined helium with the macroscopic data. While extensive thermodynamic and transport measurements of helium in porous glasses have been adequately *modeled* with a modified microscopic excitation spectrum in the past, no *direct* measurements of the excitation spectrum for these systems have been performed which corroborate the changes induced by confinement. Second, in a more general sense, these measurements illustrate that the

microscopic effects of disorder on a many-body system can be examined quite readily using inelastic neutron scattering.

The remainder of this thesis is laid out as follows. Chapter two provides an introduction to superfluidity, porous materials, and the macroscopic behavior of superfluid helium in porous materials. In chapter three a discussion of the mathematical formalism used in neutron scattering is presented as well as a discussion of the superfluid helium signature as measured using neutron scattering. The fundamentals of the measurement technique, inelastic neutron scattering, is presented in chapter four along with a review of the neutron production facilities, instrumentation used during the course of this thesis research, the main experimental details, and the data reduction methods. In chapters five, six, and seven the data analysis and interpretation are presented for the neutron scattering measurements of superfluid helium confined to porous vycor glass, silica aerogel, and silica xerogel. The main conclusions of this body of work are summarized in chapter 8.

CHAPTER 2

REVIEW OF SUPERFLUIDITY AND POROUS MEDIA

In this chapter we present a review of superfluidity and porous media thus setting the stage for the measurements discussed in this thesis. We begin with a review of macroscopic and microscopic properties of bulk superfluid helium. Reference is made to neutron scattering and thermodynamic measurements to illustrate the connection between the collective excitation spectrum and the macroscopic properties of the liquid. Next we discuss porous media and the various properties of different porous materials. Finally a review of the measurements of superfluid helium confined to porous materials to date is presented in order to provide the context for the measurements performed during the course of this thesis research.

2.1 Superfluid Helium

2.1.1. Macroscopic Properties

The only known permanent liquids in nature are ^4He and ^3He . Their classification as permanent liquids results from the fact that neither of them solidifies at any temperature under their own saturated vapor pressure. In fact it requires about 25 atmospheres of applied pressure to solidify ^4He at 1 K and about 50 atm to solidify ^3He at 1 K. Their status as permanent liquids is one of the first hints that ^4He and ^3He are dominated by

quantum effects. These effects have now been observed to give rise to many interesting phenomena such as superfluidity.

The unique properties of the condensed phases of the heliums result from the weak interactions and light mass of the helium atom. The helium atom has a closed electronic shell so that the dominant interaction between individual atoms is the weak Van der Waals force. Furthermore, since there are only two electrons in helium they are tightly bound, leading to a small polarizability, further weakening the Van der Waals forces. Due to the weakness of these interactions the quantum zero point energy (QZPE) plays a large role in the condensed phases. This energy arises from the confinement of the atom to a finite region of space. In the simplest model, an atom in the solid can be treated as being confined to a spherical well of infinite depth. In this case, the QZPE is given by

$$E = \frac{n^2 \pi^2 \hbar^2}{2mr^2}$$

where m is the atomic mass, r is the width of the well, and n is the quantum

number. As the well decreases in size the kinetic energy of the confined atom increases. For helium under its own vapor pressure the magnitude of the kinetic energy of the atom exceeds the weak trapping potential given by the Van der Waals force which prevents the helium atom from remaining confined and solidifying. A sketch of the weak Van der Waals potential for a helium atom is shown in figure 2.1. As seen in the figure the potential for the helium atom is relatively shallow compared with that of the H_2 molecule. However when the effects of the quantum zero point motion are included in the potential the well becomes even more shallow. In contrast, the potential for the H_2 molecule still

maintains a substantial well depth despite the quantum zero point motion. In fact H_2 solidifies at about 14 K. The fact that helium does not solidify even at absolute zero implies that quantum effects manifest themselves on a macroscopic scale.

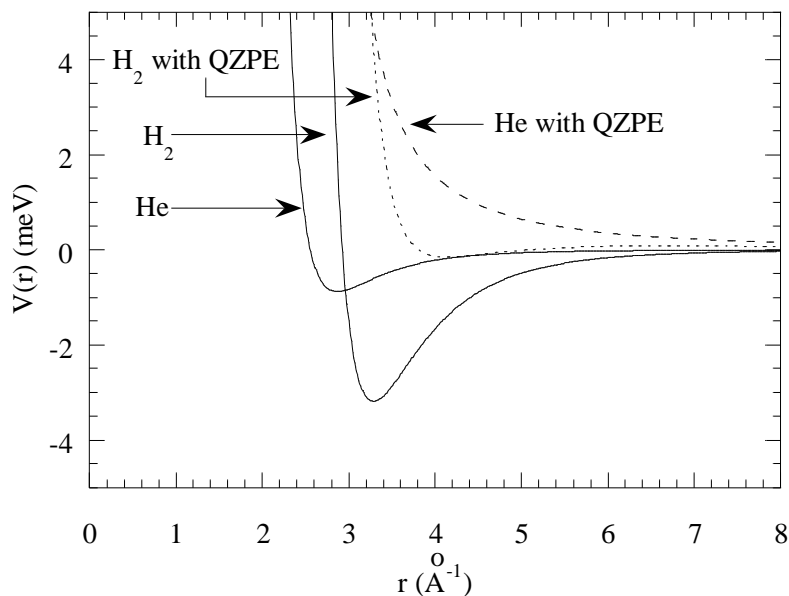


Figure 2.1 Illustration of why helium does not solidify at low temperatures.

Both of the quantum liquids, ^3He and ^4He , are interesting, but historically ^4He was the first to exhibit *superfluidity*. It liquifies at about 4.2 K exhibiting properties not unlike other liquids. As the temperature is lowered through the boiling point the liquid bubbles violently. However as the temperature is lowered through 2.17 K a remarkable transition occurs in which all boiling ceases and the liquid becomes very still (where its motionlessness has been likened to a “dry martini” [23]). Apparently the liquid undergoes a marked increase in thermal conductivity so that no “hot spots” (due to

thermal fluctuations) can occur in the liquid and no bubbles from boiling can occur. In addition, as the temperature is lowered through 2.17 K the transition is accompanied by a sharp cusp-like anomaly in the heat capacity reminiscent of the greek letter lambda as illustrated in figure 2.2.

Some further unique properties of helium below 2.18 K are listed below.

- The viscosity of the liquid as measured by the resistance of flow through small channels nearly vanishes.
- A heat pulse generated within the liquid propagates coherently as opposed to diffusively.
- A container with helium in it at very low temperatures forms a thin mobile film on its walls and empties.

These properties of *super*-flow and heat superconductivity are indicative that the liquid has undergone a transition from the normal liquid state into the superfluid state. The temperature at which the superfluid transition occurs (also referred to as the lambda temperature due to the specific heat anomaly) is about $T_\lambda = 2.17$ K.

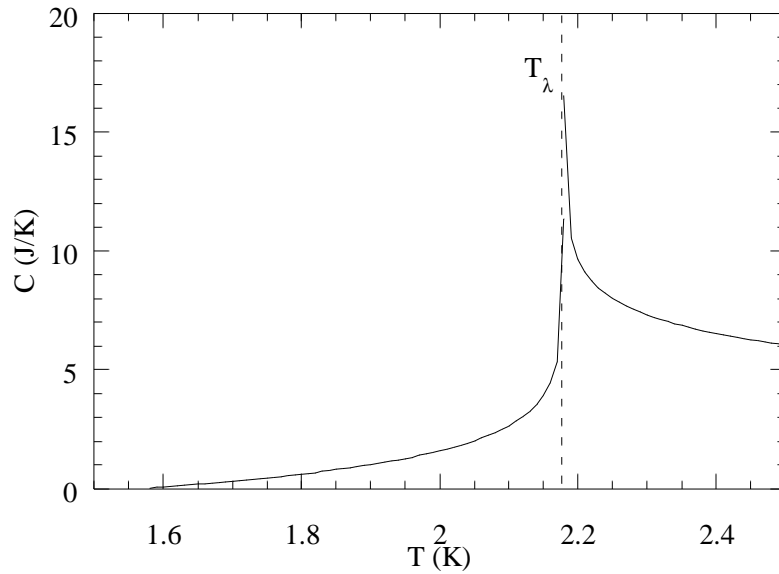


Figure 2.2 Specific heat of ^4He near T_λ .

Below T_λ , the unusual behavior of the superfluid can be described phenomenologically using the *two-fluid model*. In this model the complete mass density, ρ , of the liquid is treated as though it were composed of a normal fluid component, ρ_n , and a superfluid component, ρ_s which are completely interpenetrating but distinct. The properties of the normal fluid component are identical to those of a normal liquid which possesses a finite thermal resistance and a non-zero viscosity. The superfluid component however, possesses no thermal resistance, viscosity, nor entropy.

In the two fluid model, the normal and superfluid components possess different temperature dependences. The normal fluid fraction, ρ_n/ρ , is 1 at T_λ and decreases to zero as absolute zero is approached. Likewise the superfluid fraction, ρ_s/ρ , is zero at T_λ

and increases to 1 at absolute zero so that the sum of the two fractions is always 1. The temperature dependence of the normal fluid fraction (and hence the superfluid fraction via $\rho_s/\rho = 1 - \rho_n/\rho$) has been determined via torsional oscillator measurements in which a series of closely-spaced stacked disks are rotated in the liquid (see [24] for a description of these measurements). The normal fluid clamps to the oscillator which provides an additional inertial load that can be measured from the response of the forced oscillator. The temperature dependence of each of these components is shown in figure 2.3.

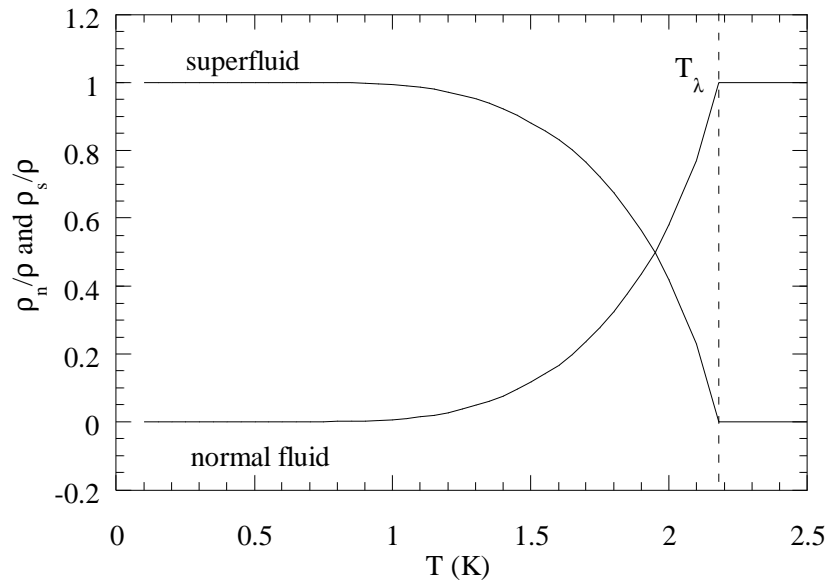


Figure 2.3 Normal and superfluid components for helium below T_λ (dashed line).

Further indications that quantum effects determine the behavior of the helium liquids at low temperatures can be seen in the phase diagram of ^3He and ^4He , shown in figure 2.4. Both liquids exhibit superfluidity. However the portion of the phase plane for ^4He

(identified as He-II in the figure) is much larger than that for ^3He . In fact ^3He is superfluid below about 3 mK but the region on the phase diagram for ^3He is far too small to be seen on this scale. The underlying reason for the lack of a large superfluid region in the ^3He system is that a ^3He nucleus has a spin $\frac{1}{2}$ thus obeying fermi statistics while the ^4He nucleus has a spin of 1 obeying bose statistics. A necessary condition for superfluidity is that the particles which make up the system obey bose statistics, a condition which is not satisfied by ^3He . However under very special circumstances ^3He can become a superfluid. This occurs when ^3He atoms join pairwise thus becoming a system of bose quasi-particles. Therefore the small superfluid region in ^3He compared with that of ^4He is due primarily to the effects of quantum statistics.

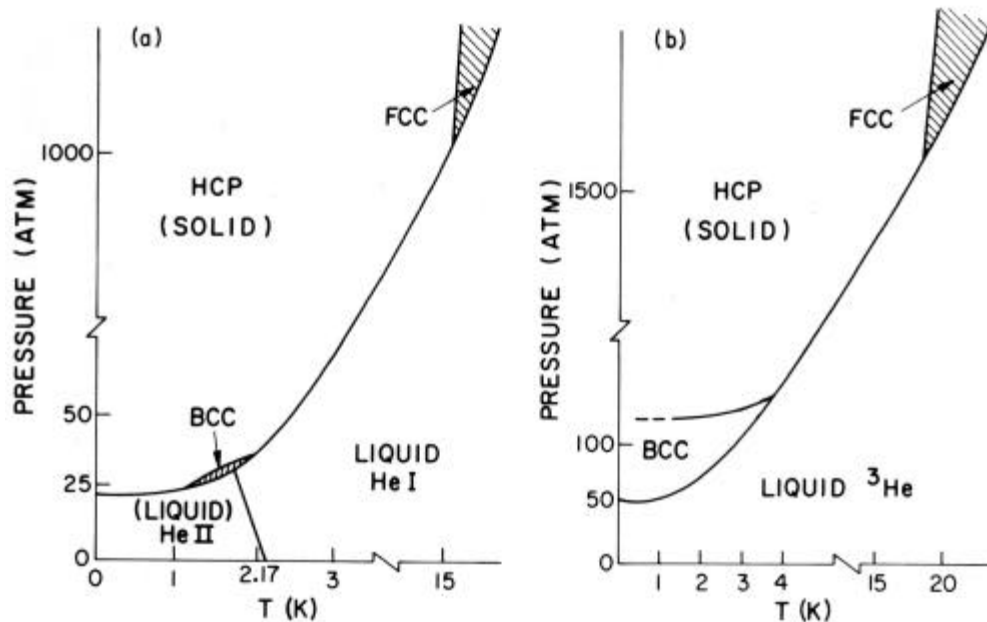


Figure 2.4 Phase diagrams of (a) ^4He and (b) ^3He [25].

2.1.2. Microscopic Properties

The macroscopic properties of superfluidity have their origins in the bose nature of the system. In an ideal (non-interacting) bose gas (IBG) a phase transition known as bose-Einstein Condensation (BEC) is predicted to occur in which the particles “condense” into the lowest momentum/energy state. This transition occurs when the thermal deBroglie wavelength of an individual particle, $\lambda_T = h(3mk_B T)^{-1/2}$, becomes comparable to the interparticle spacing. At absolute zero temperature, where the deBroglie wavelength diverges, all of the atoms are expected to occupy the lowest state. A detailed treatment of an IBG yields the BEC transition temperature

$$T_{\text{BEC}} = \frac{h^2}{2\pi m k_B} \left(\frac{N}{2.612 V} \right)^{\frac{2}{3}}, \quad (2.1)$$

where N/V is the number density of bose particles and m is the mass of a particle [26,27]. As the temperature is lowered through the BEC transition temperature the atoms begin to condense into the lowest energy/momentum state of the system until, at zero temperature, they all occupy the $p = 0$ state.

Standard quantum statistical mechanics can be used to determine the thermodynamic behavior of an IBG above and below T_{BEC} [26]. The parameter which characterizes the extent of the BEC in a system is the condensate fraction, n_0/N , defined as the number of particles which have bose-condensed divided by the total number of particles in the system. The temperature dependence of the condensate fraction for an IBG is $n_0/N = (1 -$

$t^{3/2}\theta(1-t)$ where $\theta(x)$ is the unit step function and $t = T/T_{\text{BEC}}$. The phase diagram of an IBG is quite simple and the BEC transition temperature is related to the pressure via

$$P(T_{\text{BEC}}) = \left(\frac{2\pi m}{h^2} \right)^{\frac{3}{2}} (k_B T_{\text{BEC}})^{\frac{5}{2}}, \quad (2.2)$$

thus implying that the transition temperature increases with increasing pressure.

London surmised correctly that superfluidity in ^4He is a natural manifestation of BEC [28]. Using the known properties of superfluid helium he estimated, via equation (2.1), that the transition temperature should be about 3.13 K, not very different from the superfluid lambda transition, 2.17 K. Recent work on optically-trapped alkali atoms has provided a direct realization of an (almost) IBG [29]. Unfortunately superfluid ^4He is a strongly interacting system which cannot be described using this simple model and this can be shown quite easily. For instance, the phase diagram for ^4He shown in figure 2.4 indicates that the superfluid transition actually decreases with increasing pressure. This contrasts with the case for the IBG as seen in equation (2.2) which indicates that the BEC transition increases with increasing pressure. In addition, the dispersion relationship for liquid ^4He is not parabolic, as is the case for an ideal gas where $E(p) = p^2/2m$. Instead it displays the rich structure shown in figure 2.5. The origins of this structure in the dispersion are the interactions among the helium atoms.

The *imperfect bose gas* is the next step in a microscopic treatment of superfluid helium [26]. This quantum mechanical treatment predicts the existence of low-lying excited

states with a linear dispersion at small momentum transfer consistent with the dispersion relationship in figure 2.5 at small Q and free-particle behavior, $p^2/2m$, at high momentum transfer. However no dip is predicted in the imperfect bose gas so further modifications of the wavefunction are necessary. Feynman provided the necessary modification to the wavefunction in the original quantum mechanical treatment which provided qualitative agreement with the dispersion curve shown in figure 2.5 [30,31]. Thus the interacting/imperfect bose gas was shown to be an appropriate microscopic picture of superfluidity.

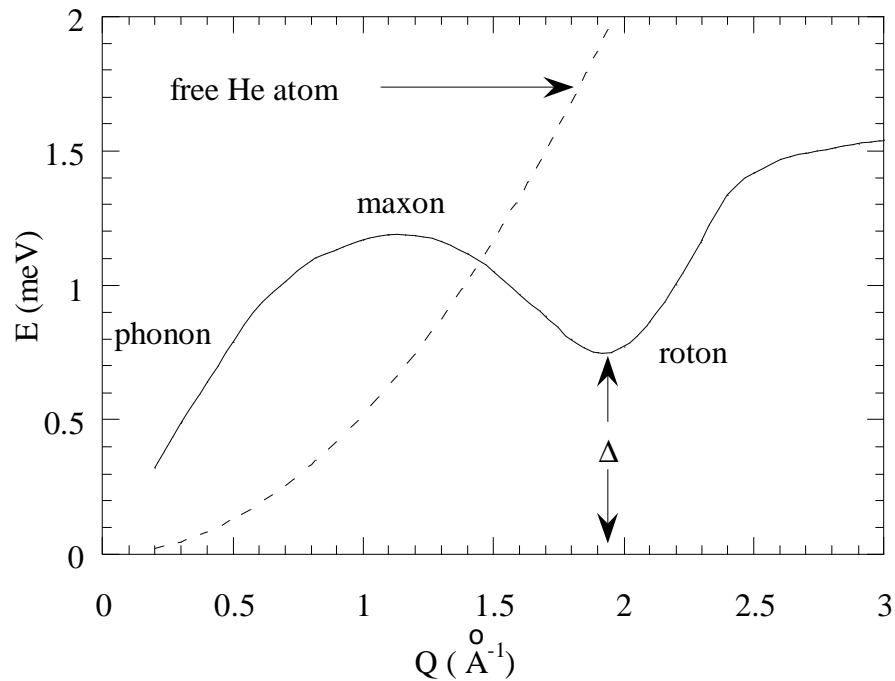


Figure 2.5 The collective excitation spectrum of superfluid helium (solid line).

In addition, Feynman also illustrated that the presence of interactions in the bose system does not preclude the existence of a bose condensate [32]. This has prompted an active search for the existence and magnitude of the bose condensate in superfluid helium. The condensate fraction, n_0/N , can be determined experimentally if one can measure the atomic momentum distribution, $n(p)$. One method of determining the momentum distribution is to use high energy inelastic neutron scattering [33]. Extensive efforts have been made to determine the condensate fraction experimentally (see [34] for a recent review) and the evidence points to the presence of a condensate, containing roughly 10% of the total number of atoms at $T=0$.

Another method which has been used recently to determine the presence of a bose condensate in superfluid helium is quantum evaporation [35]. In this technique a small heater is immersed in a bath of superfluid helium which has a free surface. When pulsed, the heater generates thermal excitations in the superfluid which move towards the liquid surface. At these low temperatures the excitations have a very long mean free path enabling them to make it all the way to the surface at which point they knock surface atoms out into the vacuum above the surface (analogous to the photoelectric effect). A measurement of the angular distribution of the atoms scattered from the surface indicates that the atoms are preferentially scattered. This scattering process naturally is momentum conserving, so that the angular distribution provides direct information on the initial momentum distribution of the atoms at the surface. The experimental observations and

subsequent analysis indicate that the surface atoms initially had zero momentum thus providing evidence that the atoms were in the condensate.

While Feynman ultimately was able to provide a microscopic basis for the excitation spectrum shown in figure 2.5 based on the bose character of the helium system, Landau determined the form of the excitation spectrum based only on the thermodynamic data available at the time and certainly *before* any direct measurements of the spectrum [36,37]. Therefore the Landau excitation model provides the link between the microscopic excitations and the macroscopic dynamics of superfluid helium.

At absolute zero, the two-fluid model states that the liquid is entirely superfluid and there are no excitations present. According to the Landau excitation model, as the temperature increases, thermal fluctuations in the liquid create excitations which contribute to the normal fluid component and thus deplete the superfluid. To obtain the connection between the macroscopic measurements of superfluid helium and the excitation spectrum the Landau excitation model makes the assumption that the macroscopic properties of the liquid are due to an ideal (non-interacting) gas of excitations. This is a good assumption except when the excitation gas is no longer dilute which is the case near T_λ .

The excitation spectrum shown in figure 2.5 is characterized by three principle regions. At low energy and momentum transfer the liquid supports long wavelength compressional modes of vibration. Due to the similarity of these modes with those in a

solid these modes are referred to as *phonons*. However since a liquid is not capable of providing a shear restoring force only longitudinal modes are possible. This is in contrast with solids which can support both longitudinal and transverse phonon modes. The dispersion of the phonons in helium are characterized by the linear relationship,

$$E(Q) = \hbar c Q, \quad (2.3)$$

where c is the speed of first sound, ~ 240 m/s. Phonons are an important excitation when considering the thermodynamics of the liquid. They are low energy and can easily be created by thermal fluctuations.

The second region in the dispersion curve is marked by the flat convex region near 1.2 \AA^{-1} known as the *maxon* region. Since this region is flat at its maximum and $(dE/dQ)^{-1}$ (which is proportional to the excitation's density of states) diverges, we expect that the maxon should make a significant contribution to the thermodynamic behavior. However the maxon excitation energy is very high ($\Delta_M \sim 1.1$ meV) compared with thermal fluctuations of the superfluid ($k_B T \sim 0.13$ meV at 1.5 K), thus making it virtually inconsequential in the thermodynamics.

Finally there is an additional region in the spectrum, the *roton*, whose density of states diverges. The roton is the name given to excitations whose dispersion follows the parabolic function,

$$E(Q) = \Delta + \frac{\hbar^2}{2\mu_R} (Q - Q_R)^2, \quad (2.4)$$

where Δ is the roton energy gap (shown in figure 2.5), μ_R is the “roton mass”, and Q_R is the roton momentum. The roton parameters are $\Delta_R = 0.741$ meV, $\mu_R = 0.15 m_{\text{He}}$, and $Q_R = 1.92 \text{ \AA}^{-1}$. Note that μ_R has been identified as the “mass” of a roton. It should only be regarded as a property of the roton which reflects the curvature of the dispersion relationship near Q_R . At $Q = Q_R$, the density of states diverges. Since the excitation energy, Δ_R , is 30% lower than the maxon energy, thermal fluctuations in the liquid make the creation of a roton *an order of magnitude* more probable than the creation of a maxon.

Based on these arguments we can guess that at low temperatures where thermal fluctuations are low in energy, an ideal gas of phonons will determine the thermodynamic behavior. At higher temperatures (of course below T_λ) rotons will determine the thermodynamic behavior. In fact experiment suggests that below 0.7 K phonons dominate the thermodynamics and above 1.1 K the rotons become very important. In the intermediate regime ($0.7 < T(\text{K}) < 1.1$) both contributions should be considered important.

The complete thermodynamic relations for an ideal gas of phonons and rotons can be worked out with knowledge of (i) the statistics they obey, and (ii) the dispersion of their energies. Since the excitations are made up of helium atoms which are Bose particles then Bose statistics must be used. In an ideal phonon gas with a dispersion given by

equation (2.3), the specific heat is the same form as for a Debye solid (corrected to account for the single polarization mode),

$$C_{\text{ph}}(T) = \frac{2\pi^2 k_B^4}{15\rho\hbar^3 c^3} T^3, \quad (2.5)$$

where ρ is the liquid density and c is the speed of sound [26]. The phonon contribution to the normal fluid is related to the total momentum of the phonon gas via

$$\rho_{\text{ph}} = \frac{P}{vV}, \quad (2.6)$$

where P is the momentum in the direction of flow, V is the liquid volume, and v is the flow speed ($v \ll c$ is assumed). A straightforward calculation of P [26] combined with equation (2.6) yields the phonon contribution to the normal fluid fraction,

$$\frac{\rho_{\text{ph}}}{\rho} = \frac{16\pi^5 k_B^4}{45\rho\hbar^3 c^5} T^4. \quad (2.7)$$

The roton contributions to the thermodynamics (in two and three dimensions) are summarized in table C1 of appendix C and, since the derivation of these for the case of the bulk liquid can be found in [24,26] for instance, they will not be repeated here. The results for a two-dimensional roton gas are discussed in detail in appendix C and the three-dimensional case is calculated in a similar manner. We simply present the results here for the roton contributions to the specific heat and the normal fluid fraction. The specific heat is given by

$$C_{\text{R}}(T) = k_B \left[\frac{3}{4} + \left(\frac{\Delta}{k_B T} \right) + \left(\frac{\Delta}{k_B T} \right)^2 \right] N_{\text{R}}(T), \quad (2.8)$$

where

$$N_R(T) = \left(\frac{\mu k_B T}{2\pi} \right)^{1/2} \frac{Q_R^2}{\pi \hbar} e^{-\frac{\Delta}{k_B T}}, \quad (2.9)$$

is the number of thermally-activated rotons. Note that $\Delta \gg k_B T$ so that the leading order term in (2.8) is given by $(\Delta/k_B T)^2$ yielding a specific heat with a temperature dependence that goes as $T^{-3/2} \exp(-\Delta/k_B T)$. The contribution to the normal fluid fraction is given by,

$$\frac{\rho_n}{\rho} = \frac{2\hbar Q_R^4}{3\pi\rho} \left(\frac{\mu}{8\pi k_B T} \right)^{1/2} e^{-\frac{\Delta}{k_B T}}. \quad (2.10)$$

The Landau excitation model, exemplified by equations (2.5)-(2.10), can be combined with the roton parameters extracted from neutron scattering data to reproduce the thermodynamic data. The normal fluid fraction, for instance, is shown in figure 2.6, over a broad temperature range where it has been computed from the Landau excitation model (solid line) in conjunction with the temperature dependent excitations (as measured by neutron scattering) and compared with the measured normal fluid data (circles). The same type of agreement has been found for the specific heat, entropy, and speed of sound which provides a very clear validation of the Landau excitation model [38,39].

Recently a theoretical model which clarifies the role of a BEC on the collective excitations of a superfluid has been suggested [40]. In this picture, referred to as the Glyde-Griffin model, the phonon modes are zero-sound collective modes (not affiliated with superfluidity or the presence of a Bose condensate) whereas the excitations beyond

the phonons (i.e. maxons and rotons) are renormalized single-particle modes considered to be excitations out of the condensate. The phonon part of the dispersion curve is actually distinct from the maxon and roton portions of the curve in this view. Although they are distinct, in the Glyde-Griffin model the smooth curve which joins the long wavelength modes with the intermediate and higher wavelength modes is due to a hybridization of the modes caused by the presence of the Bose condensate. The impetus for this designation arose from detailed analysis of the inelastic neutron scattering data where it has been observed that the phonons remain well-defined collective modes even above T_λ whereas the maxon and roton modes lose considerable intensity above T_λ . This view has been challenged recently in light of recent measurements of rotons in the bulk superfluid very close to T_λ [41]. These measurements suggest that the roton does not “abruptly appear” when decreasing the temperature through T_λ (which is predicted by the Glyde-Griffin model) but appears in a continuous fashion.

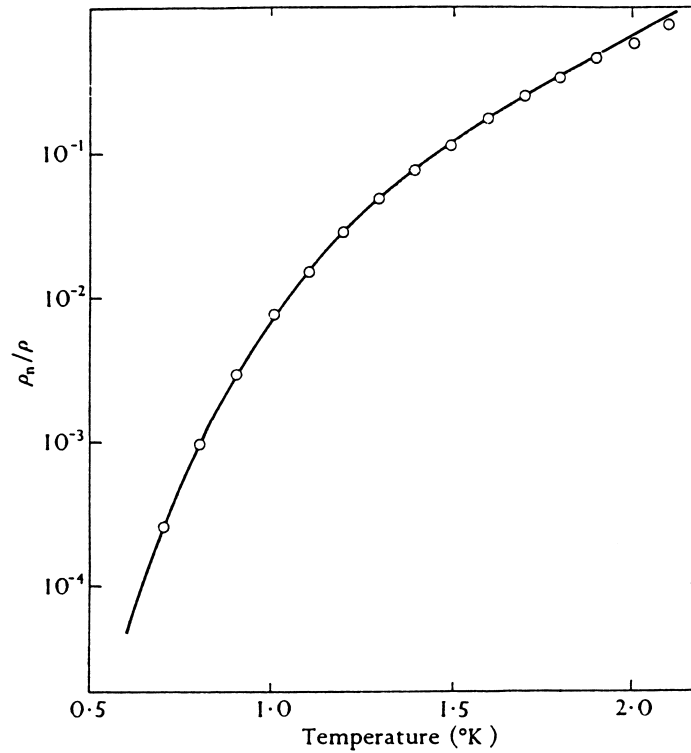


Figure 2.6 Normal fluid fraction as a function of temperature which incorporates both the phonon and roton contributions (adapted from [24]).

The temperature dependence of the excitations, particularly the phonons and rotons, coupled with the Landau excitation model, provide the agreement with the macroscopic data. The temperature dependence of the excitation energy of the roton, say, not only reflects the interactions of the rotons with each other, but it also can be used with the original equations for the Landau excitation model to provide the agreement fairly close to T_λ . Ideally, in the absence of interactions, there should be no temperature dependence of the roton energy gap, Δ . However as the temperature increases towards T_λ , the mode softens in a similar manner as phonons in a solid. In fact, since the number of excitations grows dramatically with temperature (equation (2.9)), the assumption of a non-interacting

gas breaks down. The softening of the roton mode as observed in neutron scattering is shown in figure 2.7.

The softening of the roton mode provides evidence that rotons interact with one another [42-45]. A modern theory of roton-roton interactions which provides a reasonably good model of the temperature dependence of the roton energy gap is based on the method of pseudopotentials [46] (hereafter referred to as the BPZ theory). The BPZ theory is an extension of roton-liquid-theory in which interactions of the rotons provide the temperature dependence of the excitations [43,47].

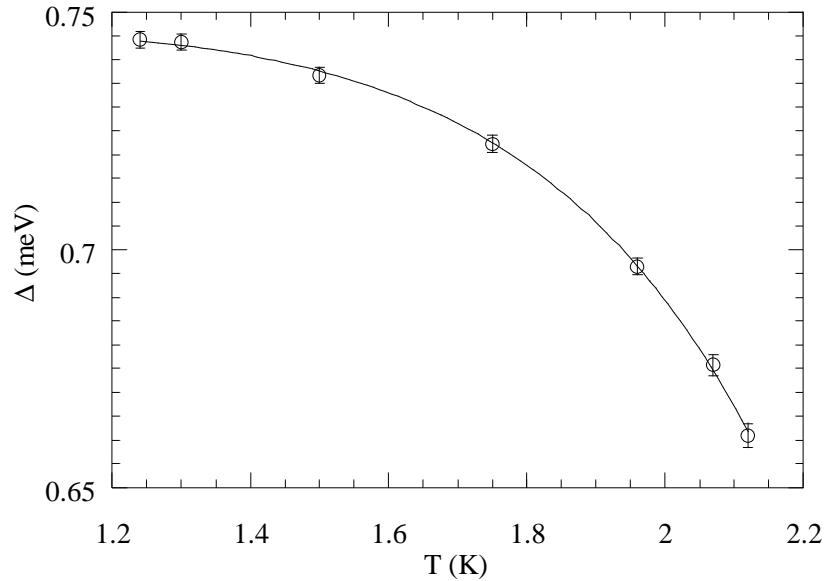


Figure 2.7 The temperature dependence of the roton energy gap, Δ for bulk superfluid helium [48]. Solid line is a fit to theory.

In the BPZ theory the temperature dependence of the roton is understood in terms of scattering processes between rotons. To first order the roton energy decreases by an amount proportional to the number of rotons, $\Delta(T) = \Delta_o - CN_R(T)$, where C is a constant and $N_R(T)$ is given by equation (2.9). The detailed calculations of the BPZ theory predict the following temperature dependence for the roton energy and roton linewidth (related to lifetime via the uncertainty principle),

$$\Delta(T) = \Delta_o - P_\Delta (1 + R\sqrt{T})\sqrt{T} \exp\left(-\frac{\Delta(T)}{T}\right), \quad (2.11)$$

and

$$\Gamma(T) = P_\Gamma (1 + R\sqrt{T})\sqrt{T} \exp\left(-\frac{\Delta(T)}{T}\right), \quad (2.12)$$

where Δ_o is the zero-temperature roton energy, P_Δ , R , and P_Γ are parameters related to roton-roton scattering and determined experimentally. High resolution measurements of the temperature dependence of the roton linewidth and energy support this model [48] as shown by the solid line fit of equation (2.11) to the data in figure 2.7.

We briefly mentioned the quantum-mechanical approach due to Feynman in which the dynamics are treated in terms of a wavepacket of excitations. In some sense this approach is more fundamental than the approach of BPZ, which is more phenomenological. Modern theoretical treatments provide a description of the superfluid as an interacting bose gas with a macroscopic many-particle wave function that describes the condensate [27]. This many particle wavefunction is represented in terms of the number of atoms in the condensate, n_o , via

$$\Psi(\vec{r}) = \sqrt{n_o} \exp[i\Phi(\vec{r})], \quad (2.13)$$

where Φ is the superfluid velocity potential field. The superfluid velocity, \mathbf{v}_s , can be found from Φ via [27]

$$\vec{v}_s = \frac{\hbar}{m} \vec{\nabla} \Phi. \quad (2.14)$$

Since the superfluid velocity field originates from potential flow, the curl of the field vanishes and it is irrotational. The curl-free nature of the superfluid velocity field suggests that another density fluctuation can exist in the superfluid, namely a *quantized vortex excitation*.

A curl-free velocity field necessarily means that the superfluid cannot be put into solid-body rotation. However solid body rotation *is* observed in superfluid helium if the helium is rotated fast enough. Feynman and Onsager rectified this paradox by postulating that an array of quantized vortex lines can form in the liquid which, when taken in total, mimic solid body rotation. The circulating flow around a vortex center does not violate the curl-free condition. In fact the violation occurs at the center of the vortex line (the vortex core) where, since the nature of the vortex core is unknown (but assumed *not* to be superfluid), the curl-free condition does not necessarily apply.

The existence of quantized vorticity in superfluid helium provides a resolution of another paradox. When superfluid helium flows fast enough through a channel, it is possible to

create excitations through the exchange of momentum with the walls of the channel. The minimum speed with which an excitation can be created is given by drawing a tangent line from the origin of the dispersion curve ($Q=0$, $E=0$) to the roton minimum. The slope of this line, dE/dQ , is proportional to the minimum speed necessary to create an excitation. The speed one obtains from this method, about 60 m/s, is far too big compared with the observed breakdown of superfluidity which occurs at only a few mm/s. Thus the breakdown of superfluidity at these small flow rates cannot be due to the creation of the thermal excitations such as phonons or rotons. The resolution is that vortex rings of atomic dimensions (which will deplete the superfluid) can be created from the helium flowing past the walls. This suggestion by Feynman has met with controversy but there are efforts investigating this possibility [49-51] .

The behavior of bulk helium near the lambda transition has been investigated extensively, mainly for its role in critical phenomena. In critical phenomena one studies the temperature dependence of an order parameter, a quantity which undergoes an observable change at the phase transition. Modern theories of phase transitions are based on the fact that the microscopic details of the system under study are not particularly important. In fact the correlation length (the extent over which the fluctuations of the order parameter are felt) is the only length scale important near the transition and it diverges at the transition temperature.

The superfluid transition is an example of a critical phase transition. As such it belongs to a class of systems in which certain thermodynamic functions or their derivatives can display divergent or discontinuous behavior at the transition. In fact because the transition is so well-defined, superfluid helium is considered a model system in which one can test the theories of critical phenomena. In a sense, superfluid helium is an ideal system for examining critical phenomena because (i) it is a pure system free of inhomogeneities, (ii) thermal relaxation times are short allowing reasonable equilibration times, and (iii) thermometry is fairly advanced so that high precision measurements can be performed extremely close to T_λ .

In the immediate vicinity of a critical transition the temperature dependence of those quantities which display singular behavior follow, to leading order, power laws in temperature (e.g. $f(t) \sim |t|^{-\lambda}$). For instance, in the vicinity of the superfluid phase transition, the temperature dependence of the superfluid fraction displays a power-law behavior,

$$\rho_s = \rho_{so} t^\zeta, \quad (2.15)$$

over 3 decades in reduced temperature, $t = (1-T/T_\lambda)$, where ζ is the critical exponent which characterizes this transition. ζ has been experimentally determined to be 0.674 [4].

In addition the specific heat has been investigated in the vicinity of T_λ . It also has a temperature dependence which can be described by a power law, $C = At^{-\alpha}$, where α is another critical exponent which characterizes the transition. Experimental determination of α yields 0. Theoretical scaling laws predict that the two critical exponents are not

independent and should be related via $\zeta = (2-\alpha)/3$. It is clear that the scaling relationship is satisfied by the experimentally observed values of the critical exponents thus providing justification for its use as a testing ground for critical phenomena.

One possible observable link between BEC and superfluidity is in the phase transition itself. Near the BEC transition the condensate fraction (for an interacting Bose gas/liquid) is predicted (based on the theory of second order phase transitions) to have a power-law dependence,

$$n_o = At^\zeta, \quad (2.16)$$

where t is the reduced temperature described previously and the critical exponent, ζ , is predicted to be 0.7 for a second-order phase transition. Experimental measurements of the superfluid fraction near T_λ indicate a power-law behavior where $\zeta = 0.674$. Recently it has been shown experimentally that the condensate fraction is also consistent with a power law behavior near T_λ with a critical exponent $\zeta = 0.7$ [52]. This merely shows, however, that critical exponent for the superfluid transition and the Bose transition are consistent with each other. This indicates, at the very least, that the Bose transition and the superfluid transition in helium are in the same universality class (i.e. display the same critical behavior) thus lending further credibility to the premise that superfluidity is linked to BEC in helium.

2.2 Porous Media

The term *porous media* encompasses a class of materials which contain a distribution of regularly or irregularly shaped pores. Examples of porous materials are bone, zeolites, fine-grained powders, sponge, aerogels, and xerogels. Novel fabrication techniques allow one to make sturdy gels from a variety of different materials including silica or even gold [53]. The mean pore sizes of the materials provide a convenient means (but not the only means) to characterize them. *Microporous* materials typically have pore sizes less than 20 Å, *mesoporous* materials have pore sizes ranging from 20-500 Å, and *macroporous* materials have pore sizes greater than ~ 500 Å. Other characteristics used to describe porous media are the porosity (usually expressed as 100 × fraction of open pore volume), specific pore volume (typically given in units of cc/g), and specific pore area, SA (m²/g). A simple relation exists between the porosity and the specific volume (SV) in cc/g,

$$SV = \frac{0.01 \times \text{porosity}}{\rho_{\text{sn}} (1 - 0.01 \times \text{porosity})}, \quad (2.17)$$

where ρ_{sn} is the bulk density of the solid network (in g/cc) making up the network of the material. Another useful relationship relating the open pore volume, V_p (in cc), to the mass of the porous material, m (in g), and the bulk density of the solid network is

$$V_p = \frac{m}{\rho_{\text{sn}}} \frac{0.01 \times \text{porosity}}{(1 - 0.01 \times \text{porosity})}. \quad (2.18)$$

Finally there is an expression which relates the average pore diameter, D (in Å), to the specific volume (cc/g) and the specific surface area (m^2/g) assuming cylindrical pore geometry,

$$D = 4 \times 10^4 \frac{SV}{SA}. \quad (2.19)$$

This expression can be obtained based on geometric considerations and provides a rough estimate of the pore diameter for a porous material if the specific volume and the specific area are given.

Porous materials have been used extensively to confine various phases of adsorbates in an effort to determine the effects of restricted geometry on the adsorbate. In many cases significant changes from the bulk system have been observed. In order to understand which aspects of confinement cause observed changes in the microscopic or macroscopic behavior of the adsorbate (i.e. large surface-to-volume ratio, interconnectedness of pores, substrate composition, etc.) it is necessary to understand the structure and chemical composition of the material confining the adsorbate. In this thesis we examine the effects of confinement in porous vycor glass, silica aerogel, and silica xerogel.

The porous materials described in this section have a variety of different uses. Vycor glass has been used for its absorption properties in electrodes in a chemical corrosion testing apparatus, for example. Silica aerogel, with its extremely good insulating properties, was an integral part of the Mars Pathfinder mission in which it was used to insulate the on-board electronics and has also been used as a collector of cosmic dust

particles in space probes. Currently it is being investigated for its thermal insulating properties to be used in a more terrestrial environment, the residential home. Xerogels have been used in the food industry for many years. In particular the brewing industry uses these materials to preferentially adsorb unwanted proteins while making beer in order to prevent an undesirable effect known as *chill-haze*.

Although there are a wide variety of practical uses for these porous media, a microscopic understanding of the effects due to confinement in these porous glasses is still lacking. A study of the effects of confinement in these materials thus begins with an understanding of the fabrication process and the underlying structure of porous glasses. We begin with vycor which is a trade name for a glass developed by Corning. We then discuss aerogel and xerogel, which share a common origin but, through different processing techniques, result in very different glasses.

Porous vycor glass is a system with a well-defined pore size distribution and a highly interconnected network of pores. Typical vycor samples are monolithic and structurally quite strong. Preparation of the glass involves three steps [54]. First a homogeneous melt made up of 75% SiO_2 , 20% B_2O_3 , and 5% Na_2O is created. This melt is then cooled until a separation into an SiO_2 -rich phase and a B_2O_3 -rich phase occurs where it is subsequently quenched. Acid is then used to leach out the boron-rich phase and a skeleton network of (almost) pure SiO_2 remains. This leaching, however, is not complete and remnant boron left over from an incomplete leach can cause significant technical

difficulties when used in a neutron scattering measurement as will be discussed in chapter 4. The resulting structure is made up of a well-defined pore structure with an average pore diameter of about 70 Å evident from molecular desorption isotherm measurements as shown in figure 2.8. However this value for the average pore diameter is based on the Brunauer-Emmet-Teller model for multilayer adsorption and the assumption of cylindrical pore geometry. This idealized model of the pore geometry is not strictly correct because the pores are not perfectly cylindrical. Nevertheless the model gives results which are consistent with transmission-electron micrograph imaging techniques [54]. The specific surface area of the resulting glass is on the order of $10^2 \text{ m}^2/\text{g}$ and the porosity is about 30%.

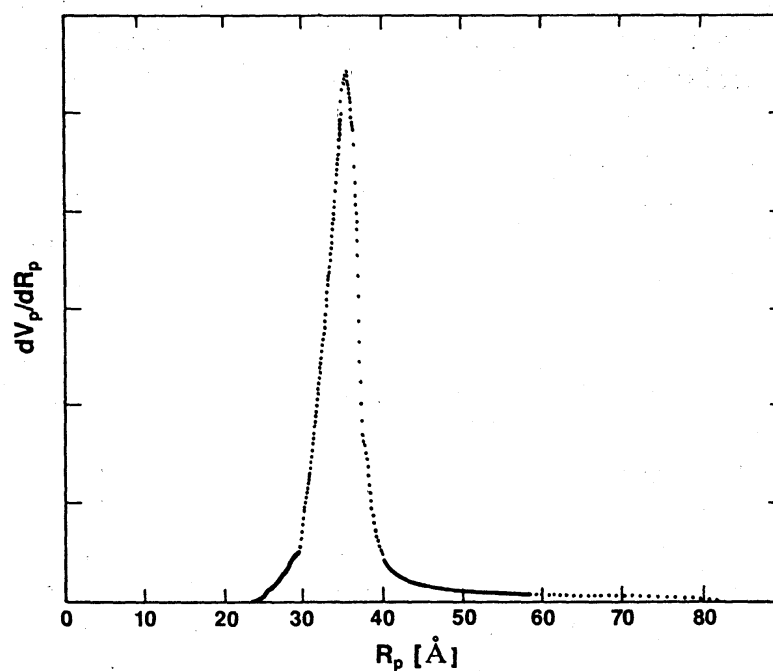


Figure 2.8 Pore size distribution for porous vycor glass [54].

Silica aerogels are materials which have micro-, meso-, and macro-porosities, thus they have a very broad pore size distribution. Fabrication of these materials has been simplified since the creation of the first aerogels in the 1930's and now consists of a two-step process [55]. The first step begins with the hydrolysis of TMOS or TEOS and a polycondensation which produces a tenuous, alcohol-submerged gel structure consisting of SiO_2 and water. To remove the water in the gel one could simply dry it in air. However drying in air leads to a considerable collapse of the delicate gel structure resulting in one common form of xerogel. Alternatively one can replace the alcohol with a liquid such as CO_2 and use supercritical drying (i.e. traversing a path in the P-V plane which circumnavigates the critical point of CO_2) to remove the *fluid*. In this way one avoids the strong capillary forces associated with drainage of a *liquid* which has surface tension. The result can be a large monolithic piece of aerogel. Microscopically the structure is composed of strands of SiO_2 roughly 50 Å in diameter with large voids separating the strands as shown in figure 2.8. Thus the description of aerogel as porous is not strictly correct. The open volume fraction for the resulting aerogel can go as high as 99 % with a density only 4 times that of air. Typical specific surface areas of aerogel can reach about 800 m^2/g [55]. The structure can withstand substantial compression forces (up to 10^5 N/m^2) but is not resistant to shear forces.

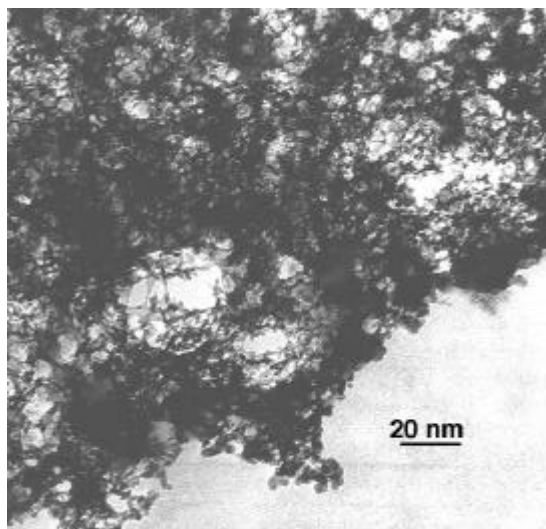


Figure 2.9 TEM of silica aerogel (from National Center for Electron Microscopy at the Lawrence Berkeley National Laboratory).

Silica xerogel is made in a manner similar to aerogel, beginning with the hydrolysis of an alkoxide, but the drying can be done at an elevated temperature in the presence of air or in an evacuated environment [56]. The resulting collapse of the structure yields few monolithic pieces of any substantial size. Typical samples are crumbled pieces or powders. The distribution of pore sizes in xerogels are usually narrow and range from 50-100 Å.

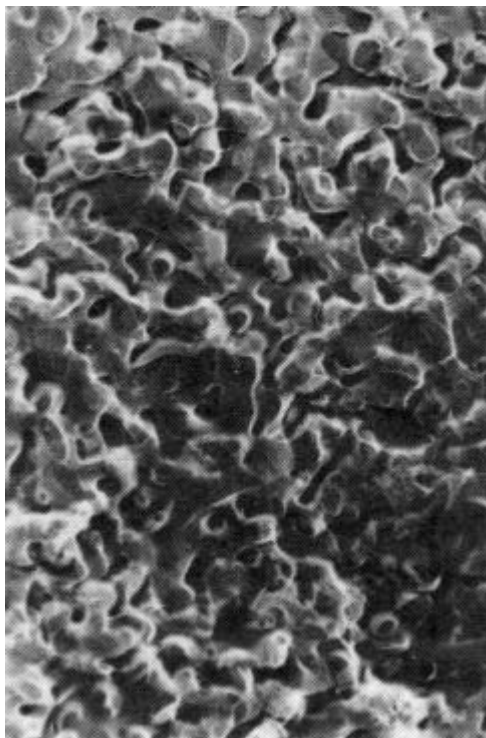


Figure 2.10 TEM of a xerogel sample [57]. Width of image is roughly 1350 Å.

The xerogel samples used in this thesis were obtained from PQ Corporation under the product name BRITESORB (ID #FB5300) which is used to chillproof beverages. Since BRITESORB is an industrially manufactured substance necessarily produced in large quantities, the production cycle is different from the process described above. BRITESORB is made from a silica hydrosol prepared by mixing sulfuric acid and sodium silicate. The hydrosol is sprayed into air and forms gel spheres. These spheres are then put into an aqueous solution of magnesium sulfate, washed multiple times in deionized water to remove the remnant sodium and magnesium salts, and finally dried [58]. It is estimated that about 1% magnesium is bound to the pore walls of the xerogel. The resulting xerogel is in powdered form and has a specific pore volume of 1.2 cc/g, a

porosity of 72%, and specific surface area of 450 m²/g. Britesorb differs from conventional xerogel in that the pore size distribution is broad but the average pore diameter is about 100 Å.

2.3 Superfluidity in Porous Media

Solids, liquids, and gases confined to porous materials can display a wide range of unique behavior. For instance both the freezing and melting points of cryogenic liquids (H, Ne, O, Ar) can be suppressed simply by adsorbing the liquid into a porous medium such as vycor or xerogel [59]. There is also a pronounced hysteresis when the liquid is thermally cycled near the freezing transition where the melting is found to occur at a higher temperature than freezing and both freezing and melting occur below the bulk melting/freezing temperature.

In some instances the suppression of a phase transition can have dramatic consequences. As an example, if one could supercool para-hydrogen in vycor for instance, so that the freezing temperature drops from its bulk value of 13.8 K down to about 6.7 K then it might become superfluid [60]. Unfortunately the lowest freezing temperature achieved by supercooling in the vycor has been 9.9 K [61].

The solid phase of materials can be altered due to confinement as well. CO₂ solidified within the pores of vycor has a structure consistent with bulk CO₂ but with a larger lattice

constant [62]. The exact reason for the difference is unknown but it is thought that the effect may be due to the attraction of the CO_2 molecules to the pore wall. Confining H_2O and D_2 in vycor results in new solid structures not present in the bulk solid [63,64]. Oxygen in silica xerogel results in a complete suppression of long-range crystalline order and the confined O_2 is amorphous [65]. Recent neutron scattering results indicate that the structure of solid helium may be significantly altered when confined as well. These measurements suggest that there may be an expanded BCC phase of solid helium confined to porous vycor [66]. This expanded phase is not unlike the case for He^3 which has a large BCC region in the phase diagram as shown in figure 2.4.

The effects of confinement and disorder on the properties of superfluid helium have been studied extensively, particularly the thermodynamic and flow effects in the vicinity of the superfluid transition. As in the bulk liquid, a great deal of interest lies in the effects of confinement at the phase transition, and because helium is a homogenous system, the substrate into which it is absorbed represents a static impurity. Perhaps one of the most important observations one can make about confined helium is whether or not it becomes a superfluid in the presence of the disorder. We will only discuss systems in which the liquid undergoes the superfluid phase transition.

To date researchers have studied the effects of confining helium in many different substrates such as jeweller's rouge, german silver, lampblack, porous gold, and porous glasses, among others. In fact one of the first published (1938) studies of superfluidity

involved an investigation of the flow properties of the liquid through a fine packed powder giving rise to the first observation of the well-known “fountain effect” [24]. The present discussion is limited to confinement in porous vycor glass, silica aerogels, silica xerogels, and thin helium films adsorbed onto crystalline substrates to provide context for the microscopic measurements presented in this thesis.

The behavior of superfluid helium confined to these systems is effectively summarized in figure 2.11 which shows the temperature dependence of the superfluid fraction in vycor, aerogel, xerogel, and the bulk liquid [67]. The most apparent difference in the superfluid fraction is that the transition is shifted in each case. In fact the transition temperature is shifted in rough proportion to the pore size of the confining system. Vycor, with the smallest pore sizes (~ 70 Å) of the glasses considered here makes the transition about 200 mK below the bulk transition temperature, whereas confinement in silica aerogel (94% porosity) suppresses the transition by only 5 mK with respect to the bulk liquid.

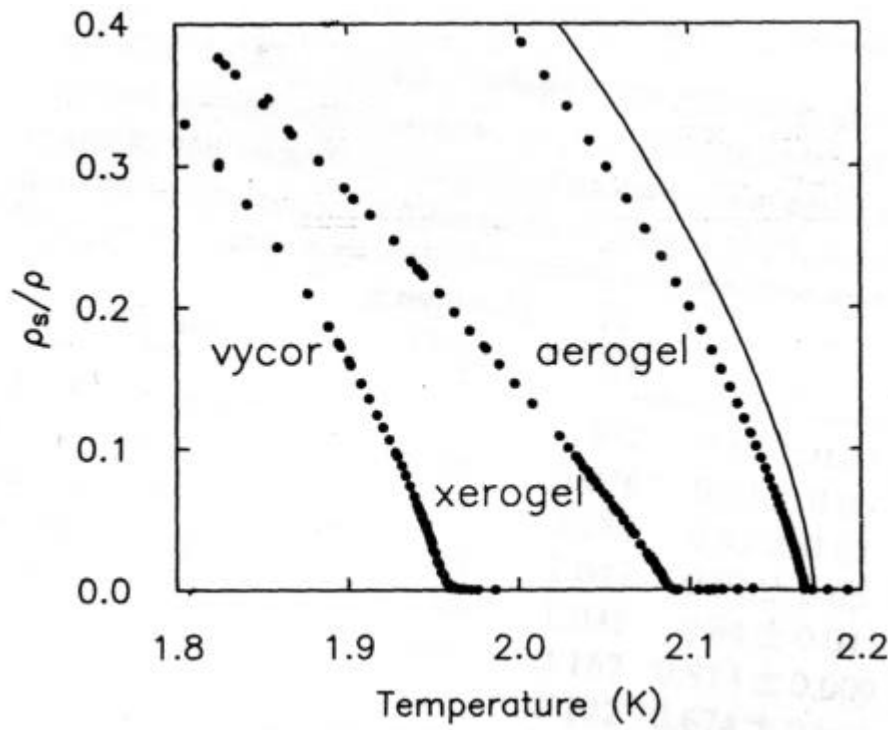


Figure 2.11 Temperature dependence of the superfluid fraction near the transition temperature for confinement in various materials. (Solid line is the superfluid fraction in the bulk liquid). Figure adapted from [67].

The temperature dependence very close to the superfluid transition for the confined superfluid can also be quite different depending on the confining medium as shown in figure 2.12. The behavior of the superfluid fraction near the transition temperature displays a power-law dependence on the reduced temperature, t^ζ , the exponent of which describes the character of the phase transition. The transition for helium in porous vycor glass yields a critical exponent almost identical to the bulk superfluid transition while confinement in aerogel and xerogel changes the critical exponent substantially.

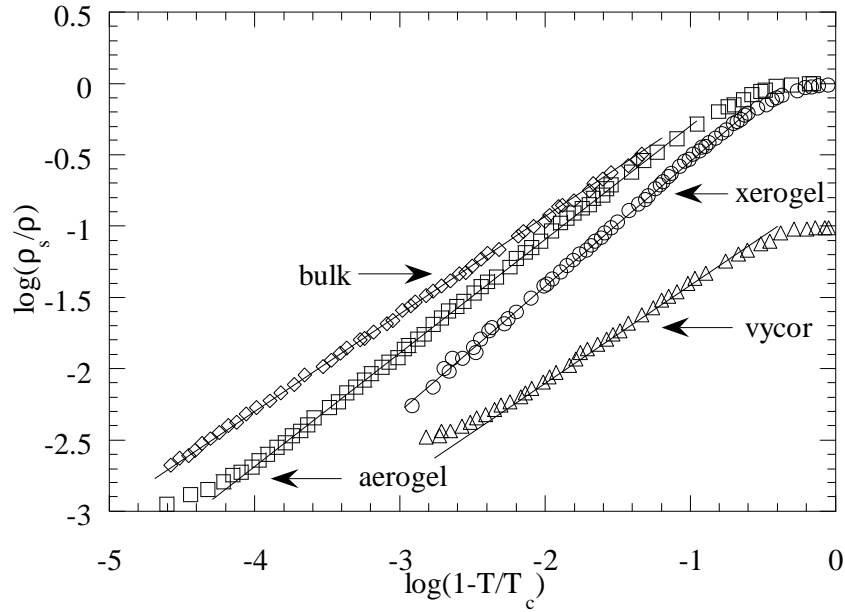


Figure 2.12 Temperature dependence of the superfluid fraction near the transition temperature for confinement in vycor and aerogel. Data have been plotted to illustrate the power-law behavior of the transition. Figure adapted from [68].

The heat capacity of the confined superfluid also exhibits behavior which is highly dependent upon the confining medium. We have seen that the bulk transition is accompanied by a sharp cusp-like feature right at the transition. In vycor there is no cusp-like anomaly but a smooth peak at the bulk transition temperature [69]. A peak in the heat capacity is predicted to exist at the suppressed vycor superfluid transition temperature but theory (critical phenomena) indicates that this peak will be extremely tiny compared with the bulk anomaly. On the other hand, there *is* a pronounced cusp-like anomaly in the heat capacity for superfluid helium in aerogel [69].

Measurements of both the heat capacity and superfluid fraction near the transition provide information about the nature of the phase transition for the bulk and confined superfluids. In addition to the effects of the finite pore size on these quantities, namely the suppression of the transition temperature, the pore geometry, network characteristics, and dimensionality are thought to contribute to the differences observed in confined superfluid helium. By studying the same adsorbate, helium, in different porous materials, one obtains hints about which characteristics of confinement affect the adsorbate. Next we discuss the effects of confinement on superfluidity in more detail.

Confinement in porous vycor glass not only suppresses the transition temperature due to the finite pore sizes but it also introduces reduced dimensionality. Since the pores in vycor glass are so small, $D \sim 70 \text{ \AA}$, and the interatomic spacing of the helium atoms is about 10% of this, the effects of dimensionality on the superfluid should be important. However, detailed studies of the nature of the phase transition indicated that the superfluid fraction follows a power-law behavior consistent with the bulk liquid [70]. This implies that the phase transition for the helium/vycor system is in the same universality class as the three-dimensional bulk liquid. This three-dimensionality of the helium/vycor system is attributed to the highly interconnected pores of the vycor. Despite the small diameters of the pores in vycor, helium behaves as a three-dimensional system. Perhaps even more remarkable than the fact that helium-filled vycor behaves as though it were a three-dimensional system is that *thin films* behave in exactly the same manner as the bulk liquid. Thus, helium films adsorbed in vycor, which would naturally

be thought of as two-dimensional, behave like the fully three-dimensional bulk liquid. When compared with the two-dimensional observations of helium adsorbed onto crystalline substrates (namely the Kosterlitz-Thouless transition) it seems that the morphology of the substrate plays a crucial role in determining the dimensionality of the system.

The measurements of superfluid helium in vycor have all been based on thermodynamic or flow properties of the confined liquid. However in an effort to understand the results on a microscopic level, some researchers have attempted to interpret their results with some form of the Landau excitation model. Brewer and co-workers fit their specific heat data for full pore vycor with a roton-like specific heat contribution (equation (2.8)) and extracted a roton energy of about 0.53 meV [71], which is over 0.2 meV lower than the bulk roton value (0.74 meV). Kiewet *et. al.* did the same with superfluid fraction data for full-pore vycor (using an expression like equation (2.10)) and extracted a roton energy of 0.5 meV [70]. However no microscopic measurements have been performed (to our knowledge) for superfluid helium in vycor glass. Chapter 6 of this thesis addresses this question in detail using new experimental measurements.

Confinement in silica aerogel can have profound effects on superfluidity. The relatively large distribution of pore sizes and the irregular structure of the substrate provide a very different medium as compared to the helium/vycor system. The effects on the phase transition are found to be dramatically different than the helium/vycor system (and bulk

liquid) as well. When the pores of aerogel (94% porosity) are filled with liquid helium there are a number of distinct effects. First the superfluid transition temperature is suppressed only by about 5 mK compared to the bulk liquid [67]. Next the onset of superfluidity is marked by a very sharp cusp in the specific heat compared with the rounded transition observed in full-pore vycor. In addition the superfluid fraction is rounded at the suppressed transition temperature, but less so than the full-pore vycor case. Finally the superfluid fraction follows a power-law behavior near the phase transition as in the bulk but the critical exponent for the transition is 0.813. The difference between the critical exponent for full-pore aerogel and bulk superfluid helium (0.67) suggests that the phase transitions for these two systems are in different universality classes.

Thin films adsorbed into silica aerogel (91% porosity) have also been investigated near the superfluid transition [72]. In a very unusual twist, the critical exponents, as determined from a power-law fit to the superfluid fraction near the transition, fall into the range of $0.56 < \zeta < 0.67$ for different pore fillings. This can be compared to the critical exponent for the full-pore aerogel (same, 91% porosity) which is 0.811. Thus the transition for full-pore aerogel is in a different universality class than the case of thin helium films in the same substrate. Recall that the critical exponents for thin films in porous vycor were almost identical to that of the full-pore vycor. The current understanding of this difference [72] between the vycor and aerogel results (full-pore vs. thin films) is due to the morphology of the liquid in the pores. In the case of helium in

vycor, both the film and the full-pore liquid have essentially the same structure and connectedness, thus the critical behavior is the same. However aerogel, with its strandlike structure and much larger open pore volume, presents a more substantial difference between the thin film and full-pore case. The full-pore case yields a reasonably well-connected superfluid whereas the thin film is dilute and poorly-connected. Therefore the structural differences between vycor and aerogel give rise to very different film morphologies. The difference in the critical exponents for full-pore vycor and full-pore aerogel are not well understood but they are thought to arise from the differences in the correlation lengths of the disorder in each substrate.

Silica xerogel also affects superfluidity in a dramatic manner. Superfluidity is present for the full-pore case as seen in the measurements of the superfluid fraction. The rounding of the transition, as observed in the superfluid fraction measurements, indicates a rounding of the transition somewhere between that of vycor and aerogel. The critical exponent for the full-pore case (60% porosity) is found to be $\zeta = 0.89$, which is much different from the bulk exponent, as opposed to the thin film case where $\zeta = 0.84$. The experimental uncertainty in these exponents makes them roughly equivalent so that the transitions are similar in nature (i.e. in the same universality class). In addition, a measurement of the critical exponent where the surface of the xerogel had been preplated with N_2 was performed and yielded no change in the critical exponent, thus illustrating that surface roughness and pore size are relatively unimportant in determining the behavior near the phase transition. The conclusion which can be drawn from these results is that the

xerogel seems to behave similarly to vycor in the context of the full-pore and thin film critical exponents but the structure of the xerogel causes the full-pore critical exponent to differ from the bulk value as the aerogel does. Once again, however, the differences and similarities are not completely understood.

There have been few microscopic measurements of confined superfluid helium. The first investigation of the collective excitations of superfluid helium confined to silica aerogel showed that the collective excitation spectrum of the confined liquid was essentially unchanged from the bulk liquid at temperature of 1.8 K. The spectrum was measured using inelastic neutron scattering on a time-of-flight instrument and two different porosity aerogel samples were studied (93.2% and 96.5%) [73,74]. No differences between the two samples were observed nor were there any differences from the bulk spectrum within instrumental resolution (160 μeV FWHM). A more recent investigation of the excitations of helium in silica aerogel (95% porosity) was performed on a spectrometer with an improvement in instrumental resolution of a factor of 8 [75]. Measurements were taken of the excitation spectrum over a broad range of temperatures and small but clear differences were found between the confined excitations and bulk excitations. These differences were later shown to be consistent with the macroscopic measurements for helium in aerogel [76]. A continuation of the work of Sokol *et. al.* is the subject of chapter five.

To our knowledge, no published measurements have been made of the microscopic excitations for helium in silica xerogel nor porous vycor. Thus the measurements discussed in chapters 6 and 7 represent the first of their kind.

To complete the discussion of the effects of confinement on superfluidity we briefly discuss measurements of thin films adsorbed onto crystalline substrates. These thin films represent a type of confinement and reduced dimensionality in the sense that, since the helium is restricted to two dimensional layers, the helium is confined in a particular direction. When adsorbed onto crystalline substrates (e.g. graphite) helium films display a very interesting behavior. It is usually accepted that the first one to two layers of adsorbed helium are dense, possibly solid, and do not participate in superfluidity. These layers are said to be in the *inert layers*. The next higher layers are less dense and participate in the superfluidity. The nature of the superfluid transition for the two-dimensional helium system is regarded as a clear realization of the Kosterlitz-Thouless transition in which vortices mediate the superfluid transition [77,78].

Theoretical calculations and experimental measurements indicate that the limited dimensionality of a thin film introduces new modes into the collective excitation spectrum (see figure 2.13). Third-sound measurements with helium films a few atomic layers thick suggest that there are thermal excitations present which are different from the bulk spectrum [17]. Third sound is a coherent wave whose motion is localized to the free surface of superfluid helium (like an ocean wave). Quantum hydrodynamic arguments

applied to the free surface of helium, similar to Landau's quantum hydrodynamics for the bulk liquid, predict that there exists a thermal excitation known as a *ripplon* which is responsible for the third-sound mode. When the surface-to-volume ratio is large as in a thin helium film, these thermal excitations make a substantial contribution to the specific heat as well as the normal fluid component of the film at low temperatures [79]. At higher temperatures and excitation energies a *surface roton* exists which was predicted from theoretical considerations [80] and subsequently observed directly using inelastic neutron scattering [81]. Such a surface excitation has a parabolic dispersion analogous to the bulk roton, equation (2.4). At higher temperatures this is expected to make a more significant contribution to the specific heat and normal fluid fraction. A comprehensive picture of superfluid films adsorbed onto a crystalline substrate has been presented using inelastic neutron scattering data accompanied by a complete theoretical interpretation of the excitations [21,22]. A contour plot showing the rich structure of the excitations in helium films is shown in figure 2.13 [22]. The ideas related to layered excitations presented in [22] have a direct bearing on the measurements of superfluid helium in vycor and xerogel as will be discussed in chapter 6 and chapter 7. Thermodynamic measurements of these systems indicate that layered excitations play a major role even in porous media. Thus a search for such excitations was undertaken in the measurements presented in chapters 6 and 7.

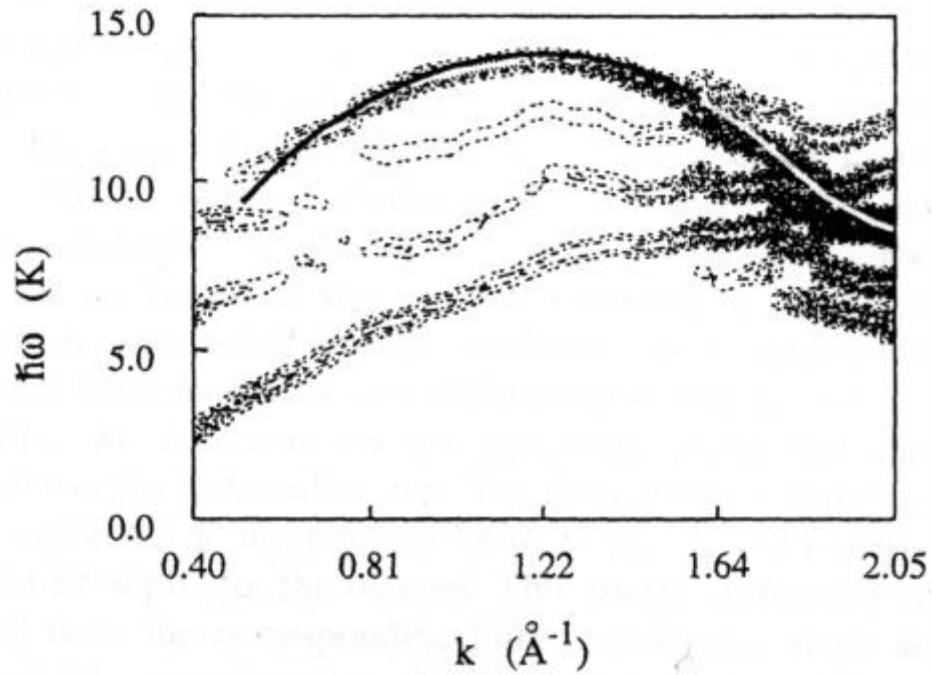


Figure 2.13 Contour plot of the excitations in thin superfluid helium films adsorbed onto exfoliated graphite [22].

The inelastic neutron scattering measurements of helium films adsorbed onto crystalline substrates is an example of superfluidity in an ordered environment and such measurements have been performed for many years. However the effects of disorder on superfluidity due to confinement in vycor, xerogel, and aerogel, for instance, have not been extensively characterized at the microscopic level. Therefore the measurements of the collective excitations of helium in aerogel, vycor, and xerogel discussed in chapters 5, 6 and 7 respectively, constitute an important step in understanding the effects of disorder on superfluidity.

CHAPTER 3

NEUTRON SCATTERING FORMALISM

A slow neutron inelastic scattering experiment provides details of the microscopic dynamics of the scatterer. In particular one can obtain information about the response of the sample to a perturbation in energy, E , and momentum, \mathbf{Q} , where the energy and momentum transfer have been delivered to the sample via the incident neutron. This information is contained in the *dynamic structure factor*, $S(\mathbf{Q}, E)$ and, for systems exhibiting well-defined cooperative atomic motions (like phonons in a solid), $S(\mathbf{Q}, E)$ can display sharp resonances depending on the values of \mathbf{Q} and E delivered to the sample. Perhaps most important is that these resonances observed in $S(\mathbf{Q}, E)$ are related to the density fluctuations in the sample in thermal equilibrium. Thus the dynamic structure factor provides a microscopic “snapshot” of how the sample responds to fluctuations in thermal equilibrium.

In this chapter we will describe a schematic of a slow neutron scattering process and the formalism which is used extensively in neutron scattering will be reviewed. To conclude the chapter and tie this information in with the subject of this thesis, we will use the formalism to motivate the model used in the lineshape analysis of superfluid helium data.

3.1 Neutron Scattering Kinematics

In order to provide a common ground for the subsequent discussion it is useful to describe a neutron scattering measurement from the point of view of scattering kinematics. In figure 3.1 both the real space and reciprocal space representations of a scattering experiment are shown. A neutron with initial momentum $m_n \vec{v}_o = \hbar \vec{k}_o$ and energy E_o is incident on some sample, the scatterer. After an interaction with the sample the neutron is scattered at an angle 2θ with respect to the incident direction and leaves with a final momentum $m_n \vec{v}_f = \hbar \vec{k}_f$ and a final energy E_f . This energy and momentum loss could be due to the creation of an excitation in the sample. Due to the relationship between the wavevector and momentum via the deBroglie relation ($\vec{p} = \hbar \vec{k}$) we will henceforth refer to \vec{k} as momentum. The momentum and energy transferred to the scattering system by the neutron (a process referred to as neutron *downscattering* if these are positive quantities and neutron *upscattering* if they are negative) are given by

$$\mathbf{Q} = \mathbf{k}_o - \mathbf{k}_f, \quad (3.1)$$

and

$$E = E_o - E_f, \quad (3.2)$$

where $E_o = \frac{\hbar^2 k_o^2}{2m_n}$ and $E_f = \frac{\hbar^2 k_f^2}{2m_n}$.

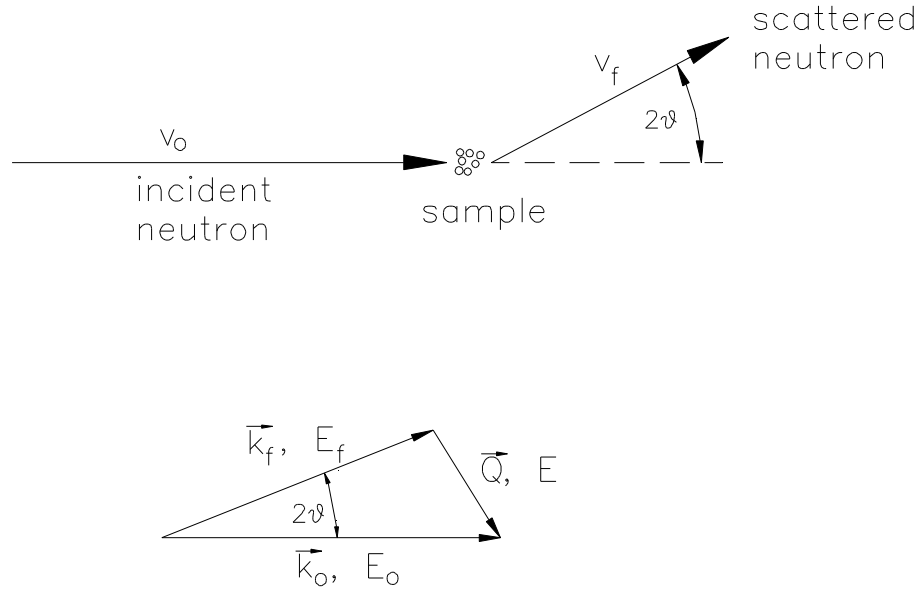


Figure 3.1 Neutron scattering kinematics in real space (top figure), and in reciprocal space (bottom figure).

The momentum transfer, when squared, yields a relationship between the incident and final momenta and the scattering angle,

$$Q^2 = k_o^2 + k_f^2 - 2 k_o k_f \cos 2\theta . \quad (3.3)$$

These equations can be combined to yield a relationship among the energy, momentum, and scattering angle. This process of *solving the scattering triangle* yields the following useful relationship between the momentum transfer, Q , the incident energy, E_o , the energy transfer, E , and the scattering angle, θ ,

$$Q^2 = \frac{1}{\alpha} [2E_o - E - 2\sqrt{E_o(E_o - E)} \cos 2\theta], \quad (3.4)$$

where $\alpha = \frac{\hbar^2}{2m_n} = 2.0717 \text{ meV \AA}^2$.

3.2 Neutron Scattering Dynamics

A neutron scattering experiment measures the partial differential cross-section of the sample, $\frac{d^2\sigma}{d\Omega dE_F}$, where Ω is the solid angle into which the neutron has been scattered and E_F is its final energy. This quantity represents the number of neutrons scattered per unit time into a small solid angle $d\Omega$ in the direction $(2\theta, \phi)$ with a final energy between E_F and $E_F + dE_F$ divided by the incident neutron flux (number of incident neutrons per unit time passing through a given cross-sectional area). The geometry for a scattering experiment is shown in figure 3.2.

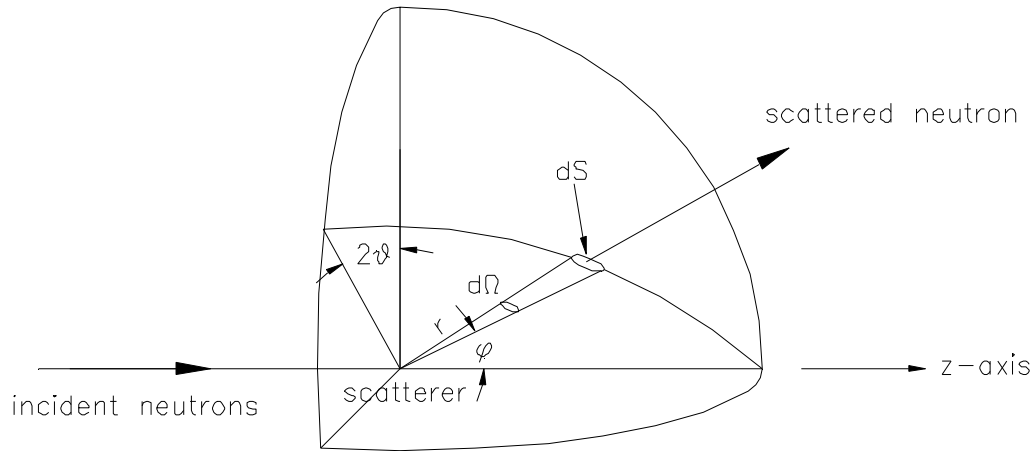


Figure 3.2 Geometry for a neutron scattering measurement.

The incident neutron is assumed to be in a plane wave state while the scattered neutron, which scatters off of the sample nuclei, is a spherical wave (s-wave scattering) whose center lies on the sample nuclei. The fact that the scattered neutron is assumed to be s-wave scattering, i.e. that the scatterer is a point object, is due to the fact that the neutron-

nuclei interaction is an extremely short-range one ($\sim 10^{-15}$ m). In fact this interaction is typically modeled using the Fermi pseudopotential,

$$V(\vec{r}) = \frac{2\pi\hbar^2}{m_n} b\delta(\vec{r}), \quad (3.5)$$

where m_n is the mass of the neutron and b is the scattering length. The scattering length, which depends on the nucleus of the scatterer and the spin of the neutron-nucleus system, is an experimentally determined quantity and typical values for b can be found in various tables [82,83]. For instance, helium has a scattering length of about 3 fm and hydrogen's scattering length is about -3.7 fm. The sign of the scattering length simply indicates the phase of the scattered waves with respect to the incident wave.

The theoretical expression for the partial differential cross-section is given by

$$\frac{d^2\sigma}{d\Omega dE_F} = \frac{k_F}{k_o} \frac{1}{2\pi\hbar} \sum_{j,j'} b_j b_{j'} \int_{-\infty}^{\infty} \langle j', j \rangle \exp(-i\omega t) dt, \quad (3.6)$$

where $\langle j', j \rangle = \langle \exp(-i\vec{Q} \cdot \vec{R}_{j'}(0)) \exp(-i\vec{Q} \cdot \vec{R}_j(t)) \rangle$. The angular braces represent a thermal average and the sum is over all of the different scattering lengths present in the sample [84,85]. The details leading up to this expression can be found in any of the standard neutron scattering references [84,85] but we will simply sketch the derivation leading to equation (3.6). The basic idea leading up to this expression is the following. The differential cross-section, in which the state of the scattering system changes from λ to λ' and the neutron changes from \vec{k}_o to \vec{k}_F , is given by

$$\left(\frac{d\sigma}{d\Omega} \right)_{\lambda \rightarrow \lambda'} = \frac{1}{\Phi} \frac{1}{d\Omega} \sum_{\vec{k}_F \text{ in } d\Omega} W_{\vec{k}_o, \lambda \rightarrow \vec{k}_F, \lambda'} , \quad (3.6)$$

where Φ is the incident neutron flux and $W_{\vec{k}_o, \lambda \rightarrow \vec{k}_F, \lambda'}$ is the transition rate of the scattering system (neutron + scatterer) from (\vec{k}_o, λ) to (\vec{k}_F, λ') . This transition rate is calculated using Fermi's Golden Rule

$$\sum_{\vec{k}_F \text{ in } d\Omega} W_{\vec{k}_o, \lambda \rightarrow \vec{k}_F, \lambda'} = \frac{2\pi}{\hbar} \rho_{\vec{k}_F} \left| \langle \vec{k}_F, \lambda' | V | \vec{k}_o, \lambda \rangle \right|^2 , \quad (3.7)$$

(where $\rho_{\vec{k}_F}$ is the density of final momentum states of the neutron) and the Fermi pseudopotential, equation (3.5), to characterize the neutron-nuclei interaction. Here the angular braces are the standard bra-ket representation of a matrix element linking the initial and final states. In addition, if E_o and E_F are the initial and final energies of the neutron, and E_λ and $E_{\lambda'}$ are the initial and final energies of the scattering system then, by conservation of energy,

$$E_o + E_\lambda = E_F + E_{\lambda'} . \quad (3.8)$$

We can combine equation (3.6) with (3.7) and (3.5) and convert to the partial differential cross-section by using a delta-function in energy to represent conservation of energy,

$$\left(\frac{d^2\sigma}{d\Omega dE_F} \right)_{\lambda \rightarrow \lambda'} = \frac{\vec{k}_F}{\vec{k}_o} \left| \sum_j b_j \langle \lambda' | \exp(i\vec{Q} \cdot \vec{R}_j) | \lambda \rangle \right|^2 \delta(E_\lambda - E_{\lambda'} + E_o - E_F) . \quad (3.9)$$

The sum over the individual nuclei which appears represents the fact that each of the nuclei *may* have a different scattering length but they *will* have different positions.

Since equation (3.9) only gives the cross-section for the particular process where the scattering system undergoes a transition from state λ to λ' , we must average over all the possible initial and final states (which must be done separately). Since the system is assumed to be in thermal equilibrium at temperature, T , then the sum over initial and final states is the standard thermodynamic average,

$$\frac{d^2\sigma}{d\Omega dE_F} = \sum_{\lambda, \lambda'} p_{\lambda} \left(\frac{d^2\sigma}{d\Omega dE_F} \right)_{\lambda \rightarrow \lambda'}, \quad (3.10)$$

where $p_{\lambda} = \frac{1}{Z} e^{-\frac{E_{\lambda}}{kT}}$ and $Z = \sum_{\lambda} \exp\left(-\frac{E_{\lambda}}{kT}\right)$. A number of mathematical details involving

converting the the delta-function in energy in equation (3.9) to its Fourier integral representation and taking advantage of the time-translation properties of the exponential Hamiltonian operator have been omitted but the resulting expression is equation (3.6).

The expression, (3.6), can be further decomposed into

$$\frac{d^2\sigma}{d\Omega dE_F} = \left(\frac{d^2\sigma}{d\Omega dE_F} \right)_{\text{COH}} + \left(\frac{d^2\sigma}{d\Omega dE_F} \right)_{\text{INC}}, \quad (3.11)$$

where the subscripts COH and INC correspond to coherent and incoherent scattering, respectively. The incoherent partial differential cross-section depends on the correlation of motions of the same nuclei at different times thus providing information on single-particle motion. The coherent partial differential cross-section depends on the correlations of different nuclei at different times, which can yield coherence effects, as well as the correlation of the same nuclei at the same times. The origin of these two

different contributions comes from considering that the scattering lengths of the nuclei in the sample are distributed according to the different types of nuclei present. The coherent partial differential cross-section is found to be

$$\left. \frac{d^2\sigma}{d\Omega dE_F} \right|_{\text{COH}} = \frac{\sigma_{\text{COH}}}{4\pi} \frac{k_F}{k_o} \frac{1}{2\pi\hbar} \sum_{j,j'} \int_{-\infty}^{\infty} \langle \exp(-i\vec{Q} \cdot \vec{R}_{j'}(0)) \exp(i\vec{Q} \cdot \vec{R}_j(t)) \rangle \exp(-i\omega t) dt, \quad (3.12)$$

and the incoherent partial differential cross-section is given by

$$\left. \frac{d^2\sigma}{d\Omega dE_F} \right|_{\text{INC}} = \frac{\sigma_{\text{INC}}}{4\pi} \frac{k_F}{k_o} \frac{1}{2\pi\hbar} \sum_j \int_{-\infty}^{\infty} \langle \exp(-i\vec{Q} \cdot \vec{R}_j(0)) \exp(i\vec{Q} \cdot \vec{R}_j(t)) \rangle \exp(-i\omega t) dt. \quad (3.13)$$

In these expressions the coherent and incoherent cross-sections are defined as

$$\sigma_{\text{COH}} = 4\pi \overline{(\overline{b})}^2, \quad (3.14)$$

and

$$\sigma_{\text{INC}} = 4\pi (\overline{b^2} - \overline{(\overline{b})}^2). \quad (3.15)$$

In equations (3.14) and (3.15) the bar over the scattering lengths denote averages over all of the different scattering lengths present in the sample. The coherent scattering can give rise to interference effects because the scattering is due to the correlation of different nuclei at different times (as well as the correlation of the same nuclei at different times), while incoherent scattering does not cause interference effects since it depends only on the correlation of the position of the same nucleus at different times.

Equations (3.12) and (3.13) can be cast into the following useful forms,

$$\left(\frac{d^2\sigma}{d\Omega dE_F} \right)_{\text{COH}} = \frac{\sigma_{\text{COH}}}{4\pi} \frac{k_F}{k_o} \text{NS}(\vec{Q}, \omega), \quad (3.16)$$

and

$$\left(\frac{d^2\sigma}{d\Omega dE_F} \right)_{\text{INC}} = \frac{\sigma_{\text{INC}}}{4\pi} \frac{k_F}{k_o} N S_i(\vec{Q}, \omega), \quad (3.17)$$

where we have defined the coherent and incoherent scattering functions as

$$S(\vec{Q}, \omega) = \frac{1}{2\pi\hbar} \int dt \frac{1}{N} \sum_{j,j'} \left\langle \exp(-i\vec{Q} \cdot \vec{R}_{j'}(0)) \exp(i\vec{Q} \cdot \vec{R}_j(t)) \right\rangle \exp(-i\omega t), \quad (3.18)$$

and

$$S_i(\vec{Q}, \omega) = \frac{1}{2\pi\hbar} \int dt \frac{1}{N} \sum_j \left\langle \exp(-i\vec{Q} \cdot \vec{R}_j(0)) \exp(i\vec{Q} \cdot \vec{R}_j(t)) \right\rangle \exp(-i\omega t). \quad (3.19)$$

Note that the functions $S(\vec{Q}, \omega)$ and $S_i(\vec{Q}, \omega)$ can be expressed in terms of energy via $E = \hbar\omega$ as $S(\vec{Q}, E)$ and $S_i(\vec{Q}, E)$. The neutron scattering data is typically displayed in terms of energy transfer, E , as opposed to frequency, ω .

For the measurements in this thesis, the scattering is entirely coherent. The coherent and incoherent scattering cross-sections for helium (^4He) are $\sigma_{\text{coh}} = 1.34$ b and $\sigma_{\text{inc}} = 0$ b [83] which means that equation (3.18) is the appropriate expression for the dynamic structure factor for the measurements in this thesis. Therefore we will limit further discussion to coherent scattering.

Equations (3.18) and (3.19) can be interpreted in terms of quantum generalizations of classical correlation functions [86]. In both equations the quantity under the integral sign is the spatial Fourier transform of the space-time pair correlation function, $G(\vec{r}, t)$. In

classical systems this correlation function is related to the probability that a particle is at position \vec{r} at time t if it was known to be at position \vec{r}' at time $t = 0$. In a neutron scattering measurement we cannot determine the space-time pair correlation function directly. We measure a quantity which is related to the magnitude of the Fourier transform of $G(\vec{r}, t)$, but we lose the phase information making it impossible to reconstruct the correlation function directly. As in x-ray scattering, though, models of $G(\vec{r}, t)$ can be made in which the calculated $S(\vec{Q}, \omega)$ can be compared with the scattering data. Simple model calculations can be found in any of the standard references on neutron scattering [82,84,85,87].

Microscopic dynamic models of a sample can be tested if the generalized susceptibility, $\chi(\omega)$, (which is simply the response of a linear system to a sinusoidal perturbation) can be calculated. The relationship between $S(\mathbf{Q}, \omega)$ and the generalized susceptibility can be found using linear response theory and the fluctuation-dissipation theorem. Details are omitted here but the idea is that the absorptive response of the sinusoidal perturbation is directly related to the spectrum of fluctuations in thermal equilibrium [88-90]. Ignoring the \mathbf{Q} -dependence in $S(\mathbf{Q}, \omega)$ for the moment, the main result is that,

$$S(\omega) = \frac{2\hbar}{1 - \exp(-\beta\hbar\omega)} \chi''(\omega), \quad (3.20)$$

where $\beta = 1/k_B T$ and $\chi(\omega) = \chi'(\omega) - i\chi''(\omega)$. If one can approximate the system of interest with a linear model and calculate the generalized susceptibility then the scattering

function can be determined via equation (3.20). In the next section we use this form (3.20) of the scattering function to determine the neutron scattering lineshape.

3.3 The Helium Lineshape

Superfluid helium displays well-defined excitations with narrow widths indicative of long excitation lifetimes $\left(\Delta E \geq \frac{\hbar}{2\Delta t} \right)$. This means that a neutron with an appropriate energy and wavelength which scatters from superfluid helium can excite a collective mode of the liquid. The generic process considered here is that a low-energy neutron creates an excitation which is free to interact with other excitations that have been created via the thermal fluctuations in the liquid. It has been a matter of debate whether such collective modes exist in other liquids [91] but they certainly have been observed via neutron scattering in solids (phonons), spin systems (magnons), and superfluid helium (phonons-maxons-rotons).

The helium lineshape for the collective excitations is based on the well-known single-phonon lineshape discussed with regard to solids. The particular model which has been used extensively to analyze the excitations in solids and superfluid helium at low energies and momentum transfers is the damped-harmonic oscillator (DHO) model [92,93]. In this section we will present a discussion of the classical DHO model in the present context of single excitations interacting with a field of thermally-excited excitations but

we will use a mechanical model to illustrate the classical origin of the lineshape. This mechanical model is illustrated in figure 3.3 [94].

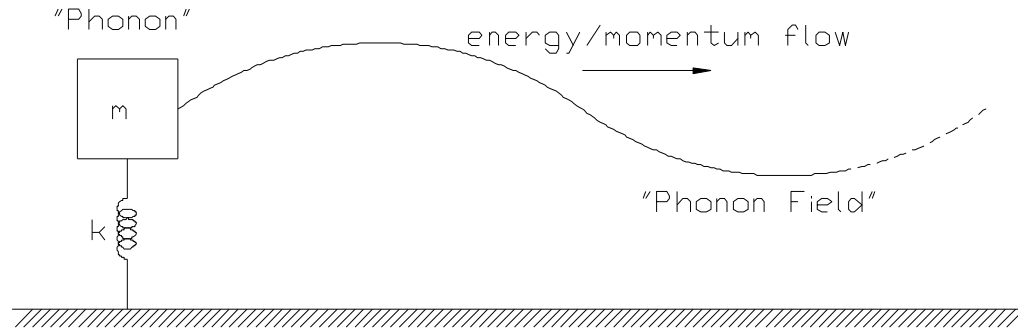


Figure 3.3 The classical mechanical analog of the damped harmonic oscillator model. The phonon created by a neutron is represented by a lumped element, the mass on a spring, while the phonon field is represented by a distributed element, a string attached to the mass. The string provides a channel to carry away the phonon's energy.

In this simple mechanical model a phonon is represented as a lumped spring-mass system and the background phonon field is represented by a distributed element, a single string under tension connected to the discrete mass which is not terminated at its right end but proceeds out an infinite distance. Thus any disturbance that originates at the mass-string interface travels away from the interface and is not reflected back. The spring-mass system has only one degree of freedom but the string has an infinite number of degrees of freedom. In fact, since the string itself can be modeled as an infinite number of harmonic oscillators, this is an appropriate model of a background field. Since the string can carry energy and momentum away from the mass, it provides a channel into which the energy and momentum of the lumped mass can be dissipated. Additionally, since energy and momentum can be transferred from the string to the mass (from infinity), the string can act as a reservoir. In this sense this is a classical analog of a particle interacting with a

field. A full quantum analysis of this system lends further credence to this notion but such a discussion will not be presented here (a discussion can be found in [95]).

A detailed analysis of the mechanical system [94] yields the equation of motion for the lumped mass,

$$m\ddot{y} + \gamma\dot{y} + ky = 2\gamma\dot{y}_{\text{in}}, \quad (3.21)$$

where $\gamma = \sqrt{\tau\rho}$ with string tension, τ , string mass density ρ , and $y_{\text{in}}(t)$, the position variation of the mass due to a disturbance propagating in towards the lumped mass. When there is no disturbance propagating along the string towards the mass then equation (3.20) reduces to an unforced damped harmonic oscillator. This expression can be rewritten in the following form,

$$\ddot{y} + 2\Gamma\dot{y} + \omega_0^2 y = f(t), \quad (3.22)$$

where we have further defined $k = m\omega_0^2$, $2\Gamma = \gamma$, and $f(t) = 4\Gamma\dot{y}_{\text{in}}(t)$. The susceptibility (the Fourier transform of the impulse response or Green function to equation (3.22)), $\chi(\omega)$, of the DHO is found by applying a Fourier transform to the entire equation (3.22).

This results in

$$\begin{aligned} \chi(\omega) &= \frac{y(\omega)}{f(\omega)} \\ &= \frac{1}{(\omega_0^2 - \omega^2) + 2i\omega\Gamma}, \end{aligned} \quad (3.23)$$

where $y(\omega)$ and $f(\omega)$ are the Fourier transforms of $y(t)$ and $f(t)$, respectively. The real and imaginary parts of the susceptibility are found via $\chi(\omega) = \chi'(\omega) - i\chi''(\omega)$ where $\chi'(\omega)$

corresponds to energy storage and $\chi''(\omega)$ corresponds to energy dissipation in the system [96]. The imaginary part can be calculated from (3.23) and is simplified to the following form,

$$\chi''(\omega) = \frac{2\Gamma\omega}{(\omega_o^2 - \omega^2)^2 + (2\Gamma\omega)^2}. \quad (3.24)$$

This can be expressed in terms of the frequency of the damped oscillator, Ω ,

$$\Omega = \sqrt{\omega_o^2 - \Gamma^2}. \quad (3.25)$$

so that (3.24) can be expressed in terms of a gain and loss term,

$$\chi''(\omega) = \frac{\Gamma}{2\Omega} \left[\frac{1}{(\omega - \Omega)^2 + \Gamma^2} - \frac{1}{(\omega + \Omega)^2 + \Gamma^2} \right]. \quad (3.26)$$

The Bose population factor, $n(E)$, is defined as $n(E) = (\exp(\beta E) - 1)^{-1}$ so that we can now combine (3.26) and (3.20) with the definition of the Bose population factor to obtain the DHO lineshape,

$$S(\omega) = (n(E) + 1) \frac{\hbar\Gamma}{\Omega} \left[\frac{1}{(\omega - \Omega)^2 + \Gamma^2} - \frac{1}{(\omega + \Omega)^2 + \Gamma^2} \right], \quad (3.27)$$

Finally we may make the substitutions $E_o = \hbar\Omega$, $\Gamma_E = \hbar\Gamma$, and $Z = \frac{\pi\hbar^2}{E_o}$ and note the

Jacobian of the transformation from ω to E ,

$$S(E) = \frac{Z}{\pi} (n(E) + 1) \left[\frac{\Gamma_E}{(E - E_o)^2 + \Gamma_E^2} - \frac{\Gamma_E}{(E + E_o)^2 + \Gamma_E^2} \right]. \quad (3.28)$$

Equation (3.28) is the lineshape used in the analysis of superfluid helium data at single values of momentum transfer, Q . To generalize this lineshape to the entire temperature

range of interest and the momentum range of the collective excitations the Q and T dependence can be simply added into the various parameters via $Z=Z(Q,T)$, $\Gamma_E=\Gamma_E(Q,T)$, and $E_o=E_o(Q,T)$. The parameters in equation (3.28) are usually identified as the oscillator strength, Z , the excitation frequency, E_o , and the excitation linewidth (half-width at half-max, HWHM), Γ_E .

The identification of E_o as the *excitation* energy has been a source of ongoing debate [92,93,97]. Both the *natural* frequency of the oscillator, ω_o , and the damped frequency, Ω , in equation (3.25) have been identified as the excitation frequency in previous studies of solids and superfluid helium. In a classical DHO like that illustrated in figure 3.3 there are actually three possible choices for the excitation frequency. In the absence of damping the resonant frequency (the frequency at which the oscillator gives the largest response when driven with a sinusoid) is ω_o . In the presence of damping and a sinusoidal driving force the oscillator has the resonant frequency $\sqrt{\Omega^2 - \Gamma^2}$. The last choice comes from the impulse response of the system defined as the motion of the oscillator after a single impulsive blow is delivered. The impulse response for the DHO is a decaying oscillation which “rings” at the damped frequency Ω . In an experiment where the probe exerts an impulsive perturbation, as in neutron scattering, the damped frequency Ω is most appropriately designated as the excitation frequency. In this thesis we will always use the damped frequency as the excitation frequency, consistent with [93]. We will see

that this lineshape is an excellent model for the roton in the bulk liquid as well as the confined liquid.

It is necessary to make one final point about the DHO lineshape. The appearance of the Bose population factor provides *detailed balance* in the scattering. At very low temperatures equation (3.28) has only a contribution from the first term in the square brackets. This corresponds to a neutron losing energy (downscattering) and creating an excitation. These are the processes which are of the most interest to us because the measured signal is much greater than the neutron upscattering term (the second term in the square brackets). At higher temperatures we expect to have an increase in the signal on the neutron-energy-gain side of the scattering. For the signal studied in this thesis (the roton), the neutron energy gain signal intensity is down by a factor 4×10^{-8} from the neutron energy loss signal at 500 mK whereas near T_λ it is down by a factor of only 10^{-2} . Near T_λ the gain signal is visible (although the width is quite large).

CHAPTER 4

MEASUREMENT TECHNIQUES

Characterization of the microscopic dynamics of a sample can be done using a number of different techniques such as the scattering of electromagnetic waves (e.g. x-rays or raman scattering) or charged particles (electrons and protons) but inelastic neutron scattering offers a number of advantages as a probe of superfluid helium. Neutrons, which are uncharged, and thus deeply penetrating, and interact only with the sample nuclei which act as point scatterers simplifying the interpretation. They can be produced with both low energies and long wavelengths, due to the neutron's large mass, which are comparable to the interatomic spacing in condensed matter systems. Charged particles are not deeply penetrating and thus are more suitable for studies of surfaces. While x-rays can be produced with very high fluxes (higher than neutron fluxes), they interact with the electronic cloud of the sample and are usually high in energy (with very short wavelengths) making the extraction of meaningful parameters from inelastic scattering difficult with current technology. Light scattering (Raman and Brillouin) is very useful for obtaining microscopic information on condensed matter samples but there are fundamental limitations in the method which allows one only to probe multiple excitation processes in helium (i.e. creation of two rotons). This limitation does not exist in inelastic neutron scattering where a single neutron can create a single elementary excitation. Thus inelastic neutron scattering offers one of the best techniques for obtaining microscopic information on superfluid helium.

Since inelastic neutron scattering was the method used to obtain the microscopic information of superfluid helium in this thesis, we present a discussion of the principles of neutron production, the details of typical instruments, and the data analysis techniques. In this chapter we review two methods of neutron production (fission and spallation), present the basic operating principles of the instruments used in this research, and discuss the techniques used to extract the dynamic structure factor, $S(\mathbf{Q}, E)$, from the raw data. Finally we discuss the experimental details for each of the measurements that have been carried out.

4.1 Neutron Production

State-of-the-art condensed matter research with neutrons requires large scale facilities capable of producing high fluxes of cold neutrons. Cold neutrons are desirable because they have wavelengths on the order of interatomic spacing and high fluxes are necessary so that experiments can be completed in a reasonable amount of time. Two experiments performed in this thesis were performed at reactor-based neutron sources, the NIST Center for Neutron Research (NCNR) in Gaithersburg, MD, and the Institut Laue-Langevin (ILL) in Grenoble, FR. Measurements were also carried out at the ISIS pulsed spallation neutron source in Oxfordshire, UK.

4.1.1 Reactor-Based Neutron Sources

Nuclear reactors, which produce neutrons via fission processes using uranium, were the first neutron sources available for condensed matter research and are still used extensively in the neutron scattering community. They provide a continuous beam of neutrons distributed over a range of energies which can be subsequently monochromated for spectrometers. Reactor design details may differ but the end product of a reactor-based facility is a continuous beam of neutrons.

A schematic illustration of a reactor-based neutron source is shown in figure 4.1. In this type of a source the neutrons are produced via fission processes using uranium. These rods are immersed in water or “heavy water”, D_2O , in order to slow down the neutrons. This is necessary because the neutrons produced in a fission process have energies on the order of MeV whereas, to sustain a fission reaction, it is necessary to have neutrons with much lower energies, ~ 25 meV. D_2O is preferred as the moderator since it has a smaller neutron absorption cross-section than H_2O thus making it a more efficient moderator.

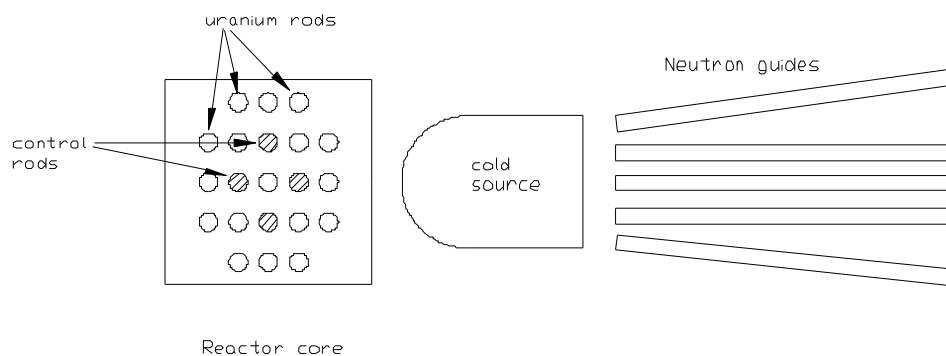


Figure 4.1 A reactor-based neutron source.

The energies of the neutron flux after thermalizing with the surrounding moderator material are distributed according to the Maxwell-Boltzmann distribution law,

$$n(E) = C \left(\frac{E}{E_T^2} \right) \exp \left(- \frac{E}{E_T} \right), \quad (4.1)$$

where C is a normalization constant and E_T is the effective temperature of the moderator material. After thermalizing with the D_2O (assumed at room temperature, 300 K) the neutrons have a distribution which has a maximum around 25 meV and the “tails” of the distribution are in the “cold neutron” region. The relative number of cold neutrons in the tails of the distribution are usually unreasonably low to be of any use. The bulk of the neutrons which have thermalized with D_2O at 300 K are referred to as “thermal neutrons”. In order to get the bulk of the thermal neutrons into the energy range of condensed matter systems, i.e. get them cold, the neutrons must undergo another moderation process. This next moderation process effectively shifts the peak in the Maxwellian distribution from the thermal range into the cold range as shown in figure 4.2. The second moderator is usually a cryogenic material like heavy ice (solid D_2O), liquid hydrogen, liquid methane, or solid methane, for instance.

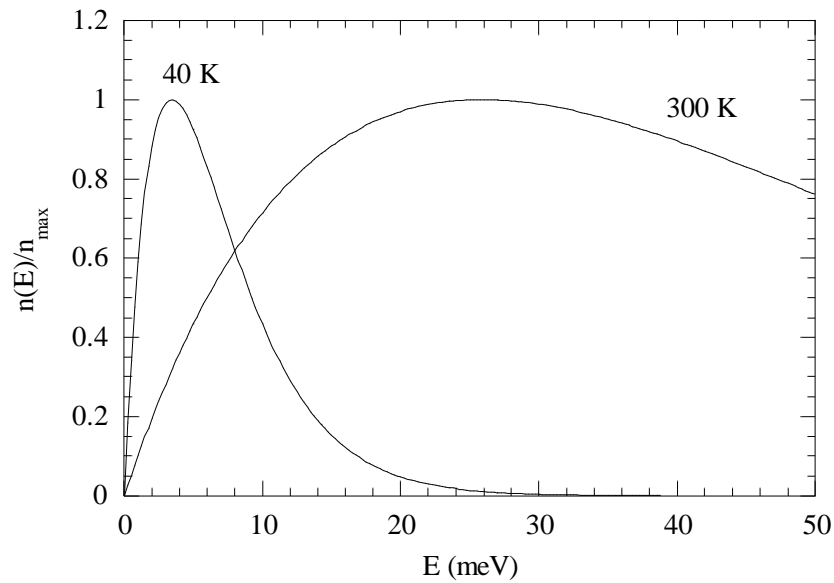


Figure 4.2 Energy distributions of neutron flux from a moderator at temperatures of 40 K (cold neutrons) and 300 K (thermal neutrons).

After the neutron energy spectrum has been shifted down into the cold region the neutrons are transported to the spectrometer via neutron guide tubes which can be tens of meters long. Here the wavelike properties of the neutron are exploited to transport the neutrons efficiently. The long distances over which these neutrons are transported necessitate the use of high efficiency guides to (nearly) eliminate the $1/r^2$ diminution of the flux intensity. The guides operate on the principle of total external reflection from the interior surface. The interior surface of the guide is typically made of highly polished glass (containing boron) and then coated with a thin layer of a nickel isotope to provide the required reflective properties. The polished glass provides a smooth surface onto which the nickel can be evaporated and the boron, which is a strong neutron absorber,

prevents the neutrons which are not completely reflected from the surface from leaving the guide. The guides operate under vacuum and are surrounded by biological shielding.

4.1.2 Spallation Neutron Sources

The operating principle of a spallation neutron source is quite different from a fission reactor. The term “spall” means to chip or splinter and is a descriptive term for the nuclear reactions which produce neutrons in a spallation neutron source. Spallation sources use high energy particles to chip away at the nucleus producing a variety of products such as neutrons.

Since nuclei are very strongly bound in atoms, a large amount of energy is necessary to liberate them. For instance at the ISIS spallation source at the Rutherford Appleton Laboratory, a synchrotron accelerates protons to energies of about 800 MeV. Initially an ion source generates hydrogen ions, H^+ , at energies on the order of 500 keV. These ions are accelerated via a LINAC to energies on the order of 100 MeV and, after passing through thin aluminum foil to strip off the two remaining electrons, they are injected into the accelerator ring. The proton synchrotron accelerates the protons up to energies of order 500-1000 MeV. The energetic protons are extracted from the synchrotron on the order of 50 times per second and these “proton bunches” ($\sim 2.5 \times 10^{13}$ protons per pulse) ultimately collide with a uranium target. A schematic illustration of this process is shown in figure 4.3.

After the protons collide with the target the resulting neutrons have energies on the order of MeV which must be reduced to the meV range to be of use for condensed matter experiments. Once again this can be accomplished by thermalization with a thermal or cryogenic moderator. Finally the neutrons are transported to the instrument via neutron guide tubes as discussed in the previous section.

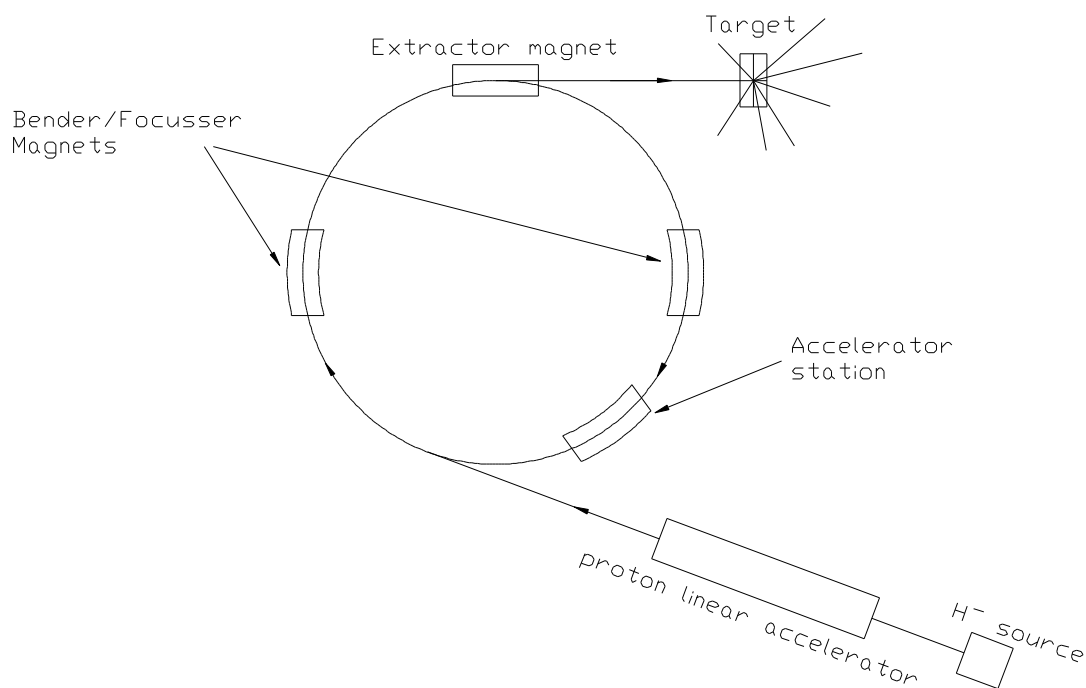


Figure 4.3 Principle components of a spallation neutron source.

4.2 Neutron Spectrometers

The information that one would like to extract from an inelastic neutron scattering measurement is the dynamic structure factor, $S(\mathbf{Q}, E)$. There are a variety of types of

instruments that allow one to obtain this information and we discuss three types. The three basic instruments used for these measurements were the triple-axis spectrometer (SPINS at the NCNR), the direct geometry chopper spectrometer (FCS at the NCNR and IN6 at the ILL), and the inverted geometry chopper spectrometer (IRIS at ISIS).

The instruments can differ in design a great deal but they all contain a *primary* spectrometer, a sample environment, and a *secondary* spectrometer. The primary and secondary spectrometers provide the same information, independent of the type of instrument. The primary spectrometer defines the incident neutron energy and wavevector and the secondary spectrometer defines the final energy and scattering angle (wavevector). Each type of instruments accomplishes these things in a different way and yields the dynamic structure factor, $S(\mathbf{Q}, E)$.

4.2.1 The Triple-Axis Spectrometer

The triple-axis spectrometer (TAS) is an instrument which takes advantage of a continuous beam of neutrons thus making it optimal for use on a reactor-based neutron source. The TAS is a versatile instrument with a simple design. As the name implies there are three degrees of rotational freedom inherent in the spectrometer as shown in figure 4.4. In the primary spectrometer the incident beam is monochromated via Bragg reflection from the monochromator crystal and the wavelength (and incident energy) is

determined by rotating the monochromator crystal (changing θ_M) via the Bragg condition,

$$n\lambda = d \sin\theta_M.$$

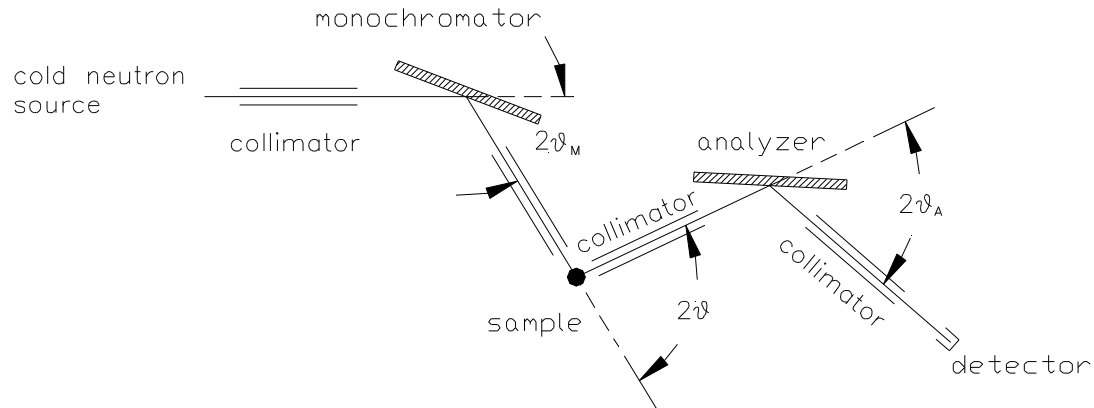


Figure 4.4 Functional diagram of a triple-axis spectrometer.

The sample environment consists of a rotating platform situated between the monochromator and analyzer arms. This rotating platform provides the second degree of rotational freedom which is necessary for the Bragg condition to be satisfied for final energy analysis. For studies of isotropic samples such as liquids this degree of freedom is not important.

In the secondary spectrometer the final wavelength (energy) of the scattered neutrons are again determined by Bragg reflection from the analyzer crystal. Neutrons with a fixed final energy (determined by θ_A) are scattered into a neutron detector. The scattering angle is determined via orientation of the spectrometer arm between the sample and analyzer.

Since the incident and final wavelengths (energies) of the neutrons are defined via Bragg reflection which requires a well-defined incident wavelength, the beams must be well-defined. Collimators are usually placed between the monochromator and sample, sample and analyzer, and analyzer and detector to serve this purpose. *Soller slits* are a general collimation system used in a TAS and are composed of thin parallel sheets made of some neutron absorbing material (e.g. cadmium). The angular divergence of the neutrons is defined by the spacing of the sheets and, hence the spacers which separate them.

The momentum and energy delivered to the sample by the incident neutrons are easily determined based on the instrument geometry shown in figure 4.4. The incident and final wavelengths in the TAS are determined by the basic equations,

$$k_o = \frac{\pi}{d_M \sin \vartheta_M}, \quad (4.2)$$

$$k_F = \frac{\pi}{d_A \sin \vartheta_A}, \quad (4.3)$$

$$\vec{Q} = \vec{k}_o - \vec{k}_F, \quad (4.4)$$

$$E = \frac{\hbar^2}{2m_n} (k_o^2 - k_F^2), \quad (4.5)$$

where the wavevector is defined as $k = 2\pi/\lambda$, d_M and d_A are the d-spacings of the monochromator and analyzer crystals, θ_M and θ_A are the monochromator and analyzer scattering angles, and \mathbf{Q} and E are the (vector) momentum and energy transfer to the scattering system, respectively.

Information on the scatterer is contained in the neutron scattering cross-section of the sample, as discussed in chapter 3. One advantage of the TAS is that it can measure particular points in \mathbf{Q} -E space with E defined in equation (4.5) and \mathbf{Q} defined in equation (4.4). The TAS can be easily adjusted so that one can carry out any type of scan in \mathbf{Q} or E. For example, a widely used configuration of the instrument, known as the “constant- \mathbf{Q} ” mode, involves a simultaneous adjustment of the monochromator angle, scattering angle, and analyzer angle. A scan in energy transfer is accomplished at a fixed value of momentum transfer resulting in a straight line path in \mathbf{Q} -E space. In such a scan one measures $S(\mathbf{Q},E)$ scaled by the number of incident neutrons so that, in principle, no additional corrections beyond instrumental resolution (discussed in section 4.3) are necessary. The TAS contrasts the other instruments described in this chapter which yield raw data that do not afford such a straightforward interpretation and require some form of “data reduction” to obtain $S(\mathbf{Q},E)$.

The SPINS TAS at the NCNR is located on beam guide NG-5 viewing a liquid hydrogen cold source (20 K). The beam guide has a rectangular cross-section (50 mm \times 120 mm) and an interior glass surface coated with Ni-58. The incident beam passes through a liquid nitrogen cooled Be filter after reflection from the monochromator (in order to remove the unwanted higher order reflections from the monochromator). Collimators are present between the monochromator and sample, sample and analyzer, and analyzer and detector but between the source and monochromator there is an open beam. Both the

monochromator and analyzer crystals are pyrolytic graphite and the 002 reflection determines the scattered neutron energy and wavelength via equations 4.2-4.5. Finally the neutrons are detected with a ^3He detector 2.54 cm in diameter and 15.09 cm long. This instrument is capable of achieving energy resolutions of 20 μeV (full-width half-max) in certain configurations with low energy transfer. However the signal probed in this thesis required larger energy transfers so that the energy resolution was approximately 50 μeV FWHM.

4.2.2 The Direct Geometry Time-of-Flight Spectrometer

A functional diagram of a typical direct geometry TOF spectrometer used on a reactor based neutron source is shown in figure 4.5. These instruments are used effectively on both reactor-based sources and pulsed sources. The principle difference between the instrument on a reactor-based source and a pulsed source is that the continuous beam provided by a reactor-based source can be monochromated by a crystal monochromator. On a pulsed source the beam is monochromated via a chopper phased with the pulsed source. The remainder of the design of the spectrometer is independent of the type of source.

The primary spectrometer is composed of the neutron guide, a crystal monochromator, and a filter to remove higher order contamination of the beam. A chopper interrupts the beam and provides a short pulse of monochromatic neutrons. This allows TOF

techniques to be used to determine the final energy of the neutron. Often the chopper used is a Fermi chopper which has a curved set of slots (as sketched in figure 4.5). When the chopper rotates the neutron sees a straight path through the chopper in its inertial frame. The distance traveled to the sample from the chopper is given by L_{CS} .

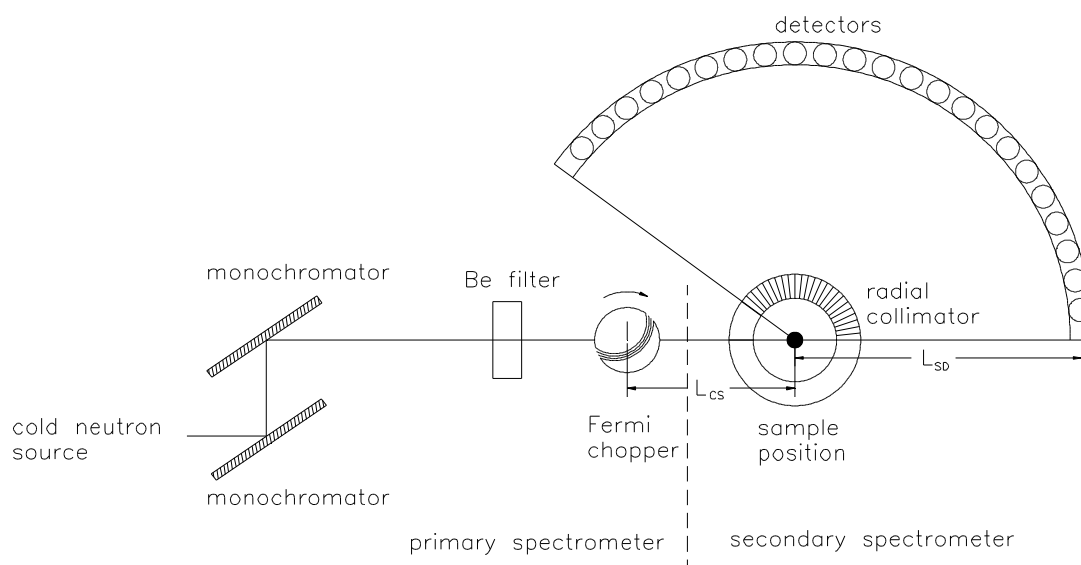


Figure 4.5 Functional diagram of a direct geometry TOF spectrometer.

The secondary spectrometer consists of the final flight path and the detectors which are located at a fixed radius from the sample whose distance is shown as L_{SD} . As shown in the figure some instruments use a radial collimator which helps to reduce scattering from components which surround the sample.

The incident and final energies of the neutron are determined in a straightforward manner. The incident energy of the beam, determined by Bragg reflection from the monochromator, is given by

$$E_o = \frac{\hbar^2}{2m_n} \left(\frac{\pi}{d_M \sin \vartheta_M} \right)^2, \quad (4.6)$$

where d_M is the d-spacing of the monochromator, m_n the mass of the neutron, and θ_M is the scattering angle from the monochromator. The chopper-to-sample time can be determined using (4.6) and

$$E_o = \frac{1}{2} m_n \left(\frac{L_{CS}}{t_{CS}} \right)^2, \quad (4.7)$$

so that

$$t_{CS} = \frac{m_n d_M L_{CS} \sin \vartheta_M}{\pi \hbar}. \quad (4.8)$$

The total flight time of the neutron, t_{tot} , is recorded, and can be used with the chopper-sample flight time, t_{CS} , so that the final energy of the neutron is given by

$$E_F = \frac{1}{2} m_n \left(\frac{L_{SD}}{t_{tot} - t_{cs}} \right)^2. \quad (4.9)$$

Equations (4.6) and (4.9) can be used to determine the energy transfer to the scattering system using equation (3.2). Using the known incident and final energies (and hence the incident and final wavevectors k_o and k_F) and the scattering angle 2θ , the momentum transfer (magnitude) can be determined using the kinematic relation (3.3) repeated below for convenience

$$Q = \left(k_o^2 + k_F^2 - 2k_o k_F \cos 2\vartheta \right)^{\frac{1}{2}}. \quad (3.3)$$

As mentioned previously a single detector on a TOF instrument does not provide a constant-Q cut through Q-E space. Rather the detector cuts a curved path through Q-E space via equations as shown in figure 4.6.

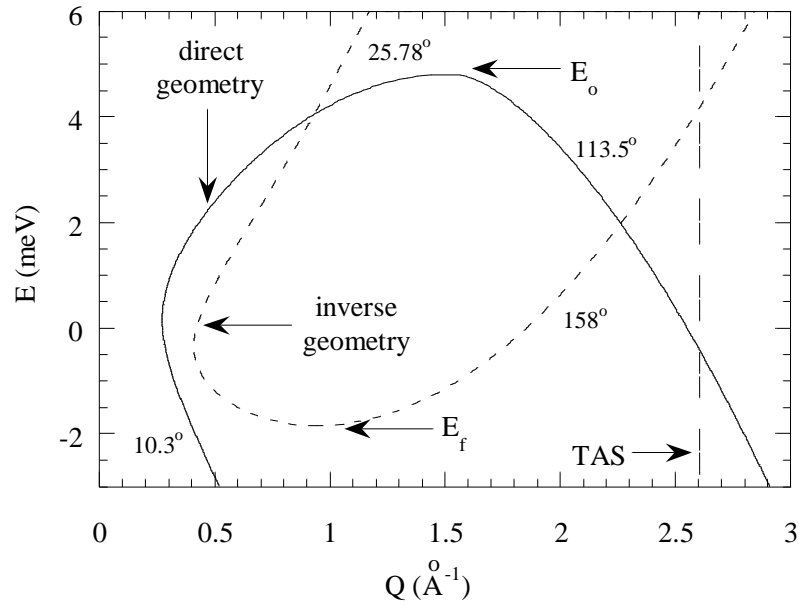


Figure 4.6 Constant angle cuts through Q-E space for a direct geometry TOF instrument (solid line) and an inverse geometry instrument (dotted line), and a constant-Q cut for a TAS (dashed line). Paths in Q-E space for two different detectors on the TOF instruments have been plotted.

The raw data recorded in a TOF experiment, $I(n_D, t_{tot})$, is the intensity as a function of detector group (scattering angle) n_D , and time-of-arrival, t_{tot} , and is recorded for each detector. The time of arrival at the neutron detectors is essentially determined by the initial and final velocities of the neutrons and the total flight path. In fact what one

actually measures in a TOF measurement is proportional to $\frac{d^2\sigma}{d\Omega dt_{\text{tot}}}$ where t_{tot} is the total

flight time from chopper to detector,

$$t_{\text{tot}} = t_{\text{CS}} + t_{\text{SD}}, \quad (4.10)$$

and $d\Omega$ is the acceptance angle subtended by an individual detector. In order to relate

$\frac{d^2\sigma}{d\Omega dt_{\text{tot}}}$ to the quantity of interest, $\frac{d^2\sigma}{d\Omega dE_F}$, one must multiply the data by a factor of

$(t_{\text{tot}} - t_{\text{CS}})^3$ which is just part of the Jacobian in the transformation from total flight time to final energy. In order to obtain the dynamic structure factor, $S(\mathbf{Q}, E)$, another factor of $(t_{\text{tot}} - t_{\text{CS}})$ must be multiplied with the data as evident from equations (3.16) and (3.17).

The direct geometry spectrometers used during the course of the research in this thesis were the Fermi Chopper Spectrometer at the NCNR and IN6 at the ILL. FCS is a very basic chopper spectrometer and figure 4.5 is based in large part on it. FCS is located on the beamline NG-6 with a beam guide of rectangular cross-section with dimensions 150×60 mm. This guide also views the same liquid hydrogen moderator as the SPINS TAS discussed previously. The double monochromator consists of two pyrolytic graphite crystals (002 reflection). The incident beam passes through a liquid nitrogen cooled Be filter after reflection from the double monochromator to minimize order contamination in the incident beam. A Fermi chopper pulses the monochromatic beam on the sample and an oscillating radial collimator surrounds the sample area to minimize parasitic scattering from components which surround the sample (e.g. the cryostat) into the detectors. The

final flight path is a radial distance 2.286 m from sample to detector and is evacuated to minimize scattering from gas molecules. Finally the neutrons are detected in a bank of 103 pressurized ^3He detectors 2.5 cm in diameter separated by 1.3° providing an angular coverage of 5° to 140° . This is a medium resolution instrument and, for the measurement in this thesis, the energy resolution was about $170\text{ }\mu\text{eV}$ FWHM.

The spectrometer IN6 is quite similar to FCS but with a number of small differences. The incident beam is extracted from beam guide H15, a cold neutron guide tube whose interior surface consists of a thin layer of Ni-58 on a glass surface. This beam guide views a liquid deuterium cold source at 25 K. The primary spectrometer consists of a monochromator made up of three pyrolytic graphite arrays (which focus the beam on the sample position), a liquid nitrogen cooled Be filter, and a Fermi chopper. The secondary spectrometer consists of an evacuated sample region, a helium filled box between the sample and the detectors (to minimize background scattering), a radial oscillating collimator (as on FCS), and 337 pressurized ^3He neutron detectors located at a radial distance of 2.47 m from the geometric center of the sample region providing an angular coverage of 10° to 114° . IN6 is a medium resolution instrument and, for the measurement in this thesis, the energy resolution was roughly $140\text{ }\mu\text{eV}$ FWHM.

Two corrections which are common to TOF measurements (both direct and inverse geometries) are the detector normalization and efficiency correction. To obtain detector normalization, a scattering measurement using a vanadium cylinder is done with the

particular instrument configuration. Since vanadium is an incoherent scatterer, and hence an isotropic scatterer, the integrated intensity of the Bragg peaks resulting from a neutron-vanadium scattering event should be constant with scattering angle. Any deviations in the integrated intensity which are measured from the vanadium sample thus result from deviations in the calibration of the individual detectors. Therefore this vanadium measurement provides the information necessary to normalize the detectors in subsequent measurements. After the data is converted to energy transfer each detector group is normalized via the information obtained from the vanadium calibration measurement (i.e. divided through by the integrated intensity of the Bragg peaks found in the vanadium calibration measurement).

The correction for the efficiency variation of the detectors is analytic. It is well-known that the efficiency of pressurized ^3He detectors (i.e. neutron absorptive properties) varies with neutron energy and ^3He density. In the case of IN6 where the detectors are pressurized to 3 bars ($\rho=7.3\times 10^{19}$ atoms/cc) and have a diameter, d , of 2.5 cm, the efficiency is calculated via

$$\begin{aligned} \text{eff}(E) &= 1 - \exp(-\rho d \sigma_a(E)) \\ &= 1 - \exp\left(-\frac{4.9}{\sqrt{E_F}}\right) . \end{aligned} \quad (4.11)$$

Note that the absorption cross-section of ^3He (5333 barns at 25.3 meV) was used to obtain $\sigma_a(E)=26825E^{-1/2}$ barns where E is in meV. A similar argument is used for the helium detectors on FCS.

4.2.3 The Inverse Geometry Time-of-Flight Spectrometer

All spectrometers previously discussed have the common feature that the incident spectrometer provides a monochromatic beam to the sample. The inverse geometry spectrometer is quite different in this respect. In an inverse geometry TOF spectrometer the beam which is incident on the sample is white and the scattered neutrons which are detected are monochromatic. In contrast to the TOF method in a direct geometry spectrometer, here the time-of-flight technique resolves the *incident* energies of particular neutrons. Perhaps one of the most important benefits of this technique is that, since the scattered neutrons undergo an almost complete backscatter into the detectors, extremely small energy resolutions are possible even with modest energy transfer to the sample.

An illustration of an inverse geometry spectrometer is shown in figure 4.7. As in the direct geometry spectrometer there is a primary and secondary spectrometer. The primary spectrometer consists of the beam guide from the cold source to the sample and two disk choppers (synchronized with the pulses of the neutron source) located between the moderator and the sample. The disk choppers define the wavelength range of the incident neutrons and prevent “frame overlap.” Frame overlap is the undesirable situation where slow neutrons in one pulse are overtaken by faster neutrons from a later pulse.

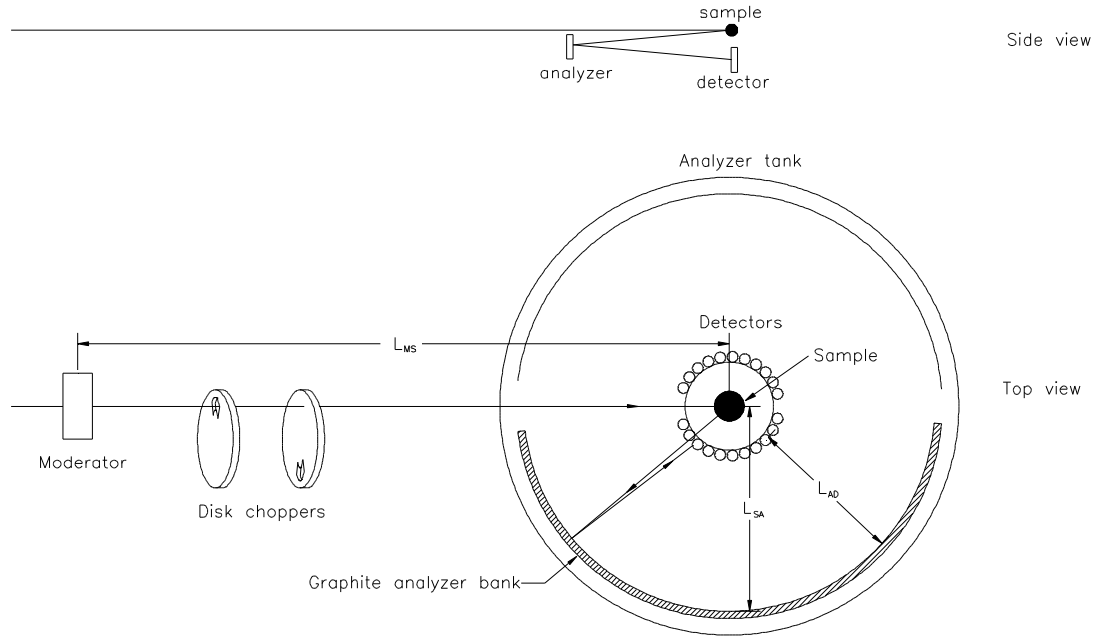


Figure 4.7 Functional diagram of an indirect geometry TOF spectrometer.

The secondary spectrometer is comprised of the analyzer tank, a crystal analyzer array, and detector bank located concentric to the sample location. The neutrons which scatter from the sample Bragg reflect from the analyzer bank and are backscattered to the detector banks. The final energy of the neutrons as determined by the Bragg reflection from the analyzer bank is given by

$$E_F = \frac{\hbar^2}{2m_n} \left(\frac{\pi}{d_A \sin \vartheta_A} \right)^2, \quad (4.12)$$

where d_A is the d-spacing of the analyzer, and θ_A is the scattering angle from the analyzer.

The incident energy of the neutrons is determined using the total flight time of the neutron, t_{tot} , the incident energy, and the neutron flight paths. The final energy can be written in terms of the flight time in the secondary spectrometer, t_2 , as

$$E_F = \frac{1}{2} m_n \left(\frac{L_{SA} + L_{AD}}{t_2} \right)^2, \quad (4.13)$$

where L_{SA} and L_{AD} are the known sample-to-analyzer and analyzer-to-detector distances respectively. Solving for t_2 yields

$$t_2 = \frac{m_n d_A (L_{SA} + L_{AD}) \sin \vartheta_A}{\pi \hbar}. \quad (4.14)$$

The total time-of-flight for a neutron scattered into the detectors, t_{tot} , is recorded and this is defined as

$$t_{\text{tot}} = t_{MS} + t_2, \quad (4.15)$$

where t_{MS} is the time for the neutron to travel the length of the primary spectrometer from moderator to the sample. Since t_{tot} is known from the data acquisition and t_2 can be calculated from (4.14) then the time for a particular neutron to travel the initial flight path is given by $t_{MS} = t_{\text{tot}} - t_2$. Therefore the incident energy of the neutron can be calculated via

$$E_o = \frac{1}{2} m_n \left(\frac{L_{MS}}{t_{\text{tot}} - t_2} \right)^2, \quad (4.16)$$

where L_{MS} is the known distance from the moderator to the sample position. The energy transfer can be calculated from $E = E_o - E_F$ and the momentum transfer can be determined from equation (3.3) as usual.

At this point the information can be used in a similar way as for a direct geometry measurement (see previous section) to find $S(Q,E)$. The quantity measured, $\frac{d^2\sigma}{d\Omega dt_{\text{tot}}}$, is related to the quantity of interest, $\frac{d^2\sigma}{d\Omega dE_F}$, via a factor of $(t_{\text{tot}}-t_2)^3$ and $S(Q,E)$ is obtained by multiplying through another factor of $(t_{\text{tot}}-t_2)$.

The IRIS spectrometer, the basis for the schematic illustration shown in figure 4.6, is located on beamline N6(A) at the ISIS pulsed source. It views a liquid hydrogen cold source (25 K) which provides a high flux of cold neutrons (at full ISIS intensity the flux at sample is about 5×10^7 n/cm² s). The incident neutrons travel along a curved neutron guide (Ni-plated glass tubes of rectangular cross-section 65 mm \times 43 mm) a distance of about 33 m passing through two disk choppers rotating at 50 Hz and phased with the pulsed source. The final beam guide component is a 2.5 m long titanium-nickel supermirror guide (rectangular cross-section which reduces to 32 mm \times 21 mm) which provides a flux gain of a factor of almost 3 at 5 Å. The analyzer tank 2 m in diameter is kept under vacuum. There are two analyzer banks, a mica bank and a pyrolytic graphite bank, and these are cooled with gaseous helium down to about 25 K to reduce the thermal diffuse scattering. The experiment discussed in this thesis used the pyrolytic graphite (002 reflection) exclusively due to the energy and momentum transfer requirements. In addition a 25 K Be filter is situated between the sample and analyzer to minimize higher order contamination of the scattered beam. Finally two 51-element ZnS scintillator

detector banks provide coverage of the scattering angles between 26° and 158° . Note that these detectors are positioned at a scattering angle of 175° from the analyzers in a near-backscattering condition.

4.3 Instrumental Resolution

After the raw data has been reduced to $S(\mathbf{Q}, E)$ as discussed in the previous sections the information contained in the dynamic structure factor is still distorted due to instrumental broadening. The underlying mechanisms contributing to the instrumental broadening are different for each instrument. Non-idealities of the instrument prevent one from probing an exact point in Q-E space. Rather the *instrumental resolution function* or *point spread function* smears the actual Q-E point which is measured. In this section we discuss the factors which contribute to the instrumental resolution and present the method with which the data in this thesis was corrected for instrumental resolution.

The instrumental resolution of a TAS is due to mosaic spread of the monochromator and analyzer crystals, the divergence angles of the collimation system, and finite sample size [98]. The resolution may be calculated with some simple and well-justified assumptions. The principle assumptions of the calculation of the resolution function is that the mosaic spread of the crystals and the angular divergence of the collimation system are both distributed in accord with gaussian statistics. For example the transmission function of an ideal *Soller collimator* (made up of parallel slats of perfectly neutron absorbing

material) is a triangle function. However, the slats are not perfect absorbers leading to a rounding of the transmission function which may be approximated by a gaussian. The simplifying assumptions lead to an overall instrumental resolution function which is a four-dimensional ellipsoid in **Q**-E space (shown in figure 4.8) that has a different orientation depending on its location in **Q**-E space. Note that when studying samples which are isotropic, like liquids, then one is only concerned with the magnitude of the momentum vector , $Q = |\mathbf{Q}|$.

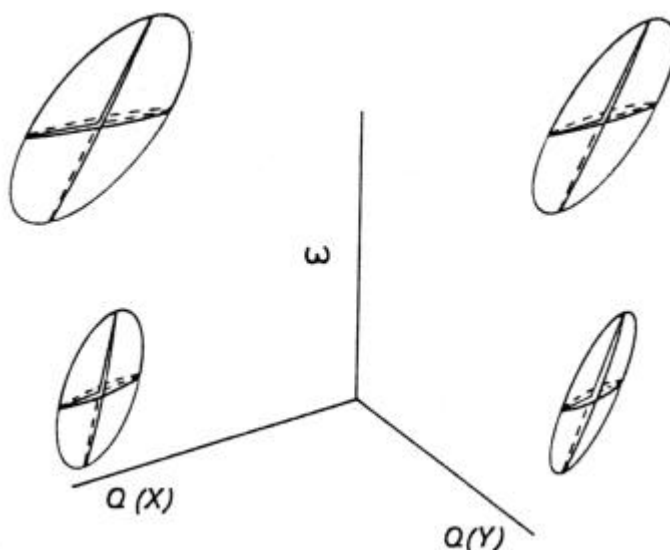


Figure 4.8 Resolution ellipsoids for a TAS at various points in the four-dimensional **Q**-E space. Adapted from [98].

The instrumental resolution of a direct geometry TOF spectrometer results from the geometry of the instrument, the spatial, angular, energy, and time spread of the incident neutron pulse, as well as the finite time channel width of the TOF analyzer. The effects on the beam after thermalization (excluding the sample effects), can be modeled reasonably accurately as individual gaussian processes. On a pulsed source where the

neutron burst passes through the moderator, the resulting distribution of neutron energies from the moderator is asymmetric. Thus the distortion that this asymmetric pulse suffers from the subsequent instrumental effects is not trivial and, in general, not analytically calculable. If necessary, a numerical Monte-Carlo simulation *can* be performed which simulates the instrument [99,100]. The simulation is based on a number of factors including the instrument geometry, energy and momentum transfer of the neutrons, and shape of the neutron burst. In a reactor-based source where the incident beam is continuous and monochromated by a crystal monochromator, the beam which emerges from the chopper is fairly symmetric, thus allowing one to perform a reasonably accurate calculation of the instrumental resolution.

Analytical calculation of the instrumental resolution of an inverse geometry spectrometer has similar difficulties associated with it as the direct geometry spectrometer. Namely, the principle contributions come from the mosaic spread of the analyzer, Bragg angle of the analyzer, and the time spread of the incident pulse. These principle components, when convoluted together, yield the overall energy resolution. One can arrive at an estimate of the resolution by approximating the various contributions as gaussians, as in the case of the TAS. In this approximation the resolution for an inverse geometry instrument is [101]

$$\Delta E \approx 2E \left(\frac{\Delta t_{\text{mod}}}{t_{\text{tot}}} \right) \otimes \left(\frac{\Delta d_A}{d_A} \right) \otimes (\cot \vartheta_A \cdot \Delta \vartheta_A), \quad (4.17)$$

where E is the energy transfer, t_{tot} is the total flight time for the neutron, Δt_{mod} is the time spread of incident neutrons due to the uncertainty in the precise “center” of the moderator, Δd_A is the uncertainty in the lattice spacing of the analyzer crystals, and $\Delta \theta_A$ is the uncertainty in the Bragg angle of the analyzer. As is evident from equation (4.17) the near backscattering condition ($2\theta_A \sim 180^\circ$) reduces the last term a great deal providing the excellent energy resolution of this type of spectrometer.

In many cases the instrumentally broadened scattering data can be expressed as a one-dimensional convolution in terms of an *effective* resolution function, $R_{\text{eff}}(E)$, and the intrinsic lineshape, $S_{\text{int}}(E)$,

$$\begin{aligned} S_{\text{obs}}(E) &= S_{\text{int}}(E) \otimes R_{\text{eff}}(E) \\ &= \int dE_1 R_{\text{eff}}(E - E_1) S_{\text{int}}(E_1), \end{aligned} \quad (4.18)$$

where the symbol, \otimes , represents the convolution operation. If the scatterer is known to have a narrow intrinsic linewidth and does not exhibit significant dispersion then $R_{\text{eff}}(E)$ can be considered a good approximation to the actual instrumental resolution, $R(Q, E)$. With a scatterer like superfluid helium which is known to have an extremely narrow intrinsic lineshape at low temperatures however, the shape of the line can be significantly distorted, especially away from the roton minimum. In spite of this distortion, $R_{\text{eff}}(E)$ as determined by low temperature superfluid helium, can be used for analyzing data with the same type of dispersion (i.e. other helium data). Except for the SPINS measurement, the effective instrumental resolution function, $R_{\text{eff}}(E)$, was determined in exactly this same

way for each instrument, namely using scattering data from low temperature bulk superfluid helium.

At 500 mK the linewidth (FWHM) at the roton minimum is extremely narrow, about 0.1 μeV [102]. Recall that the superfluid lineshape is the DHO discussed in chapter 3 and given by equation (3.28). For small linewidths (appropriate for our low temperature superfluid excitations), the DHO model can be approximated by the difference of two delta functions,

$$\begin{aligned} S_0(Q, E) &= \lim_{\Gamma \rightarrow 0} S_{\text{DHO}}(Q, E) \\ &= \frac{Z}{\pi(1 - e^{-\beta E})} [\delta(E - E_o(Q)) - \delta(E + E_o(Q))] \end{aligned} \quad (4.18)$$

At low temperatures, $\beta \rightarrow \infty$, so that the detailed balance factor eliminates the second delta function in equation (4.18). This simply is a mathematical way of saying that there are no excitations present in the liquid at low temperatures which can give up energy to a neutron. When this low-temperature limit of the scattering is convoluted (at a particular Q) with the effective instrumental resolution function, $R_{\text{eff}}(Q, E)$, the result is simply a scaled and shifted form of the resolution function,

$$S_0(Q, E) \otimes R_{\text{eff}}(Q, E) = \frac{Z}{\pi} R_{\text{eff}}(E - E_o(Q)). \quad (4.19)$$

To obtain the resolution function, $R_{\text{eff}}(Q, E)$, from equation (4.19) it is necessary first, to use the known bulk helium dispersion, $E_o(Q)$ in order to shift $S_0(Q, E) \otimes R_{\text{eff}}(Q, E)$ to the origin and second, normalize this result. To illustrate this procedure, the resolution functions for IRIS, IN6, SPINS, and FCS at the roton minimum are shown in figure 4.9.

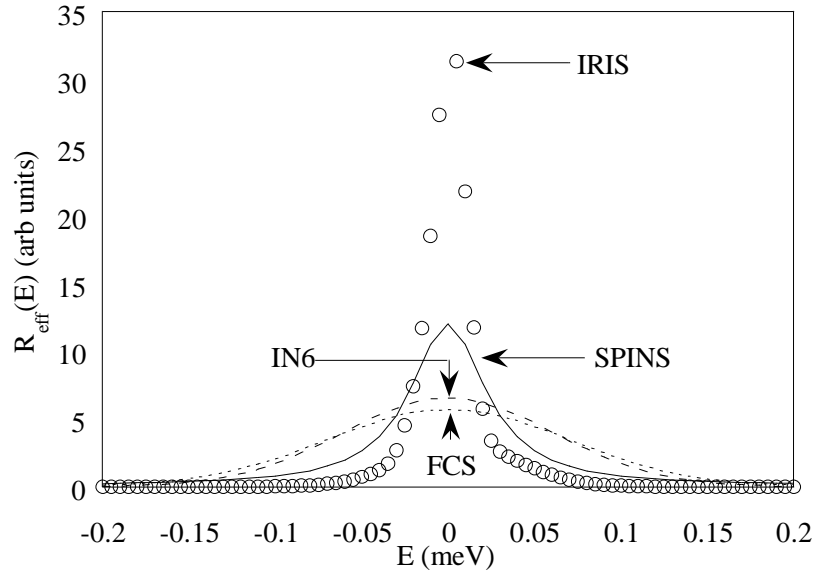


Figure 4.9 Effective instrumental resolution function determined at the roton minimum for different instruments used in this thesis.

4.4 Experimental Details

The measurements performed in this thesis required three items beyond the neutron source and spectrometer: a sample cell, cryostat, and gas-handling system. The sample cells were essentially similar in design (except for the xerogel experiment), the most stringent requirement being that they were free of super-leaks. The requirements for the cryogenics are obvious in the sense that it was always necessary to be in the superfluid phase but different cryostats were used in each measurement depending on the desired

temperature range of the measurement. The gas-handling systems were all similar in design and enabled a controlled amount of helium to be condensed into the sample cell. In this section we discuss the details of each of the measurements and the data reduction.

4.4.1 Common Procedures

The porous media in these studies all have large surface area. Therefore it is necessary to ensure that oil does not backstream from the mechanical pump into the cell during sample evacuation. This could cause undesirable contamination of the porous media resulting in a large incoherent scattering signal from the (hydrogen in the) oil. To avoid this possibility, careful measures were taken to ensure that the sample was never in a situation where oil could stream down the fill line into the cell. To this end the sample cells were pressurized to just over 1 atmosphere with helium gas and valved off. Next the center stick was placed in a top-loading cryostat at room temperature and connected to a pumping station having both a mechanical roughing pump and a turbo pump. The mechanical pump roughed away the overpressure of helium gas and, once down to a reasonable pressure (about 50 mTorr) the turbo pump took over. The sample exhibited substantial outgassing so it was pumped on until the cryostat had to be cooled down. Standard operating procedure was to continue pumping on the sample for at least 24-36 hours. At the end of this period the samples usually exhibited little outgassing. After evacuation of the sample, the sample cell was isolated from the gas handling system and the cryostat was cooled to base temperature. The temperature of the cryostat was

controlled electronically with a stability to within ± 0.015 mK and the sample cell was usually measured with a calibrated germanium thermometer.

To avoid overfilling the pores of the porous media, 95% of the open pore volume of the media was filled with liquid helium. The amount of liquid necessary to fill 95% of the open pore volume was determined from the known open pore volume of the materials via the density and the porosity consistent with adsorption isotherm measurements and the density of liquid helium at low temperature. The gas-handling system (GHS) used to decant the appropriate amount of helium were simple in design as shown in figure 4.10. The primary storage volume plus the volume in the tubing in the manifold amount to 31.586 liters in total.

The procedure for filling the sample cell with liquid helium was simple. The large storage volume was filled with gaseous helium up to a pressure of 760 Torr. The gas-equivalent of the liquid was determined from the necessary amount of liquid to fill the pores to 95% capacity. The valve connecting the GHS to the sample cell was slowly opened to let the gas bleed into the sample cell, which was at a temperature well below the superfluid transition temperature. Bleeding the gas in had to be done slowly because the warm gas warmed the cell up substantially. Once the required amount of helium had been condensed into the sample cell, the cell was valved off, the GHS manifold and storage volume were evacuated, and the valve on the cell was opened back up to the manifold and large storage volume for safety and to monitor the pressure in the cell.

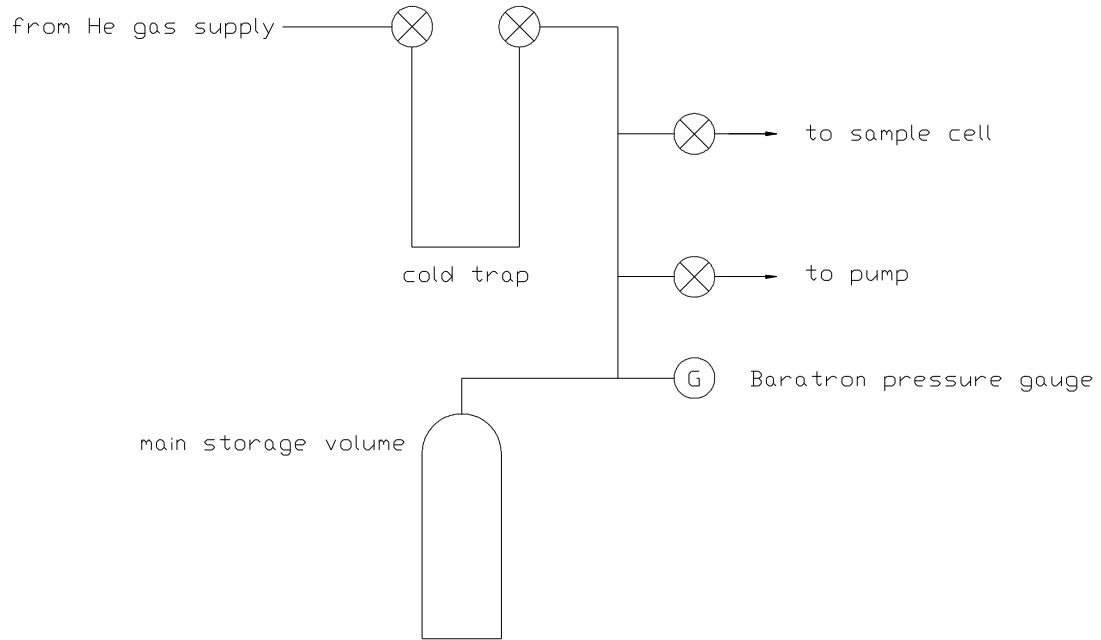


Figure 4.10 Schematic illustration of the gas handling system used in the SPINS and FCS measurements. The large storage volume used in the SPINS measurement (storage volume + manifold = 31.586 liters) was replaced with a 22.24 liter storage volume for the FCS measurement.

4.4.2 The Aerogel Measurements

The excitations of helium in aerogel were measured using the SPINS and IRIS spectrometers. The details of the two measurements are discussed in this section.

SPINS was operated in constant-Q mode with a fixed final analyzer energy of 2.6 meV. Since our primary interest was the temperature dependence of the roton, the energy scans were performed at a constant momentum transfer, $Q = 1.92 \text{ \AA}^{-1}$. In the present

configuration the instrumental resolution at 1.92 \AA^{-1} was about $53 \text{ } \mu\text{eV}$ (FWHM of the resolution function).

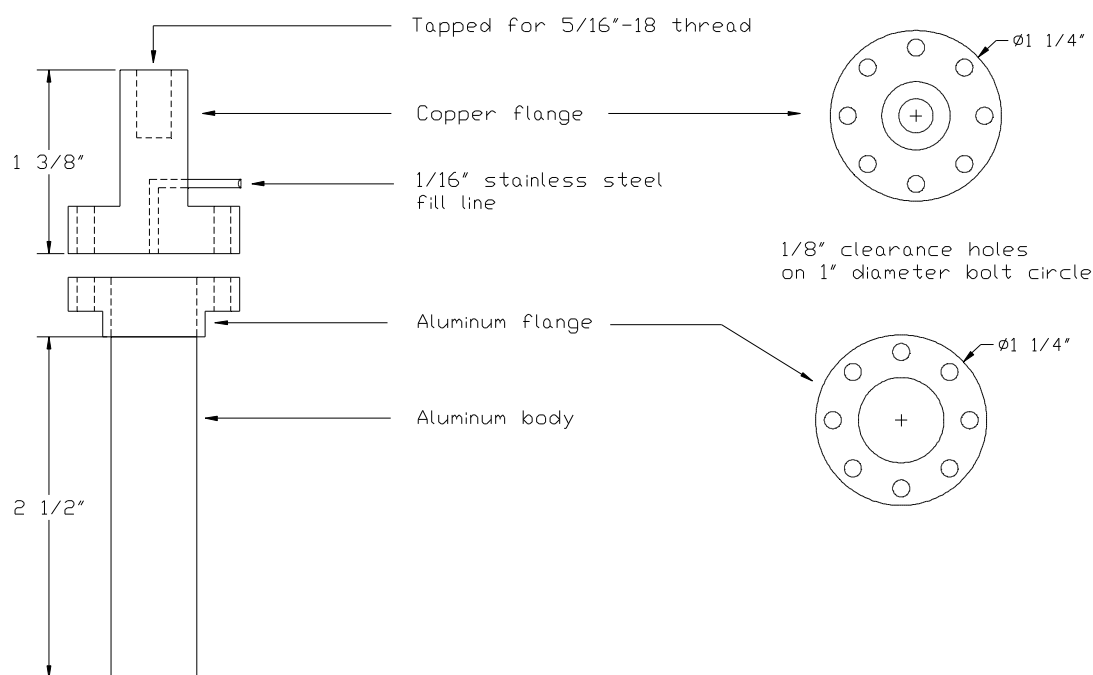


Figure 4.11 Schematic illustration of the sample cell used in the SPINS measurement.

The sample for the measurement consisted of 1 g of silica aerogel (multiple irregularly-shaped monolithic pieces), obtained from Airglass Co., which was placed into a thin-walled aluminum sample can illustrated in figure 4.11. The porosity of these samples, 95%, was determined by molecular adsorption/desorption measurements. The sample can was mounted onto the bottom of the center stick via an aluminum bolt (5/16"-18) which was in thermal contact with the center stick's cold plate. A 1/16" stainless steel fill line ran from the sample cell at the bottom of the center stick up 37" to the top of the stick where it was connected to a manual valve. A cadmium mask (Cd is a strong

neutron absorber) was formed and fixed onto the flanges on the cell to minimize elastic scattering.

Bulk superfluid helium data was not available to characterize the instrumental resolution of SPINS so a low temperature helium/aerogel scan was used to calibrate the instrument to a previous high-resolution measurement of helium in aerogel. The “low temperature” run at 1.48 K (shown in figure 4.12), was used to calibrate the energy scale in the SPINS measurement to a previous high-resolution measurement of helium in 95% porosity aerogel [75]. In particular, the instrumental resolution function of SPINS was determined by convoluting the known lineshape of helium confined to 95% porosity aerogel at 1.4 K [75] with the (unknown) SPINS resolution function and performing a least-squares fit to the data at 1.48 K. The known lineshape of helium confined to 95% aerogel is the damped harmonic oscillator model (DHO). The DHO model, discussed at length in chapter 3, provides an excellent model for the confined liquid [75]. The DHO is parameterized as

$$S(Q,E) = \frac{Z}{\pi(1 - e^{-\beta E})} \frac{4\Gamma E E_0}{(E^2 - (E_0^2 + \Gamma^2))^2 + (2\Gamma E)^2}, \quad (4.20)$$

where $Z(Q,T)$ is the peak strength, $\beta = 1/k_B T$, $\Gamma(Q,T)$ is the half-width at half maximum (HWHM), and $E_0(Q,T)$ is the excitation energy. The known DHO lineshape parameters at 1.4 K are $E_0 = 738 \mu\text{eV}$ and $\Gamma = 25 \mu\text{eV}$ [75]. Z , the oscillator strength, was arbitrarily set equal to 1.0. The oscillator strength is unimportant when determining the

instrumental resolution in this manner since the integrated intensity of the resolution will subsequently be set to unity anyway.

The best fit to the data was obtained using a Lorentzian function with an offset,

$$R(E) = C + \frac{A\Gamma}{\pi} \frac{1}{(E - E_o)^2 + \Gamma^2}, \quad (4.21)$$

where $C = 4.3$, $A = 38.0$, $E_o = 2.4 \mu\text{eV}$, and $\Gamma = 26.6 \mu\text{eV}$. The result of convoluting the resolution function with the DHO is shown in figure 4.12 along with the data. This function was subsequently normalized and used as the instrumental resolution function in the analysis of the data at 1.92 K, 2.01 K, and 2.11 K.

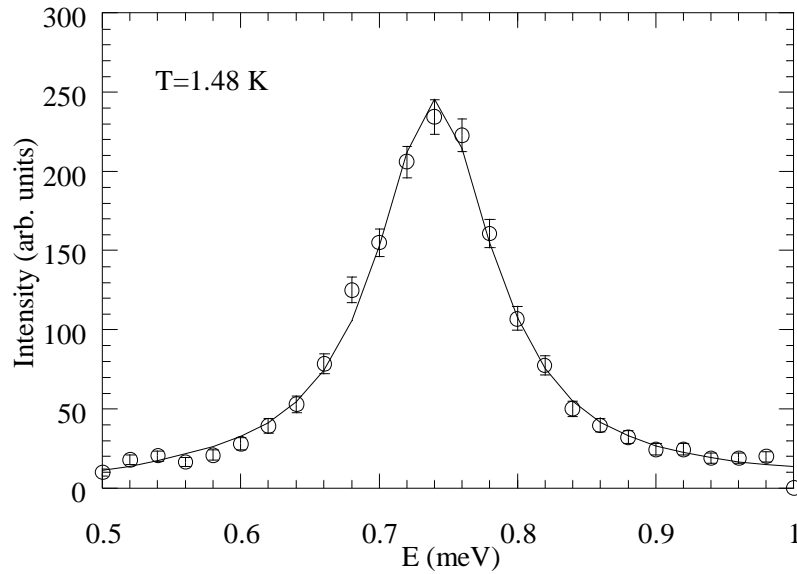


Figure 4.12 Scattering at the roton momentum at 1.48 K. Solid line is a fit of the instrumental resolution function convoluted with the DHO discussed in the text.

Measurements were also carried out on the IRIS spectrometer which has as an elastic energy resolution of about $15 \mu\text{eV}$. However, because it is an inverse geometry instrument, the instrumental resolution gets progressively worse with neutron energy loss. At the roton minimum, for instance, the resolution is about $20 \mu\text{eV}$. In the present configuration the 002 analyzer reflection yields a fixed final energy of 1.8463 meV which, combined with the range of scattering angle, provides adequate coverage of Q-E space to include the roton as shown in figure 4.13.

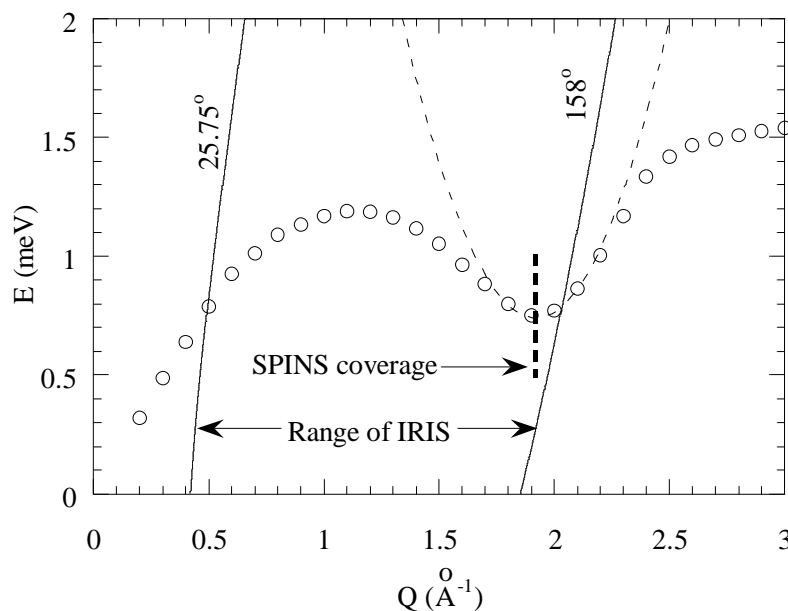


Figure 4.13 Range of the IRIS spectrometer (solid curves) and the SPINS spectrometer (bold dashed line for reference). The bulk helium dispersion curve is shown as the open circles indicating that both measurements covered the roton excitation. The dashed line indicates the Landau parabolic roton dispersion curve.

Measurements on the IRIS spectrometer offer two clear advantages over those on the SPINS spectrometer. First, the energy resolution of IRIS is much better enabling smaller features in the scattering to be resolved which might be difficult to see on SPINS. Second, since IRIS is a TOF instrument with multiple detectors, a large portion of the dispersion curve can be measured at one time. Near the roton minimum, where the dispersion of bulk helium is parabolic, the excitation energies can be fit to the Landau dispersion curve, equation (2.4), so that a more precise value of Δ can be extracted than is possible with a measurement at a single Q on SPINS. Figure 4.13 shows the difference in coverage of each instrument in each measurement clearly.

The aerogel samples used in the IRIS measurement were fabricated at the Penn State Materials Research Laboratory using techniques discussed in chapter 2. The porosity of these samples as determined by molecular adsorption/desorption isotherm measurements was about 90%.

Approximately 27 cc of helium were condensed into an aluminum sample can 3.5 cm in diameter and 6 cm high containing 17 monolithic aerogel rods. Due to limitations in the fabrication process, particularly in the hypercritical drying step where the dimensions of an autoclave limited the size of the sample as well as the number of samples produced per unit time, the maximum size for an aerogel rod was 51 mm long and 6.9 mm in diameter. Thus 17 such rods were placed into the sample can. Measurements were performed at 1.55 K, 1.7 K, 1.9 K, and 2.06 K.

The TOF data from IRIS were reduced using the techniques discussed in section 4.2.3. The conversion from time to energy and the vanadium normalization were both performed using the IDA (Interactive Data Analysis) and GENIE (“a language for spectrum manipulation and display”) software packages available at the ISIS facility. The subsequent data sets were converted from binary to ascii with a GENIE routine called IGB2A and ported back to Penn State for the detailed data reduction and analysis.

The instrumental resolution function was determined using bulk helium data taken at 500 mK [103]. The resolution function was fit using the standard method discussed in section 4.3 and the results (at the roton minimum) are shown in figure 4.9. The data was then rebinned into energy bins 5 μeV wide and momentum bins 0.03 \AA^{-1} wide using a simple one-dimensional rebinning algorithm for each variable. Since rebinning is mathematically equivalent to a convolution with a rectangle function, this has the benefit of smoothing the data for subsequent lineshape analysis.

4.4.3 The Vycor Measurement

The excitations of helium in porous vycor glass were measured using the IN6 direct geometry chopper spectrometer discussed in 4.2.2. The incident neutron wavelength (energy) was 4.12 \AA^{-1} (4.818 meV) which, combined with the angular coverage of the

secondary spectrometer, yielded adequate coverage of the roton excitation as shown in figure 4.14.

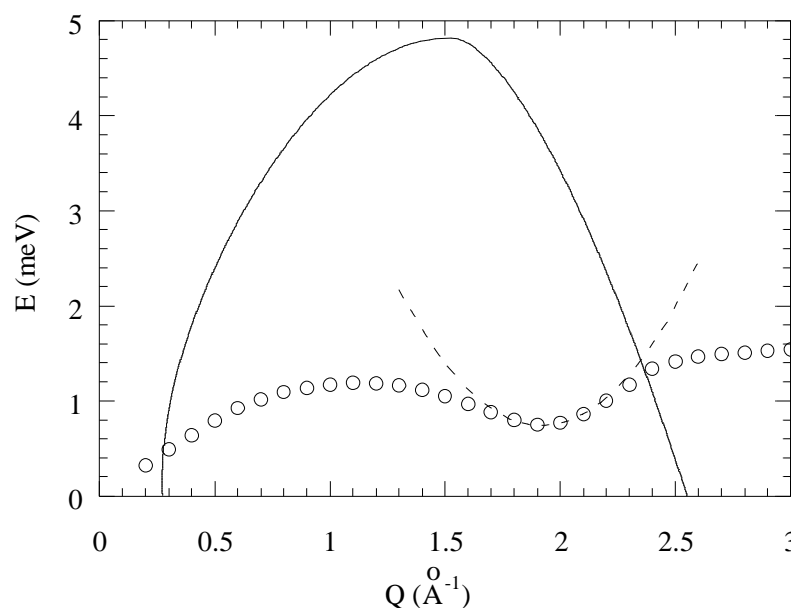


Figure 4.14 Range of IN6 (solid curve) in this configuration. Bulk helium dispersion curve shown as circles and dashed line is the Landau parabolic dispersion curve for rotons.

Eight disks with a nominal diameter of 14.5 mm and an average thickness of 6.35 mm were cut from a single vycor rod. These samples were cleaned using standard methods [62] by boiling in a 30% hydrogen peroxide solution, rinsed in acetone, isopropyl alcohol, and distilled water, and finally dried at an elevated temperature. The clean vycor disks were placed into a cylindrical sample can, shown in figure 4.15, whose dimensions allowed a snug fit. In order to minimize multiple scattering, thin cadmium disks (a strong neutron absorber) with the same diameter as the vycor disks were placed between every two vycor disks. The vycor disks only filled the cell halfway and another cadmium spacer was placed on the top vycor disk. The cryostat was able to be moved vertically to

allow different portions of the cell to be illuminated by the neutron beam. This allowed two measurements with one sample cell: a bulk liquid helium measurement (with the vycor disks no longer in the path of the incoming beam) and the confined helium measurements.

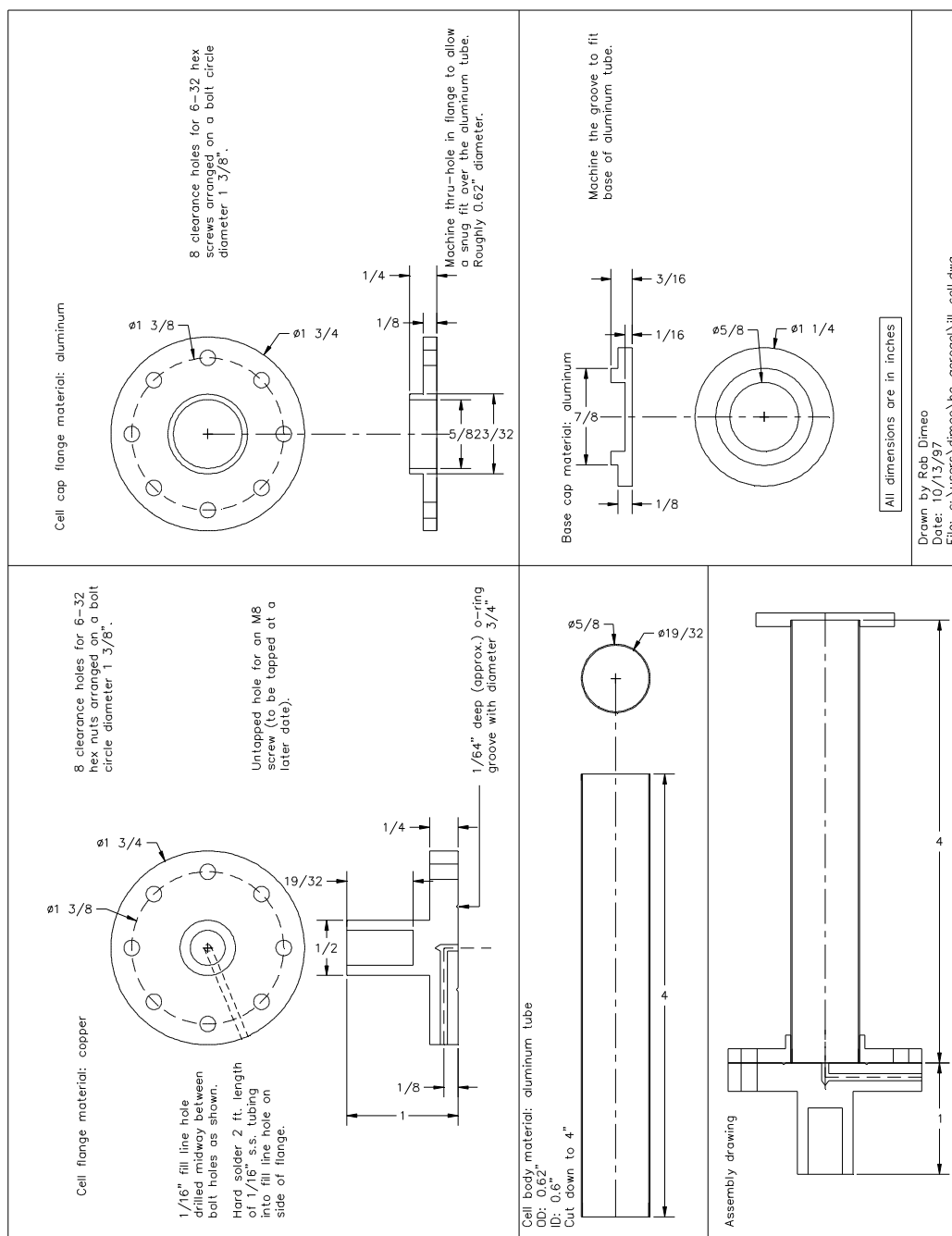


Figure 4.15 Design drawing for sample cell used in the IN6 measurement of helium in vycor and bulk helium.

High purity helium was condensed into the sample cell using procedures identical to those discussed in the aerogel measurements. Due to unforeseen circumstances research grade helium was unavailable at the ILL in its conventional form (i.e. in a standard gas cylinder). Therefore helium gas boiled off in a liquid helium dewar (used to fill the cryostat) was used to charge the gas handling system. Since this helium evaporated off of a helium reservoir it is expected to be high purity although the exact purity is unknown. 2.5 cc of liquid helium were condensed into the cell at 500 mK, thus filling the open pore volume to 95% capacity.

For all measurements the helium was kept at its saturated vapor pressure. Measurements were performed at four temperatures: 500 mK, 1.1 K, 1.6 K, and 1.9 K. At these temperatures the confined liquid is superfluid (macroscopic measurements have shown that the superfluid transition temperature for helium in vycor is 1.95 K) [67]. An additional measurement of bulk helium was done at 500 mK in order to obtain the instrumental resolution function. This measurement was done in the same sample cell but the cryostat was lowered to illuminate the portion of the sample cell containing bulk helium only.

Remnant boron, not removed by leaching of the boron-rich phase provides a strong neutron absorption component in the total scattering cross-section ($\sigma_{\text{abs}}=755$ barns). This strong absorption had a direct impact on this measurement and the best confined helium signals obtained were from the intense roton excitation and the excitations around the

roton minimum. As in the case of bulk helium the scattering is most intense in the momentum transfer range $1.6 < Q(\text{\AA}^{-1}) < 2.2$. Also since the roton is detected in a reflection geometry and the phonon and maxon regions of the dispersion curve are in transmission the roton signal was strongest (neutrons are not as penetrating into materials with large absorption cross-sections). To account for the strong absorption as well as the elastic scattering an empty vycor (no helium) run was performed. This measurement was done at 500 mK and the data was used in the background subtraction in the subsequent measurements of the confined liquid. The empty vycor scattering showed no distinguishing features other than a resolution broadened Bragg peak.

The time-of-flight data was reduced using standard techniques for measurements performed on a direct geometry chopper spectrometer. An example of the raw TOF data is shown in figure 4.16. The raw data, in the form of intensity vs. time, $I(2\theta, t)$, for each of the detectors at a fixed scattering angle, 2θ , was converted to $S(2\theta, E)$ using the equations discussed in section 4.2.2 of this chapter.

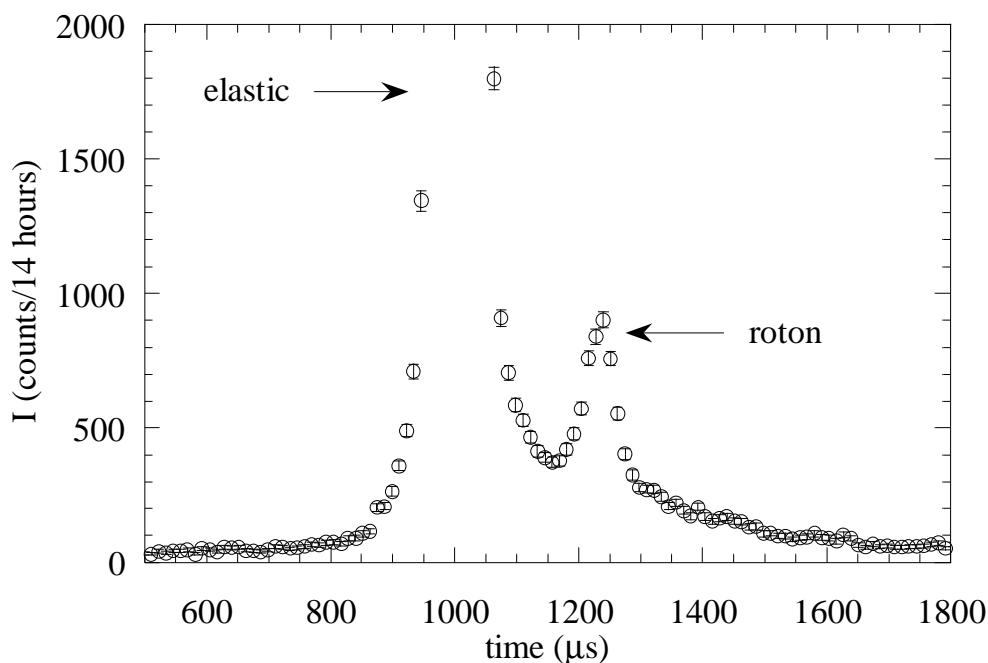


Figure 4.16 Example TOF spectrum from detector group 72 ($2\theta=80.28^\circ$) for helium in vycor. Scattering angle for this detector group is coincident with momentum transfer for the bulk roton. First peak in time is the elastic scattering component and the second peak is the bulk-like roton signal.

The vycor data had to undergo an additional correction due to sample absorption. There is some remnant boron left in the vycor matrix from the fabrication process. Since boron has an extremely large absorption cross-section the effect of this absorption on the scattering data was considered. A transmission measurement was performed at the outset of the measurement which yielded a result of 6%. A numerical integration was performed over the volume of the sample cell to determine the angle dependence of the attenuation due to the boron [104]. This calculation was calibrated to the measurement of the transmission ($2\theta=0^\circ$ scattering angle) of the empty vycor. A further correction was done to allow for the change in scattering length of the helium/vycor system using the

amount of helium present in the sample and the result of the numerical integration. The attenuation length for helium in vycor was calculated to be about 4 mm which means that the scattering center and the geometric center of the sample cell are not coincident.

Since the geometric center of the sample and the scattering center are not coincident there is another technical problem to consider. Given the dimensions of the vycor disks, this means that the neutrons which scatter from the sample and are detected *only* scatter on average from the part of the sample facing the incident beam. Since this is a time-of-flight measurement where we assume that the scattering occurs at the geometric center of the sample cell it is clear that a further correction is necessary to obtain accurate values for neutron time-of-arrival at the detectors and hence accurate final energies. In fact a geometric calculation for a neutron-roton scattering event at the front face of the vycor yields a peak which would be measured about $26 \pm 2 \mu\text{eV}$ too low. This shift must be corrected for in the extraction of the energies.

In inelastic neutron scattering measurements one typically converts the scattering function from $S(2\theta, E)$ to $S(Q, E)$ for the detailed analysis as we did for the aerogel data discussed in the previous chapter. The relationship between 2θ and Q (and E) is nonlinear meaning that a line of constant 2θ in Q - E space is a curved path. Since the neutrons are detected in a TOF spectrometer along lines of constant scattering angle and not constant Q , this conversion from 2θ to Q necessarily involves a rebinning procedure which smooths the data. Since we are interested in some relatively weak scattering

which could get *washed out* in the conversion we elected to analyze the data in constant scattering angle.

4.4.4 The Xerogel Measurement

The measurements of helium in xerogel were carried out on FCS. The xerogel samples used in this study were obtained from PQ Corporation under the product name BRITESORB (ID #FB5300) discussed in chapter 2.

11.51 g of xerogel were placed in a slab sample cell 117 mm high \times 43 mm wide \times 10 mm deep made of copper with aluminum windows 1 mm thick as shown in figure 4.17. The slab geometry was selected in order to minimize the amount of multiple scattering. Previous neutron scattering measurements of helium in aerogel which used large quantities of the substrate resulted in spurious Q-independent signals (multiple scattering) due to elastic scattering events between the collective excitations of the helium and the substrate [75]. We can calculate the neutron mean-free-path in the helium/xerogel system readily by making the assumption that 70% of the system is helium and 30% of the system is SiO₂. The scattering cross-sections for the sample constituents are $\sigma_s(\text{He})=1.34$ b, $\sigma_s(\text{Si})=2.18$ b, and $\sigma_s(\text{O})=4.2$ b where 1 b= 10^{-24} cm². The mass densities of each component are $\rho(\text{SiO}_2)=2.18$ g/cc and $\rho(\text{He})=0.145$ g/cc. The inverse scattering length (where the scattering length is defined as the distance a neutron travels before being scattered once) for SiO₂ is given by

$$\begin{aligned}
\Sigma_s(\text{SiO}_2) &= \frac{\rho_{\text{SiO}_2}}{m_{\text{SiO}_2}} N_A [\sigma_s(\text{Si}) + 2\sigma_s(\text{O})] \\
&= \frac{2.18 \text{ g/cc}}{60 \text{ g/mol}} \times 6.02 \times 10^{23} \text{ mol}^{-1} [2.18 \text{ b} + 2 \times 4.2 \text{ b}] \times 10^{-24} \text{ cm}^2/\text{b}, \quad (4.22) \\
&= 0.23 \text{ cm}^{-1}
\end{aligned}$$

The analogous calculation for helium (4 g/mol) yields $\Sigma_s(\text{He}) = 0.0292 \text{ cm}^{-1}$. The total mean free path of the neutron is given by

$$L_{\text{MFP}} = \frac{1}{\Sigma_{\text{tot}}} = 11.2 \text{ cm}, \quad (4.23)$$

where $\Sigma_{\text{tot}} = 0.3 \Sigma(\text{SiO}_2) + 0.7 \Sigma(\text{He})$ has taken into account the finite amounts of helium and glass in the sample. Finally we may determine the sample thickness such that 10% of the incident neutrons scatter (90% transmission) via

$$T = \exp\left[-\frac{d}{L_{\text{MFP}}}\right], \quad (4.24)$$

where T is the transmission and d is the cell thickness. Using 11.2 cm as the mean free path results in a cell thickness, d , of 1.18 cm. This preventative design measure proved successful since no such multiple scattering was observed in these measurements.

The sample cell was cooled using a standard helium flow “orange” cryostat capable of reaching a base temperature of 1.36 K. For nearly all of the measurements discussed here the temperature was fixed at base temperature. The cryostat with the sample stick in place was bolted into the sample environment on the instrument platform. The signal we wished to measure occurs in a backscattering geometry. In order to minimize multiple scattering the sample cell was rotated to optimize the signal.

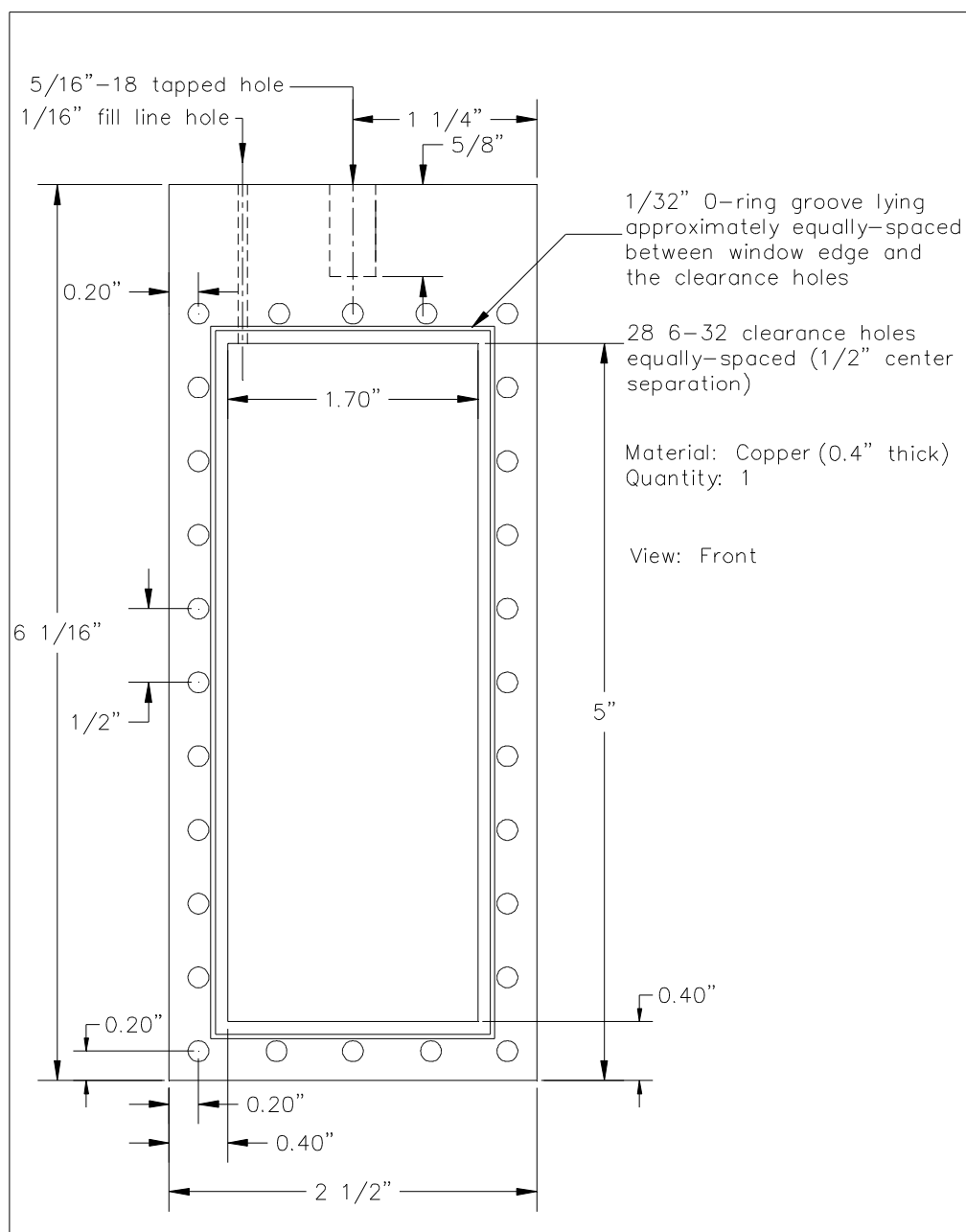


Figure 4.17 Design drawing of sample cell for helium in xerogel measurement.

High purity helium was condensed into the sample cell until the sample was filled to the desired fraction of open pore volume consistent with adsorption isotherm measurements. For example at 72% porosity a fill fraction of 0.95 corresponds to almost 12 cc of liquid. For all measurements the helium was kept at its saturated vapor pressure and measurements were performed at six filling fractions: 0.0 (empty cell), 0.25, 0.4, 0.6, 0.8, and 0.95. In addition, a measurement was performed at 1.7 K at a filling fraction of 0.95. Finally, a measurement of the bulk liquid was performed at 1.36 K in the same cell after the xerogel had been removed. The purpose of the bulk measurement was to calibrate the energies in the measurement and determine the instrumental resolution.

The incident neutron wavelength (energy) for the FCS measurement was 4.8 \AA^{-1} (3.55 meV). This wavelength provided adequate coverage of Q-E space to encompass the region of the roton excitation. Figure 4.18 illustrates the region of Q-E space covered by FCS along with the dispersion curve for the bulk helium excitations [105].

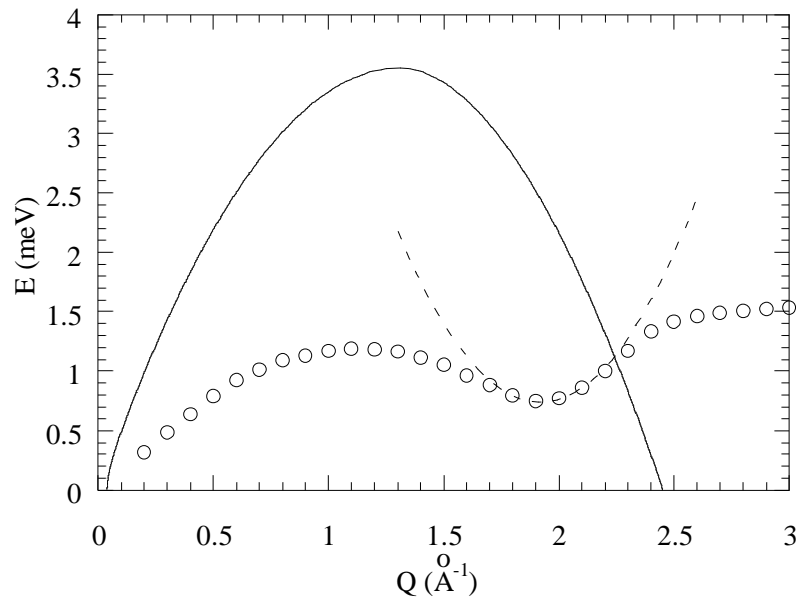


Figure 4.18 Range of FCS (solid curve) in the current configuration. Bulk helium dispersion curve shown as circles and dashed line is the Landau parabolic dispersion curve for rotons.

The time-of-flight data were reduced using the standard techniques already discussed. Due to the presence of *dark counts* (non-zero detector signal when no scattering signal should be present) the raw data was corrected for a finite (but featureless) offset (not observed in the IN6 data). The raw data, in the form of intensity vs. time $I(2\theta, t)$ for each of the detectors at a fixed scattering angle, was converted to $S(2\theta, E)$ in the usual manner for a TOF measurement on a direct geometry instrument. A vanadium incoherent scatterer was used to determine the calibration of each detector and the detector efficiencies were corrected analytically via equation (4.11). In addition, since we are interested in some relatively weak scattering which could get *washed out* in the

conversion from $S(2\theta, E)$ to $S(Q, E)$ we elected to analyze the data in constant scattering angle.

In order to determine the instrumental resolution of the FCS at the roton momentum transfer (1.92 \AA^{-1}), the xerogel was removed from the cell and 57 cc of bulk helium was condensed into it. Since the bulk helium lineshape is known to have a narrow intrinsic width at this temperature ($\approx 15 \text{ } \mu\text{eV}$) then this observed scattering from bulk helium is an excellent approximation to the effective instrumental resolution function. Data was collected at 1.36 K for over 20 hours and an empty cell measurement was performed for the same time period resulting in a high-statistics determination of the instrumental resolution. At the roton momentum, the effective instrumental resolution (the bulk data with empty cell subtracted) was fit well by a gaussian with a FWHM of $167 \text{ } \mu\text{eV}$.

CHAPTER 5

SUPERFLUID HELIUM IN SILICA AEROGEL

Superfluid helium confined to silica aerogel displays very unique behavior. The superfluid transition is suppressed by only 5 mK, however the critical exponent for the superfluid transition (0.813) is quite different from that of the bulk superfluid (0.674). This suggests that the phase transition for the confined liquid is in a different universality class than the bulk. This is remarkable considering that only 6% of the liquid has been replaced by silica solid. In fact, changes in the critical exponent have been seen for aerogels made up of only 0.5% silica solid. Until recently, however, little has been done experimentally to understand the microscopic origins of these differences.

The first inelastic neutron scattering measurements of superfluid helium in silica aerogel revealed that the excitation spectrum was very similar to the bulk excitation spectrum [73,74]. In fact, within the instrumental resolution, no deviations from the bulk behavior were observed. Recent measurements, performed by Sokol *et. al.* [75,76], were done on the IRIS spectrometer with 95% porous aerogel using superior instrumental resolution compared with the first study [73,74] and over a broad temperature range. They found that the roton energy gap remained relatively temperature-independent compared with the bulk liquid at least up to 1.9 K. However, because these measurements were only done at temperatures up to 1.9 K it was unclear whether this weak temperature-dependence persisted up to T_λ .

The experiments described in this chapter serve two main purposes. The first experiment, performed on the TAS spectrometer SPINS (described in chapter 4), is a continuation of the measurement of the temperature dependence of the excitations confined in 95% porosity silica aerogel done by Gibbs [75]. The goal for the SPINS measurement was to determine if the weak temperature-dependence of the roton energy gap persists to temperatures higher than 1.9 K or if the roton energy displays a substantially stronger temperature dependence. Further measurements were done on the IRIS spectrometer using different aerogel samples, this time with porosities of about 90%. With the experience gained from the first aerogel measurement on IRIS done by Gibbs *et. al.* the excitations were probed over an even broader temperature range than that first measurement including temperatures less than and greater than 1.9 K. These measurements reveal that, microscopically, superfluid helium in aerogel displays some very interesting and unique characteristics. Finally, as will be shown, this unusual microscopic behavior is entirely consistent with the macroscopic dynamics of the liquid.

5.1 Data Analysis

The data from the SPINS measurement of helium in 95% porosity aerogel and the IRIS measurement of helium in 90% porosity aerogel were analyzed in almost the same manner. In each case the data, in the form $S(Q,E)$, were fit to the DHO model convoluted with the instrumental resolution function.

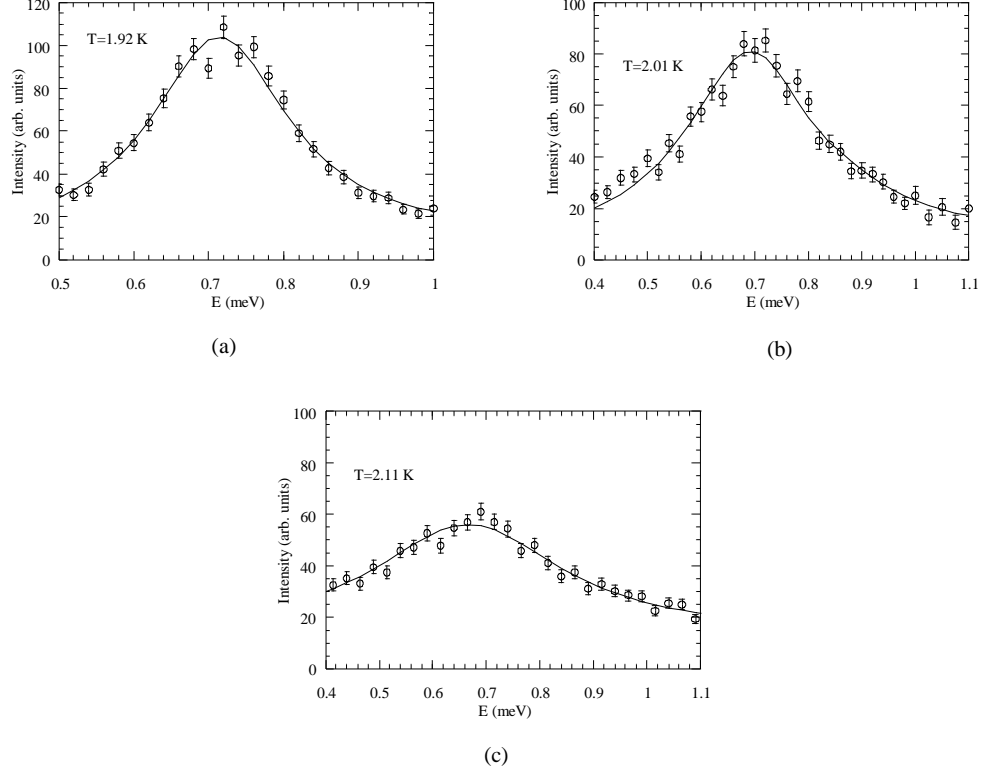


Figure 5.1 SPINS scattering data at $Q = 1.92 \text{ \AA}^{-1}$ at temperatures of (a) 1.92 K, (b) 2.01 K, and (c) 2.11 K.

The data at the different temperatures were fitted in a least-squares sense to the convolution of the DHO model (3.28) with the instrumental resolution function whose determination was discussed in section 4.3. The data at each temperature for the SPINS measurement are presented in figure 5.1 along with the fits (shown as solid lines). Since the TAS data yields pointwise information in Q - E space and scans were performed in energy only we can obtain no further information on the roton dispersion such as the curvature (related to the roton mass). In this series of measurements we have explicitly

assumed that the roton momentum is 1.92 \AA^{-1} . The roton energy at each temperature is presented in table 5.1 along with the previously measured values of Gibbs [75].

Table 5.1 Summary of roton parameters in 95% porosity aerogel. The asterisk (*) denotes values determined by Gibbs *et. al.* [75].

T (K)	D (meV)	$Q_R (\text{\AA}^{-1})$	$m_R (m_{\text{He}})$
1.3 [*]	742 ± 1	1.926 ± 0.002	0.167 ± 0.012
1.4 [*]	738 ± 2	1.923 ± 0.003	0.159 ± 0.014
1.7 [*]	731 ± 1	1.927 ± 0.002	0.155 ± 0.011
1.9 [*]	726 ± 2	1.929 ± 0.002	0.148 ± 0.010
1.92	713 ± 2	-	-
2.01	703 ± 3	-	-
2.11	666 ± 6	-	-

In the IRIS measurement, the data at each Q between 1.83 \AA^{-1} and 1.98 \AA^{-1} were least squares fit to the same damped harmonic oscillator (DHO) model used in the SPINS analysis (equation (4.17)) convoluted with the instrumental resolution at that momentum transfer. An additional contribution was found in the scattering at all momentum transfers due to roton-aerogel scattering events. The result of the elastic scattering of excitations is a Q -independent ridge (this feature will be referred to as multiple scattering from now on) located somewhat higher in energy than the roton energy ($\sim 0.79 \text{ meV}$) and this has been observed before in scattering from confined helium [73,75]. Resolution-

broadened data for the confined liquid at 1.7 K which shows this Q-independent ridge is shown in figure 5.2. This portion of the scattering is easily observable at Q's away from the roton momentum and can be fit to a simple Lorentzian lineshape. It is necessary to include this in the fit at the roton because the integrated intensity of the multiple-scattering is about 1/10 of the integrated intensity of the roton, thus presenting a non-negligible contribution to the roton linewidth. The center, width and amplitude of the multiple-scattering were then fixed to their values at $Q = 1.6 \text{ \AA}^{-1}$ when fitting the peak near the roton. The multiple-scattering was clearly present at all temperatures up to and including 1.9 K where it was used in the fitting procedure. However the excitation gets too broad above 1.9 K (due to the proliferation of thermally-activated excitations) so that the multiple-scattering could not be separated from the collective excitation at any Q value. Thus the multiple-scattering was not included in the fit for the higher temperatures. Typical fits at 1.55 K of the DHO plus the multiple scattering function convoluted with the instrumental resolution are shown in figure 5.3 as the solid lines.

At each temperature the excitation energies, $E_o(Q,T)$, were extracted from the fits of the DHO (4.17) and the dispersion of these energies was found to be in excellent agreement with the Landau dispersion relationship,

$$E(Q,T) = \Delta(T) + \frac{\hbar^2}{2\mu_r(T)} (Q - Q_r(T))^2, \quad (5.1)$$

as can be seen in figure 5.4. By fitting the data to the Landau dispersion in this way we can reliably extract the roton parameters, Δ , μ_R , and Q_R . These roton parameters at each temperature are listed in table 5.2.

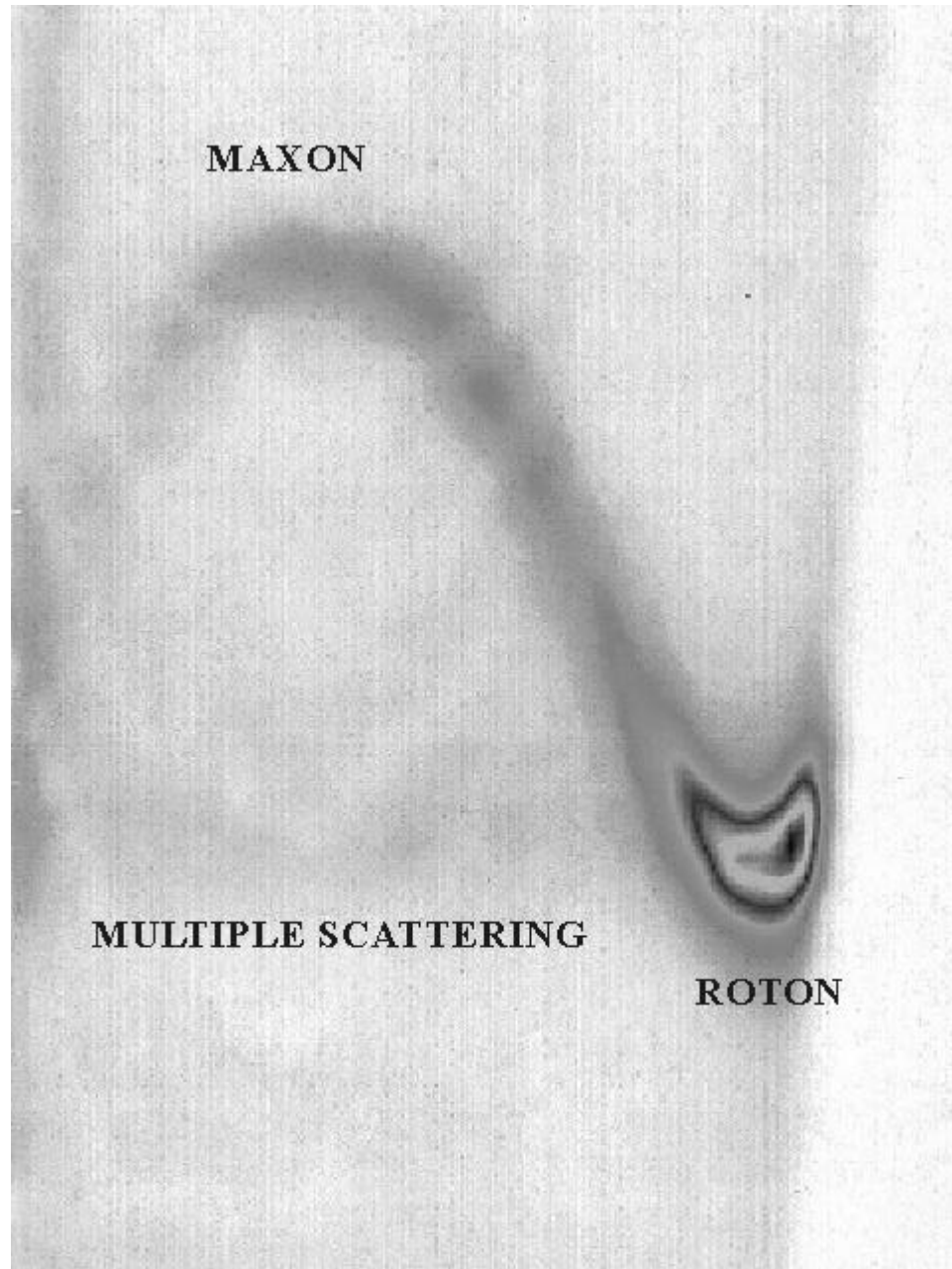


Figure 5.2 Resolution-broadened scattering data for helium in 90% porous aerogel. The vertical axis is in increasing energy and the horizontal axis is momentum transfer.

Table 5.2 The temperature dependence of the roton parameters in 90% porous aerogel.

T (K)	D (meV)	Q_R (\AA^{-1})	m_R (m_{He})
1.55	731.0 ± 0.3	1.9292 ± 0.0007	0.144 ± 0.005
1.7	728.3 ± 0.2	1.9271 ± 0.0005	0.133 ± 0.002
1.9	717.5 ± 0.4	1.930 ± 0.001	0.138 ± 0.005
1.98	683.5 ± 1.2	1.934 ± 0.004	0.12 ± 0.01
2.01	662 ± 2	1.934 ± 0.005	0.09 ± 0.01

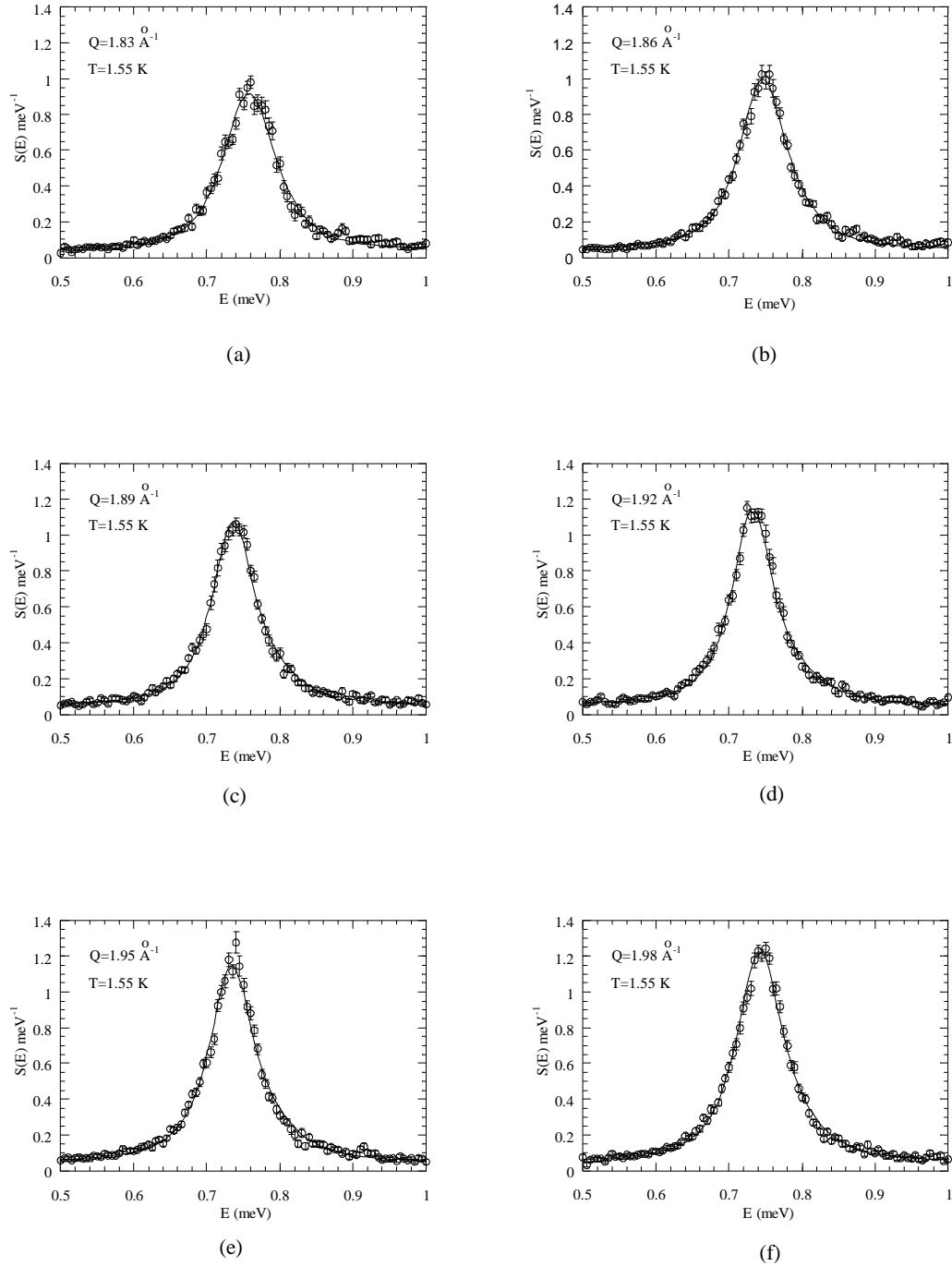


Figure 5.3 Scattering from helium in aerogel at 1.55 K on the IRIS spectrometer. The solid line is a fit of the DHO model (equation (4.17)) convoluted with the instrumental resolution function.

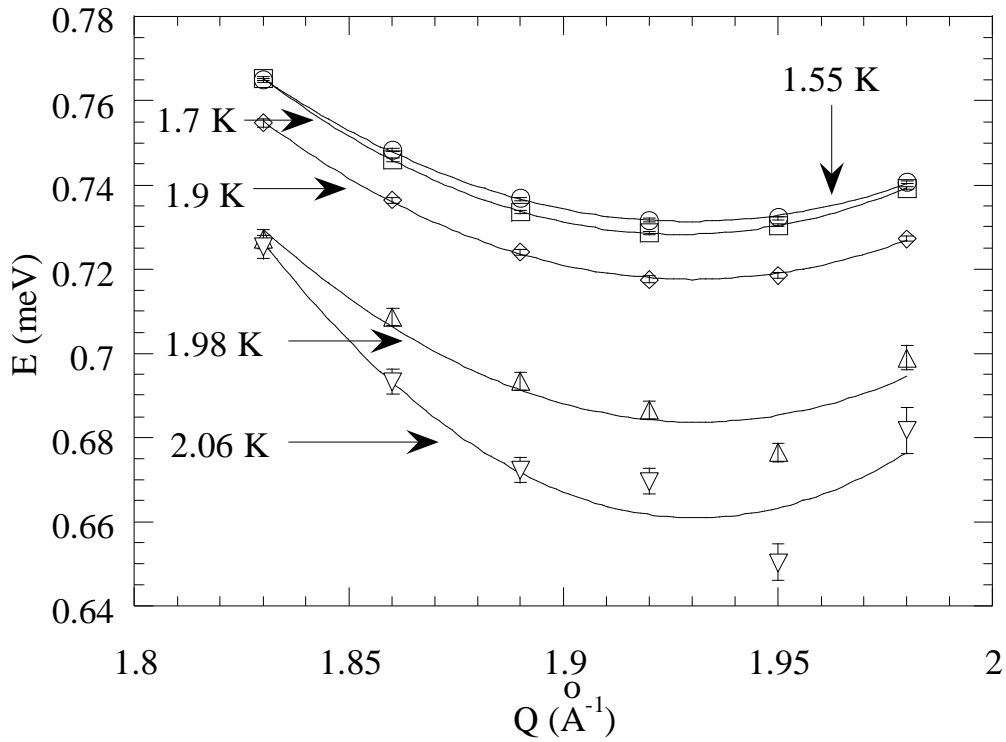


Figure 5.4 Dispersion of the collective excitations near the roton minimum at each temperature. The solid lines are the fits of the Landau parabolic dispersion relation to the extracted peak centers.

5.2 Results

The roton energy gap, Δ , for helium confined to silica aerogel exhibits a very unusual temperature dependence as shown in figures 5.5 (a) and (b). In both cases (90% and 95% porous aerogel) the roton energy can be divided into two regions. Below about 1.9 K the roton energy seems to be less temperature dependent than the bulk superfluid while

above about 1.9 K it appears to be more strongly temperature dependent than the bulk. The actual difference between the bulk and the confined liquid is exemplified in figure 5.6 (a) where we present the scattering from helium in 90% aerogel (IRIS) at 1.9 K at $Q = 1.92 \text{ \AA}^{-1}$. The location of the bulk peak is illustrated by the arrow and the peak center is shown by the solid vertical line. Clearly the peak positions are different. We plot the SPINS data at 1.92 K and $Q = 1.92 \text{ \AA}^{-1}$ in a similar manner in figure 5.6 (b). Due to the fluctuations near the top of the peak it is not as convincing as in 5.6 (a) but the difference is present.

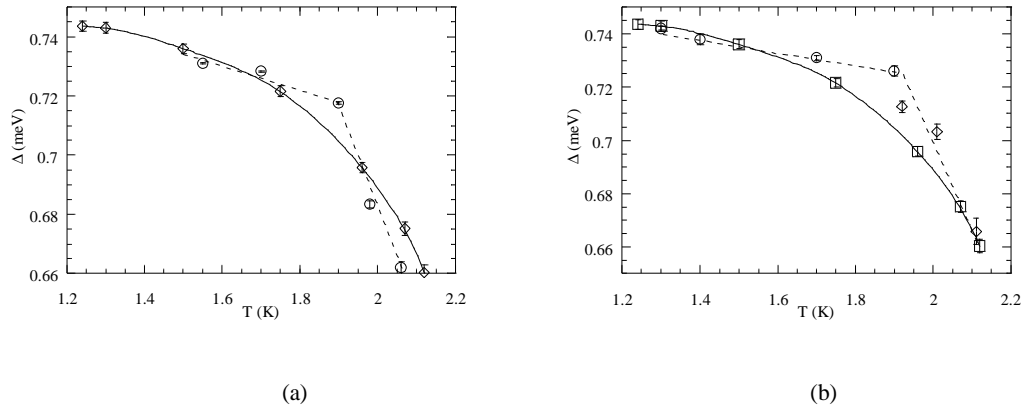


Figure 5.5 Temperature dependence of the roton energy in (a) 90% porous aerogel and (b) 95% porous aerogel. Bulk data shown by squares [48]. In (a) the confined data shown with the circles and in (b) the confined data are shown with circles [75] and diamonds (SPINS data).

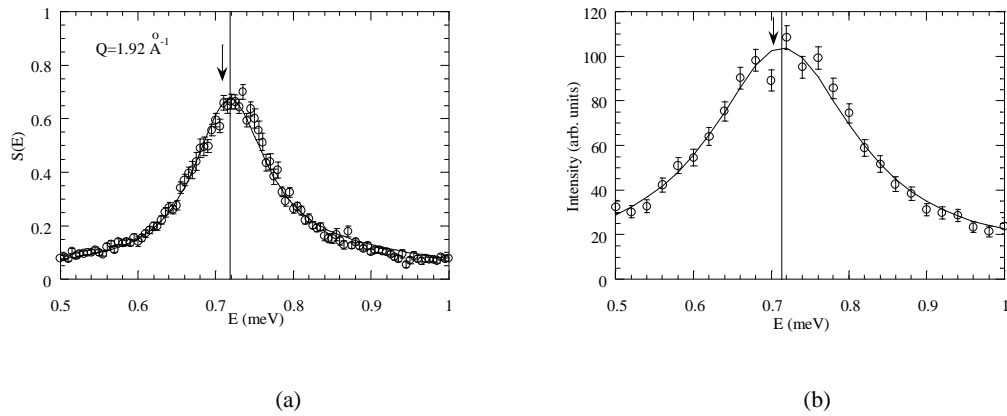


Figure 5.6 Scattering data indicating the difference in peak position at (a) 1.9 K (IRIS data) and (b) 1.92 K (SPINS data) with respect to the bulk peak position (arrow). The peak position for this data is shown by the solid vertical line.

The roton linewidth also exhibits similar crossover behavior as the roton energy for confinement in both porosities of aerogel as seen in figures 5.7 (a) and (b). Below about 1.9 K the temperature dependence is gradual while above 1.9 K the temperature dependence is quite strong compared to the bulk superfluid. The bulk widths, also shown on the plot, have been fit to a theoretical expression based on roton-roton interactions due to Bedell *et. al.* [46] and the agreement between the bulk linewidths and the theory is excellent. However no suitable parameters could be found to fit the theoretical linewidth to the experimental data for helium in aerogel. It should be noted however that for the SPINS data, where multiple-scattering was not used in the fitting procedure, the actual linewidths may be narrower than the points shown in figure 5.7 (b). Naturally multiple-scattering will tend to increase the overall width of the line. Unfortunately since no measurements were taken on the TAS at momentum transfers away from the roton where

we could characterize the multiple-scattering we were unable to correct this data set for this broadening mechanism.

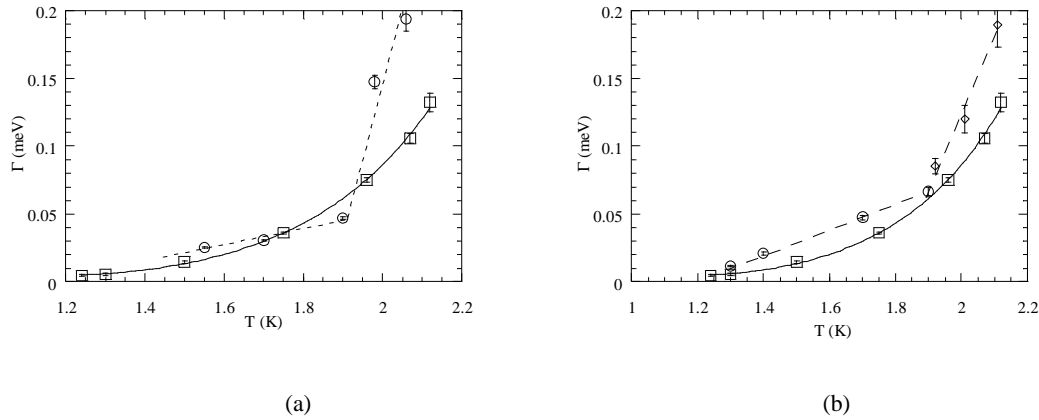


Figure 5.7 Roton linewidth (HWHM) in (a) 90% porosity aerogel and (b) 95% porosity aerogel. In (a) and (b) the squares are the bulk linewidths [48]. In (b) the circles are the data of Gibbs et. al. [75] and the diamonds are the SPINS data.

The reason for the difference in temperature dependence we have observed in the roton energy and linewidth remains an open question. Theories of the temperature dependence of the roton excitations depend in large part to roton-roton interactions [42-44,46]. A result predicted by these theories is a softening of the roton mode with increasing temperature as is observed in the bulk liquid. This is in contrast to our observations for the superfluid confined to aerogel (see figures 5.5 (a) and (b)). Although our roton data is admittedly sparse over the observed crossover region, nevertheless the temperature dependence is clearly different from the bulk liquid. The crossover behavior is observed in two different porosity aerogels.

We can attempt to understand this anomalous temperature dependence using the essential ideas of current theories of the temperature dependence of the roton in the bulk liquid as a starting point. These theories state that the temperature dependence of the roton energy is due to roton-roton scattering and can be characterized by a single length scale, namely the roton mean-free-path. In the bulk liquid where rotons are thermally-activated, when the temperature increases the number of rotons increases and, hence, the roton mean-free-path decreases. The increasing number of collisions between rotons and the corresponding decrease in the roton lifetime exhibits itself as a broadening of the roton seen in neutron scattering measurements. Further, because the roton energy depends to first order on the number of rotons present and the roton-roton interaction is attractive, the roton energy softens as the temperature increases [42]. The main point is that there is a single temperature-dependent length scale which essentially describes the system. This single length scale is the roton mean-free-path.

We can calculate the roton mean-free path in terms of the roton-roton scattering cross-section, σ_{RR} ,

$$\ell_{RR} = \frac{1}{\sqrt{2}n_R\sigma_{RR}}, \quad (5.2)$$

where the number of thermally activated rotons present at temperature T is given by the expression,

$$n_R(T) = \frac{2Q_R^2}{\hbar} \left(\frac{\mu k_B T}{8\pi^3} \right)^{1/2} e^{-\frac{\Delta}{k_B T}}. \quad (5.3)$$

Therefore the mean-free-path of the rotons has the temperature dependence

$\ell_{\text{RR}}(T) \propto T^{-1/2} e^{\frac{\Delta}{k_B T}}$. Although this temperature dependent length scale is dominant in the bulk liquid, confinement can introduce an additional temperature-independent length scale.

Confinement of the helium in aerogel imposes a new temperature-independent length scale, ℓ_m , determined by scattering of the excitations from the fixed confining medium. The magnitude of this length scale depends on the size of the confining media and on the strength of the interaction between the roton and the aerogel substrate. A schematic illustration of these two length scales is presented in figure 5.8. At low temperatures the roton mean-free-path is much larger than ℓ_m and the roton energy is determined by the roton-media scattering. In this temperature regime, therefore, the roton energy is relatively independent of temperature. At higher temperatures, above the point of intersection of the two curves, the roton mean-free-path is smaller than ℓ_m . When the mean-free-path is smaller than ℓ_m then roton-roton interactions determine the temperature-dependence of the roton properties.

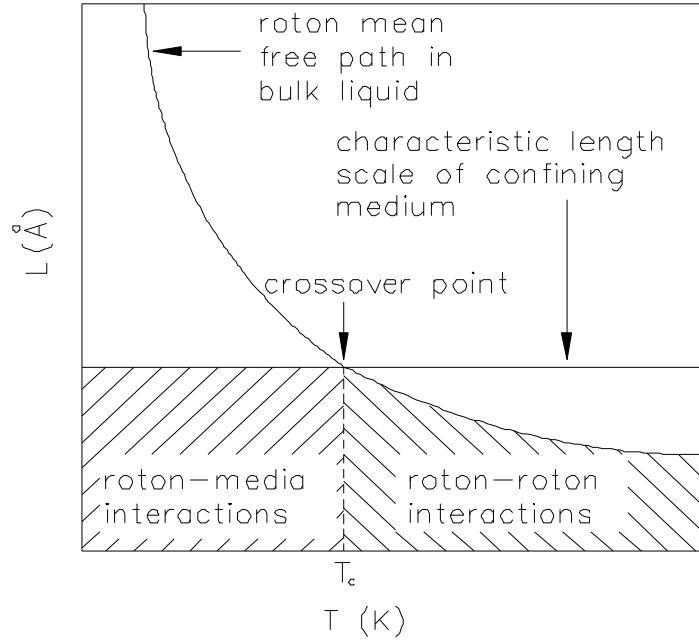


Figure 5.8 Schematic illustration of the competing length scales for helium in aerogel. Intersection of the two curves occurs at the crossover temperature. Above the crossover temperature, roton-roton interactions dominate while below the crossover temperature roton-media interactions dominate.

As we discussed in chapter 2, the temperature dependence of the excitations in the bulk superfluid is described well by the BPZ theory. However, the temperature dependence of the roton energy for the confined liquid is not consistent with the BPZ theory nor any of the roton theories in which a single length scale determines the temperature dependence. The interacting roton theories discussed in chapter 2 predict that the temperature dependence of the roton energy behaves as (equation (2.11)),

$$\Delta(T) = \Delta_o - P_\Delta (1 + R\sqrt{T})\sqrt{T} \exp\left(-\frac{\Delta(T)}{T}\right). \quad (5.4)$$

Equation (5.4) merely states that the temperature dependent roton energy decreases (to first order) linearly with the number of thermally-activated rotons present (equation (2.9)). This suggests that plotting the temperature dependent roton energies as $\ln((\Delta_0 - \Delta(T))/T^{1/2})$ vs. Δ/T will yield a straight line. In fact the bulk data behaves in just this manner as shown in figure 5.9. However the roton energy for helium in aerogel displays a significant departure from this behavior, also seen in figure 5.9. The difference is most apparent at the crossover temperature, 1.9 K. The fact that there is such a large deviation illustrates the inadequacy in treating the temperature dependence in terms of a single length scale and reinforces the requirement for an additional scattering mechanism present in the confined geometry.

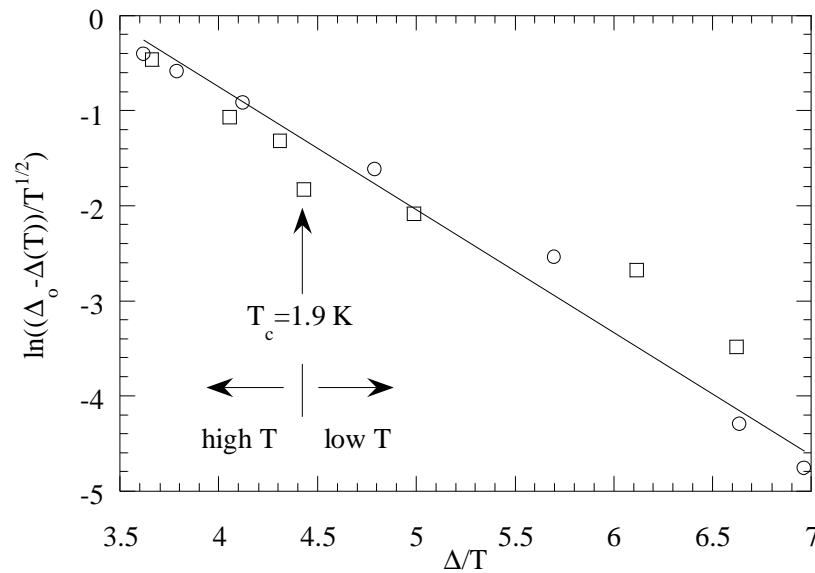


Figure 5.9 Plot of the temperature dependent roton energy for the bulk superfluid (circles) [48] and confined to 95% porosity aerogel (squares).

The point of intersection of the two curves can be determined from the experimental data and hence the length scale, ℓ_m , can be determined. If we assume that this *crossover temperature*, T_c , is about 1.9 K then we can use the expression for the roton mean free path (with $\sigma_{RR} \sim 10 \text{ \AA}^2$ [106]) and the number density of rotons at 1.9 K (9×10^{-4} rotons/ \AA^3) then we obtain the estimate $\ell_m \approx 108 \text{ \AA}$. The aerogel pore diameters have a broad distribution (from 100-1000 \AA) with an average pore size on the order of about 450 \AA . The silica strands, about 20-50 \AA in diameter, provide fixed scattering centers for the rotons. However, the mean free path of a roton moving in a field of fixed scattering centers of silica strands (assumed to be 20 \AA in diameter and occupy 95% of the total aerogel volume) turns out to be about 4500 \AA . Clearly this mean free path is far too large to explain the value of ℓ_m obtained from these measurements. This implies that the effect of rotons interacting with the silica strands is negligible compared to the roton-roton interactions. Thus there must be an additional mechanism causing the decrease in the roton mean-free-path.

One possible explanation for our observations of a decreased mean-free-path of the roton is the presence of trapped vorticity. Trapped vortex lines which are pinned in the pores between the silica strands of the aerogel or even enclosing the strands completely could provide an additional scattering mechanism for the rotons (see figure 5.10). Experimental observations have been made of trapped vortex lines in superfluid helium confined between plates of narrow separation even in the absence of superflow [107]. The areal vortex line density for trapped vortex lines in confined geometry was found to

behave as $\sigma \sim 2 \frac{\ln(D/a_o)}{D^2}$ where D is the length scale of the confining medium and a_o is the typical vortex core size. The core size of a vortex has been estimated at about 1 Å [108] and we use $D \sim 450$ Å for the average pore size in aerogel. The roton-vortex scattering length, b_{RV} , has been investigated in numerical simulations and is estimated to be about 150 Å [109]. Combining this scattering length with the areal line density in aerogel ($\sigma \sim 6 \times 10^{-5} / \text{Å}^2$) we obtain a roton mean free path, $\ell = \frac{1}{\sigma b_{RV}}$, due to roton-vortex line scattering of about 110 Å. This is in agreement with the mean free path due to roton-roton scattering at 1.9 K in the bulk liquid. Thus the idea that the rotons are interacting with trapped vorticity is consistent with the length scales present in the system.

The roton linewidths also seem to suggest a crossover behavior in temperature as shown in figures 5.7 (a) and (b). In particular the width appears relatively temperature-independent below 1.9 K and strongly temperature-dependent above 1.9 K. As mentioned previously, however, the SPINS data has not been corrected for multiple scattering. This contribution to the linewidth should be kept in mind when considering the data shown figure 5.7 (b) at temperatures of 1.92 K and above. The data from IRIS have been corrected for multiple scattering so that the linewidths shown in figure 5.7 (a) are representative of the inverse lifetime of the excitations ($\Delta E \Delta t \geq \hbar/4\pi$ where ΔE represents the linewidth, 2Γ).

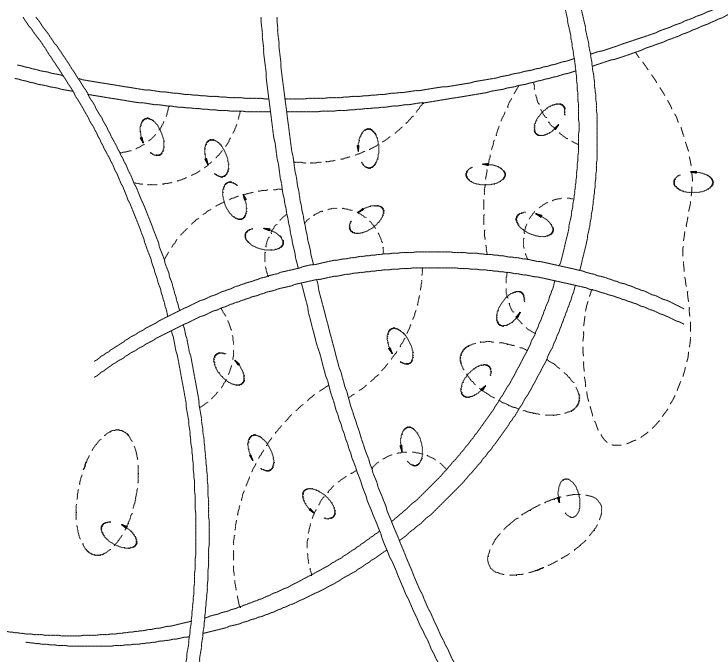


Figure 5.10 Conceptual drawing of the vortex lines (dashed lines) decorating the interior of the aerogel. Most of the vortex lines terminate on the strands of the aerogel (solid lines) while some close in on themselves (vortex rings).

In order to make this argument more convincing it would be ideal to observe the trapped vorticity directly with neutrons. Unfortunately the presence of vorticity in confined helium (or even bulk helium) has not been detected directly with neutron scattering measurements to the best of our knowledge. While direct observation of the vortex lines in superfluid helium has not been made via neutron scattering, theoretical predictions indicate that vorticity should be observable with small angle neutron scattering [110]. The main difficulty with the confined helium measurements is that the substrate provides a significant small angle scattering signal which would likely diminish the scattering signal due to the vorticity.

The arguments we have presented are based on the length scale of the confining medium. Further measurements with porous materials having different pore sizes, preferably with a narrow distribution of sizes, could also illuminate the role of trapped vorticity. To date we have performed additional measurements on helium confined to porous vycor glass and silica xerogel (described in the following chapters). While other novel features were observed in the excitation spectrum, including the observation of additional excitations, no shifts in the roton energy were observed (within the resolution of the spectrometers used in the measurements). However, in materials with small pore sizes like vycor and xerogel ($D \sim 70\text{-}100 \text{ \AA}$), the roton-vortex line scattering length can exceed the pore size which is not sensible. Furthermore the original estimate of the areal vortex line density was for confining length scales much larger than the typical pore size for vycor. Therefore these arguments might fall apart for length scales this small.

5.3 Connection with Macroscopic Measurements

The temperature dependence of the collective excitations can be used with the bulk helium Landau excitation model to illustrate that the excitations are directly related to the macroscopic response of the confined liquid [111]. We can illustrate this correspondence using our data for the excitation spectrum and the results of detailed studies of the heat capacity and the normal fluid fraction for helium confined to silica aerogel [67,112].

We present the agreement between the microscopic and macroscopic measurements [67,113] with the bulk liquid in figure 5.11. In the figure we plot the functions $F_1 = \ln((\rho_n/\rho)T^{1/2})$ and $F_2 = \ln(CT^{3/2})$ vs. Δ/T where the temperature dependence of Δ as determined by neutron scattering is included [48]. In the temperature range of 1 K up to temperatures near T_λ , the bulk response is dominated by rotons so that equations (2.8) and (2.10) describe the heat capacity and normal fluid fraction well. Therefore the (theoretical) functions, F_1 and F_2 defined above, have slopes of -1 when plotted against Δ/T . In fact both macroscopic quantities for the bulk superfluid fall on a straight line of slope -1 clearly showing the connection. The connection between the microscopic and macroscopic quantities for the confined liquid is also seen quite easily. The data for helium confined to aerogel with 94% porosity [67,112] have also been plotted in figure 5.11 where we have used the temperature dependence of the roton energy found in these recent high resolution measurements. As seen in the figure the agreement between the microscopic excitation, the roton, and the macroscopic quantities is excellent for the confined liquid within the Landau excitation model.

As mentioned in the introduction to this chapter, the behavior of superfluid helium confined to aerogel is quite different from the bulk superfluid, especially near the phase transition. The fact that the universality class of the confined liquid is so different from the bulk transition is also seen, perhaps on a more fundamental level, in the effects on the collective excitations. In both cases studied here a relatively temperature-independent roton energy was observed at temperatures below 1.9 K whereas it was strongly

temperature dependent above 1.9 K. This stronger temperature dependence is completely consistent with the fact that the transition is in a different universality class (i.e. it agrees with the superfluid fraction data within the Landau excitation model), as seen in figure 5.11.

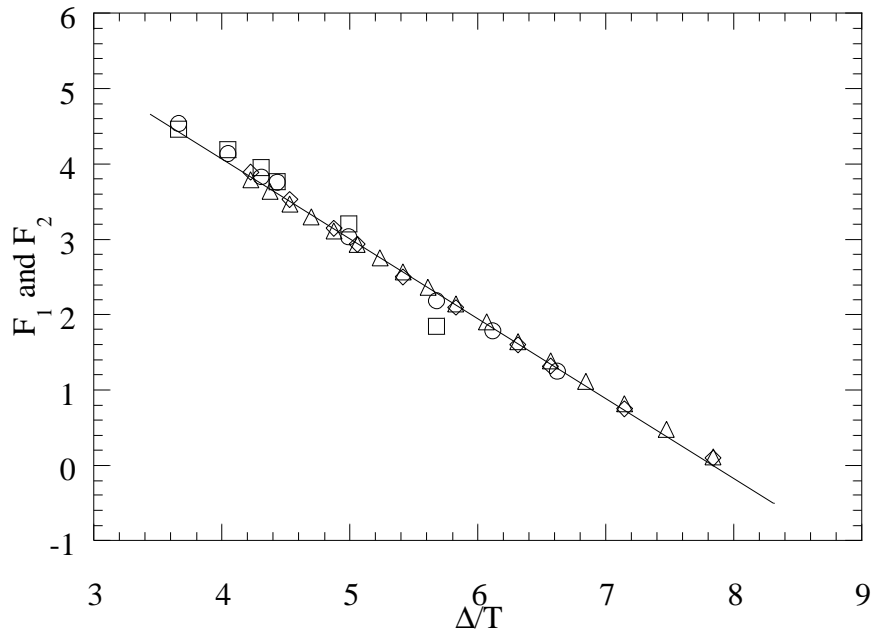


Figure 5.11 The normal fluid fraction and heat capacity for the bulk liquid (triangles and diamonds) [48,67,113] and confined liquid (squares and circles) [67,112] plotted in a manner to illustrate the validity of the Landau excitation model. The functions plotted in terms of the data are $F_1 = \ln((\rho_n/\rho)T^{1/2})$ and $F_2 = \ln(CT^{3/2})$ vs. Δ/T .

5.4 Recent Measurement of Helium in Aerogel

We conclude this chapter with a comment on a recent measurement of the excitations of helium in deuterated silica aerogel (94% porosity) done by a group at the ILL [114] and compare their results with ours. The results they obtained for the roton were somewhat different from ours so it is worthwhile mentioning the principle differences in our measurements and offer some possible origins of the different results. The ILL measurement was performed on the IN12 triple-axis spectrometer (operating in constant Q mode) with an instrumental resolution of $120 \mu\text{eV}$ at the roton momentum. They performed energy scans in the temperature range $0.5 \text{ K} < T < 2.25 \text{ K}$ at four momentum transfers including the roton, 1.92 \AA^{-1} . Since our research concentrated on the roton exclusively we will only consider their results for the roton. First we summarize their results for the roton.

Since the results were performed on a TAS, the constant-Q cut through Q-E space eliminates the possibility of extracting the roton mass, μ_R , or the roton momentum, Q_R , which can be obtained with TOF spectrometers. The two quantities they extract are the roton energy and the linewidth. Their results were threefold. First they find that the low-temperature (500 mK) roton energy is systematically $8 \pm 2 \mu\text{eV}$ lower than the bulk roton energy. Next they claim that the low-temperature linewidth is $6 \pm 1 \mu\text{eV}$ [114]. Finally they observed no crossover behavior in the roton energy.

The origin of these differences could be as simple as the difference in the aerogel samples themselves. In the ILL measurement the sample of silica aerogel was grown in-situ in their sample using deuterated materials in an effort to reduce multiple scattering of excitations. In fact they made the claim that the multiple scattering component was an order of magnitude smaller than that observed in our IRIS measurements. As mentioned in section II-B of chapter 5, at the roton momentum we estimated that the multiple scattering was about 10% of the integrated intensity of the roton signal which means that their observed multiple scattering was about 1% of the roton. The presence of the multiple scattering, if not characterized well, could lead to the extraction of erroneous excitation parameters. For instance, an additional scattering component can broaden out an intrinsic lineshape and/or shift the excitation energy. However, as discussed in this chapter, the fitting procedure used in our data analysis took the presence of the multiple scattering into account. Thus it seems highly unlikely that the deuteration of the aerogel caused the differences in the observed behavior.

The systematic shift in roton energy at 500 mK compared with the bulk was based on a bulk helium measurement performed on the same instrument. The ILL group performed a bulk helium measurement using the same experimental configuration in order to obtain the instrumental resolution function and compare their excitation energies directly to the bulk results. For our IRIS measurement we did not perform the bulk measurement but rather used the results from a previous measurement done on the same spectrometer at

500 mK to obtain the instrumental resolution. This low-temperature bulk data was calibrated to a previous high-accuracy measurement of bulk helium [48] and this provided our energy scale. Our lowest temperature measurement of the roton energy in 90% porosity aerogel was performed at 1.55 K which showed a similar shift downwards in energy. However the measurement of Gibbs *et. al.* [75]. on the 95% porosity aerogel did not show such a downwards shift. At their lowest temperature, 1.48 K, they extracted a roton energy of $742 \pm 1 \mu\text{eV}$ which is comparable to the bulk roton energy. Since the porosity of the ILL sample was not characterized (it was assumed to have a particular porosity based on samples created using the same procedure) it may be that their sample was of lower porosity.

The ILL group reports that there is a broadening of the roton linewidth which is at odds with a recent very high resolution measurement of rotons in 95% aerogel [115]. The ILL group claims a $6 \pm 1 \mu\text{eV}$ linewidth at 500 mK. This is in distinct contrast to a recent very high resolution (resolution function has a $\text{FWHM} = 0.65 \mu\text{eV}$) measurement performed on the IN10 backscattering spectrometer at the ILL [115]. At 800 mK Anderson *et. al.* observed no broadening of the roton in aerogel beyond instrumental broadening. This means that for 95% porosity aerogel, the roton linewidth is less than $1 \mu\text{eV}$. It is highly unlikely that a measurement on IN12 with an instrumental resolution of $120 \mu\text{eV}$ can resolve a broadening as small as $6 \mu\text{eV}$. Such a tiny broadening constitutes a 0.13% change over the instrumental resolution. Given that their peak was defined by roughly 12 points and the IN10 data was defined by almost an order of magnitude more

points we are fairly safe in refuting this claim of the ILL group. It should be mentioned also that the IN10 data indicates that the peak position at a temperature of 800 mK is consistent with the bulk roton energy [115] which is consistent with the findings of Gibbs et. al. [75].

The unique crossover behavior we observed was not observed by the ILL group. In fact their measurement suggested that the confined roton was quite bulk-like in its behavior. However they made a *single* measurement at *one* momentum transfer with only *one* aerogel sample on an instrument with a resolution almost an order of magnitude poorer than the principle spectrometer used in our studies. This crossover behavior we report was observed using IRIS which is a very high resolution instrument with *two* different porosity samples of aerogel. Furthermore the crossover temperature data point observed on IRIS in two different measurements was confirmed using the SPINS TAS instrument. The effect is not as pronounced but the shift is still evident, especially in the raw data. While it is not clear exactly why they did not observe this crossover behavior, since it has been seen in essentially three separate measurements, we believe that this effect is quite real.

We should make one final related comment about the difference in the way that the roton energies are extracted with a TOF measurement and a TAS measurement. This mainly affects the *precision* with which the quantity is measured. As seen in the section on the analysis of the SPINS TAS data we extracted the roton energy simply by convoluting a

DHO with the instrumental resolution function at a single momentum transfer (as in the IN12 measurement). Thus the precision is limited by the measurement at a single point in Q-E space. In a TOF measurement we have many more momentum transfers available so that, after extracting the excitation energies from the convolution of a DHO with the instrumental resolution function, we fit those energies to the Landau roton dispersion, equation (5.4). This type of fit can decrease the error bar on a single excitation energy by 50% providing a more *precise* estimate of the roton energy.

CHAPTER 6

SUPERFLUID HELIUM IN POROUS VYCOR GLASS

When superfluid helium is confined to porous vycor glass its behavior near the superfluid transition is very similar to the bulk transition. The major difference between bulk helium and the superfluid helium confined to vycor is that in the helium/vycor system, the heat capacity peak is rounded and small with no cusp-like behavior (see figure 6.1) and the transition temperature is suppressed by about 200 mK. Early measurements of the heat capacity were explained in terms of a lower energy roton compared with the bulk roton [71]. Using the conventional Landau excitation model with the reduced energy rotons one can obtain reasonable agreement with the heat capacity and normal fluid fraction data [116,117]. Unfortunately no published measurements of superfluid helium in vycor have appeared so there have been no direct observations of these lower energy rotons.

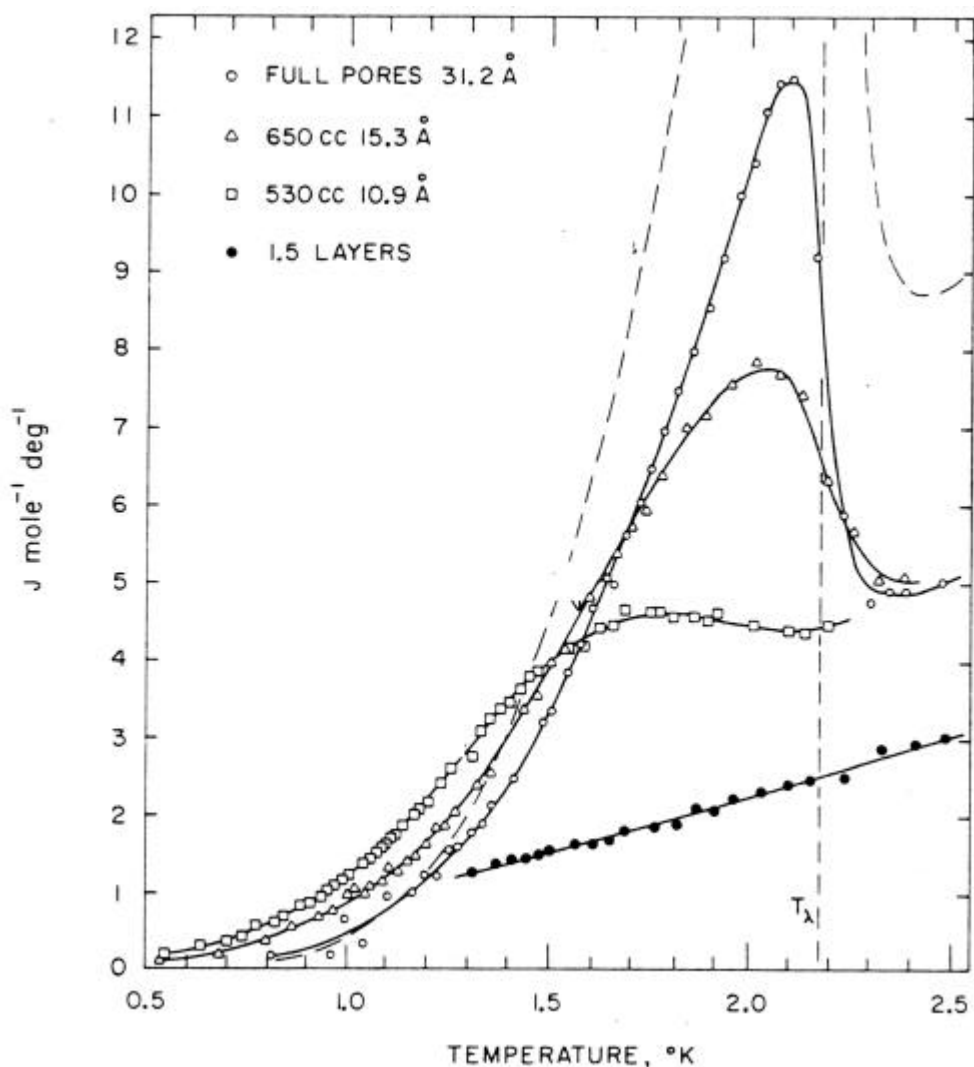


Figure 6.1 Specific heat for helium in vycor as a function of pore filling. Full pore vycor (open circles) displays significant rounding in the peak but there is no cusp-like behavior. Adapted from [116].

The principal result of this measurement, the first published inelastic neutron scattering measurement of the excitations of helium in vycor, is the observation of *layered excitations*, previously observed only in thin helium films adsorbed onto crystalline substrates, in addition to bulk-like excitations. Until now there had been only speculation of the existence of layered excitations in the helium/vycor system and the arguments for

the existence of these excitations mainly were provided by macroscopic measurements. This measurement provides evidence of the existence of these layered excitations via direct observation. In addition, this new excitation provides a much-needed link between the collective excitations of the confined superfluid and the thermodynamic measurements of the helium/vycor system. As in the helium/aerogel system the microscopic dynamics can be linked to the macroscopic measurements, but in the helium/vycor system the layered excitations modify the overall excitation spectrum in a distinctive way.

6.1 Data Analysis

The measurements of helium in vycor revealed an excitation spectrum very similar to the bulk spectrum. Near the roton minimum (corresponding to a scattering angle near 82.5°) the bulk helium roton signal was modeled well with a gaussian centered at the excitation energy and a multiphonon contribution. Multiphonon processes, which are due to scattering events between individual excitations, have been observed in bulk helium neutron scattering studies. Significant structure at energies higher than the roton energy have been observed and identified with roton-roton, roton-maxon, and maxon-maxon processes [118]. The multiphonon contribution, which has a small amplitude compared to the single-phonon scattering and extends from the roton energy upwards, was modeled with a broad gaussian multiplied by the convolution of a narrow gaussian with a unit step

function. There is no theoretical basis for the functional form used but it modeled the multiphonon contribution well. In terms of normalized gaussians,

$$S_{\text{mp}}(E) = G_{\text{broad}}(E)[G_{\text{narrow}}(E) \otimes \theta(E)], \quad (6.1)$$

where

$$G_{\text{broad}}(E) = \frac{1}{\sqrt{2\pi\sigma_b^2}} \exp\left(-\frac{1}{2}\left(\frac{E - E_b}{\sigma_b}\right)^2\right) \quad (6.2)$$

represents the instrumental resolution,

$$G_{\text{narrow}}(E) = \frac{1}{\sqrt{2\pi\sigma_n^2}} \exp\left(-\frac{1}{2}\left(\frac{E - E_n}{\sigma_n}\right)^2\right) \quad (6.3)$$

convoluted with the step function is due to the excitations, and $\theta(E)$ is the unit step function. Equation (6.1) can be evaluated by performing the convolution and it is expressed analytically as

$$S_{\text{mp}}(E) = \left(\frac{1}{\sqrt{2\pi\sigma_b^2}} \exp\left(-\frac{1}{2}\left(\frac{E - E_b}{\sigma_b}\right)^2\right) \right) \left(\frac{1}{2} + \frac{1}{2} \operatorname{erf}\left(\frac{E - E_n}{\sqrt{2}\sigma_n}\right) \right). \quad (6.4)$$

An example of this function in terms of its gaussian components is illustrated in figure 6.2. Since the multiphonon scattering observed here was so small, this simple function was easily fit to the higher energy ($E > 0.9$ meV) scattering.

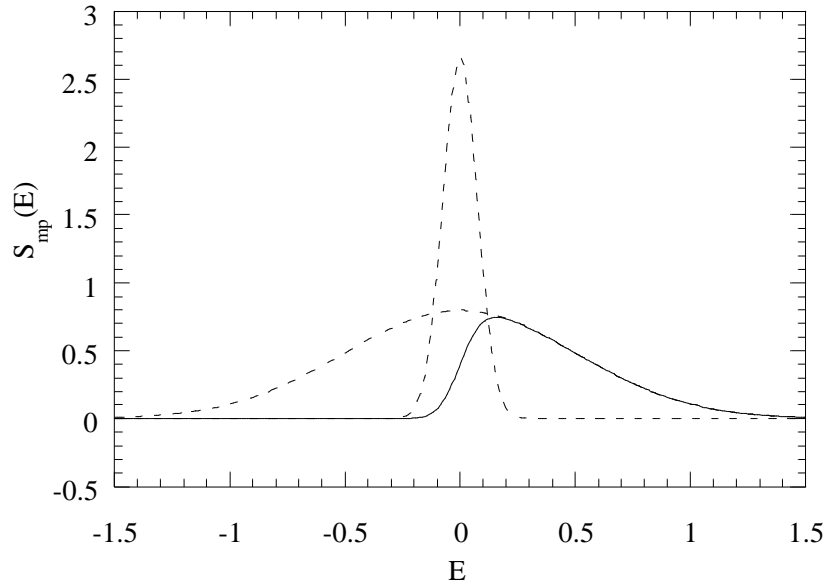


Figure 6.2 Illustration of the function used to model the multiphonon component of the scattering. Dashed lines are the narrow and broad gaussians defined in (6.2) and (6.3) and the solid line is the analytic expression (6.4).

The bulk excitation energies were systematically higher by about 26 μeV than the known values [48] at the roton minimum and varied slowly but linearly across the roton minimum. This shift in the peak position was probably due to an uncertainty in the distance in the final flight path used in the time-to-energy conversion but posed no problem in the determination of the resolution function because we were able to calibrate our bulk helium measurement to a previous one done on the same instrument [48,119].

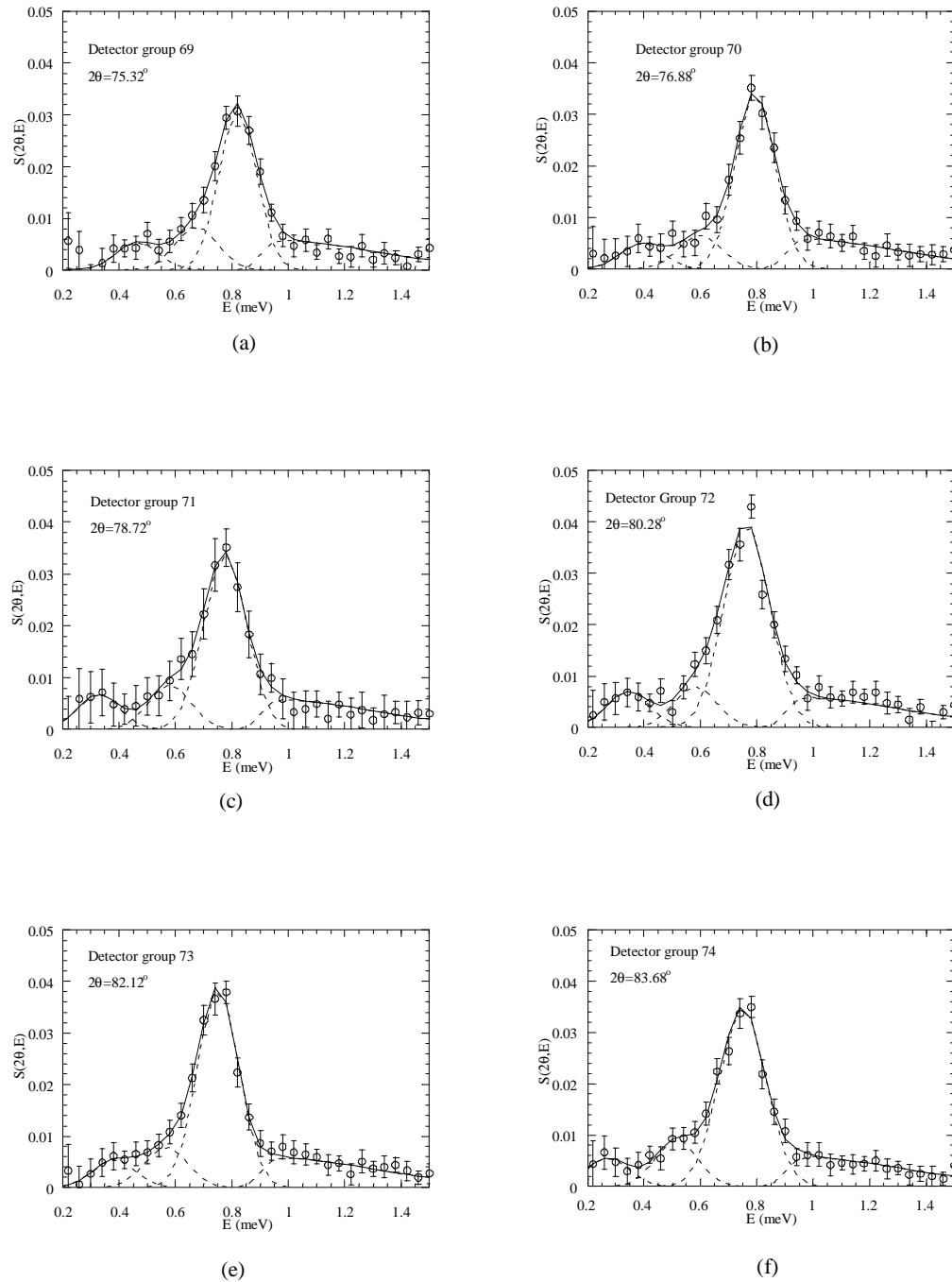


Figure 6.3 Constant angle data near the roton minimum for helium in vycor at 500 mK. Dashed lines are the individual components of the total fit and the solid lines are the overall fits. Values of Q at the bulk-like roton energy are (a) 1.78 \AA^{-1} , (b) 1.81 \AA^{-1} , (c) 1.85 \AA^{-1} , (d) 1.89 \AA^{-1} , (e) 1.92 \AA^{-1} , and (f) 1.95 \AA^{-1} .

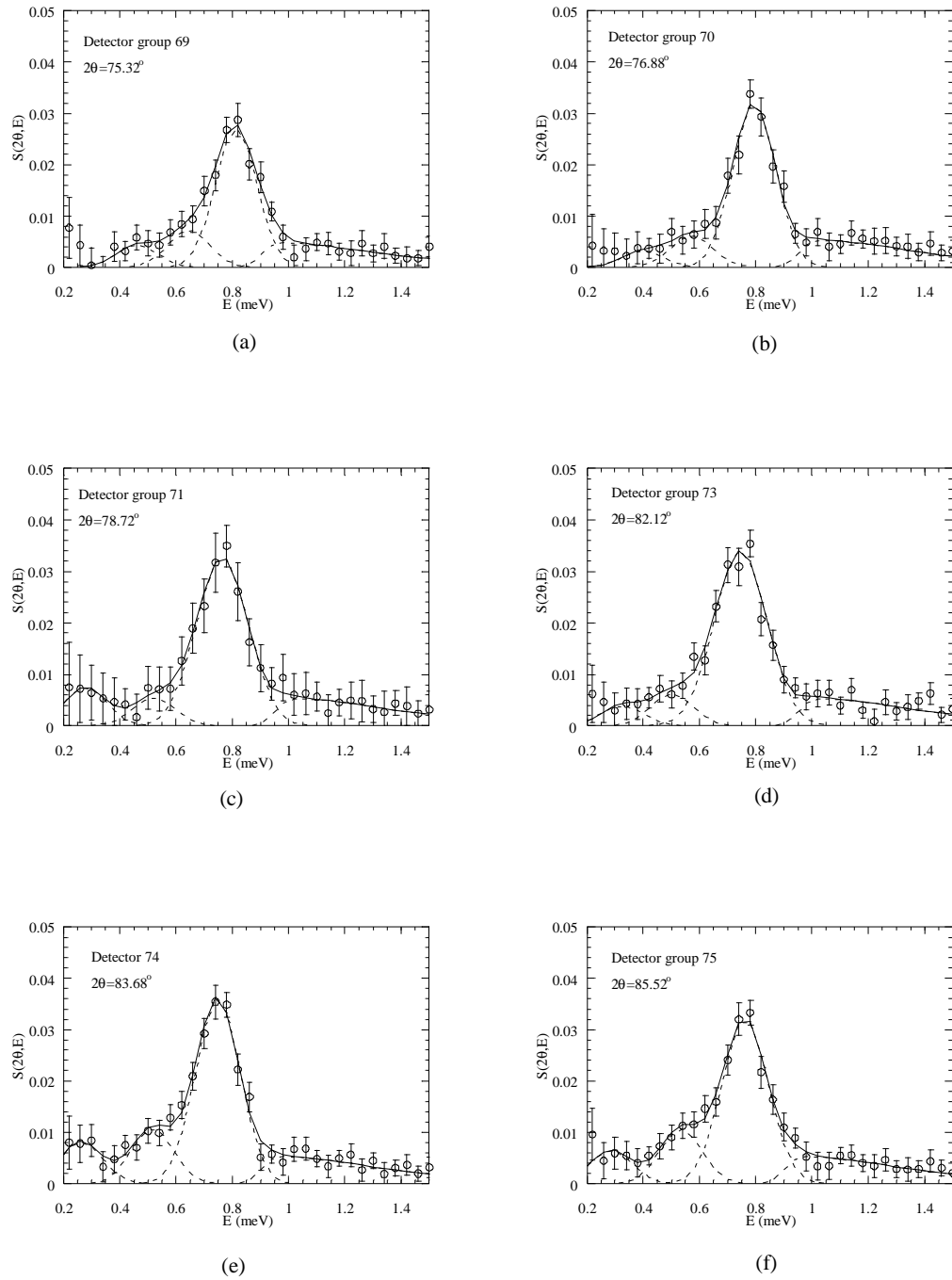


Figure 6.4 Constant angle data near the roton minimum for helium in vycor at 1.1 K. Dashed lines are the individual components of the total fit and the solid lines are the overall fits. Values of Q at the bulk-like roton energy are (a) 1.79 \AA^{-1} , (b) 1.82 \AA^{-1} , (c) 1.86 \AA^{-1} , (d) 1.93 \AA^{-1} , (e) 1.96 \AA^{-1} , and (f) 1.99 \AA^{-1} .

The scattering data at 500 mK and 1.1 K for 6 detectors near the bulk roton minimum (after background subtraction) shown in figures 6.3 and 6.4 respectively, display a rich structure. As in previous bulk superfluid measurements there is a bulk-like excitation which is resolution-limited with an approximate width (FWHM) of $140 \mu\text{eV}$. However a simple scattering function made up of a single resolution-limited peak does not fit the scattering data well.

As mentioned previously, the bulk helium excitations were shifted up in energy by about $26 \mu\text{eV}$ due to inaccurate flight path knowledge but the scattering from the front portion of the vycor disks resulted in the energies shifted down by about the same amount. Both of these effects were incorporated into the overall effective resolution function and the net result was that the energies extracted from the observed scattering were scaled correctly and not shifted. This exact cancellation is probably not completely correct because *all* of the neutrons do not scatter from the front face of the sample. However since *most* of the neutrons do scatter from the front face then the assumption is probably justified.

The background-subtracted data was modeled well by one resolution-limited gaussian for the elastic peak, a multiphonon contribution (equation (6.4)), and three resolution-limited gaussians. The basis for this model was the published scattering data for superfluid films where multiple excitations lower in energy than the bulk roton were observed [22]. Initially we fit the background-subtracted data with only two inelastic gaussians, one for

the bulk-like excitation and one for the lower energy excitation, [120]. This provided an adequate model of the inelastic scattering. Motivated by the scattering results from thin films, we found that the inclusion of an additional resolution-limited gaussian provided a still better fit to the data. Thus our model for the data consists of three inelastic resolution-limited gaussians, a single elastic resolution-limited gaussian, and a multiphonon contribution. The origin of all of these components will be discussed in the next section.

6.2 Results

First, although not shown in these figures (but seen in the raw TOF data in figure 4.16), there is an intense scattering component centered at $E=0$ which we attribute to elastic scattering from the solid helium present on the pore walls. Unfortunately we cannot estimate the amount of solid adhering to the pore walls from these measurements since the scattering involves vycor-vycor and vycor-helium correlations. This makes it difficult to disentangle the solid helium contribution from the net scattering, especially considering that the net elastic peak is the result of subtracting two large peaks.

The next feature, which is the most intense inelastic portion of the scattering signal, is a resolution-limited gaussian centered very close to the bulk roton energy. Since it has an energy close to the bulk roton energy we refer to this feature as the *bulk-like* roton. The Q-dependence of the center of the bulk-like roton follows the Landau parabolic

dispersion relationship, equation (2.4), very closely. In fact, for each of the temperatures studied, the centers of the bulk-like lines were fit (at their corresponding momentum transfer) to equation (2.4) and the roton parameters (Δ , μ_R , and Q_R) were extracted. The bulk-like roton parameters are summarized in table 6.1.

Table 6.1 Summary of the bulk-like roton parameters for helium in vycor.

T (K)	Δ (meV)	Q_R (\AA^{-1})	m_R (m_{He})
0.5	746 ± 6	1.905 ± 0.011	0.139 ± 0.053
1.1	741 ± 4	1.911 ± 0.006	0.139 ± 0.019
1.6	717 ± 7	1.914 ± 0.011	0.122 ± 0.030
1.9	685 ± 29	1.916 ± 0.025	0.102 ± 0.067

The temperature dependence of the bulk-like roton energy gap and roton mass is plotted in figures 6.5 (a) and (b). Theoretical predictions (BPZ) of this temperature dependence based on pseudopotentials [46] which have been shown to be in good agreement with the bulk data also agree with the temperature dependence of the bulk-like roton in vycor. The temperature dependence of the bulk-like roton is displayed in figure 6.5 (a) along with a smooth curve which is a least-squares fit to the theoretical prediction of Bedell *et al.* [46],

$$\Delta(T) = \Delta_0 - P_\Delta (1 + R\sqrt{T})\sqrt{T} \exp\left(-\frac{\Delta(T)}{T}\right). \quad (2.11)$$

In the bulk liquid, $\Delta_0=0.745$ meV, $P_\Delta=2.13$, and $R=0.063$. Our measurements of the bulk-like roton in vycor yield best-fit parameters of $\Delta_0=0.742$ meV, $P_\Delta=1.13$, and $R=1.29$. These parameters are in good agreement except for R . The disagreement is misleading, though, since the uncertainty on the R is about ± 20 . Thus no conclusions can be drawn from the differences in R .

The temperature dependence of the roton mass, shown in figure 6.5 (b), for the confined liquid behaves as we might expect based on the fact that it has a lower transition temperature. It has a temperature dependence similar to the bulk liquid except near the superfluid transition temperature where it appears to have a stronger temperature dependence. However since the error bars are so large on the data no conclusions about the behavior can be drawn.

Unlike aerogel, the scattering could not be fit by a single bulk roton-like signal. Two additional contributions lower in energy than the bulk-like roton were observed. These two components of the scattering data were fit with resolution-limited gaussians and occur at an energy transfer lower than the bulk roton. To our knowledge no known excitation has been observed in bulk superfluid helium at energies lower than the bulk roton at these momentum transfers. However, a feature remarkably similar to this *has* been observed in inelastic neutron scattering data from thin helium films [22]. Unfortunately no conclusions could be drawn from the observation of these two low energy modes in the thin helium films other than some speculative remarks. Currently

we may only speculate as to the origins of this additional scattering in our measurements but now we have three separate measurements which provide some much-needed additional clues: the previous thin-film scattering data [22], the current helium in vycor data, and the helium in silica xerogel data presented in the next chapter. We will discuss these possibilities below and, in so doing, we will apply some of the arguments of Clements *et. al.*.

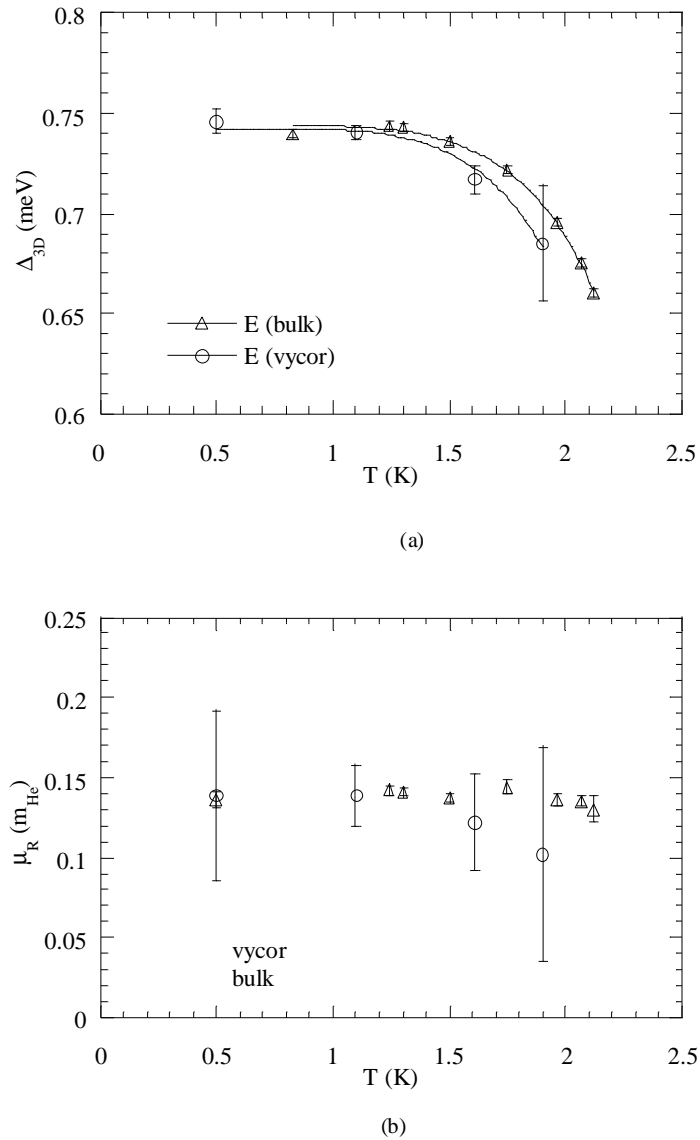


Figure 6.5 Temperature variation of the (a) bulk-like roton energy gap (circles) and (b) the roton mass (circles). The bulk values are shown for reference (triangles) [48]. Smooth lines are fits of the BPZ expression to the roton energy gap.

The origin of these additional scattering components is one of two possibilities. The first and most pessimistic possibility is that neither of these low energy scattering components are collective modes of the confined liquid at all. Multiple scattering has been

responsible for the observation of Q -independent ridges in the dispersion as discussed in chapter 5. However such multiple scattering features reflect the density of states of the helium which, for the bulk liquid, is quite large for the roton. Thus the multiple scattering would not provide a scattering signal below the roton energy as is observed here. Furthermore, we believe that they *are* indeed real modes because these same features were not only observed in thin helium films, but we also observed them in helium confined to silica xerogel (described in chapter 7), helium in vycor on two different instruments (an FCS measurement of helium in vycor was performed but the results have not been presented here), and completely different sample geometries (cylindrical and slab). The second possibility, and the one which we are in favor of, is that they are *both* in fact modes known as layered excitations. Such a layered excitation, the two-dimensional roton, was predicted in the early 70's [80] and observed in helium films in the late 70's and early 80's by neutron scattering [81].

Initially the macroscopic experimental data for helium in vycor was modeled with a single lower-energy roton contribution. Recent theoretical predictions and experimental results for films indicate that bulk-like excitations in films can coexist with (possibly) multiple layered excitations. This view might be adopted for helium in a system like porous vycor as well. One can imagine a simple model of helium condensed in vycor where well-defined layers of solid comprise the region adjacent to the pore wall (the inert layer), a few superfluid layers cover the inert layers, and a bulk-like superfluid exists

within the central volume of the pore. Thus it is possible that some of the features seen in thin superfluid helium films might also be present in the superfluid-filled vycor.

If we adopt this model that the helium-filled vycor has similar characteristics as the films then it is possible that the layered excitations could have different energies due to their localization in different layers [22]. The lowest energy modes would be closest to the solid layer near the pore wall and the next highest energy mode would be in the next highest layer. Both layers containing the layered excitations would have different densities than the bulk liquid in the main pore volume giving rise to the different excitation energies. As will be seen in chapter 7 with the xerogel results, this picture is consistent with the observations for partial filling fractions. The intensity of both modes in xerogel is relatively independent of fill fraction (the bulk-like mode is *highly* dependent on fill fraction) until the amount of liquid in the pores is insufficient for superfluidity to be present. We believe that the arguments presented above suggest that the additional scattering below the roton are indeed collective modes of the confined liquid. Subsequent analysis and discussion assumes that these are modes.

The peak centers of the two lowest energy gaussians are shown in figure 6.6 (along with the dispersion of the bulk-like mode). The lowest energy mode appears to show a parabolic dispersion similar to the bulk-like mode. In fact one can fit the excitation energies of the lowest modes (shown by the solid line through the lowest energy points) and extract the following parameters: $\Delta_{2D}=339\pm24$ μeV , $\mu_{2DR}=0.03\pm0.01$ m_{He} , and

$Q_{2DR}=1.91\pm0.01 \text{ \AA}^{-1}$. Note that we have used the subscript 2D to denote that this is an excitation constrained to one of the dense liquid layers in the pore. However it is easily seen that the next highest mode is relatively dispersionless over the limited region shown. This is indicative of an excitation with an extremely large effective mass ($\mu \cong 20m_{\text{He}}$) but it is not clear why an excitation in the next highest layer would have an effective mass much larger than in the layer below it.

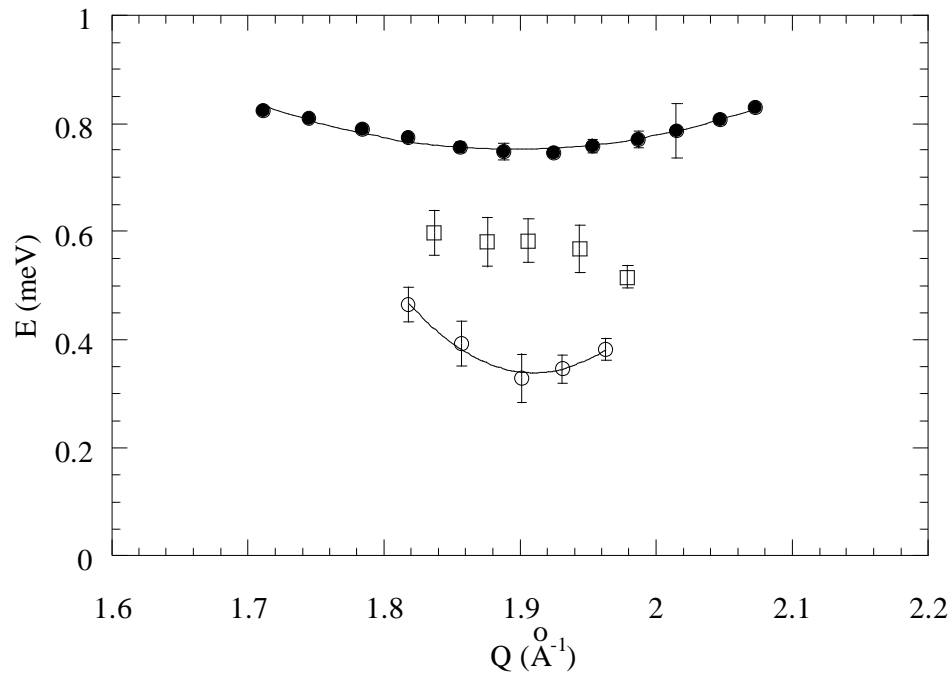


Figure 6.6 Dispersion of the bulk-like roton (solid circles) and the two additional scattering contributions represented by the lower energy gaussians in figure 6.3.

The two lower energy gaussian components were also observed at 1.1 K and the data plus the fits to the data are shown in figure 6.4. Again the dispersion of all three modes were analyzed and the results are displayed in figure 6.7. The lowest excitation can easily be fit to the Landau parabolic dispersion relation with the following parameters:

$\Delta_{2D}=291\pm51 \mu\text{eV}$, $\mu_{2DR}=0.027\pm0.026 \text{ m}_{\text{He}}$, and $Q_{2DR}=1.92\pm0.05 \text{ \AA}^{-1}$. In this case the next highest mode also exhibits a relatively dispersionless behavior. However the excitation energy of the lowest mode is less than at 500 mK which is consistent with the temperature dependence of the roton energy in bulk helium.

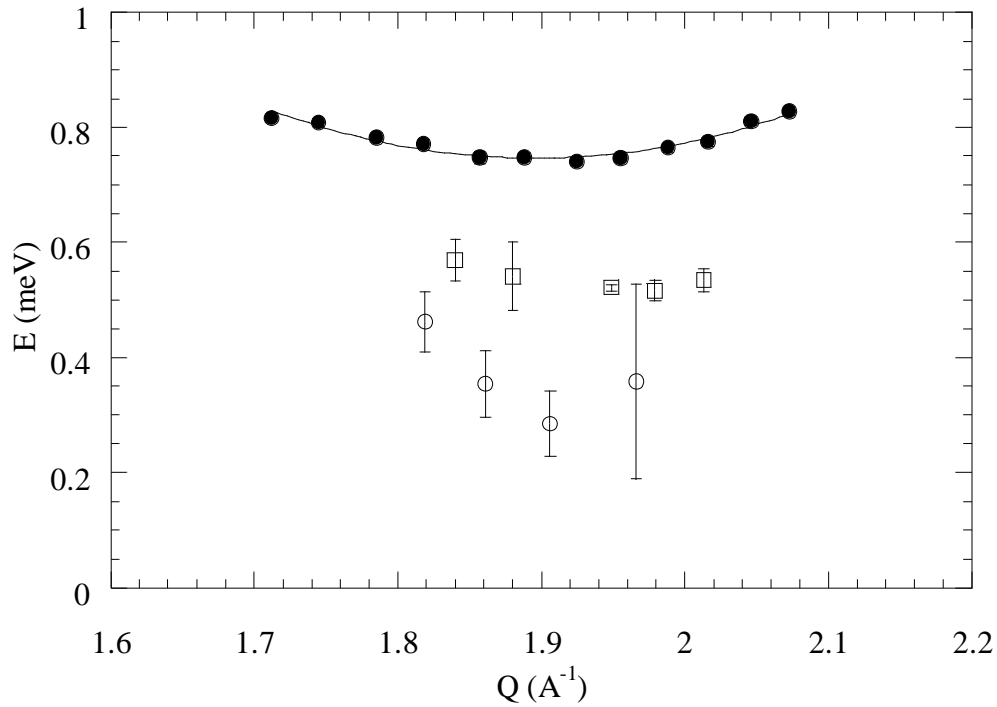


Figure 6.7 Dispersion of the bulk-like roton (solid circles) and the two additional scattering contributions represented by the lower energy gaussians in figure 6.4.

6.3 Connection with Macroscopic Measurements

We can establish a connection with the macroscopic measurements via the Landau excitation model as we did with the helium in aerogel results in the previous chapter. However to obtain good agreement with the macroscopic data it is necessary to augment

the Landau excitation model with new excitations that have lower energies than the bulk-like roton. We will thus identify our lower energy modes observed in the scattering as two different layered, or 2-D, rotons. The detailed derivation of the contribution to the heat capacity and normal fluid fraction from 2-D rotons is presented in appendix C and the resulting expressions can also be found in the published literature [18] and [16].

The Landau excitation model can easily be extended to include the layered excitations which have been observed in thin helium films [13,20,20-22,81,81,121,121] and postulated to exist in confined helium systems. Values for the layered excitation energies were suggested as early as 1965 where measurements of the heat capacity of helium-filled vycor yielded energies of about 0.525 meV [71]. Subsequent torsional oscillator and heat capacity measurements of helium in vycor yielded energies between 0.48 and 0.53 meV [116,117,117].

The layered roton heat capacity and normal fluid fraction have been found (see appendix C) for layered (two-dimensional) excitations and are given by [16]

$$C_R^{2D}(T) = \left(\frac{\mu}{2\pi} \right)^{\frac{1}{2}} \frac{k_B Q_R \Delta^2}{\rho \pi \hbar (k_B T)^{\frac{3}{2}}} \exp\left(-\frac{\Delta}{k_B T} \right), \quad (6.5)$$

and [18]

$$\frac{\rho_n^{2D}}{\rho}(T) = \frac{\hbar Q_R^3}{\rho} \left(\frac{\mu}{8\pi k_B T} \right)^{\frac{1}{2}} \exp\left(-\frac{\Delta}{k_B T} \right). \quad (6.6)$$

The temperature dependence for the quantities in 2 and 3 dimensions are the same but the roton parameters are different in each case. The densities (ρ) in equations (6.5) and (6.6), for instance, are areal densities, as opposed to the volume densities in the bulk liquid's relationships.

In figure 6.8(a) the total heat capacity which was fit to the data is the sum of two layered contributions and the bulk-like contribution. In the fits we have assumed that the bulk-like roton has a temperature dependence similar to the roton in the bulk liquid but scaled in temperature to the superfluid transition temperature for helium in vycor. This assumption does not seem unreasonable given the temperature dependence seen in figure 6.5. The individual contributions have been displayed as well to indicate that only the sum of the contributions provide a reasonable fit over the temperature range shown. Figure 6.8(b) shows a similar plot except in terms of the normal fluid fraction. Recall that the same plots for helium in aerogel (as well as the bulk liquid of course) resulted in a straight line with a slope of -1 thus illustrating the dominant role of the roton in aerogel and the validity of an unmodified Landau excitation model. For confinement in vycor the difference is strikingly clear. Figure 6.8 clearly indicates the necessity of including the layered contributions with the bulk-like contribution. The inclusion of both layered excitations and the bulk-like excitation is necessary for the microscopic and macroscopic measurements to agree.

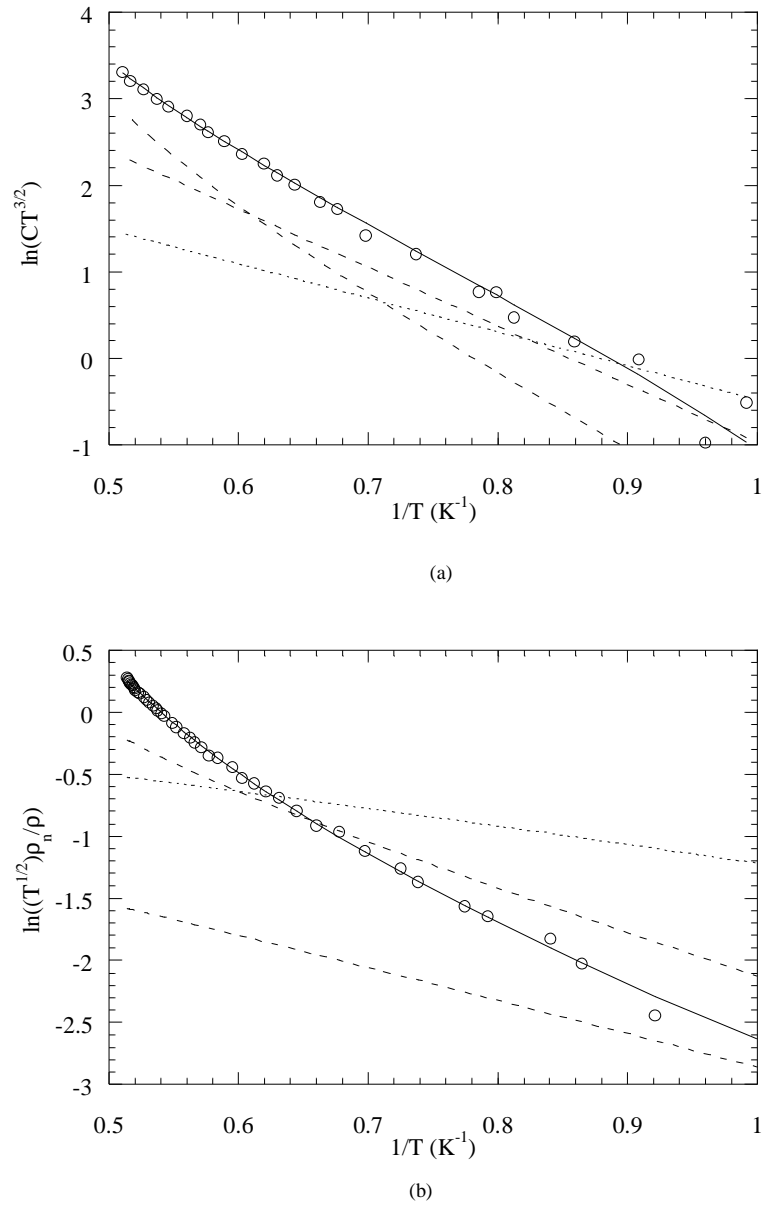


Figure 6.8 (a) Heat capacity data [116] and (b) normal fluid fraction data [69] for helium in vycor plotted to illuminate the 2-D and 3-D character in different temperature regimes.

We conclude this chapter by returning to the critical behavior of the confined liquid. As mentioned in the introduction the phase transition (via the normal fluid fraction) for the confined liquid is in the same universality class as the bulk liquid. This is entirely

consistent with our observation that the bulk-like roton has a BPZ-like (bulk-like) temperature dependence (see figure 6.5 (a)). We know that in the vicinity of the superfluid transition the bulk-like roton makes the largest contribution to the thermodynamic properties of the system. Therefore the bulk-like roton is the microscopic origin of the macroscopic behavior near the superfluid transition.

CHAPTER 7

SUPERFLUID HELIUM IN SILICA XEROGEL

Macroscopic measurements indicate that the behavior of superfluid helium confined in silica xerogel differs from superfluid helium confined to either aerogel or vycor. Not only is the superfluid transition temperature suppressed but the critical exponents for the transition are different from the bulk liquid. The critical exponent for the superfluid phase transition in xerogel is 0.89, greater than in the bulk (0.67), vycor (0.67), or aerogel (0.81). These macroscopic measurements also indicate that the temperature dependence of the thermodynamic properties of the helium/xerogel system is different from that of the bulk superfluid over a broad range of temperatures. Once again the origins of the discrepancies in the thermodynamic data for the confined system can be traced to the presence of layered excitations discussed in the previous chapter.

In this chapter we discuss the results of our search for the presence of layered excitations in helium confined to silica xerogel. Not only are multiple layered excitations present but they display a physically plausible dependence on the amount of helium present in the pores. Perhaps most important is that the dependence on fill fraction supports the notion that these layered excitations are indeed localized to layers near the pore wall. Finally, inclusion of these layered excitations in a modified Landau excitation model provides a reasonable description of the thermodynamic behavior of the silica/xerogel system.

7.1 Data Analysis

Measurements carried out on the TOF instrument FCS for helium in xerogel showed the clear presence of excitations similar to the bulk excitations. Since the time-of-flight data in each detector were somewhat noisy, the xerogel data from three detector groups were grouped together in order to improve the statistics. Similar structure in the scattering was observed as in the helium/vycor data discussed in the previous chapter. Therefore a similar fitting procedure was adopted where resolution-limited gaussians were used in the fits. In particular, the widths of the gaussians were fixed at the instrumental resolution ($\sigma_{\text{res}} = 70 \text{ } \mu\text{eV}$) and the amplitudes and centers were allowed to vary freely. As in the vycor data, near the bulk roton momentum three gaussians fit the inelastic scattering data best plus a multiphonon contribution. An additional elastic scattering component was again present in the data due to scattering from the dense helium layer(s) bound to the pore walls. However no attempt was made to analyze the elastic peaks.

7.2 Results

The inelastic scattering was modeled well by three resolution-limited gaussians, a multiphonon component, and a flat background at filling fractions of 0.6, 0.8, and 0.95. The data in figure 7.1 show the fits for filling fractions of 0.4, 0.6, 0.8, and 0.95 for detector groups 13-15 corresponding to an average scattering angle of about 108° (with a momentum transfer $Q \cong 2 \text{ } \text{\AA}^{-1}$ near roton energy). The existence of the bulk-like roton is

clear for the three fill fractions (0.95, 0.8, and 0.6) and is shown by the highest energy gaussian.

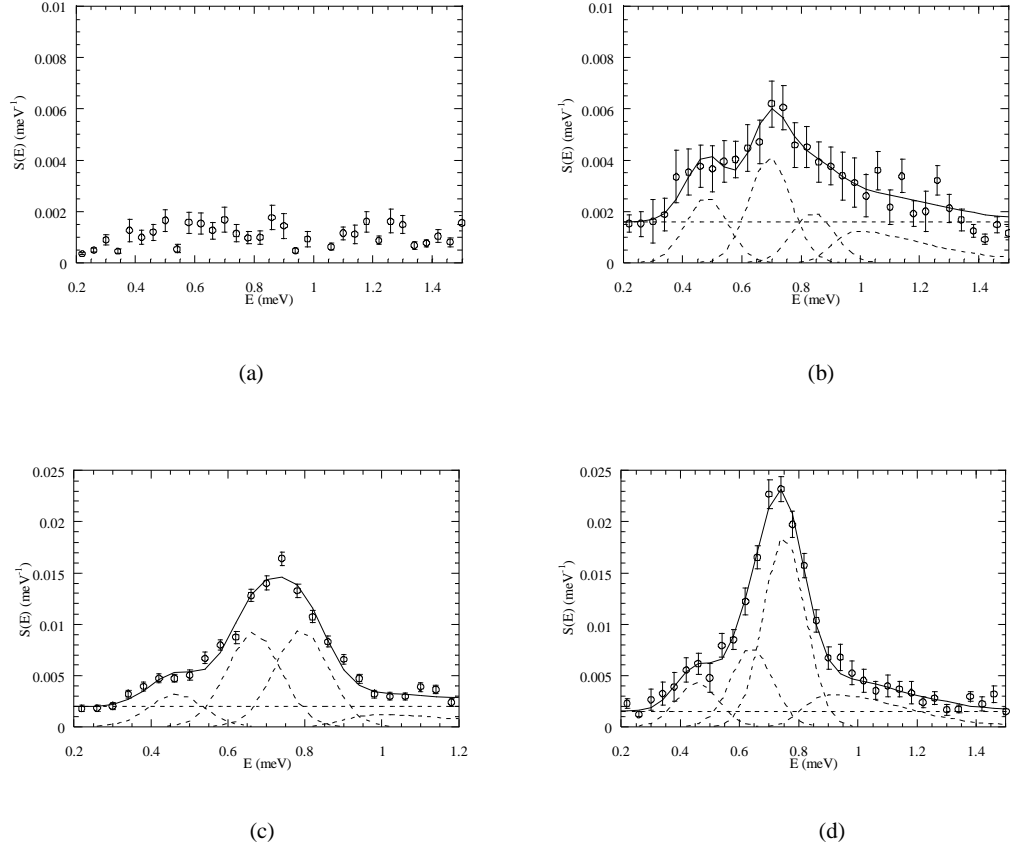


Figure 7.1 Fits to the scattering data of helium in xerogel at the roton minimum (momentum) at fill fractions of (a) 0.4, (b) 0.6, (c) 0.8, and (d) 0.95 and a temperature of 1.36 K. Fit functions are represented by the dashed lines and the sum of the fit functions is shown by the solid line. Detector groups 13-15 have been added together to improve statistics.

The two lower energy gaussians are interpreted in the same way as in the vycor data, namely that they are two-dimensional rotons in different layers. We can extract useful information about these excitations from their peak centers and fill fraction dependence

of their integrated intensities. At full pore filling, the lower energy gaussian is peaked at about 470 μeV and the other is peaked at about 670 μeV . Their centers and integrated intensities, which provide information on the number of excitations present, are relatively independent of fill fraction as shown in figures 7.2 and 7.3. This fact suggests that, if they are indeed collective excitations of the confined liquid, then they are constrained to the layers near the pore wall. If they were not then we would expect them to exhibit a stronger variation with filling fraction which the bulk-like roton clearly displays. Unfortunately since we are unable to resolve these lower energy scattering components at multiple angles we cannot comment on the dispersion of this additional scattering intensity as was possible with the vycor data. In light of the vycor data and the dispersion of the low energy modes observed in that measurement, it seems unlikely that the low energy scattering components in the xerogel data are due to multiple scattering. Of course we cannot rule out this possibility without further measurements which effectively probe the dispersion of these low energy modes.

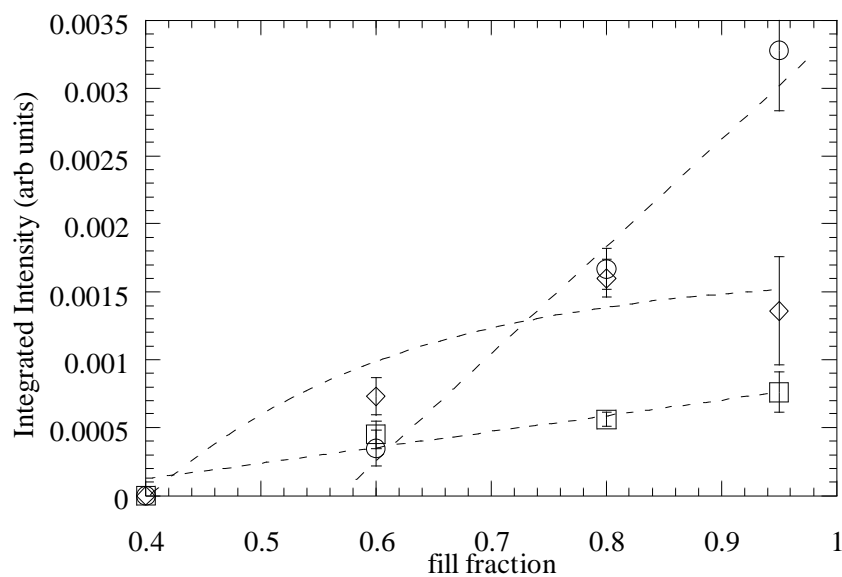


Figure 7.2 The variation of integrated intensity of the bulk-like (circles) and two lower energy components (diamonds and squares) with fill fraction for helium in xerogel. Dashed lines have been added as a guide to the eye.

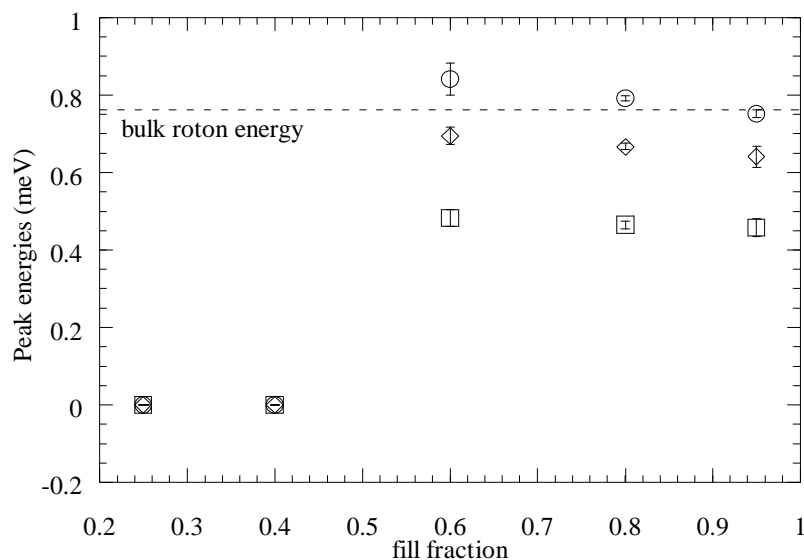


Figure 7.3 The variation of the center of the bulk-like (circles) and two lower energy components (diamonds and squares) with fill fraction for helium in Britesorb. Dashed line is the value of the bulk roton energy found on this instrument.

The integrated intensity of the bulk-like roton increases dramatically with increased pore filling as seen in figure 7.1 and displayed explicitly in figure 7.2. In the case of the bulk-like excitations shown in figure 7.2 the simplest assumption we can make is that the integrated intensities, which are proportional to the number of excitations, have a linear dependence on the amount of bulk-like material present. Thus we can attempt to fit the bulk-like integrated intensities with a line. The zero-crossing occurs at a fill fraction of about 0.56 which suggests the particular fill fraction at which the formation of bulk-like rotons commences. Since we have only three points with which to define the line this alone is not a convincing argument for the linear extrapolation. However the particular zero-crossing value of 0.56 is *physically* plausible. Simple geometrical arguments based on a cylindrical pore (which is admittedly a rough assumption) combined with the known amount of helium adsorbed into the pores suggest that a fill fraction of 0.56 corresponds to roughly three to four adsorbed layers of helium. It is generally accepted that about two layers of helium are adsorbed into a high density inert layer which does not participate in superfluidity [116]. This leaves one to two layers remaining. However, in measurements of superfluid films adsorbed onto a crystalline substrate (Graphon), scattering from the bulk-like is observed to disappear at about three total layers [81], which is consistent with our bulk roton onset estimate for helium in xerogel. The integrated intensity as a function of coverage for helium on Graphon, reproduced in figure 7.4, clearly shows the linearity of the integrated intensity as a function of coverage for the bulk-like roton.

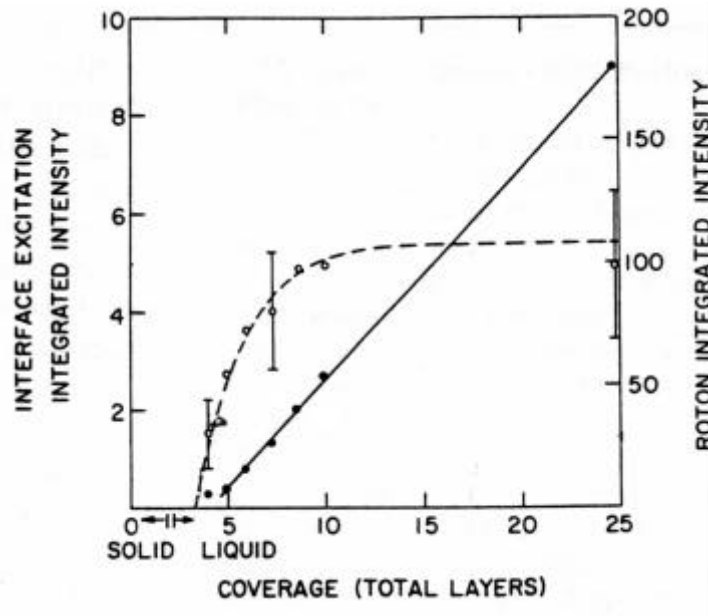


Figure 7.4 Coverage dependence of the integrated intensity of the bulk-like roton (closed circles) and the two-dimensional roton (open circles) for helium on Graphon. Adapted from [81].

Also displayed in figure 7.4 is the coverage dependence of the integrated intensity of the two-dimensional roton for helium on Graphon. On Graphon the two-dimensional signal has a non-trivial coverage dependence which, at first, appears to disagree with our result shown in figure 7.2. The coverage dependence of the integrated intensity can be modeled as a simple process in which the incident neutron can scatter from a layer excitation if there are enough layers present (given by n_o) to support the two-dimensional roton. In this model if we assume that there is a random distribution of collision lengths with a mean-free-path, n_{pd} , for the neutron in the presence of the two-dimensional excitations, then the number of scattered neutrons will follow the form

$$I(n) = I_{\infty} \left[1 - \exp \left(- \left(\frac{n - n_o}{n_{pd}} \right) \right) \right], \quad (7.1)$$

where I_{∞} is the saturation value of the integrated intensity, n_o is the layer coverage at which the excitation appears (the inert layer), and n_{pd} characterizes the depth (in layers) into which the excitation can penetrate (the 2-d layer) [81]. The signal from layered excitations can be modeled well with this model as shown in figure 7.4 by the dashed line. A schematic illustration of the geometry used in this model is shown in figure 7.5. This expression is based on an orderly arrangement of consecutive helium layers. In the fit shown in figure 7.4 the parameters which were extracted were $n_o = 3.3$ layers and $n_{pd} = 2.3$ layers.

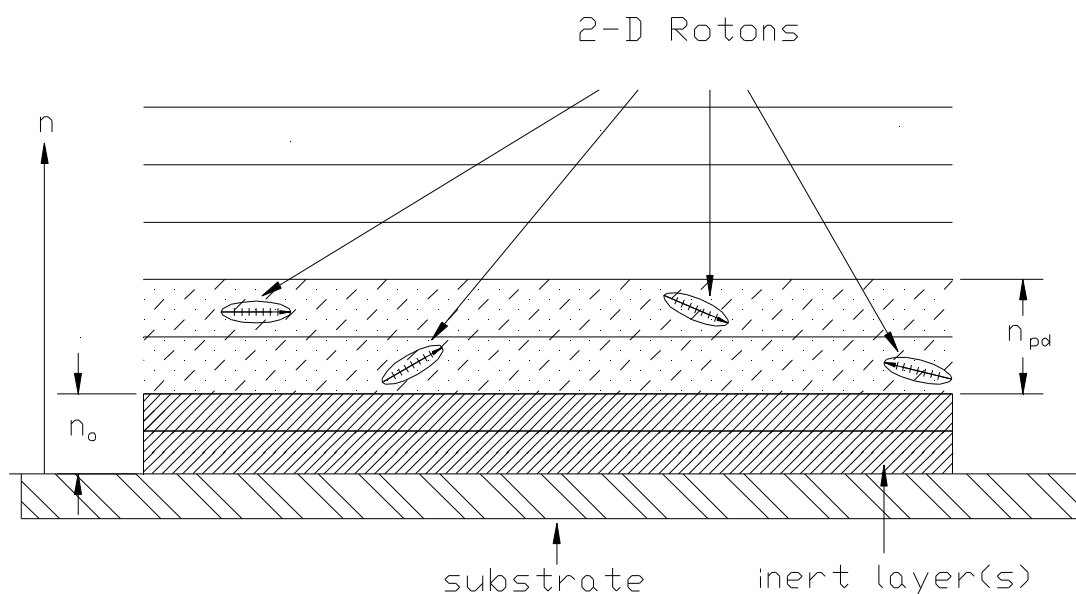


Figure 7.5 Film geometry used to obtain equation (7.1).

The integrated intensities for the xerogel data can be also be plotted as a function of pore coverage and compared with the layered results if one makes the rough assumption that the helium is confined to perfectly cylindrical pores and forms well-defined layers. Of

course we do not expect that the pores are perfectly cylindrical but this provides a basis for comparison with one of the very few results of excitations in films. This assumption can be used in conjunction with the known amount of helium which was condensed into the xerogel to obtain estimates of the number of layers present at different filling fractions. The integrated intensities for helium in xerogel are modeled quite well by the empirical curve, equation (7.1), as shown in figure 7.6. By fitting the xerogel data we can extract values for n_o and n_{pd} . In particular we find that $n_o = 3.0 \pm 0.2$ layers and $n_{pd} = 2.6 \pm 0.8$ layers which are consistent with Graphon data. Unfortunately we only have *four* points with which to fit the model (equation (7.1)) which has *three* free parameters so further measurements of different filling fractions are necessary to confirm this model.

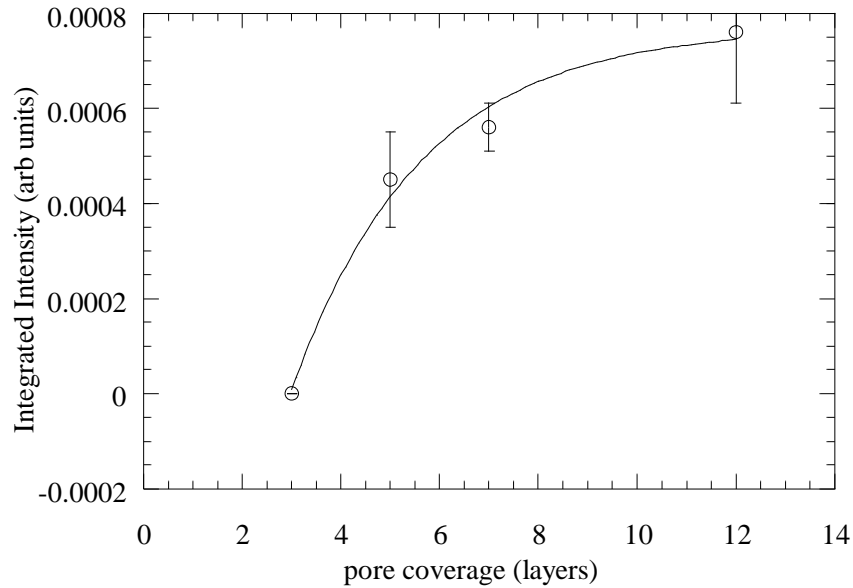


Figure 7.6 Integrated intensity of the two-dimensional roton as a function of pore coverage for helium in xerogel. Solid line is a fit of equation (7.1) to the data.

The peak center for the bulk-like roton in xerogel, as shown in figure 7.3, is relatively independent of fill fraction and about the same energy as the bulk. In these measurements the bulk-like roton energy is about 0.751 meV consistent with our direct measurement of the roton energy (0.748 meV) in the true bulk superfluid. The bulk-like roton energy on Graphon is also relatively independent of fill fraction, as shown in figure 7.7. However, it is slightly lower in energy than the roton in the true bulk liquid. It should be mentioned that the bulk value shown by the arrow in figure 7.7 (0.775 meV) is about 0.035 meV higher than the currently accepted value of 0.74 meV. The origin of the bulk value shown in figure 7.7 is not referenced in [81] but most likely it originated from a previous independent measurement. The consequence of this is that the energies quoted in the bulk measurement and the Graphon measurement might not be calibrated in the

same manner. Thus they may actually be the same energy which bring their results into agreement with ours.

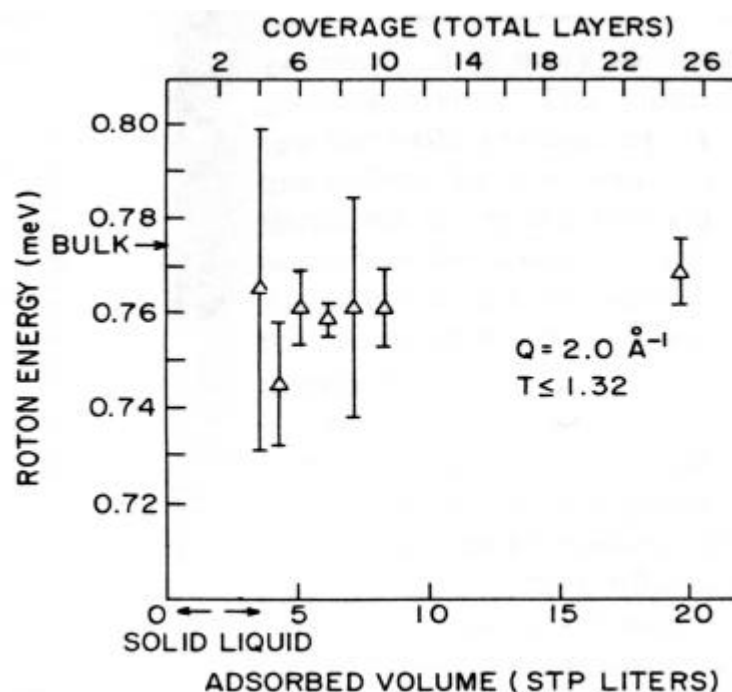


Figure 7.7 Coverage dependence of the bulk-like roton energy for helium on Graphon. Adapted from [81].

We have resolved two lower energy excitations which we attribute to layer excitations but only a single layer excitation was resolved in the Graphon system. In light of recent measurements it seems likely that multiple excitations indeed were present in the helium/Graphon system but it was not possible to resolve them with the instrumental resolution of the spectrometer used in that investigation (not quoted in [81] but resolution appears to be 0.2-0.3 meV FWHM). If an intermediate-energy excitation (i.e. between bulk-like and lowest-energy layer excitation) were unresolved but present in the

helium/Graphon system then its energy could be folded into that of the lower energy layered excitation, thus causing it to be higher in energy. Their quoted value for the layered roton energy of 0.6 meV is higher than our lowest energy layer excitation, 0.46 meV, which could be due to folding lowest energy layered excitations with the intermediate energy layered excitations. Our lowest energy and intermediate energy excitation energies were 0.46 meV and 0.64 meV, respectively. Certainly a weighted average of the two, consistent with folding the two energy distributions, can mimic the Graphon result. Recent extensive measurements of Clements *et. al.* have indicated that there are indeed multiple layered excitations present in the helium/graphite system [22]. Thus it seems at least plausible that there are multiple excitations present in the helium/Graphon system.

7.3 Connection with Macroscopic Measurements

As was the case for helium in aerogel and helium in vycor, we can establish the connection between the microscopic excitation spectrum and the macroscopic properties of the confined liquid using modified Landau excitation model. However before we discuss the macroscopic xerogel data we must note that, since we did not use xerogel samples prepared in the same way as those used in the macroscopic thermodynamic measurements, a direct comparison is not strictly valid. However the structural properties such as porosity, surface area, and pore size distribution (which are thought to cause the

differences in behavior between the bulk and confined liquids) of the Britesorb are similar to xerogels used in other studies.

The normal fluid fraction data for helium confined to silica xerogel have been plotted in figure 7.8 in a form similar to the corresponding plot in figure 6.7(b). Again the total normal fluid fraction is the sum of two layered contributions and the bulk-like contribution. Also we have assumed that the bulk-like roton exhibits a temperature dependence similar to that in the bulk liquid but scaled in temperature to the superfluid transition in xerogel. Here the fit is good but not quite as good as in the case of the helium confined to the vycor, especially at low temperatures. There are a number of possibilities for the disagreement. First, we only were able to evaluate the energies at one particular Q value in this measurement and the energies used in the fit were those found for 95% pore filling. To obtain accurate estimates we would need energies at multiple Q 's to extract the layered (and bulk-like) roton energies from a fit to the Landau dispersion curve. The other reason may be that the xerogel used in the experiment shown in figure 7.8 is sufficiently different in structure that the excitation energies of the confined liquid are different than those observed here. In fact the porosity of the xerogel sample used in the experiment in figure 7.8 was stated to be 60% which is different from our samples [67].

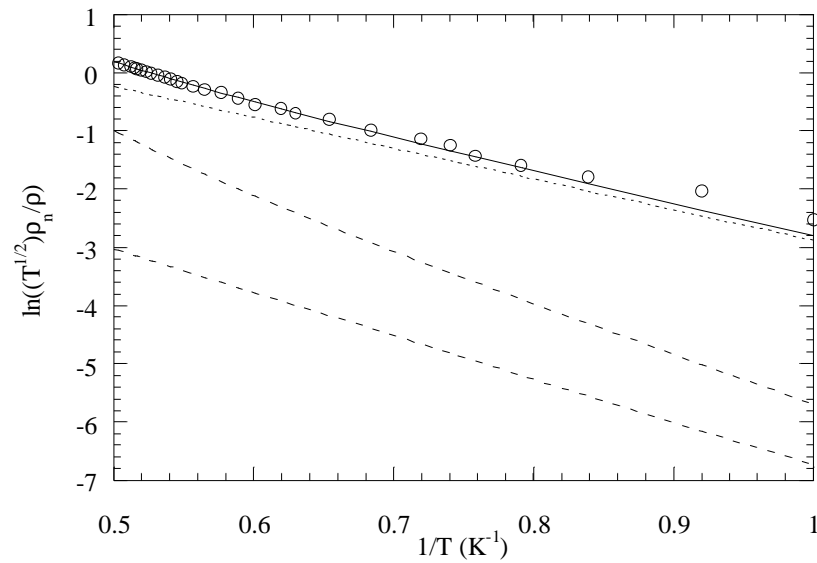


Figure 7.8 Normal fluid fraction data for helium in xerogel plotted to illuminate the 2-D and 3-D character in different temperature regimes.

An ideal comparison between the microscopic and macroscopic dynamics for either helium confined in xerogel or vycor would be to perform the inelastic neutron scattering measurements and the macroscopic measurements with the same sample. This was not possible in our case but the agreement between the macroscopic measurements and our inelastic neutron scattering results suggest that the (modified) Landau excitation model remains valid for the confined liquid for xerogel/Britesorb.

CHAPTER 8

CONCLUSION

In this thesis the effects of disorder induced by confinement on superfluid helium have been presented. The principle result of this study is that rotons, which are the microscopic excitations responsible for the macroscopic behavior of the bulk liquid above 1 K, have a similarly dominant role in the confined liquid. In each case of confinement the excitation spectrum is modified in some way. Confinement in aerogel, characterized by a strand-like geometry with large open spaces, modifies the temperature dependence of the roton while confinement in vycor and xerogel, which have smaller pore sizes, causes the addition of lower energy excitations to the usual bulk superfluid dispersion curve. The Landau excitation model which relates the excitation parameters to the thermodynamic behavior completes the connection between the modified spectra and the thermodynamic behavior.

We conclude this thesis with a summary of the main results of this investigation as well as discuss some of the outstanding questions raised by this work.

8.1 Confinement in Silica Aerogel

When superfluid helium is confined to silica aerogel with porosities of 95% and 90% the excitation spectrum looks very similar to that of the bulk liquid, displaying the phonon-

maxon-roton portions of the bulk spectrum. However the temperature dependence of the roton energy gap, Δ , does not follow the typical mode softening behavior as in the bulk. In fact there appears to be a crossover behavior in temperature which occurs around 1.9 K. Below 1.9 K the roton energy is relatively temperature independent. However above this crossover temperature the roton energy displays a strong temperature dependence.

This unusual temperature dependence has been explained in terms of a competition between length scales. The usual length scale in superfluid helium at these temperatures, $1 < T \text{ (K)} < T_\lambda$, is the roton mean free path whose temperature dependence is dictated by collisions with other rotons and the number of other thermally-activated rotons present in the liquid. Confinement necessarily introduces a new length scale into the helium system, namely a geometrical confinement length.

If the length scale which confinement imposes is small enough, it is possible that confinement can induce the proliferation of vorticity in superfluid helium. Since rotons are known to interact with quantized vorticity present in superfluid helium one possibility for this additional length scale is the roton-vortex line mean free path. Unfortunately it has not been possible to observe vorticity directly with neutron scattering so alternative measurements would be necessary to confirm this hypothesis.

The novel temperature dependence of rotons in silica aerogel can be related to the macroscopic quantities. We have shown that the different temperature dependence seen

in the thermodynamic and transport properties is consistent with the modified temperature dependence of the roton.

As we have seen, layered excitations play an important role in the microscopic and macroscopic dynamics of superfluid helium in vycor and xerogel, but we have not observed them directly in silica aerogel. These excitations are most likely present but the signal from them is far too small to be observed when compared with the extremely large bulk-like roton signal.

8.2 Confinement in Porous Vycor Glass

The excitation spectrum for helium in porous vycor glass is very similar to the bulk spectrum. In addition to the usual phonon-maxon-roton spectrum in the bulk, however, additional scattering is observed which is lower in energy than the roton but consistent with layered excitations known as two-dimensional rotons. Two-dimensional rotons have been predicted to be present in the helium/vycor system but no direct measurements of their presence have been published until now.

Our measurements suggest that there are at least two such layered excitations present in the helium/vycor system which appear to have a well-defined dispersion not unlike the Landau parabolic roton dispersion. This result is consistent with the neutron scattering

data for thin superfluid helium films adsorbed onto crystalline substrates. In fact our results are surprisingly similar to the thin film data.

These layered excitations, when used in a modified Landau excitation model that includes two-dimensional excitations, provide the link so that the microscopic dynamics agree with the macroscopic superfluid dynamics.

8.3 Confinement in Silica Xerogel

The measurements of helium adsorbed in xerogel suggest that multiple layered excitations are present in this system as well as in vycor. In addition to confirming the existence of the layered excitations for helium-filled xerogel, measurements of the fill-fraction dependence were performed. The helium fill-fraction dependence of these excitations suggests that the two lower lying excitations observed in the scattering data are indeed layered. The integrated intensity of these excitations, which is proportional to their number density, is relatively independent of fill fraction while the integrated intensity of the bulk-like excitations shows a strong filling-fraction dependence.

When the pores are full the bulk-like roton displays a very strong signature in the scattering. However this decreases progressively with fill fraction until it cannot be seen at 40% full-pore capacity. The data suggest that the bulk-like roton appears between 40% and 60%. An estimate was made of the number of layers necessary for bulk-like

rotons to commence formation based on a model of layered films of helium [81]. A simple linear interpolation of the data indicates that the onset of the bulk-like roton occurs at about 56% full-pore capacity. Geometric arguments applied to the scattering data and a more physically realistic coverage model suggest that the bulk-like roton onset occurs at 3 helium layers adsorbed onto the xerogel surface. The agreement with the scattering results for the coverage dependence of helium on crystalline substrates is quite good considering that, strictly speaking, the xerogel is more disordered.

The layered excitations are the final entities which ultimately complete the connection between the microscopic dynamics of the confined liquid and the thermodynamic and transport properties of the liquid via the Landau excitation model.

8.4 Outstanding Questions and Final Remarks

The results of this investigation have answered a number of questions in the affirmative. The most general question, “can the unusual behavior of confined superfluid helium be explained by the microscopic excitations as in the bulk?”, can be answered with an unqualified yes. In addition the answer to “is the roton energy lowered when superfluid is confined to vycor?” is a qualified yes. The qualifier is that there are lower energy rotons with different energies in addition to the bulk-like rotons. However some outstanding questions have arisen during the course of this research which could not be answered with and were motivated by these measurements.

The possibility that quantized vorticity causes the anomalous temperature dependence of the roton energy gap in aerogel is intriguing and, admittedly, speculative. One of the main points of the argument is that the confining medium has a single dominant length scale. As was mentioned, aerogel has a broad distribution of pore sizes, apparently weakening the argument. However an average over a pore size distribution centered about the aerogel average pore size with a substantial width also yields a similar length scale. One test of the trapped vorticity model is to investigate the temperature dependence of the roton energy gap for helium confined to a number of porous aerogels whose pore size distribution are relatively narrow with widths of the order of a few hundred Å. The trapped vorticity model predicts that, since the number of trapped vortex lines depends strongly on the pore size, then the crossover temperature will be different for different pore sizes. Thus a direct test of this model can be made.

Another test of the trapped vorticity hypothesis exists which does not involve the use of porous media. Vorticity can be created in superfluid helium confined to a capillary in which a small heater at one end is pulsed creating a counterflow of the normal fluid and superfluid (the thermo-mechanical effect). If the flow rate created by the heater is large enough, turbulence sets in and a dense tangle of vortex lines is created. The relationship between the resulting flow rate of the normal liquid and the density of the subsequent vortex tangle is established thus enabling one to create a well-characterized density of vortices [122]. In effect, by adjusting the heater power and thus creating a suitable vortex

density, one can mimic the vortex density arising from confinement in a porous material with a particular pore size distribution. It is possible that a number of such superfluid-filled capillaries could be used in a single sample cell in an inelastic neutron scattering experiment so that, by measuring the roton energy at different flow rates, the vortex-line density dependent crossover temperature can be confirmed.

The crossover behavior in temperature was not observed for superfluid-filled porous vycor glass. The arguments used in explaining the aerogel data suggest that indeed there should be a crossover temperature somewhat higher than that found in aerogel. One possible explanation for the absence of a crossover behavior is that the channels in which the liquid flows in vycor are too small to support the relatively long-ranged flow fields (\sim hundreds of \AA 's) associated with quantized vorticity. The experimental verification of the effects of confinement on vorticity were originally done with confinement length scales on the order of 1 cm [107]. Thus an extrapolation to the length scales found in porous vycor glass (i.e. $D \sim 70 \text{ \AA}$) may be not be appropriate. Furthermore, the roton-vortex line scattering length is estimated to be about 150 \AA which is not a sensible result for helium in pores 70 \AA in diameter.

The situation for superfluid in xerogel may be different since it has somewhat larger pore sizes than vycor. Therefore trapped vorticity (and the associated roton-vortex line scattering) may be present in superfluid-filled xerogel. A complete study of the temperature-dependence of the excitations in xerogel has not been performed yet, but we

have performed a preliminary measurement at 1.7 K (not presented in this thesis) indicating that the bulk-like roton energy *does not decrease at all* (within an uncertainty of $\pm 11 \mu\text{eV}$). Since the transition temperature is about 2 K, we can estimate that the bulk-like roton energy in xerogel at 1.7 K should be lower than the low-temperature value by about $50 \mu\text{eV}$. Therefore this *may* be an indication that the bulk-like roton has a crossover behavior in its temperature dependence and we have not reached temperatures high enough to see it. If this is the case, then the temperature dependence above this crossover temperature would be even stronger than that seen in the aerogel causing the critical exponent to be larger than for helium in aerogel. This strong temperature dependence above the crossover temperature for xerogel would explain the different critical exponent observed in normal fluid fraction studies. Clearly a characterization of the temperature dependence of the bulk-like roton is necessary to establish this intriguing possibility.

A number of outstanding issues exist for the layered excitations. For instance, the temperature dependence of these excitations is unknown but assumed to display a softening like the bulk (and bulk-like) roton. A complete characterization of the temperature dependence of the layered excitations would be a difficult task given that the signal is so weak even at low temperatures but it would help to complete the microscopic picture. Matters are further complicated at higher temperatures near the transition temperature where the signature broadens, potentially making the duration of the experiment prohibitive.

Another outstanding issue is the *nature* of the layered excitations. There has been extensive theoretical development for the problem of excitations in superfluid films on ordered substrates, but few attacks have been made on the problem of superfluid excitations in disorder. The theoretical problem is no doubt formidable, but this investigation has shown that there are remarkable similarities between the microscopic dynamics of thin superfluid films and the superfluid in porous vycor and silica xerogel. While disorder is not typically treated in a perturbative fashion theoretically, perhaps in these two cases the disorder is weak enough to afford such an approach.

We conclude with a speculative comment. The motivation for the study undertaken here was to explore the microscopic effects of *disorder induced by confinement* on superfluid helium. However, all of the effects we have observed using neutron scattering can be understood in terms of *confined* but *ordered* systems. For example, the layered excitations observed in vycor and xerogel are very similar to the layered excitations observed on thin helium films which is an ordered helium system. In addition, the existence of trapped vorticity requires confinement (or turbulent flow) only but not necessarily disorder. If the origin of the superfluid transition in porous media is linked to the bulk-like roton as dictated by the Landau excitation model, then the different critical exponents should be explained by a different temperature dependence of the roton energy. Therefore it may be possible that the effects of disorder on the behavior of superfluid helium are miniscule in comparison with the simple effects of confinement.

Admittedly this is a speculative observation but, if found to be true, this could have a profound impact on the current understanding of the nature of the superfluid transition.

The number of questions discussed above is a clear indication that there is still a great deal of work, theoretical and experimental, remaining. In summary we have found that, while the confinement can have a profound influence on the excitations of superfluid helium, the modifications in the excitations are consistent with the macroscopic dynamics of the confined liquid as determined via thermodynamic and transport measurements. Therefore each of these measurements provide a much-needed link between the microscopic excitations of confined helium and the macroscopic properties which have been the subject of investigation for some time.

APPENDIX A

NEUTRON SCATTERING PARAMETERS AND CONSTANTS

The published literature is inconsistent in the use of units used in neutron scattering, especially energy. In this appendix we collect together various conversion factors and constants which proved very useful in the data reduction and analysis. All of the information presented here can be found in the standard texts on neutron scattering [82,84,85].

Energy Conversion

1 meV	$= 1.6 \times 10^{-19} \text{ J}$
1 meV	$= 11.6 \text{ K}$
1 meV	$= 0.24 \times 10^{12} \text{ Hz}$
1 meV	$= 8.07 \text{ cm}^{-1}$

1 J	$= 0.62 \times 10^{-22} \text{ meV}$
1 K	$= 0.086 \text{ meV}$
10^{12} Hz	$= 4.135 \text{ meV}$
1 cm^{-1}	$= 0.124 \text{ meV}$

Constants and Useful Combinations of Constants

$k_B = 1.38 \times 10^{-23} \text{ J/K}$	$\hbar = 1.05 \times 10^{-34} \text{ J s}$
$N_A = 6.02 \times 10^{23}$	$\hbar c = 1.97 \times 10^6 \text{ meV } \text{\AA}$
$1 \text{ amu} = 931.5 \times 10^9 \text{ meV}/c^2$	$1 \text{ barn} = 1.0 \times 10^{-24} \text{ cm}^2$

Equations

Units of quantities in equations below: λ [\AA], k [\AA^{-1}], v [km/s], E [meV]

λ [\AA]	$= 6.283 / k$
λ [\AA]	$= 3.956 / v$
λ [\AA]	$= 9.045 / \sqrt{E}$
λ [\AA]	$= 30.81 / \sqrt{T}$

E [meV]	$= 0.0862 T$
E [meV]	$= 5.227 v^2$
E [meV]	$= 81.81 / \lambda^2$
E [meV]	$= 2.072 k^2$

APPENDIX B

DATA REDUCTION AND ANALYSIS PROGRAMS

A series of general purpose utility programs were written in the IDL (Interactive Data Language) programming language. A common scattering data format was decided upon and all raw data from the instruments used in the research in this thesis were converted to this common form. A brief description of each program is listed below but, due to space limitations, the complete program listings are only available as an internal document.

Data Conversion Programs

READ_FCS.PRO

Converts data from the FCS program TOF2ASCII (which resides on the instrument computer) to standard scattering data format.

READ_IN6.PRO

Converts data from IN6 format to standard scattering data format.

READ_IRIS.PRO

Converts data from IGB2A (routine which runs in GENIE on instrument computer) to standard scattering data format. It is assumed that the data has been converted from time to energy and the vanadium calibration has been performed.

READ_SPINS.PRO

Converts data from SPINS format to standard scattering data format.

Data Reduction Programs**ABS_COR.PRO**

Corrects a data file, specifically $S(\phi, E)$, for sample attenuation if the sample is a cylinder.

Requires sample diameter and inverse absorption length. Calculation is based on the Paalman and Pings calculation for absorption in a cylindrical cell [104].

ADD_DETS.PRO

User can add any detectors together in a single data file, thus creating new groups for each sum, and write out to a new file.

APPEND_ENERGY.PRO

This set of procedures appends energies from Triple-Axis Spectrometer data. It is assumed that the data files are normalized to the same factor. In the case of the SPINS data sets, this normalization has been performed in the procedure READ_SPINS.PRO.

Note that this assumes the the files which are being appended together have NO overlapping points.

CORRECT_EFF.PRO

Corrects the data file (assumed to be already converted to energy) for detector efficiency and normalization via the vanadium run (requires the use of the .CAL file). Also this is only valid for FCS and IN6 files. Future TOF instruments will require modification of this file so that the parameter ENUM is included. This is based on the detector geometry and pressure (for He³).

DEL_GROUPS.PRO

Allows the user to write out any (or all) of the existing groups in the file to a new file. Can be used at any stage of the data reduction process. However if the data has not been converted from time to energy (and the user will eventually do so) then the user must ensure that the monitor group is written out.

DIFF2SIG.PRO

A new data file (based on an existing scattering file) is written where the difference field overwrites the signal field (same goes for the error fields) and the background and difference fields are zeroed out.

FIT_SCAT.PRO

General purpose curve fitting program. Reads in a standard scattering data file format and use can fit any number of curves to the data. Instrumental resolution can be included so that the fit function is convoluted with the instrumental resolution function.

LIMITRANGE.PRO

User can choose upper and lower time or energy limits and write out a new file with data only from those ranges.

PHI2Q.PRO

The momentum transfer field, Q , is filled in and the new data is written out to a new file.

PHI2QINVERSE.PRO

The momentum transfer field, Q , is filled in for an inverse geometry instrument and the new data is written out to a new file.

PLOTSCAT.PRO

General purpose plotting program which enables user to plot any of the fields and any number of detectors from a standard scattering file. Can be used at any step of the data reduction process.

QREBIN.PRO

Data file, $S(\phi, E)$, is rebinned onto constant Q bins resulting in $S(Q, E)$. These Q bins replace the detector groups in the new file which is written out.

REBINSCAT.PRO

User can rebin the existing scattering data from any time (energy) binning onto any new constant time (energy) grid.

SUB_BG.PRO

Reads in a background and a foreground file and writes out a file with the signal, signal error, background, background error, difference, and difference error fields filled in appropriately. The difference field is defined as the difference between the foreground and some fraction of the background (not necessarily 1) fields.

TIME2ENERGY.PRO

Reads in a TOF file, specifically $S(\phi, t)$, and converts the time channels to energy channels, $S(\phi, E)$.

TOFFSETCOR.PRO

Reads in a TOF file and subtracts of a constant value from the data in each group. This constant value is the average value of the scattering data (for that particular group) where the average is calculated over an interval of the user's choosing. Typically this should be near the end of the time series where little scattering occurs and the spectrum should be relatively flat. This correction is necessary for data involving "dark counts" as are found in a reactor-based neutron source.

VANAREA.PRO

Reads in a TOF file (should be a vanadium run not yet converted to energy) and calculates the areas under the elastic peaks in each group. Another file, ending in .CAL is written with normalized intensities (normalized with respect to the first group).

APPENDIX C

THE STATISTICAL MECHANICS OF TWO DIMENSIONAL ROTONS

In this appendix we derive expressions for the roton contribution to the heat capacity, normal fluid component, and entropy for superfluid helium with a two dimensional constraint imposed on the system. In particular we assume that the roton energy spectrum has the same functional form as in the bulk liquid,

$$\begin{aligned} E(Q) &= \Delta_{2D} + \frac{(p - p_R)^2}{2\mu} \\ &= \Delta_{2D} + \frac{\hbar^2}{2\mu} (Q - Q_R)^2 \end{aligned} \quad (C.1)$$

where Δ_{2D} is the energy of a two-dimensional roton. The calculations proceed in the same manner as Landau's original arguments [36,37] but here the integration is over a 4 dimensional phase space volume element as opposed to a 6 dimensional phase space volume element as in the case of the bulk liquid. The N-particle partition function for a non-interacting gas of 2-D rotons is given by

$$Z_N = \frac{1}{N!} \left[\int \frac{d^2r d^2p}{(2\pi\hbar)^2} e^{-\beta E(p)} \right]^N \quad (C.2)$$

where $p = \hbar Q$ and $\beta = \frac{1}{k_B T}$. We have assumed that, like their 3-D counterparts, the 2-D rotons can be treated classically. The number of rotons is found by calculating the Helmholtz free energy,

$$F = -k_B T \ln Z_N, \quad (C.3)$$

and setting the derivative with respect to N equal to zero (see p. 344 of [23], for instance). This results in the following expression for the number of rotons per unit 2-D volume (area) of

$$\begin{aligned} N_R &= \int \frac{d^2 p}{(2\pi\hbar)^2} \exp\left(-\frac{E(p)}{k_B T}\right) \\ &= \frac{1}{(2\pi\hbar)^2} \int_0^{2\pi} d\phi \int_0^\infty dp p \exp\left(-\frac{\Delta_{2D}}{k_B T}\right) \exp\left(-\frac{(p - p_R)^2}{2\mu k_B T}\right). \end{aligned} \quad (C.4)$$

As is the case for the 3-D roton gas we assume that the exponential term (in momentum) in the integral is a sharply peaked function, specifically $\frac{\mu k_B T}{\hbar^2 Q_R^2} \ll 1$, and that minimal error is introduced by replacing the exponential term by the delta function momentum distribution

$$\exp\left(-\frac{(p - p_R)^2}{2\mu k_B T}\right) \cong (2\pi\mu k_B T)^{\frac{1}{2}} \delta(p - p_R). \quad (C.5)$$

This results in a roton number per unit area ($[N_R] = 1/L^2$) of

$$N_R(T) = \left(\frac{\mu k_B T}{2\pi}\right)^{\frac{1}{2}} \frac{Q_R}{\hbar} \exp\left(-\frac{\Delta_{2D}}{k_B T}\right). \quad (C.6)$$

The heat capacity can be found using the expression above. In terms of the Helmholtz free energy, F , the heat capacity per unit area ($[C_R] = E/T \cdot L^2$) is given by

$$C_R(T) = \left(\frac{\partial U}{\partial T}\right)_v = -T \left(\frac{\partial^2 F}{\partial T^2}\right)_v, \quad (C.7)$$

which can be rewritten in terms of the roton number density as

$$C_R(T) = 2k_B T \frac{\partial N_R}{\partial T} + k_B T^2 \frac{\partial^2 N_R}{\partial T^2}. \quad (C.8)$$

The result of carrying out the necessary differentiations is

$$C_R(T) = k_B \left[\frac{3}{4} + \left(\frac{\Delta_{2D}}{k_B T} \right) + \left(\frac{\Delta_{2D}}{k_B T} \right)^2 \right] N_R^{2D}(T), \quad (C.9)$$

or with its explicit temperature dependence,

$$C_R(T) = \left(\frac{\mu}{2\pi} \right)^{\frac{1}{2}} \frac{k_B Q_R \Delta_{2D}^2}{\hbar (k_B T)^{\frac{3}{2}}} \left[1 + \left(\frac{k_B T}{\Delta_{2D}} \right) + \frac{3}{4} \left(\frac{k_B T}{\Delta_{2D}} \right)^2 \right] \exp\left(-\frac{\Delta_{2D}}{k_B T} \right). \quad (C.10)$$

Note that the temperature dependence of the heat capacity due to the 2-D roton is identical to that of the 3-D roton.

The portion of fluid that contributes to the normal fluid is determined by the density of rotons in mass motion with respect to the superfluid. For rotons moving with a drift velocity, \vec{v} , their momentum density (momentum per unit area) is expressed as $\vec{J}_r = \rho_r \vec{v}$ where ρ_r is the mass density of the rotons. In the reference frame of the rotons with drift velocity \vec{v} and energy E , the mean occupation number of energy levels $E(p)$ is $n(E - \vec{v} \cdot \vec{p})$. Thus the momentum density is calculated from the integral

$$\vec{J}_r = \frac{1}{(2\pi\hbar)^2} \int n(E - \vec{v} \cdot \vec{p}) \vec{p} d^2 p. \quad (C.11)$$

This procedure is identical to that for a 3-dimensional gas of rotons except here the volume element is A (area) and the integration is in two-dimensional momentum space.

For small drift velocities, \vec{v} , we can make the approximation

$n(E - \vec{v} \cdot \vec{p}) \cong n(E) - \vec{v} \cdot \vec{p} \frac{\partial n}{\partial E}$ where we have assumed that the rotons obey a Boltzmann distribution so that $\frac{\partial n}{\partial E} = -\beta n(E)$. This approximation is certainly valid for the 3-D rotons where $\vec{v} \cdot \vec{p} \approx 1.2 \mu\text{eV}$ and $E \approx 740 \mu\text{eV}$ and we are assuming also that it is valid for the 2-D case. The first term from the expansion vanishes due to symmetry of the integral and we are left with

$$\begin{aligned} \vec{J}_r &= \frac{\beta}{(2\pi\hbar)^2} \int n(E) \vec{p} (\vec{p} \cdot \vec{v}) d^2p \\ &= \frac{\beta}{(2\pi\hbar)^2} \int n(E) (p \cos\theta)^2 \vec{v} d^2p \end{aligned} \quad (\text{C.12})$$

from which we can extract the integral for the roton mass density

$$\rho_r = \frac{\beta}{(2\pi\hbar)^2} \int n(E) (p \cos\theta)^2 d^2p. \quad (\text{C.13})$$

The angular portion of the integral is easily found and the momentum portion is evaluated in the same manner as that leading up to (C.6) (using the approximation C.5). The final result for the normal fluid component of the density ($[\rho_R] = M/L^2$) due to rotons (i.e. $\rho_n = \rho_r$) is

$$\rho_n = \left(\frac{\mu}{8\pi k_B T} \right)^{\frac{1}{2}} \hbar Q_R^3 e^{-\frac{\Delta_{2D}}{k_B T}} \quad (\text{C.14})$$

The entropy per unit area of a two-dimensional roton gas ($[S_R] = E/T \cdot L^2$) is found using

$$\begin{aligned} S_R(T) &= - \left(\frac{\partial F}{\partial T} \right)_N \\ &= k_B N_R + k_B T \frac{\partial N}{\partial T} \end{aligned} \quad (\text{C.15})$$

which is found to be

$$S_R(T) = \frac{3k_B}{2} \left(1 + \frac{2}{3} \frac{\Delta_{2D}}{k_B T} \right) N_R^{2D}(T), \quad (\text{C.16})$$

or

$$S_R(T) = \frac{3k_B Q_R}{2\hbar} \left(\frac{\mu k_B T}{2\pi} \right)^{\frac{1}{2}} \left(1 + \frac{2}{3} \frac{\Delta_{2D}}{k_B T} \right) e^{-\frac{\Delta_{2D}}{k_B T}}. \quad (\text{C.17})$$

For convenience the important relationships for the statistical mechanics of a non-interacting gas of two-dimensional rotons along with the corresponding expressions for the three-dimensional roton case are summarized in table C.1.

Table C.1 Summary of statistical mechanics of ideal roton gases in two and three dimensions [37].

Two-Dimensional Roton Gas	Three-Dimensional Roton Gas
$N_R(T) = \left(\frac{\mu k_B T}{2\pi} \right)^{1/2} \frac{Q_R}{\hbar} e^{-\frac{\Delta_{2D}}{k_B T}}$	$N_R(T) = \left(\frac{\mu k_B T}{2\pi} \right)^{1/2} \frac{Q_R^2}{\pi \hbar} e^{-\frac{\Delta_{3D}}{k_B T}}$
$C_R(T) = k_B \left[\frac{3}{4} + \left(\frac{\Delta_{2D}}{k_B T} \right) + \left(\frac{\Delta_{2D}}{k_B T} \right)^2 \right] N_R^{2D}(T)$	$C_R(T) = k_B \left[\frac{3}{4} + \left(\frac{\Delta_{3D}}{k_B T} \right) + \left(\frac{\Delta_{3D}}{k_B T} \right)^2 \right] N_R^{3D}(T)$
$\rho_n(T) = \hbar Q_R^3 \left(\frac{\mu}{8\pi k_B T} \right)^{1/2} e^{-\frac{\Delta_{2D}}{k_B T}}$	$\rho_n(T) = \frac{2\hbar Q_R^4}{3\pi} \left(\frac{\mu}{8\pi k_B T} \right)^{1/2} e^{-\frac{\Delta_{3D}}{k_B T}}$
$S_R(T) = \frac{3k_B}{2} \left(1 + \frac{2}{3} \frac{\Delta_{2D}}{k_B T} \right) N_R^{2D}(T)$	$S_R(T) = \frac{3k_B}{2} \left(1 + \frac{2}{3} \frac{\Delta_{3D}}{k_B T} \right) N_R^{3D}(T)$

The density of states for a two-dimensional roton gas is another useful quantity and it can be found easily using the N-roton partition function. The single-roton partition function Z_1 can be evaluated explicitly using the approximation (C.5) and the N-roton partition function can be calculated using equation (C.2) or $Z_N = \frac{Z_1^N}{N!}$. The single-roton partition function is

$$Z_1 = \frac{A}{\hbar^2} \left(\frac{\mu k_B T}{2\pi} \right)^{1/2} e^{-\frac{\Delta_{2D}}{k_B T}} \quad (C.18)$$

so that

$$Z_N = \frac{A^N}{N! \hbar^{2N}} \left(\frac{\mu k_B T}{2\pi} \right)^{\frac{N}{2}} e^{-\frac{N\Delta_{2D}}{k_B T}} \quad (\text{C.19})$$

is the N-roton partition function. The density of states, $g(E)$, is found by noting that the N-particle partition function of an ideal gas can be represented by the following integral equation [26]

$$Z_N = \int_0^\infty dE g(E) e^{-\beta E}. \quad (\text{C.20})$$

Equating (C.19) and (C.20) yields the following density of roton energy states,

$$g(E) = \frac{A^N}{N! \hbar^{2N}} \left(\frac{\mu k_B T}{2\pi} \right)^{\frac{N}{2}} \delta(E - N\Delta_{2D}). \quad (\text{C.21})$$

This expression simply states mathematically that the energies each of the individual rotons are equal to Δ_{2D} which is not an unexpected result.

APPENDIX D

PROGRAM LISTING FOR FIT_SCAT.PRO

The program FIT_SCAT.PRO is listed here in its entirety since it contains useful read and write routines which are repeated in the data reduction programs discussed in APPENDIX B.

```
; FIT_SCAT.PRO
; General purpose curve fitting program.
;
; These routines read in data sets and fit them to the functions
; listed below with parameter uncertainties based on minimizing
; CHI-SQUARED. User can import an instrumental resolution function
; in the fit. User can now (12/7/98) also write out the resolution
; function from a fit.
;
; Types of functions in curve fitting:
; Gaussian:                1
; Lorentzian:              2
; Polynomial:              3
; Modified Gaussian:       4
; Helium DHO:              5
;
; When running for the first time, compile this program
; at least twice.
;
; Written by R.M.Dimeo (9/23/98)
; Modified by RMD (12/7/98)

PRO OPENFILE,FILENAME
COMMON READINFO,LUN
  OPENR, LUN, FILENAME, /GET_LUN
RETURN
END

PRO CLOSEFILE,FILENAME
COMMON READINFO,LUN
  FREE_LUN, LUN
RETURN
END

PRO SELECT_FILE,FILENAME
  cd,'d:\users\dimeo\development'
  FILENAME = "
  FILENAME = DIALOG_PICKFILE(TITLE='Select a file to plot', FILTER = '*.out')
```



```

RETURN
END

```

```

PRO READHEADER,NGROUPS,MONLOC,EO,NFIELDS,NCH,INSTRINFO,HEADER,GROUPS
; Reads header from a formatted scattering data file (assumed open).
;-----
; NGROUPS:      number of total groups in file (output)
; MONLOC:       group number containing the monitor counts (output)
; EO:           incident neutron energy (output)
; NFIELDS:      number of data fields (output)
; NCH:          vector containing the number of channels in each group (output)
; INSTRINFO:    numerical array containing instrument information (output)
; HEADER:       string array containing text information (output)
; GROUPS:       vector containing the identities of each of the groups (output)

```

```

COMMON READINFO,LUN
READF, LUN,NGROUPS,MONLOC,EO,NFIELDS
NCH=INTARR(NGROUPS)
GROUPS=INTARR(NGROUPS)
READF, LUN,NCH
READF, LUN,GROUPS
READF,LUN,"
placeholder="
INSTRINFO=FLTARR(100,5)
instdum1=0.0 & instdum2=0.0 & instdum3=0.0
instdum4=0.0 & instdum5=0.0
; Read the numerical instrument information (5 cols by 100 rows)
FOR i=0,99 DO BEGIN
  READF,LUN,instdum1,instdum2,instdum3,instdum4,instdum5
  INSTRINFO[i,0:4]=[instdum1,instdum2,instdum3,instdum4,instdum5]
ENDFOR
READF,LUN,"
HEADER=STRARR(21)
; Read the string information (20 rows of 80 character strings each)
READF,LUN,HEADER
;READF,LUN,placeholder
RETURN
END

```

```

PRO READGROUP,GRPSEL,NGRPS,DATA,NCHAN,NCH,NSEL,CURGRP,ANGLE
; Reads an individual group (identified by the integer GRPSEL)
; from a formatted scattering data file.
;-----
; GRPSEL:       selected group to read (input)
; NGRPS:        total number of groups in current file (input)
; DATA:        data in current group (output)
; NCHAN:        number (scalar) of channels in currently selected group (output)
; NCH:          vector containing the number of channels in each group (input)
; NSEL:         number of selected group currently being read (output)
; CURGRP:       number of currently selected group in file (input/output)
; ANGLE:        angle corresponding to selected group (output)

```

```

COMMON READINFO,LUN

```

```

IF CURGRP EQ -1 THEN BEGIN
  CURGRP=-1
  i=0
  NSEL=0
ENDIF

nfields=9
dum1=0.0
dumnum=0.0
NCH1=0
grp=0
angle1=0.0 & ANGLE=0.0
d1=0.0 & d2=0.0 & d3=0.0 & d4=0.0 & d5=0.0
d6=0.0 & d7=0.0 & d8=0.0 & d9=0.0
i=NSEL
WHILE CURGRP NE GRPSEL DO BEGIN
  d=FLTARR(nfields)
  READF,LUN,grp,angle1,NCH1
  CURGRP=grp
  FOR k=0,5-1 DO BEGIN
    READF,LUN,dumnum,dumnum,dumnum,dumnum,dumnum,FORMAT='(5(E15.6,x))'
  ENDFOR
  IF grp EQ GRPSEL THEN BEGIN
    time=FLTARR(NCH1) & signal=FLTARR(NCH1) & sigerr=FLTARR(NCH1)
    energy=FLTARR(NCH1) & momentum=FLTARR(NCH1)
    bg=FLTARR(NCH1) & difference=FLTARR(NCH1)
    bgerr=FLTARR(NCH1) & differr=FLTARR(NCH1)
  ENDIF
  FOR j=0,NCH1-1 DO BEGIN
    ; read the 9 fields
    READF,LUN,d1,d2,d3,d4,d5,d6,d7,d8,d9,format='(9(E15.6,x))'
    IF grp EQ GRPSEL THEN BEGIN
      time[j]=d1 & energy[j]=d2 & momentum[j]=d3 & signal[j]=d4 & sigerr[j]=d5
      bg[j]=d6 & bgerr[j]=d7 & difference[j]=d8 & differr[j]=d9
      NSEL=i
      ANGLE=angle1
    ENDIF
  ENDFOR
  dum1="
  READF,LUN,dum1
  i=i+1
ENDWHILE

DATA=FLTARR(NCH[NSEL],nfields)
DATA[0:NCH[NSEL]-1,0]=time[0:NCH[NSEL]-1]
DATA[0:NCH[NSEL]-1,1]=energy[0:NCH[NSEL]-1]
DATA[0:NCH[NSEL]-1,2]=momentum[0:NCH[NSEL]-1]
DATA[0:NCH[NSEL]-1,3]=signal[0:NCH[NSEL]-1]
DATA[0:NCH[NSEL]-1,4]=sigerr[0:NCH[NSEL]-1]*signal[0:NCH[NSEL]-1]
DATA[0:NCH[NSEL]-1,5]=bg[0:NCH[NSEL]-1]
DATA[0:NCH[NSEL]-1,6]=bgerr[0:NCH[NSEL]-1]*bg[0:NCH[NSEL]-1]
DATA[0:NCH[NSEL]-1,7]=difference[0:NCH[NSEL]-1]

```

```
DATA[0:NCH[NSEL]-1,8]=differr[0:NCH[NSEL]-1]*difference[0:NCH[NSEL]-1]
NCHAN=NCH[NSEL]
```

```
RETURN
END
```

```
PRO LOAD_SCAT,DATAOUT,NCHAN,NGRPS,DISPANGLE
; Procedure to read in data from standard scattering data
; format.
f1=0 & f2=1 & ferr=2
READ,f1,PROMPT='Enter the independent variable (0=time,1=energy,2=momentum):'
READ,f2,PROMPT='Enter the dependent variable (3=signal,5=background,7=difference):'
CASE f2 OF
  3: ferr=4
  5: ferr=6
  7: ferr=8
ENDCASE
SELECT_FILE,filename
OPENFILE,filename
READHEADER,ngrps,monloc,Eo,nfields,nch,instrinfo,header,grps
DATAOUT=FLTARR((nch[0])*ngrps,3)
curgrp=-1
dispangle=FLTARR(ngrps)
print,'Groups  Angles'
FOR i=0,ngrps-1 DO BEGIN
  READGROUP,grps[i],ngrps,DATA,nchan,nch,nsel,curgrp,angle
  DATAOUT[i*nchan:(i+1)*nchan-1,0]=DATA[0:nchan-1,f1]
  DATAOUT[i*nchan:(i+1)*nchan-1,1]=DATA[0:nchan-1,f2]
  DATAOUT[i*nchan:(i+1)*nchan-1,2]=DATA[0:nchan-1,ferr]
  dispangle[i]=angle
  print,grps[i],dispangle[i]
ENDFOR
CLOSEFILE,filename
RETURN
END
```

```
PRO SELGROUP,DATAIN,NGRPS,DISPANGLE,NCHAN,DATAOUT
; User selects a data group to view from currently
; loaded data set.
grpssel=1
GROUPS=1+INDGEN(NGRPS)
print,'Group  Angle'
FOR i=0,NGRPS-1 DO BEGIN
  print,GROUPS[i],DISPANGLE[i]
ENDFOR
DATAOUT=FLTARR(nchan,3)
READ,grpssel,PROMPT='Enter the group to analyze: '
DATAOUT[0:nchan-1,0]=DATAIN[(grpssel-1)*nchan:(grpssel)*nchan-1,0]
DATAOUT[0:nchan-1,1]=DATAIN[(grpssel-1)*nchan:(grpssel)*nchan-1,1]
DATAOUT[0:nchan-1,2]=DATAIN[(grpssel-1)*nchan:(grpssel)*nchan-1,2]
RETURN
END
```

```
PRO DISPLAY_PARDS,FITFUNCS,PARMS,NUMPARMS,FIXEDPARMS
```

```
; Unentangles the arrays carrying all of the fit information
; and prints the fits and parameters out to the screen in an
; easy-to-read way.
; FITFUNCS: identifies individual fit functions
; PARMS: parameters in individual fits
```

```
nfits=N_ELEMENTS(FITFUNCS)
nparms=INTARR(nfits)
name=""
FOR i=0,nfits-1 DO BEGIN
  name=[name],[EQNAME(FITFUNCS[i])]
  nparms[i]=NUMPARMS[i]
ENDFOR
name=name[1:n_elements(name)-1] ; remove first blank element
count=0
FOR i=0,nfits-1 DO BEGIN
  print,string(i+1)+'. '+name[i]
  FOR j=0,nparms[i]-1 DO BEGIN
    print,count,PARMS[count],FIXEDPARMS[count]
    count=count+1
  ENDFOR
  print,"
ENDFOR
RETURN
END
```

```
PRO DISPLAY_FIT_PARDS,FITFUNCS,PARMS,UNCERTAINTIES,NUMPARMS
```

```
; Unentangles the arrays carrying all of the fit information
; and prints the fits and parameters out to the screen in an
; easy-to-read way.
; FITFUNCS: identifies individual fit functions
; PARMS: parameters in individual fits
```

```
nfits=N_ELEMENTS(FITFUNCS)
nparms=INTARR(nfits)
name=""
FOR i=0,nfits-1 DO BEGIN
  name=[name],[EQNAME(FITFUNCS[i])]
  nparms[i]=NUMPARMS[i]
ENDFOR
name=name[1:n_elements(name)-1] ; remove first blank element
count=0
FOR i=0,nfits-1 DO BEGIN
  print,name[i]
  FOR j=0,nparms[i]-1 DO BEGIN
    print,string(PARMS[count])+ ' +/- '+string(DOUBLE(UNCERTAINTIES[count]))
    count=count+1
  ENDFOR
  print,"
ENDFOR
RETURN
```

END

PRO FIX_PARAMETERS,FITFUNCS,PARMS,NUMPARMS,FIXEDPARMS

DISPLAY_PARMS,FITFUNCS,PARMS,NUMPARMS,FIXEDPARMS

nsl=250

READ,nsl,PROMPT='Enter the parameter you wish to toggle (-1 to quit): '

WHILE nsl NE -1 DO BEGIN

IF FIXEDPARMS[nsl] EQ 1 THEN BEGIN

FIXEDPARMS[nsl]=0

ENDIF ELSE BEGIN

FIXEDPARMS[nsl]=1

ENDELSE

DISPLAY_PARMS,FITFUNCS,PARMS,NUMPARMS,FIXEDPARMS

READ,nsl,PROMPT='Enter the parameter you wish to toggle (-1 to quit): '

ENDWHILE

RETURN

END

PRO ADD_FIT_FUNC,FITFUNCS,PARMS,FIXEDPARMS,NUMPARMS

; User is prompted to add a fitting function from the available choices

; and enter the appropriate parameters for a first guess.

nchoices=5 ; number of choices available

FOR i=1,nchoices DO BEGIN

print,string(i+'). '+string(EQNAME(i))

ENDFOR

READ,funcselect,PROMPT='Enter your choice: '

CASE funcselect OF

1: BEGIN

IF N_ELEMENTS(PARMS) EQ 0 THEN BEGIN

PARMS=DBLARR(3)

READ,amp,wid,cen,PROMPT='Enter amp,wid,cen'

PARMS=[amp,wid,cen]

FIXEDPARMS=[1,1,1]

FITFUNCS=1

NUMPARMS=3

ENDIF ELSE BEGIN

READ,amp,wid,cen,PROMPT='Enter amp,wid,cen'

PARMS=[PARMS,amp,wid,cen]

FIXEDPARMS=[FIXEDPARMS,1,1,1]

FITFUNCS=[FITFUNCS,1]

NUMPARMS=[NUMPARMS,3]

ENDELSE

END

2: BEGIN

IF N_ELEMENTS(PARMS) EQ 0 THEN BEGIN

PARMS=DBLARR(3)

READ,amp,wid,cen,PROMPT='Enter amp,wid,cen'

PARMS=[amp,wid,cen]

FIXEDPARMS=[1,1,1]

FITFUNCS=2

NUMPARMS=3

```

ENDIF ELSE BEGIN
  READ,amp,wid,cen,PROMPT='Enter amp,wid,cen'
  PARMS=[PARMS,amp,wid,cen]
  FIXEDPARMS=[FIXEDPARMS,1,1,1]
  FITFUNCS=[FITFUNCS,2]
  NUMPARMS=[NUMPARMS,3]
ENDELSE
END
3: BEGIN
  IF N_ELEMENTS(PARMS) EQ 0 THEN BEGIN
    READ,deg,PROMPT='Degree of polynomial'
    PARMS=DBLARR(deg+1)
    FOR i=0,deg DO BEGIN
      READ,wugga,PROMPT='Enter coefficient of x^'+string(i)+' : '
      PARMS[i]=wugga
    ENDFOR
    FIXEDPARMS=REPLICATE(1,deg+1)
    PARMS=PARMS[0:deg]
    FITFUNCS=3
    NUMPARMS=deg+1
  ENDIF ELSE BEGIN
    READ,deg,PROMPT='Degree of polynomial'
    NEWPARMS=DBLARR(deg+1)
    FOR i=0,deg DO BEGIN
      READ,wugga,PROMPT='Enter coefficient of x^'+string(i)+' : '
      NEWPARMS[i]=wugga
    ENDFOR
    PARMS=[PARMS,NEWPARMS[0:deg]]
    FIXEDPARMS=[FIXEDPARMS,REPLICATE(1,deg+1)]
    FITFUNCS=[FITFUNCS,3]
    NUMPARMS=[NUMPARMS,deg+1]
  ENDELSE
END

4: BEGIN
  IF N_ELEMENTS(PARMS) EQ 0 THEN BEGIN
    PARMS=DBLARR(5)
    READ,amp,wid1,cen1,wid2,cen2,PROMPT='Enter amp,wid1,cen1,wid2,cen2'
    PARMS=[amp,wid1,cen1,wid2,cen2]
    FIXEDPARMS=[1,1,1,1,1]
    FITFUNCS=4
    NUMPARMS=5
  ENDIF ELSE BEGIN
    READ,amp,wid1,cen1,wid2,cen2,PROMPT='Enter amp,wid1,cen1,wid2,cen2'
    PARMS=[PARMS,amp,wid1,cen1,wid2,cen2]
    FIXEDPARMS=[FIXEDPARMS,1,1,1,1,1]
    FITFUNCS=[FITFUNCS,4]
    NUMPARMS=[NUMPARMS,5]
  ENDELSE
END
5: BEGIN
  IF N_ELEMENTS(PARMS) EQ 0 THEN BEGIN
    PARMS=DBLARR(4)

```

```

    READ,amp,wid,cen,temperature,PROMPT='Enter amp,wid,cen,temperature'
    PARMS=[amp,wid,cen,temperature]
    FIXEDPARMS=[1,1,1,1]
    FITFUNCS=5
    NUMPARMS=4
ENDIF ELSE BEGIN
    READ,amp,wid,cen,temperature,PROMPT='Enter amp,wid,cen,temperature'
    PARMS=[PARMS,amp,wid,cen,temperature]
    FIXEDPARMS=[FIXEDPARMS,1,1,1,1]
    FITFUNCS=[FITFUNCS,5]
    NUMPARMS=[NUMPARMS,4]
ENDELSE
END
ENDCASE
RETURN
END

```

PRO SUB_FIT_FUNC,FITFUNCS,PARMS,FIXEDPARMS,NUMPARMS
; User is prompted to subtract a fitting function from the available choices

```

ncurves=N_ELEMENTS(FITFUNCS)
nparms=INTARR(ncurves)
DISPLAY_PARMS,FITFUNCS,PARMS,NUMPARMS,FIXEDPARMS

subsel1=0
READ,subsel1,PROMPT='Enter the curve you wish to remove: (-1 to quit)'
subindex=subsel1-1 ; index of function in FITFUNCS vector user wishes to remove

```

IF subsel1 NE -1 THEN BEGIN

```

    nremparms=NUMPARMS[subindex] ; number of parameters to remove

```

; from

PARMS and FIXEDPARMS

```

; Find position in the FITFUNCS, PARMS, and FIXEDPARMS vectors
; and shorten them appropriately
FOR k=0,ncurves-1 DO BEGIN
    nparms[k]=NUMPARMS[k]
ENDFOR
TOTPARMS=TOTAL(nparms)

```

```

IF subindex EQ 0 THEN BEGIN
    FITFUNCS=FITFUNCS[1:ncurves-1]
    PARMS=PARMS[nremparms:TOTPARMS-1]
    FIXEDPARMS=FIXEDPARMS[nremparms:TOTPARMS-1]
    NUMPARMS=NUMPARMS[1:ncurves-1]
ENDIF

```

```

IF subindex EQ ncurves-1 THEN BEGIN
    FITFUNCS=FITFUNCS[0:ncurves-2]
    NUMPARMS=NUMPARMS[0:ncurves-2]
    PARMS=PARMS[0:TOTPARMS-nremparms-1]

```

```

    FIXEDPARMS=FIXEDPARMS[0:TOTPARMS-nremparms-1]
ENDIF

IF (subindex NE 0) AND (subindex NE (ncurves-1)) THEN BEGIN
    position=0
    FITFUNCS=[FITFUNCS[0:subindex-1],FITFUNCS[subindex+1:ncurves-1]]
    NUMPARMS=[NUMPARMS[0:subindex-1],NUMPARMS[subindex+1:ncurves-1]]
    FOR i=0,subindex-1 DO BEGIN
        position=position+nparms[i]
    ENDFOR
    PARMS=[PARMS[0:position-1],PARMS[position+nremparms:TOTPARMS-1]]
    FIXEDPARMS=[FIXEDPARMS[0:position-1],FIXEDPARMS[position+nremparms:TOTPARMS-1]]
ENDIF

;READ,subsell,PROMPT='Enter the curve you wish to remove: (-1 to quit)'
subindex=subsell-1      ; index of function in FITFUNCS vector user wishes to remove
ENDIF
RETURN
END

PRO CHANGE_PARMS,FITFUNCS,PARMS,FIXEDPARMS,NUMPARMS
; User can change the current parameters in the fit
print,'Current fitting parameters'
print,"
DISPLAY_PARMS,FITFUNCS,PARMS,NUMPARMS,FIXEDPARMS
READ,paramselect,value,PROMPT='Enter the parameter you wish to change and the new value: '
PARMS[paramselect]=value

RETURN
END

FUNCTION READ_DAT,filename
; Reads in three columns of data of unknown length
; but less than 50000

    OPENR, lun, filename, /GET_LUN
    nbig=50000
    x  = FLTARR(nbig)
    y  = FLTARR(nbig)
    yerr = FLTARR(nbig)
    x1  = 0.0
    y1  = 0.0
    z1  = 0.0
    count = 0
    WHILE (NOT EOF(lun)) DO BEGIN
        READF, lun, x1,y1,z1
        x[count] = x1
        y[count] = y1
        yerr[count] = z1
        count = count + 1
    ENDWHILE
    FREE_LUN, lun
    x = x[0:count-1]

```



```

y = y[0:count-1]
yerr = yerr[0:count-1]

yerr = (yerr[0:count-1])*(y[0:count-1])
; Test for zero error bars. If so then replace
; with the average of the two nearest neighbor's
; errors. This isn't a very satisfactory fix to
; the problem but the real problem lies in the
; rebinning procedure. This will be fixed at a
; later date.
zero_err_index=WHERE(yerr EQ 0.0)
nzeros=N_ELEMENTS(zero_err_index)
IF nzeros GT 0 THEN BEGIN
  FOR j=0,nzeros-1 DO BEGIN
    IF zero_err_index[j] EQ 0 THEN BEGIN
      yerr[0]=yerr[1]
    ENDIF
    IF zero_err_index[j] EQ count-1 THEN BEGIN
      yerr[count-1]=yerr[count-2]
    ENDIF
    IF zero_err_index[j] NE 0 AND zero_err_index[j] EQ count-1 THEN BEGIN
      yerr[zero_err_index[j]]=0.5*(yerr[1+zero_err_index[j]]+yerr[zero_err_index[j]-1])
    ENDIF
  ENDFOR
ENDIF
datout=DBLARR(count,3)
datout[0:count-1,0]=x[0:count-1]
datout[0:count-1,1]=y[0:count-1]
datout[0:count-1,2]=yerr[0:count-1]
RETURN,datout
END

FUNCTION READ_RES,filename
; Reads in two columns of data of unknown length
; but less than 50000. This is specifically for
; the instrumental resolution function.

OPENR, lun, filename, /GET_LUN
nbig=50000
x = FLTARR(nbig)
y = FLTARR(nbig)
x1 = 0.0
y1 = 0.0
count = 0
WHILE (NOT EOF(lun)) DO BEGIN
  READF, lun, x1,y1
  x[count] = x1
  y[count] = y1
  count = count + 1
ENDWHILE
FREE_LUN, lun
x = x[0:count-1]
y = y[0:count-1]

```

```

    datout=DBLARR(count,2)
    datout[0:count-1,0]=x[0:count-1]
    datout[0:count-1,1]=y[0:count-1]
RETURN,datout
END

```

```

PRO LOAD_DATA,dat
; Loads data set in of users choice. Must be three columns of
; data as in x,y,yerror.
CD, 'd:\users\dimeo\development'
file = DIALOG_PICKFILE(TITLE='Choose the file you wish analyze', FILTER = '*.dat')
dat=READ_DAT(file)
n=N_ELEMENTS(dat)/3
xdat=DBLARR(n)
xdat[0:n-1]=dat[0:n-1,0]
ydat=DBLARR(n)
ydat[0:n-1]=dat[0:n-1,1]
erdat=DBLARR(n)
erdat[0:n-1]=dat[0:n-1,2]
plot,xdat,ydat,psym=4
errplot,xdat,ydat-erdat,ydat+erdat
yfit=DBLARR(n)
yfit=0.0*DINDGEN(n)

RETURN
END

```

```

PRO LOAD_RES,RES
; Loads resolution function in of users choice. Must be two columns of
; data defined the same way as the data file (same domain).

file = DIALOG_PICKFILE(TITLE='Choose the resolution file', FILTER = '*.rez')
dat=READ_RES(file)
n=N_ELEMENTS(dat)/2
xres=DBLARR(n)
xres[0:n-1]=dat[0:n-1,0]
yres=DBLARR(n)
yres[0:n-1]=dat[0:n-1,1]
RES=DBLARR(n,2)
RES=dat
RETURN
END

```

```

PRO RANGE_FIT,DATA,DATAFIT
; User limits the range of the data set

n=N_ELEMENTS(DATA)/3
xdat=DBLARR(n)
xdat[0:n-1]=DATA[0:n-1,0]
ydat=DBLARR(n)
ydat[0:n-1]=DATA[0:n-1,1]
erdat=DBLARR(n)
erdat[0:n-1]=DATA[0:n-1,2]

```

```

xlo=0.0 & xhi=1.0
READ,xlo,xhi,PROMPT='Enter the limits of the fitting range (lo,hi): '
range=WHERE((xdat GT xlo) and (xdat LT xhi))
DATAFIT=DATA[MIN(range):MAX(range),0:2]
RETURN
END

```

```

;-----Fitting functions and their derivatives-----;
FUNCTION GAUSSFUN,X,A
; The gaussian distribution with A[0] the area under the
; curve, A[1] the standard deviation, and A[2] the center.
pi=!Pi
F = (A[0]/sqrt(2.0*pi*A[1]^2))*exp(-0.5*((X-A[2])/A[1])^2)
D0=F/A[0]
D1=((A[2]^2-2*A[2]*X+X^2-A[1]^2)/A[1]^3)*F
D2=((X-A[2])/A[1]^2)*F
OUTPUT=[F],[D0],[D1],[D2]
RETURN,OUTPUT
END

```

```

FUNCTION LORFUN,X,A
; The gaussian distribution with A[0] the area under the
; curve, A[1] the standard deviation, and A[2] the center.
pi=!Pi
F = (A[0]*A[1]/pi)/((X-A[2])^2+A[1]^2)
D0=F/A[0]
D1=(A[0]*((X-A[2])^2-A[1]^2)/pi)/((X-A[2])^2+A[1]^2)^2
D2=(2.0*A[0]*A[1]*(X-A[2])/pi)/((X-A[2])^2+A[1]^2)^2
OUTPUT=[F],[D0],[D1],[D2]
RETURN,OUTPUT
END

```

```

FUNCTION POLYFUN,X,A
; Polynomial function of order length of A
; A[0]+A[1]*X+A[2]*X^2+...
;
npts=N_ELEMENTS(X)
degplus1=N_ELEMENTS(A)

F=POLY(X,A)
OUTPUT=DBLARR(degplus1+1,npts)
OUTPUT[0,0:npts-1]=F[0:npts-1]
FOR m=0,degplus1-1 DO BEGIN
  OUTPUT[m+1,0:npts-1]=X^m
ENDFOR
OUTPUT=TRANPOSE(OUTPUT)
RETURN,OUTPUT
END

```

```

FUNCTION NARLINE,X,A
; For a very narrow lineshape (compared to the instrumental
; resolution) this line is approximated by a very narrow

```

```

; gaussian. The convolution is approximated using the error
; function.
COMMON FITSHARE1, FITFNCS, nparms, RANGE, DATA, RES
  pi=!Pi
  npts=N_ELEMENTS(RES)/2
  yres=RES[0:npts-1,1]
  xdat=DATA[0:npts-1,0]
  amp=A[0] & sig=A[1] & xo=A[2]
  F=0.0 & D0=0.0 & D1=0.0 & D2=0.0

  FOR i=1,npts-2 DO BEGIN
    F=F+yres[i]*(ERRORF((X-xo-xdat[i-1])/(sig*sqrt(2.0)))-$
      ERRORF((X-xo-xdat[i+1])/(sig*sqrt(2.0))))
    D1=D1+yres[i]*((X-xo-xdat[i+1])*exp(-0.5*((X-xo-xdat[i+1])/sig)^2)-$
      (X-xo-xdat[i-1])*exp(-0.5*((X-xo-xdat[i-1])/sig)^2))
    D2=D2+yres[i]*(exp(-0.5*((X-xo-xdat[i+1])/sig)^2)-exp(-0.5*((X-xo-xdat[i-1])/sig)^2))
  ENDFOR
  F=F*0.25*amp
  D0=F/amp
  D1=(amp/sqrt(8.0*pi*sig^2))*D1
  D2=(amp/sqrt(8.0*pi*sig^4))*D2
  OUTPUT=[F],[D0],[D1],[D2]
RETURN,OUTPUT
END

FUNCTION MODGAUS,x,a
; Modified Gaussian function. Gaussian and the convolution
; product of another Gaussian and a step function (resulting
; in a smoother step function) are multiplied by each other
; to yield an asymmetric gaussian.

pi=!Pi
npts=N_ELEMENTS(x)

y =DBLARR(npts)
g1 =DBLARR(npts)
f1 =DBLARR(npts)
dy1=DBLARR(npts)
dy2=DBLARR(npts)
dy3=DBLARR(npts)
dy4=DBLARR(npts)
dy5=DBLARR(npts)
amp = a[0]
wid1 = a[1]
x1 = a[2]
wid2 = a[3]
x2 = a[4]
OUTPUT=DBLARR(6,npts)

FOR i=0,npts-1 DO BEGIN
  f1[i] =.5*(1.0+ERRORF((x[i]-x1)/wid1))
  g1[i] =(amp/sqrt(2.0*pi*wid2^2))*exp(-.5*((x[i]-x2)/wid2)^2)
  y[i] =f1[i]*g1[i]

```

```

dy1[i]=y[i]/amp
dy2[i]=-(2./sqrt(pi*wid1^2))*(exp(-((x[i]-x1)/wid1)^2))*g1[i]
dy3[i]=-(2.*(x[i]-x1)/sqrt(pi*wid1^4))*(exp(-((x[i]-x1)/wid1)^2))*g1[i]
dy4[i]=((x2-2.0*x2*x[i]+(x[i])^2-wid2^2)/(wid2^3))*g1[i]*f1[i]
dy5[i]=((x[i]-x2)/wid2^2)*f1[i]*g1[i]
ENDFOR
output=TRANPOSE([y],[dy1],[dy2],[dy3],[dy4],[dy5])
RETURN,output
END

```

```

FUNCTION HEL_DHO,x,a
; Damped harmonic oscillator weighted with a Bose
; population factor. Note that the derivatives with
; respect to the fit parameters are all correct except
; for temperature. It is assumed that the temperature
; will be fixed during the fit.

```

```

pi=!Pi
npts=N_ELEMENTS(x)

```

```

y =DBLARR(npts)
dy1=DBLARR(npts)
dy2=DBLARR(npts)
dy3=DBLARR(npts)
dy4=DBLARR(npts)
Z      = a[0]
HWHM = a[1]
Eo  = a[2]
T   = a[3]

```

```

OUTPUT=DBLARR(5,npts)

```

```

FOR i=0,npts-1 DO BEGIN
y[i] =(4.0*Z*HWHM*x[i]*Eo/(pi*(1.0-exp(-11.6*x[i]/T))))/$
((x[i]^2-(Eo^2+HWHM^2))^2+(2.0*HWHM*x[i])^2)
dy1[i]=y[i]/Z
dy2[i]=(4.0*Z*x[i]*Eo/(pi*(-1.0+exp(-11.6*x[i]/T))))*$
(-x[i]^4+2.*(x[i]*Eo)^2+2.*(HWHM*x[i])^2-Eo^4+2.*(HWHM*Eo)^2+3.0*HWHM^4)/$
(x[i]^4-2.*(x[i]*Eo)^2+2.*(HWHM*x[i])^2+Eo^4+2.*(HWHM*Eo)^2+HWHM^4)^2
dy3[i]=-(4.0*Z*HWHM*x[i]/(pi*(-1.0+exp(-11.6*x[i]/T))))*$
(x[i]^4+2.*(x[i]*Eo)^2+2.*(HWHM*x[i])^2-3.0*Eo^4-2.*(HWHM*Eo)^2+HWHM^4)/$
(x[i]^4-2.*(x[i]*Eo)^2+2.*(HWHM*x[i])^2+Eo^4+2.*(HWHM*Eo)^2+HWHM^4)^2
dy4[i]=dy1[i]
ENDFOR
output=([y],[dy1],[dy2],[dy3],[dy4])
RETURN,output
END

```

```

;-----;
FUNCTION CON2FUN_NEW,X,YRES,Y
; This function returns the result of the convolution
; of two functions. The domain of each function must
; be the same. The functions' domains need NOT be symmetric

```

; about zero but their domains must include zero.

```

n=N_ELEMENTS(X)
dX=X[1]-X[0]
ycon=FLTARR(n)
ycon=CONVOL(Y,YRES[0:n-2],TOTAL(YRES[0:n-2]),center=0,EDGE_WRAP=1)
n21=WHERE(MIN(X))
XNEW=FLTARR(n)
XNEW=X+X[n21[0]]
ycon=SHIFT(ycon,-n21[0])
; The result is not necessarily folded about zero so
; that a linear interpolation is performed to get the
; proper result.
yinterp=FLTARR(n)
yinterp=INTERPOL(ycon,XNEW,X)

```

```

RETURN,yinterp
END

```

```

FUNCTION CON2FUN,X,YRES,Y
; This function returns the result of the convolution
; of two functions. The domain of each function must
; be the same. The functions' domains need NOT be symmetric
; about zero but their domains must include zero.

```

```

n=N_ELEMENTS(X)
dX=X[1]-X[0]

IF (n)MOD(2) EQ 1 THEN BEGIN
; pad the function with zeros for case where there are an odd
; number of data points
ynew=DBLARR(3*n-2)
ycon=DBLARR(3*n-2)
ynew=[REPLICATE(Y[0],n-1),y[0:n-1],REPLICATE(Y[n-1],n-1)]
ycon=CONVOL(ynew,YRES,TOTAL(YRES),center=0)
n21=WHERE(ABS(X) LE 0.5*dX)
ycon=SHIFT(ycon,-n21[0]+0)
ycon=ycon[n:2*n-1]
ENDIF ELSE BEGIN
; pad the function with zeros for case where there are an even
; number of data points
ynew=DBLARR(3*n)
ycon=DBLARR(3*n)
ynew=[REPLICATE(Y[0],n-1),y[0:n-1],REPLICATE(Y[n-1],n-1)]
ycon=CONVOL(ynew,YRES,TOTAL(YRES),center=0)
n21=WHERE(ABS(X) LE 0.5*dX)
ycon=SHIFT(ycon,-n21[0]+1)
ycon=ycon[n:2*n-1]
ENDELSE

RETURN,ycon
END

```

```

FUNCTION FITFUN,X,A
COMMON FITSHARE1, FITFNCS, nparms, RANGE, DATA, RES
; The fitting function (or sum of fitting functions).

; Test to see if a resolution function is present. If so
; then perform the convolution with the fitting functions
; and their derivatives before fitting to the data.
npts=N_ELEMENTS(DATA)/3
xdat=DATA[0:npts-1,0]
ydat=DATA[0:npts-1,1]

IF N_ELEMENTS(RES) LT 5 THEN BEGIN
  nfits=N_ELEMENTS(FITFNCS)
  DERIVATIVE=DBLARR(100)
  F=0.0
  count=0
  npold=0
  FOR i=0,nfits-1 DO BEGIN
    AA=DBLARR(nparms[i])
    npnew=nparms[i]
    AA[0:nparms[i]-1]=A[npold:npold+npnew-1]
    npold=npold+npnew
    FNCOOUT=CALL_FUNCTION(EQNAME(FITFNCS[i]),X,AA[0:nparms[i]-1])
    FOR j=0,nparms[i]-1 DO BEGIN
      DERIVATIVE[count]=FNCOOUT[j+1]
      count=count+1
    ENDFOR
    F=F+FNCOOUT[0]
  ENDFOR
  OUTPUT=[F]
  FOR i=0,count-1 DO BEGIN
    OUTPUT=[[OUTPUT],[DERIVATIVE[i]]]
  ENDFOR

ENDIF ELSE BEGIN
  yres=RES[0:npts-1,1]
  nfits=N_ELEMENTS(FITFNCS)
  DERIVATIVE=DBLARR(npts)
  DER=DBLARR(100)
  DERCON=DBLARR(npts)
  F=0.0
  count=0
  FCON=DBLARR(npts)
  F=DBLARR(npts)
  F=0.0*DINDGEN(npts)
  FNAR=0.0
  FNAR0=0.0
  npold=0
  FOR i=0,nfits-1 DO BEGIN
    IF FITFNCS[i] EQ 33 THEN BEGIN
      FNAR=DBLARR(nparms[i]+1)
      AA=DBLARR(nparms[i])
      npnew=nparms[i]

```

```

AA[0:nparms[i]-1]=A[npold:npold+npnew-1]
npold=npold+npnew

FNAR=CALL_FUNCTION(EQNAME(FITFNCS[i]),X,AA[0:nparms[i]-1])
FNAR0=FNAR0+FNAR[0]
FOR j=0,nparms[i]-1 DO BEGIN
  DER[count]=FNAR[j+1]
  count=count+1
ENDFOR
ENDIF ELSE BEGIN
  FNCOUT=DBLARR(npts,nparms[i]+1)
  AA=DBLARR(nparms[i])
  npnew=nparms[i]
  AA[0:nparms[i]-1]=A[npold:npold+npnew-1]
  npold=npold+npnew
  FNCOUT[0:npts-1,0:nparms[i]]=CALL_FUNCTION(EQNAME(FITFNCS[i]),xdat,AA[0:nparms[i]-
1])
  FOR j=0,nparms[i]-1 DO BEGIN
    DERIVATIVE[0:npts-1]=FNCOUT[0:npts-1,j+1]
    DERCON[0:npts-1]=CON2FUN_NEW(xdat,yres,DERIVATIVE)
    DER[count]=DERCON[WHERE(xdat EQ X)]
    count=count+1
  ENDFOR
  F=F+FNCOUT[0:npts-1,0]
  ENDELSE
ENDFOR
FCON=CON2FUN_NEW(xdat,yres,F)
Fsingle=FCON[WHERE(xdat EQ X)]+FNAR0
OUTPUT=[Fsingle]
FOR i=0,count-1 DO BEGIN
  OUTPUT=[[OUTPUT],[DER[i]]]
ENDFOR
ENDELSE

RETURN,OUTPUT
END

FUNCTION FITFUNS,X,A
COMMON FITSHARE1, FITFNCS, nparms, RANGE, DATA, RES
; The fitting function (sum of fitting functions and
; the individual fitting functions).

; Test to see if a resolution function is present. If so
; then perform the convolution with the fitting functions
; and their derivatives before fitting to the data.
npts=N_ELEMENTS(DATA)/3
xdat=DATA[0:npts-1,0]
ydat=DATA[0:npts-1,1]
nx=N_ELEMENTS(X)

nfits=N_ELEMENTS(FITFNCS)
yfits=DBLARR(nfits,nx)

```



```

DERIVATIVE=DBLARR(100)
F=0.0
count=0
npold=0
FOR i=0,nfits-1 DO BEGIN
  AA=DBLARR(nparms[i])
  npnew=nparms[i]
  AA[0:nparms[i]-1]=A[npold:npold+npnew-1]
  npold=npold+npnew
  FNCOUT=CALL_FUNCTION(EQNAME(FITFNCS[i]),X,AA[0:nparms[i]-1])
  yfits[i,0:nx-1]=FNCOUT[0:nx-1,0]
ENDFOR
RETURN,yfits
END

FUNCTION FEVALS,X,A
; Evaluation of fit functions for arbitrary A
COMMON FITSHARE1, FITFNCS, nparms, RANGE, DATA, RES
n=N_ELEMENTS(X)
nfits=N_ELEMENTS(FITFNCS)
y1=DBLARR(nfits,n)
Y=DBLARR(nfits,n)
FOR i=0,n-1 DO BEGIN
  Y[0:nfits-1,i]=FITFUNS(X[i],A)
ENDFOR
RETURN,Y
END

FUNCTION FEVAL,X,A
; Evaluation of fit function for arbitrary A
COMMON FITSHARE1, FITFNCS, nparms, RANGE, DATA, RES
n=N_ELEMENTS(X)
Y=DBLARR(n)
FOR i=0,n-1 DO BEGIN
  y1=FITFUN(X[i],A)
  Y[i]=y1[0]
ENDFOR
RETURN,Y
END

FUNCTION EQNAME,EQN
; Returns the name of the fit function.
;
CASE EQN OF
  1: name='GAUSSFUN'          ; Gaussian
  2: name='LORFUN'           ; Lorentzian
  3: name='POLYFUN'          ; Linear
  33: name='NARLINE'         ; Narrow lineshape
  4: name='MODGAUS'          ; Modified Gaussian (asymmetric)
  5: name='HEL_DHO'          ; Helium lineshape (DHO) with Bose population factor
ENDCASE
RETURN, name
END

```

```

PRO CHANGEVIEW,RANGE
; User can change the viewing range

xlo=0.0 & xhi=1.0 & ylo=0.0 & yhi=1.0
RANGE=DBLARR(4)
READ,xlo,xhi,ylo,yhi,PROMPT='Enter the viewing range (xlo,xhi,ylo,yhi): '
RANGE=[xlo,xhi,ylo,yhi]

RETURN
END

```

```

PRO PLOT_DAT,DATA,RANGE
; Plots the data with error bars

xlo=RANGE[0]
xhi=RANGE[1]
ylo=RANGE[2]
yhi=RANGE[3]
window,0,xsize=500,ysize=400,colors=256
npts=N_ELEMENTS(DATA)/3
xdat=DATA[0:npts-1,0]
ydat=DATA[0:npts-1,1]
erdat=DATA[0:npts-1,2]
plot,xdat,ydat,psym=4,xrange=[xlo,xhi],yrange=[ylo,yhi],xstyle=1,ystyle=1
errplot,xdat,ydat-erdat,ydat+erdat
RETURN
END

```

```

PRO FIT_IT,DATA,PARMS,UNCERTAINTIES,FIXEDPARMS
; Procedure which uses the LMFIT function to fit the
; selected curves to the data.

npts=N_ELEMENTS(DATA)/3
xdat=DBLARR(npts)
ydat=DBLARR(npts)
erdat=DBLARR(npts)
xdat=DATA[0:npts-1,0]
ydat=DATA[0:npts-1,1]
erdat=DATA[0:npts-1,2]

coefs = LMFIT(xdat, ydat, PARMS, WEIGHTS = (1.0/erdat^2), FITA = FIXEDPARMS, $
          FUNCTION_NAME = 'FITFUN',SIGMA=UNCERTAINTIES,CHISQ=chival, $
          ITMAX=50,TOL=1.0e-7)

print,'(Reduced) Chi-squared: '+string(chival/(npts-N_ELEMENTS(PARMS)))
print,'P(Chi-squared): '+string(CHISQR_PDF(chival, npts-N_ELEMENTS(PARMS)))
RETURN
END

```

```

PRO
REPLACE_GAUSS,DAT,PARMS,UNCERTAINTIES,FIXEDPARMS,NPARM,FITFUNCS,NARFLAG
; Redo the fit if any gaussians used in the fit have very narrow widths.
; Convolutions with gaussians are replaced with error functions.
COMMON FITSHARE1, FITFNCS, nparms, RANGE, DATA, RES

npts=N_ELEMENTS(DAT)/3
X=DBLARR(npts)
X=DAT[0:npts-1,0]
dX=X[1]-X[0]

; Are there any gaussians in the fit?
gausindex=WHERE(FITFNCS EQ 1)
ngaus=N_ELEMENTS(gausindex)

nfits=N_ELEMENTS(FITFUNCS)
IF (gausindex[0] NE -1) THEN BEGIN
  FOR i=0,ngaus-1 DO BEGIN
    ; Determine width of ith gaussian
    IF gausindex[i] EQ 0 THEN BEGIN
      width=PARMS[1]
    ENDIF
    IF gausindex[i] EQ nfits-1 THEN BEGIN
      width=PARMS[TOTAL(NPARM)-2]
    ENDIF
    IF ((gausindex[i] NE 0) AND (gausindex[i] EQ nfits-1)) THEN BEGIN
      position=0
      FOR j=0,gausindex[i]-1 DO BEGIN
        position=position+nparms[j]
      ENDFOR
      width=PARMS[position+1]
    ENDIF
    IF width LT 10.0*dX THEN BEGIN
      FITFUNCS[gausindex[i]]=33
      NARFLAG=1.0
    ENDIF
  ENDFOR
ENDIF

RETURN
END

PRO PLOT_FIT,DATA,PARMS,RANGE
; Plots the data with error bars

xlo=RANGE[0]
xhi=RANGE[1]
ylo=RANGE[2]
yhi=RANGE[3]
window,0,xsize=500,ysize=400,colors=256
npts=N_ELEMENTS(DATA)/3
xdat=DATA[0:npts-1,0]
ydat=DATA[0:npts-1,1]

```

```

erdat=DATA[0:npts-1,2]
plot,xdat,ydat,psym=4,xrange=[xlo,xhi],yrange=[ylo,yhi],xstyle=1,ystyle=1
errplot,xdat,ydat-erdat,ydat+erdat
yfit=DBLARR(npts)
yfit=FEVAL(xdat,PARMS)
oplot,xdat,yfit,psym=0
RETURN
END

```

```

PRO PLOT_ALL_LINES,DATA,PARMS,RANGE,FITFUNCS,NPARMS
; Plots the data with error bars, the fit to the data, and
; all of the underlying lines in the fit (shown as dashed
; lines).

```

```

xlo=RANGE[0]
xhi=RANGE[1]
ylo=RANGE[2]
yhi=RANGE[3]
nfits=N_ELEMENTS(FITFUNCS)

window,0,xsize=500,ysize=400,colors=256
npts=N_ELEMENTS(DATA)/3
xdat=DATA[0:npts-1,0]
ydat=DATA[0:npts-1,1]
erdat=DATA[0:npts-1,2]
plot,xdat,ydat,psym=4,xrange=[xlo,xhi],yrange=[ylo,yhi],xstyle=1,ystyle=1
errplot,xdat,ydat-erdat,ydat+erdat

y=DBLARR(nfits,npts)
y=FEVALS(xdat,PARMS)

yfit=DBLARR(npts)
yfit=FEVAL(xdat,PARMS)
oplot,xdat,yfit,psym=0
FOR i=0,nfits-1 DO BEGIN
  oplot,xdat[0:npts-1],y[i,0:npts-1],psym=0,linestyle=2
ENDFOR
RETURN
END

```

```

PRO WRITE_FITS,DATA,PARMS,RANGE,FITFUNCS,NPARMS
; Writes the data and all of the fits (including
; the sum of the fits) out to a text file.

```

```

nfits=N_ELEMENTS(FITFUNCS)
npts=N_ELEMENTS(DATA)/3

xdat=DATA[0:npts-1,0]
ydat=DATA[0:npts-1,1]
erdat=DATA[0:npts-1,2]

y=DBLARR(nfits,npts)
y=FEVALS(xdat,PARMS)

```

```

yfit=DBLARR(npts)
yfit=FEVAL(xdat,PARMS)

data_out1=FLTARR(npts,nfits+4)
data_out1[0:npts-1,0:2]=DATA[0:npts-1,0:2]
data_out1[0:npts-1,3]=yfit[0:npts-1]
data_out1[0:npts-1,4:4+nfits-1]=TRANSPOSE(y[0:nfits-1,0:npts-1])

filename=""
filename = DIALOG_PICKFILE(TITLE='Name of the file?',FILTER='*.fit')
OPENW, data3, filename+'.fit', /GET_LUN

FOR i=0,npts-1 DO BEGIN
  FOR j=0,4+nfits-1 DO BEGIN
    printf,data3,data_out1[i,j],format=('$,E15.6,x')
  ENDFOR
  printf,data3,"
ENDFOR
;printf,data3, data_out1
FREE_LUN, data3

RETURN
END

PRO WRITE_PARMS,FITFUNCS,NUMPARMS,PARMS,UNCERTAINTIES
; Writes the current fit information out to a file
; ending in .fit. This information can be read in
; using LOAD_PARMS.

n=N_ELEMENTS(FITFUNCS)
nfitpars=N_ELEMENTS(PARMS)
name = DIALOG_PICKFILE(TITLE='Name of the new file?')
openw, data3, name+'.fit', /GET_LUN
printf,data3,n
FOR i=0,n-1 DO BEGIN
  printf,data3,FITFUNCS[i]
ENDFOR

FOR i=0,n-1 DO BEGIN
  printf,data3,NUMPARMS[i]
ENDFOR

FOR i=0,nfitpars-1 DO BEGIN
  printf,data3,PARMS[i]
ENDFOR

FOR i=0,nfitpars-1 DO BEGIN
  printf,data3,UNCERTAINTIES[i]
ENDFOR

FREE_LUN, data3

```

```

RETURN
END

```

```

PRO LOAD_PARDS,FITFUNCS,NUMPARMS,PARMS,UNCERTAINTIES
; Reads a previously saved .fit file which
; contains the complete fit information generated
; using WRITE_PARDS.

```

```

filename = DIALOG_PICKFILE(TITLE='Select a fit file', FILTER = '*.fit')
OPENR, lun, filename, /GET_LUN

```

```

READF, lun, n
FITFUNCS=DBLARR(n)
NUMPARMS=DBLARR(n)

```

```

FOR i=0,n-1 DO BEGIN
  READF, lun,fitval
  FITFUNCS[i]=fitval
ENDFOR

```

```

FOR i=0,n-1 DO BEGIN
  READF, lun,numval
  NUMPARMS[i]=numval
ENDFOR

```

```

parmtotal=TOTAL(NUMPARMS)
PARMS=DBLARR(parmtotal)
UNCERTAINTIES=DBLARR(parmtotal)
FOR i=0,parmtotal-1 DO BEGIN
  READF,lun,parmval
  PARMS[i]=parmval
ENDFOR

```

```

FOR i=0,parmtotal-1 DO BEGIN
  READF,lun,errval
  UNCERTAINTIES[i]=errval
ENDFOR

```

```

FREE_LUN, lun

```

```

RETURN
END

```

```

PRO DEL_RES,RES
; Deletes the resolution function.
RES=0.0
RETURN
END

```

```

PRO WRITE_RES,DATA,PARMS,RANGE,FITFUNCS,NPARMS
; Writes the current domain and fit out to a .rez
; file.

```

```

nfits=N_ELEMENTS(FITFUNCS)
npts=N_ELEMENTS(DATA)/3

xdat=DATA[0:npts-1,0]
ydat=DATA[0:npts-1,1]
erdat=DATA[0:npts-1,2]
xhi=xdat[npts-1] & xlo=xdat[0]

y=DBLARR(nfits,npts)
y=FEVALS(xdat,PARMS)

yfit=DBLARR(npts)
yfit=FEVAL(xdat,PARMS)

; Ask to shift the data
resp='y'
READ,resp,PROMPT='Would you like to shift the data? (y or n): '

IF resp EQ 'y' THEN BEGIN
  eshift=0.0
  READ,eshift,PROMPT='Enter the shift: '
  xold=FLTARR(npts)
  xshift=FLTARR(npts)
  ynew=FLTARR(npts)
  FOR i=0,npts-1 DO BEGIN
    xshift[i]=xdat[i]+eshift
  ENDFOR
  ynew=INTERPOL(yfit,xshift,xdat)
ENDIF ELSE BEGIN
  ynew=FLTARR(npts)
  ynew=yfit
ENDELSE

dx=(xhi-xlo)/(npts-1)
READ,resp,PROMPT='Normalize the resolution function? (y or n): '
IF resp EQ 'y' THEN BEGIN
  normfact=dx*TOTAL(ynew)
ENDIF

data_out1=FLTARR(npts,2)
data_out1[0:npts-1,0]=DATA[0:npts-1,0]
data_out1[0:npts-1,1]=ynew[0:npts-1]

filename=""
filename = DIALOG_PICKFILE(TITLE='Name of the file?',FILTER='*.rez')
OPENW, data3, filename+'.rez', /GET_LUN

FOR i=0,npts-1 DO BEGIN
  PRINTF,data3,data_out1[i,0],data_out1[i,1],format='(2(E15.6),x)'
ENDFOR
FREE_LUN, data3

RETURN

```

```

END
;
;
;
; Main program follows
;
;
PRO FIT_SCAT
; Curve fitting program which uses the IDL routine called
; LMFIT.PRO. Reads in data created in GENDAT.PRO.

COMMON FITSHARE1, FITFNCS, nparms, RANGE, DATA, RES
RES=0.0
; Print user menu
print,"
print,'1. Load data from scattering file'
print,'2. Add fitting function'
print,'3. Delete a fitting function'
print,'4. Change fit parameters'
print,'5. Fit current setup'
print,'6. Display parameters'
print,'7. Display current fit parameters'
print,'8. Plot data'
print,'9. Write fit parameters and uncertainties to a file'
print,'10. Read fit parameters and uncertainties in from a file'
print,'11. Plot current fit on the data'
print,'12. Limit fit range'
print,'13. Fix some fit parameters'
print,'14. Change viewing range'
print,'15. Load resolution function'
print,'16. Delete resolution function'
print,'17. Plot current fit on the data with all curves shown'
print,'18. Write data and fits out to a file'
print,'19. Enter the group to analyze'
print,'20. Load data from 3-column text file'
print,'21. Write out fit as a resolution function'
print,'-1. Exit'
menselect=10
READ,menselect,PROMPT='Your choice? '
WHILE menselect NE -1 DO BEGIN

CASE menselect OF
1: BEGIN
LOAD_SCAT,DATAOUT,NCHAN,NGRPS,DISPANGLE
xlo=DATAOUT[0,0]
xhi=DATAOUT[NCHAN-1,0]
ylo=MIN(DATAOUT[0:NCHAN-1,2])
yhi=MAX(DATAOUT[0:NCHAN-1,2])
RANGE=[xlo,xhi,ylo,yhi]
END
2: BEGIN
ADD_FIT_FUNC,FITFNCS,A,fita,parms
PRINT,parms

```



```

    PLOT_FIT,DATA,A,RANGE
END
3: BEGIN
    SUB_FIT_FUNC,FITFNCS,A,fita,nparms
    PLOT_FIT,DATA,A,RANGE
END
4: BEGIN
    CHANGE_PARDS,FITFNCS,A,fita,nparms
    PLOT_FIT,DATA,A,RANGE
END
5: BEGIN
    PARMSOLD=A
    FIT_IT,datfit,A,errors,fita
    GAUSFLAG=0.0
    IF N_ELEMENTS(RES) GT 1 THEN BEGIN
        REPLACE_GAUSS,datfit,PARMSOLD,errors,fita,nparms,FITFNCS,GAUSFLAG
        IF GAUSFLAG EQ 1.0 THEN BEGIN
            FIT_IT,datfit,PARMSOLD,errors,fita
            A=PARMSOLD
        ENDIF
    ENDIF
    PLOT_FIT,DATA,A,RANGE
    DISPLAY_FIT_PARDS,FITFNCS,A,errors,nparms
END
6: BEGIN
    DISPLAY_PARDS,FITFNCS,A,nparms,fita
END
7: BEGIN
    DISPLAY_FIT_PARDS,FITFNCS,A,errors,nparms
END
8: BEGIN
    PLOT_DAT,DATA,RANGE
END
9: BEGIN
    WRITE_PARDS,FITFNCS,nparms,A,errors
END
10: BEGIN
    LOAD_PARDS,FITFNCS,nparms,A,errors
    fita=REPLICATE(1,N_ELEMENTS(A))
END
11: BEGIN
    PLOT_FIT,DATA,A,RANGE
    DISPLAY_PARDS,FITFNCS,A,nparms,fita
END
12: BEGIN
    RANGE_FIT,DATA,datfit
END
13: BEGIN
    FIX_PARAMETERS,FITFNCS,A,nparms,fita
END
14: BEGIN
    CHANGEVIEW,RANGE
END

```

```

15: BEGIN
    LOAD_RES,RES
    END
16: BEGIN
    DEL_RES,RES
    END
17: BEGIN
    PLOT_ALL_LINES,DATA,A,RANGE,FITFNCS,nparms
    END
18: BEGIN
    WRITE_FITS,DATA,A,RANGE,FITFNCS,nparms
    END
19: BEGIN
    SELGROUP,DATAOUT,NGRPS,DISPANGLE,NCHAN,DATA
    datfit=DATA
    RANGE=[min(DATA[*],0),max(DATA[*],0),min(DATA[*],1),max(DATA[*],1)]
    END
20: BEGIN
    LOAD_DATA,DATA
    datfit=DATA
    RANGE=[min(DATA[*],0),max(DATA[*],0),min(DATA[*],1),max(DATA[*],1)]
    END
21: BEGIN
    LOAD_SCAT,DATAOUT,NCHAN,NGRPS,DISPANGLE
    SELGROUP,DATAOUT,NGRPS,DISPANGLE,NCHAN,DATA
    WRITE_RES,DATA,A,RANGE,FITFNCS,nparms
    END
ENDCASE
print,"

print,'1. Load data from scattering file'
print,'2. Add fitting function'
print,'3. Delete a fitting function'
print,'4. Change fit parameters'
print,'5. Fit current setup'
print,'6. Display parameters'
print,'7. Display current fit parameters'
print,'8. Plot data'
print,'9. Write fit parameters and uncertainties to a file'
print,'10. Read fit parameters and uncertainties in from a file'
print,'11. Plot current fit on the data'
print,'12. Limit fit range'
print,'13. Fix some fit parameters'
print,'14. Change viewing range'
print,'15. Load resolution function'
print,'16. Delete resolution function'
print,'17. Plot current fit on the data with all curves shown'
print,'18. Write data and fits out to a file'
print,'19. Enter the group to analyze'
print,'20. Load data from 3-column text file'
print,'21. Write out current fit as the resolution function'
print,'-1. Exit'
READ,menselect,PROMPT='Your choice? '

```

ENDWHILE

END

APPENDIX E

LISTING OF RAW DATA FILES

The raw data files from all of the measurements performed in this thesis have been written onto a CD-ROM for permanent storage. The complete list of the files including sample details and comments is contained in the following table.

Table E.1 Raw data file listing.

Directory/File name	Sample	T (K)	Comments
SPINS-October 1996			
SPINS/ahein001.ng5	^4He in 95% aerogel	1.48	Test run
SPINS/ahein002.ng5	^4He in 95% aerogel	1.48	Test run
SPINS/ahein003.ng5	^4He in 95% aerogel	1.48	Test run
SPINS/ahein004.ng5	^4He in 95% aerogel	1.48	$Q=1.92 \text{ \AA}^{-1}$
SPINS/ahein005.ng5	^4He in 95% aerogel	1.48	$Q=1.95 \text{ \AA}^{-1}$
SPINS/ahein006.ng5	^4He in 95% aerogel	1.48	$Q=1.90 \text{ \AA}^{-1}$
SPINS/ahein007.ng5	^4He in 95% aerogel	1.48	$Q=1.85 \text{ \AA}^{-1}$
SPINS/ahein008.ng5	^4He in 95% aerogel	1.55	$Q=1.80 \text{ \AA}^{-1}$
SPINS/ahein009.ng5	^4He in 95% aerogel	1.92	$Q=1.92 \text{ \AA}^{-1}$
SPINS/ahein010.ng5	^4He in 95% aerogel	1.92	$Q=1.95 \text{ \AA}^{-1}$
SPINS/ahein011.ng5	^4He in 95% aerogel	1.92	$Q=1.90 \text{ \AA}^{-1}$
SPINS/ahein012.ng5	^4He in 95% aerogel	1.92	$Q=1.85 \text{ \AA}^{-1}$
SPINS/ahein013.ng5	^4He in 95% aerogel	1.92	$Q=1.80 \text{ \AA}^{-1}$
SPINS/ahein014.ng5	^4He in 95% aerogel	2.01	$Q=1.92 \text{ \AA}^{-1}$
SPINS/ahein015.ng5	^4He in 95% aerogel	2.01	$Q=1.95 \text{ \AA}^{-1}$
SPINS/ahein016.ng5	^4He in 95% aerogel	2.01	$Q=1.90 \text{ \AA}^{-1}$
SPINS/ahein017.ng5	^4He in 95% aerogel	2.01	$Q=1.85 \text{ \AA}^{-1}$
SPINS/ahein018.ng5	^4He in 95% aerogel	2.01	$Q=1.80 \text{ \AA}^{-1}$
SPINS/ahein019.ng5	^4He in 95% aerogel	1.92	$Q=1.92 \text{ \AA}^{-1}$
SPINS/ahein020.ng5	^4He in 95% aerogel	1.92	$Q=1.92 \text{ \AA}^{-1}$
SPINS/ahein021.ng5	^4He in 95% aerogel	1.92	$Q=1.95 \text{ \AA}^{-1}$
SPINS/ahein022.ng5	^4He in 95% aerogel	1.92	$Q=1.95 \text{ \AA}^{-1}$

Directory/Filename	Sample	T (K)	Comments
SPINS/ahein023.ng5	^4He in 95% aerogel	1.92	$Q=1.90 \text{ \AA}^{-1}$
SPINS/ahein024.ng5	^4He in 95% aerogel	1.92	$Q=1.90 \text{ \AA}^{-1}$
SPINS/ahein025.ng5	^4He in 95% aerogel	1.92	$Q=1.85 \text{ \AA}^{-1}$
SPINS/ahein026.ng5	^4He in 95% aerogel	1.92	$Q=1.85 \text{ \AA}^{-1}$
SPINS/ahein027.ng5	^4He in 95% aerogel	1.92	$Q=1.80 \text{ \AA}^{-1}$
SPINS/ahein028.ng5	^4He in 95% aerogel	1.92	$Q=1.80 \text{ \AA}^{-1}$
SPINS/ahein029.ng5	^4He in 95% aerogel	2.01	$Q=1.92 \text{ \AA}^{-1}$
SPINS/ahein030.ng5	^4He in 95% aerogel	2.01	$Q=1.92 \text{ \AA}^{-1}$
SPINS/ahein031.ng5	^4He in 95% aerogel	2.01	$Q=1.95 \text{ \AA}^{-1}$
SPINS/ahein032.ng5	^4He in 95% aerogel	2.01	$Q=1.95 \text{ \AA}^{-1}$
SPINS/ahein033.ng5	^4He in 95% aerogel	2.11	$Q=1.92 \text{ \AA}^{-1}$
SPINS/ahein034.ng5	^4He in 95% aerogel	2.11	$Q=1.95 \text{ \AA}^{-1}$
SPINS/ahein035.ng5	^4He in 95% aerogel	2.11	$Q=1.90 \text{ \AA}^{-1}$
SPINS/ahein036.ng5	^4He in 95% aerogel	2.11	$Q=1.85 \text{ \AA}^{-1}$
SPINS/ahein037.ng5	^4He in 95% aerogel	2.11	$Q=1.80 \text{ \AA}^{-1}$
SPINS/ahein038.ng5	^4He in 95% aerogel	2.01	$Q=1.90 \text{ \AA}^{-1}$
SPINS/ahein039.ng5	^4He in 95% aerogel	2.01	$Q=1.85 \text{ \AA}^{-1}$
SPINS/ahein040.ng5	^4He in 95% aerogel	2.01	$Q=1.80 \text{ \AA}^{-1}$
SPINS/ahein041.ng5	^4He in 95% aerogel	2.22	$Q=1.92 \text{ \AA}^{-1}$
SPINS/ahein042.ng5	^4He in 95% aerogel	2.22	$Q=1.80 \text{ \AA}^{-1}$

IRIS-January 1997

IRIS/Helium.txt	Bulk ^4He (Svennson)	0.5	-
IRIS/IRS13937.txt	^4He in 90% aerogel	1.55	-
IRIS/IRS13938.txt	^4He in 90% aerogel	1.55	-
IRIS/IRS13939.txt	^4He in 90% aerogel	1.55	-
IRIS/IRS13940.txt	^4He in 90% aerogel	1.70	-
IRIS/IRS13941.txt	^4He in 90% aerogel	1.70	-
IRIS/IRS13942.txt	^4He in 90% aerogel	1.70	-
IRIS/IRS13943.txt	^4He in 90% aerogel	1.70	-
IRIS/IRS13944.txt	^4He in 90% aerogel	1.70	-
IRIS/IRS13945.txt	^4He in 90% aerogel	1.70	-
IRIS/IRS13950.txt	^4He in 90% aerogel	1.90	-
IRIS/IRS13951.txt	^4He in 90% aerogel	1.90	-
IRIS/IRS13952.txt	^4He in 90% aerogel	1.90	-
IRIS/IRS13954.txt	^4He in 90% aerogel	2.06	-
IRIS/IRS13955.txt	^4He in 90% aerogel	2.06	-
IRIS/IRS13956.txt	^4He in 90% aerogel	2.06	-
IRIS/IRS13957.txt	^4He in 90% aerogel	2.06	-
IRIS/IRS13958.txt	^4He in 90% aerogel	2.06	-
IRIS/IRS13959.txt	^4He in 90% aerogel	2.06	-

Directory/File name	Sample	T (K)	Comments
IRIS/IRS13965.txt	^4He in 90% aerogel	1.98	-
IRIS/IRS13966.txt	^4He in 90% aerogel	1.98	-
IRIS/IRS13967.txt	^4He in 90% aerogel	1.98	-
IRIS/IRS13968.txt	^4He in 90% aerogel	1.98	-
IRIS/IRS13969.txt	^4He in 90% aerogel	1.98	-
IRIS/ADD155.txt	^4He in 90% aerogel	1.55	Sum of runs
IRIS/ADD17.txt	^4He in 90% aerogel	1.70	Sum of runs
IRIS/ADD190.txt	^4He in 90% aerogel	1.90	Sum of runs
IRIS/ADD198.txt	^4He in 90% aerogel	1.98	Sum of runs
IRIS/ADD206.txt	^4He in 90% aerogel	2.06	Sum of runs

IN6-October 1997

IN6/09868	Empty vycor	300	Transmission
IN6/09869	Empty vycor	T<300	Cooling
IN6/09870	Empty vycor	T<300	Cooling
IN6/09871	Empty vycor	1.6	-
IN6/09872	Empty vycor	~2	-
IN6/09873	Empty vycor	~2	-
IN6/09874	Empty vycor	~2	-
IN6/09875	Empty vycor	~2	-
IN6/09876	Empty vycor	~2	-
IN6/09877	Empty vycor	~2	-
IN6/09878	Empty vycor	~2	-
IN6/09879	Empty vycor	~2	-
IN6/09880	Empty vycor	~2	-
IN6/09881	Empty vycor	~2	-
IN6/09882	Empty vycor	~2	-
IN6/09883	Empty vycor	~2	Removed mask
IN6/09884	Filling vycor with ^4He	~2	Replaced mask
IN6/09885	Filling vycor with ^4He	~2	-
IN6/09886	^4He in vycor (full)	0.5	-
IN6/09887	^4He in vycor (full)	0.5	-
IN6/09888	^4He in vycor (full)	0.5	-
IN6/09889	^4He in vycor (full)	0.5	-
IN6/09890	^4He in vycor (full)	0.5	-
IN6/09891	^4He in vycor (full)	0.5	-
IN6/09892	^4He in vycor (full)	0.5	-
IN6/09893	^4He in vycor (full)	1.61	-
IN6/09894	^4He in vycor (full)	1.61	-
IN6/09895	^4He in vycor (full)	1.61	-
IN6/09896	^4He in vycor (full)	1.61	-

Directory/Filename	Sample	T (K)	Comments
IN6/09897	^4He in vycor (full)	1.61	-
IN6/09898	^4He in vycor (full)	1.90	-
IN6/09899	^4He in vycor (full)	1.90	-
IN6/09900	^4He in vycor (full)	1.90	-
IN6/09901	^4He in vycor (full)	1.90	-
IN6/09902	^4He in vycor (full)	1.10	-
IN6/09903	^4He in vycor (full)	1.10	-
IN6/09904	^4He in vycor (full)	1.10	-
IN6/09905	^4He in vycor (full)	1.10	-
IN6/09906	^4He in vycor (full)	1.10	-
IN6/09907	^4He in vycor (full)	~1.75	T unstable
IN6/09908	^4He in vycor (full)	~1.75	T unstable
IN6/09909	^4He in vycor (full)	~1.80	T unstable
IN6/09910	^4He in vycor (full)	~1.80	T unstable
IN6/09911	^4He in vycor (full)	1.10	T unstable
IN6/09912	Bulk ^4He	T<2.03	cooling
IN6/09913	Bulk ^4He	T<1.60	cooling
IN6/09914	Bulk ^4He	0.59	-
IN6/09915	Bulk ^4He	0.58	-
IN6/09916	Empty vycor	T<10	cooling
IN6/09917	Empty vycor	0.50	-
IN6/09918	Empty vycor	0.47	-
IN6/09919	Empty vycor	0.47	-
IN6/09920	Empty vycor	0.47	-
IN6/09921	vanadium	300	-
IN6/09922	Vanadium	300	-

FCS-July 1998

FCS/mt_cool.txt	Empty Britesorb	T<300	cooling
FCS/bil_baset.txt	^4He in Britesorb-25% full	1.36	-
FCS/full_17.txt	^4He in Britesorb-95% full	1.7	-
FCS/full_baset.txt	^4He in Britesorb-95% full	1.36	-
FCS/quin_baset.txt	^4He in Britesorb-60% full	1.36	-
FCS/sept_baset.txt	^4He in Britesorb-80% full	1.36	-
FCS/tril_baset.txt	^4He in Britesorb-40% full	1.36	-
FCS/mt_xero.txt	Empty Britesorb	1.36	-

FCS-August 1998

FCS/Bulk.fcs	Bulk ^4He	1.36	-
FCS/mtcell.txt	Empty cell	1.36	-
FCS/vanadium.txt	Vanadium cylinder	1.36	-

REFERENCES

- [1]. Tilley, D.R. & Tilley, J. *Superfluidity and Superconductivity* (Institute of Physics Publishing, Bristol, 1990).
- [2]. Hendry, P.C., Lawson, N.S., Lee, R.A.M., McClintock, P.V.E. & Williams, C.D.H. *Nature* **368**, 315(1994).
- [3]. Sokol, P.E., Silver, R.N. & Clark, J. in *Momentum Distributions* (eds Silver, R.N. & Sokol, P.E.) 1-35 (Plenum, New York, 1989).
- [4]. Ahlers, G. in *Quantum Liquids* (eds Ruvalds, J. & Regge, T.) 1-26 (North Holland, New York, 1978).
- [5]. Cowley, R.A. & Woods, A.D.B. *Can.J.Phys.* **49**, 177(1971).
- [6]. Hertz, J. *Physica Scripta* **T10**, 1-43 (1985).
- [7]. Careri, G. *Order and Disorder in Matter* (Benjamin/Cummings, Menlo Park, 1984).
- [8]. Jones, W. & March, N.H. *Theoretical Solid State Physics: Non-equilibrium and disorder* (Dover, New York, 1985).
- [9]. De Gennes, P.G. & Prost, J. *The Physics of Liquid Crystals* (Oxford University Press, Oxford, 1995).
- [10]. Huse, D.A., Fisher, M.P.A. & Fisher, D.S. *Nature* **358**, 553(1992).
- [11]. Bishop, D.J., Gammel, P.L., Huse, D.A. & Murray, C.A. *Science* **255**, 165-172 (1992).
- [12]. Charnaya, E.V., Kumzerov, Y.A., Tien, C. & Wur, C.S. *Solid State Communications* **94**, 635-641 (1995).
- [13]. Lambert, B., Salin, D., Joffrin, J. & Scherm, R. *Journal de Physique* **38**, L377-L380(1977).
- [14]. Reut, L.S. & Fisher, I.Z. *Soviet Physics JETP* **33**, 981-983 (1971).
- [15]. Edwards, D.O., Eckardt, J.R. & Gasparini, F.M. *Phys.Rev.A* **9**, 2070-2077 (1974).
- [16]. Saam, W.F. & Cole, M.W. *Phys.Rev.B* **11**, 1086-1105 (1975).

- [17]. Rutledge, J.E., McMillan, W.L. & Mochel, J.M. Phys.Rev.B **18**, 2155-2168 (1978).
- [18]. Chester, M. & Eytel, L. Phys.Rev.B **13**, 1069-1076 (1976).
- [19]. Lauter, H.J., Frank, V.L.P., Godfrin, H. & Leiderer, P. in *Elementary Excitations in Quantum Fluids* (eds Ohbayashi, K. & Watabe, M.) Vol.1, 99-104 (Springer-Verlag, Berlin Heidelberg, 1989).
- [20]. Lauter, H.J., Godfrin, H. & Leiderer, P. J.Low Temp.Phys. **87**, 425(1992).
- [21]. Clements, B.E., Krotscheck, E. & TYMCZAK, C.J. Phys.Rev.B **53**, 12253-12275 (1996).
- [22]. Clements, B.E., Godfrin, H., Krotscheck, E., et al. Phys.Rev.B **53**, 12242-12252 (1996).
- [23]. Goodstein, D.L. *States of Matter* (Prentice Hall, New Jersey, 1975).
- [24]. Wilks, J. *The Properties of Liquid and Solid Helium* (Clarendon Press, Oxford, 1967).
- [25]. Glyde, H.R. & Svensson, E.C. in *Methods of Experimental Physics Vol. 23B* (eds Price, D.L. & Skold, K.) 303 Academic Press, New York, 1987).
- [26]. Pathria, R.K. *Statistical Mechanics* (Butterworth-Heinemann, Oxford, 1972).
- [27]. Huang, K. *Statistical Mechanics* (Wiley, New York, 1987).
- [28]. London, F. *Superfluids, Vol. 2* (Wiley, New York, 1954).
- [29]. Anderson, M.H., Ensher, J.R., Matthews, M.R., Wieman, C.E. & Cornell, E.A. Science **269**, 198(1995).
- [30]. Feynman, R.P. in *Reports on Progress in Low Temperature Physics* 17-53 (North Holland, 1955).
- [31]. Feynman, R.P. & Cohen, M. Phys.Rev. **102**, 1189(1956).
- [32]. Feynman, R.P. Phys.Rev. **90** , 1116(1953).
- [33]. Hohenberg, P.C. & Platzman, P.M. Phys.Rev. **152**, 198-200 (1966).
- [34]. Sokol, P.E. in *Bose-Einstein Condensation* (ed Griffin, A.) 51 Cambridge, N.Y., 1995).

- [35]. Wyatt, A.F.G. *Nature* **391**, 56-58 (1998).
- [36]. Landau, L.D. *J.Phys.USSR* **5**, 71(1941).
- [37]. Landau, L. *J.Phys.USSR* **11**, 91(1947).
- [38]. Donnelly, R.J., Donnelly, J.A. & Hills, R.H. *J.Low Temp.Phys.* **44**, 471-489 (1981).
- [39]. Bendt, P.J., Cowan, R.D. & Yarnell, J.L. *Phys.Rev.* **113**, 1386(1959).
- [40]. Glyde, H.R. & Griffin, A. *Phys.Rev.Lett.* **65**, 1454-1457 (1994).
- [41]. Montfrooij, W. & Svensson, E.C. *Czech.J.Phys.* **46**, 259-260 (1996).
- [42]. Ruvalds, J. *Phys.Rev.Lett.* **27**, 1769-1771 (1971).
- [43]. Bedell, K., Pines, D. & Fomin, I.A. *J.Low Temp.Phys.* **48**, 417-433 (1982).
- [44]. Titulaer, U.M. & Deutch, J.M. *Phys.Rev.A* **10**, 1345-1354 (1974).
- [45]. Donnelly, R.J. & Roberts, P.H. *J.Low Temp.Phys.* **27**, 687-736 (1977).
- [46]. Bedell, K., Pines, D. & Zawadowski, A. *Phys.Rev.B* **29**, 102-122 (1984).
- [47]. Landau, L.D. & Khalatnikov, I.M. *Zh.Eksp.Teor.Fiz.* **19**, 637(1949).
- [48]. Andersen, K.H. & Stirling, W.G. *J.Phys.:Condens.Matter* **6**, 5805-5822 (1994).
- [49]. Williams, G.A. *J.Low Temp.Phys.* **89**, 91(1993).
- [50]. Williams, G.A. *Phys.Rev.Lett.* **68**, 2054(1992).
- [51]. Williams, G.A. *Phys.Rev.Lett.* **71**, 392-390 (1993).
- [52]. Snow, W.M., Wang, Y. & Sokol, P.E. *Europhysics Letters* **19; 5**, 403-408 (1992).
- [53]. Yoon, J. & Chan, M.H. *Phys.Rev.Lett.* **78**, 4801-4804 (1997).
- [54]. Levitz, P., Ehret, G., Sinha, S.K. & Drake, J.M. *J.Chem.Phys* **95**, 6151-6161 (1991).
- [55]. FRICKE, J. *Journal of Non-Crystalline Solids* **100**, 169-173 (1988).
- [56]. Shafer, M.W., Awschalom, D.D., Warnock, J. & Ruben, G. *J.Appl.Phys.* **61**, 5438(1987).

- [57]. Awschalom, D.D., Warnock, J. & Schafer, M.W. *Phys.Rev.Lett.* **57**, 1607(1986).
- [58]. Berg, K.A., Witt, R.H. & Derolf, R. inventor. PQ Corporation, assignee. US Patent #5,149,553. Pennsylvania, USA. 5,149,553. (1991).
- [59]. Molz, E., Wong, A.P.Y., Chan, M.H.W. & Beamish, J.R. *Phys.Rev.B* **48**, 5741-5750 (1993).
- [60]. Ginzburg, V.L. & Sobyenin, A.A. *Sov.Phys.JETP Lett.* **15**, 242-240 (1972).
- [61]. Seidel, G.M., Maris, H.J., Williams, F.I.B. & Gordon, J.G. *Phys.Rev.Lett.* **56**, 2380-2382 (1986).
- [62]. Brown, D.W., Sokol, P.E., Clarke, A.P., Alam, M.A. & Nuttal, W.J. *Journal of Physics: Condensed Matter* **9**, 7317-7325 (1997).
- [63]. Bellissent-Funel, M.-C., Lal, J. & Bosio, L. *J.Chem.Phys.* **98 No. 5**, 4246-4252 (1993).
- [64]. Brunauer, S., Emmett, P.H. & Teller, E. *J.Amer.Chem.Soc.* **60**, 309-300 (1938).
- [65]. Schirato, B.S., Fang, M.P., Sokol, P.E. & Komarneni, S. *Science* **267**, 369-371 (1995).
- [66]. Sokol, P.E., Dimeo, R.M., Kent, T., Azuah, R. & Stirling, W.G. *Bull.Am.Phys.Soc.* **43**, 267-267 (1998).
- [67]. Chan, M.H.W., Blum, K.I., Murphy, S.Q., Wong, G.K.S. & Reppy, J.D. *Phys.Rev.Lett.* **61**, 1950(1988).
- [68]. Chan, M.H.W. *Physica B* **169**, 135-143 (1991).
- [69]. Reppy, J.D. *J.Low Temp.Phys.* **87**, 205-206 (1992).
- [70]. Kiewiet, C.W., Hall, H.E. & Reppy, J.D. *Phys.Rev.Lett.* **35**, 1286(1975).
- [71]. Brewer, D.F., Symonds, A.J. & Thomson, A.L. *Phys.Rev.Lett.* **15**, 182-184 (1965).
- [72]. Crowell, P.A., Reppy, J.D., Mukherjee, S., Ma, J., Chan, M.H.W. & Schaefer, D.W. *Phys.Rev.B* **51**, 12721-12736 (1995).
- [73]. De Kinder, J., Coddens, G. & Millet, R. *Z.Phys.B* **95**, 511-514 (1994).

- [74]. Coddens, G., De Kinder, J. & Millet, R. *Journal of Non-Crystalline Solids* **188**, 41-45 (1995).
- [75]. Gibbs, M.R., Sokol, P.E., Stirling, W.G., Azuah, R.T. & Adams, M.A. *J.Low Temp.Phys.* **107**, 33-49 (1997).
- [76]. Sokol, P.E., Gibbs, M.R., Stirling, W.G., Azuah, R.T. & Adams, M.A. *Nature* **379**, 616-618 (1996).
- [77]. Kosterlitz, J.M. & Thouless, D.J. *J.Phys.C: Solid State Phys.* **5**, L124(1972).
- [78]. Kosterlitz, J.M. & Thouless, D.J. *J.Phys.C: Solid State Phys.* **6**, 1181(1973).
- [79]. Atkins, K.R. *Can.J.Phys.* **31**, 1165-1169 (1953).
- [80]. Padmore, T.C. *Phys.Rev.Lett.* **32**, 826-829 (1974).
- [81]. Thomlinson, W., Tarvin, J.A. & Passel, L. *Phys.Rev.Lett.* **44**, 266-269 (1980).
- [82]. Windsor, C.G. *Pulsed Neutron Scattering* (Taylor & Francis Ltd, Halsted Press, London, New York, 1981).
- [83]. Sears, V.F. in *Methods of Experimental Physics Vol. 23a* (eds Price, D.L. & Skold, K.) Academic Press, New York, 1987).
- [84]. Squires, G.L. *Introduction to the Theory of Thermal Neutron Scattering* (Cambridge University Press, Cambridge, London, New York, Melbourne, 1978).
- [85]. Lovesey, S.W. *Theory of Neutron Scattering from Condensed Matter* (Clarendon Press, Oxford, 1984).
- [86]. Van Hove, L. *Phys.Rev.* **95**, 249-262 (1954).
- [87]. Egelstaff, P.A. *An introduction to the Liquid State* (Academic Press, 1967).
- [88]. Callen, H. & Welton, T.A. *Phys.Rev.* **83**, 34-40 (1951).
- [89]. Callen, H. in *Fluctuation, Relaxation, and Resonance In Magnetic Systems* (ed Ter Haar, D.) 15-23 (1962).
- [90]. Kubo, R. *J.Phys.Soc.Jpn.* **12**, 570-586 (1957).
- [91]. Zwanzig, R. in *Statistical Mechanics* (eds Rice, Freed & Light) 229-239 (University of Chicago Press, 1972).
- [92]. Tarvin, J.A. & Passell, L. *Phys.Rev.B* **19**, 1458-1462 (1979).

- [93]. Talbot, E.F., Glyde, H.R., Stirling, W.G. & Svensson, E.C. *Phys.Rev.B* **38**, 11229-11244 (1988).
- [94]. Yurke, B. *Am.J.Phys.* **52**, 1099-1102 (1984).
- [95]. Yurke, B. *Am.J.Phys.* **54**, 1133-1139 (1986).
- [96]. Chaikin, P.M. & Lubensky, T.C. *Principles of Condensed Matter Physics* (Cambridge University Press, Cambridge, 1995).
- [97]. Halley, J.W. & Hastings, R. *Phys.Rev.B* **15**, 1404-1414 (1977).
- [98]. Cooper, M.J. & Nathans, R. *Acta.Cryst.* **23**, 357-367 (1967).
- [99]. Esch, L.J., Bischoff, F.G. & Moore, W.E. *Nuc.Inst.Meth.* **95**, 125-130 (1971).
- [100]. Bischoff, F.G., Yeater, M.L. & Moore, W.E. *Nucl.Sci.Eng.* **48**, 266-280 (1972).
- [101]. Carlile, C.J. & Adams, M.A. *Physica B* **182**, 431-440 (1992).
- [102]. Andersen, K.H., Bossy, J., Cook, J.C., Randl, O.G. & Ragazzoni, J.-L. *Phys.Rev.Lett.* **77**, 4043-4045 (1996).
- [103]. Crevecoeur, R., Smorenburg, H.E., De Schepper, I.M., Montfrooij, W. & Svensson, E.C. *Czech.J.Phys.* **46**, 257-258 (1996).
- [104]. Paalman, H.H. & Pings, C.J. *J.Appl.Phys.* **33**, 2635-2639 (1962).
- [105]. R.A.Cowley & A.D.B.Woods. *Can.J.Phys.* **49**, 177-200 (1971).
- [106]. Roberts, P.H. & Donnelly, R.J. *J.Low Temp.Phys.* **15**, 1-27 (1974).
- [107]. Awschalom, D.D. & Schwarz, K.W. *Phys.Rev.Lett.* **52**, 49(1984).
- [108]. Rayfield, G.W. & Reif, F. *Phys.Rev.* **136**, A1194-A1190(1964).
- [109]. Samuels, D.C. & Donnelly, R.J. in *Excitations in 2D and 3D Quantum Fluids* (eds Wyatt, A.J. & Lauter, H.J.) Plenum, New York, 1991).
- [110]. Morgan, C.J., Jackson, H.W. & Werner, S.A. *Phys.Rev.B* **18**, 2145-2154 (1978).
- [111]. Dimeo, R.M., Sokol, P.E., Anderson, C.R., Stirling, W.G. & Adams, M.A. to appear in *J.Low Temp.Phys.* (1998).
- [112]. Wong, G.K.S., Crowell, P.A., Cho, H.A. & Reppy, J.D. *Phys.Rev.B* **48**, 3858(1993).

- [113]. Brooks, J.S. & Donnelly, R.J. J.Phys.Chem.Ref.Data **6**, 51(1977).
- [114]. Plantevin, O., Fak, B., Glyde, H.R., Bossy, J. & Beamish, J.R. Phys.Rev.B **57**, 10 775-10 784(1998).
- [115]. Anderson, C.R., Stirling, W.G., Andersen, K.H., et al. in preparation (1998).
- [116]. Brewer, D.F. J.Low Temp.Phys. **3**, 205-224 (1970).
- [117]. Tait, R.H. & Reppy, J.D. Phys.Rev.B **20**, 997-1019 (1979).
- [118]. Andersen, K.H., Stirling, W.G., Scherm, R., et al. J.Phys.:Condens.Matter **6**, 821-834 (1994).
- [119]. Andersen, K.H. A Neutron Scattering Study of Liquid Helium-4. (1991). University of Keele.
- [120]. Dimeo, R.M., Sokol, P.E., Anderson, C.R., Stirling, W.G., Andersen, K.H. & Adams, M.A. Phys.Rev.Lett. **81**, 5860-5863 (1998).
- [121]. Lauter, H.J., Godfrin, H., Frank, V.L.P. & Leiderer, P. Phys.Rev.Lett. **68**, 2484-2480 (1992).
- [122]. Donnelly, R.J. *Quantized Vortices in Helium II* (Cambridge University Press, Cambridge, 1991).

VITA

Robert M. Dimeo

Born	January 13, 1969 in New Hartford, NY
Education	Ph.D. Physics, The Pennsylvania State University M.S. Electrical Engineering, The Pennsylvania State University, 1994 B.S. Physics The Pennsylvania State University, 1991
Honors	1997 Penn State Physics Graduate Student Outstanding Teaching Award
Employment	Graduate Research Assistant (Penn State): 1997-1998 Graduate Teaching Assistant (Penn State): 1996-1997 Graduate Assistant (Argonne National Lab): 1994-1995

Selected Publications

Localized Collective Excitations in Superfluid Helium in Vycor, R.M. Dimeo, P.E. Sokol, C.R. Anderson, W.G. Stirling, K.H. Andersen, and M.A. Adams, Phys. Rev. Lett. **81**, 5860 (1998).

Confinement Effects on Superfluid Helium, R.M. Dimeo, P.E. Sokol, C.R. Anderson, W.G. Stirling, and M.A. Adams, J. Low Temp. Phys. **113**, 369 (1998).

Confinement effects on the roton in helium, Sokol, P.E., Dimeo, R.M., Brown, D.W., Stirling, W.G., Anderson, C.R., Adams, M.A., and Lee, S.H., Physica B **241-243**, 929 (1998).

The Momentum Distribution of ^3He , Dimeo, R.M., Sokol, P.E., Stirling, W.G., Azuah, R.T., Bennington, S.M., and Guckelsberger, K., Physica B **241-243**, 952 (1998).

Effects of Disorder on the Collective Excitations in Helium, R.M. Dimeo, P.E. Sokol, D.W. Brown, C.R. Anderson, W.G. Stirling, M.A. Adams, S.H. Lee, C. Rutiser, and S. Komarneni, Phys. Rev. Lett. **79**, 5274 (1997).

The Dynamic Physics Virtual Learning Environment, R.M. Dimeo and P.E. Sokol, Phys. Teach. **35**, 84 (1997).

National Television Appearance

ABC Sports broadcast of Penn State vs. Wisconsin football game, November 22, 1997, demonstrating consequences of high-impact inelastic corporeal collisions in violent pursuit-evasion games. Featuring Brent Musberger, Ron Dayne, and Paul Sokol.